Vilnius University

Topological Phenomena In Driven Quantum Gases

Jakov Braver

DOCTORAL DISSERTATION
2025

Natural Sciences
Physics **N 002**

https://doi.org/10.15388/vu.thesis.860
https://orcid.org/0000-0002-7598-2569

VILNIUS UNIVERSITY
CENTER FOR PHYSICAL SCIENCES AND TECHNOLOGY

Jakov Braver

Topological Phenomena In Driven Quantum Gases

DOCTORAL DISSERTATION

Natural Sciences,
Physics (N 002)

VILNIUS 2025

The dissertation was prepared between 2021 and 2025 at the Vilnius University, Institute of Theoretical Physics and Astronomy.
The research was supported by the Research Council of Lithuania.

Academic Supervisor — **Prof. Dr. Egidijus Anisimovas** (Vilnius University, Natural Sciences, Physics, N 002).

Dissertation Defence Panel:

Chairman — **Dr. Vidas Regelskis** (Vilnius University, Natural Sciences, Physics, N 002).
Members:
Prof. Dr. Darius Abramavičius (Vilnius University, Natural Sciences, Physics, N 002),
Prof. Dr. Kęstutis Aidas (Vilnius University, Natural Sciences, Physics, N 002),
Dr. Arkadiusz Kosior (University of Innsbruck, Natural Sciences, Physics, N 002),
Dr. Viktor Novičenko (Vilnius University, Natural Sciences, Physics, N 002).

The dissertation shall be defended in a public meeting of the Dissertation Defence Panel at 14:00 on 15 December 2025 in Room A101 of the National Center for Physical Sciences and Technology.
Address: Saulėtekio av. 3, Vilnius, Lithuania.

The text of this dissertation can be accessed at the Vilnius University Library as well as on the website of Vilnius University:
`www.vu.lt/lt/naujienos/ivykiu-kalendorius/20251215`

https://doi.org/10.15388/vu.thesis.860
https://orcid.org/0000-0002-7598-2569

VILNIAUS UNIVERSITETAS
FIZINIŲ IR TECHNOLOGIJOS MOKSLŲ CENTRAS

Jakov Braver

Topologiniai reiškiniai žadinamose kvantinėse dujose

DAKTARO DISERTACIJA

Gamtos mokslai,
Fizika (N 002)

VILNIUS 2025

Disertacija rengta 2021–2025 metais Vilniaus universiteto Teorinės fizikos ir astronomijos institute.
Mokslinius tyrimus rėmė Lietuvos mokslo taryba.

Mokslinis vadovas – **prof. dr. Egidijus Anisimovas** (Vilniaus universitetas, gamtos mokslai, fizika, N 002).

Gynimo taryba:
Pirmininkas – **dr. Vidas Regelskis** (Vilniaus universitetas, gamtos mokslai, fizika, N 002).
Nariai:
prof. dr. Darius Abramavičius (Vilniaus universitetas, gamtos mokslai, fizika, N 002),
prof. dr. Kęstutis Aidas (Vilniaus universitetas, gamtos mokslai, fizika, N 002),
dr. Arkadiusz Kosior (Insbruko universitetas, gamtos mokslai, fizika, N 002),
dr. Viktor Novičenko (Vilniaus universitetas, gamtos mokslai, fizika, N 002).

Disertacija ginama viešame Gynimo tarybos posėdyje 2025 m. gruodžio mėn. 15 d. 14 val. Nacionaliniame fizinių ir technologijos mokslų centre A101 auditorijoje.
Adresas: Saulėtekio al. 3, Vilnius, Lietuva.

Disertaciją galima peržiūrėti Vilniaus universiteto bibliotekoje ir Vilniaus universiteto interneto svetainėje adresu:
`www.vu.lt/lt/naujienos/ivykiu-kalendorius/20251215`

Contents

Introduction

The search for universal principles in physics has long relied on symmetry and conservation laws to classify and understand different states of matter. In recent decades, however, it has become clear that another organising principle — topology — plays a central role in shaping quantum phenomena [1, 2]. Unlike geometric properties, which can change continuously, topological characteristics remain invariant under continuous deformations, making them robust descriptors of physical systems. This robustness has profound implications in quantum theory, where *topological invariants* govern the stability of quantum states and phases of matter.

A prominent example is the integer quantum Hall effect [3], in which the Hall conductance is quantised in integer multiples of e^2/h (elementary charge squared divided by the Planck's constant), each integer corresponding to a sum of integer topological invariants known as the *Chern numbers* [4, 5]. Remarkably, topology ensures the quantisation of a macroscopic quantity rather than a microscopic one (such as the energy of a single atom). By encoding global properties of wave functions and Hamiltonians, it offers a powerful lens through which to classify and predict exotic phases of matter, often beyond the reach of classical paradigms.

A particularly versatile platform to explore topological effects is offered by ultracold atomic gases in optical lattices [6], where properties of the system can be engineered and probed with high controllability [7, 8]. Optical lattices and artificial gauge fields [9–12] allow for the simulation of band structures with tuneable topology [13–16], while advanced detection techniques provide access to the geometric and topological properties of quantum states. Crucially, ultracold atom experiments are not limited by impurities or lattice defects inherent in solid-state materials, making them uniquely suited for exploring topological phenomena under clean and adjustable conditions.

Beyond static systems, the role of external driving has opened new avenues for engineering topological phases. Periodic driving, formalised through Floquet theory, provides a route to dynamically modify band structures [17] and

induce effective Hamiltonians that host nontrivial topological properties [18–24]. This approach, known as *Floquet engineering*, has enabled the realisation of phases such as Floquet fractional Chern insulators [20, 25, 26], Floquet topological insulators [27, 28], and anomalous Floquet topological insulators [18, 29–31], the latter ones having no static counterparts. Moreover, the interplay between periodic driving and symmetry breaking has led to the discovery of *discrete time crystals* — phases of matter that spontaneously break the externally imposed discrete time translation symmetry into one with a larger period [32, 33]. Recent developments in time-crystal research [34–37] include the study of *time crystalline structures* — closed quantum systems that are driven by time-periodic external signals — with the aim to take advantage of thereby induced regular periodic repetition observed in the time domain. In this way, time is endowed with properties of an extra coordinate axis. In such scenarios [38, 39], the time-periodic structure is indeed imposed externally; here one does not need to rely on the favourable role of particle interactions for its spontaneous formation. Nevertheless, the manifestation of the periodic regularity in the time domain is no less intriguing due to its ability to simulate the familiar spatially periodic solid state systems and phenomena of the condensed-matter realm. Systematic studies resulted in a growing list of condensed-matter phases reproduced or generalised in the time domain: Anderson-localised and many-body-localised states, Mott insulator states, as well as topological phases have been reported [38–48]. A further extension was provided by the proposal of time-space crystalline structures [49] that combine periodicity in time and in space. Viewed as an introduction of synthetic dimensions, such time-space lattices pave the way to potential doubling of the number of dimensions.

Another rich manifestation of topology in quantum physics emerges through *topological defects*. They arise when the order parameter, which characterises the state of the system, cannot be made continuous everywhere due to underlying topological constraints. These defects cannot be removed by local perturbations, as their existence is tied to the global structure of the order-parameter space. In condensed matter systems, topological defects manifest in various forms in ferromagnets, crystals, and superfluids [50, 2]. In the context of superfluids and atomic Bose–Einstein condensates, the quintessential topological defects are vortices, characterised by quantised circulation and phase winding of the order parameter [51]. The study of vortices has broad implications, ranging from quantum turbulence [52, 53] to connections with superconductivity [54] and the structure of neutron stars [55–57].

This brief overview of the field highlights a multitude of paradigms involved in our present understanding of different states of matter. It is the aim of the present thesis to push the understanding further by drawing connections

between them, using topology as a unifying principle. In particular, we will consider manifestations of topological phenomena in Floquet-engineered phases, namely the time-space crystalline structures, elucidating the role of time in systems with synthetic dimensions. We will also explore the properties of unconventional, strongly localised vortices in Bose–Einstein condensates, which, although not topologically stable, will be stabilised by external driving.

Main objectives

The thesis achieves four specific objectives:

1. Realise the Thouless pumping in the time-space crystalline structures. The following tasks were carried out:
   (a) Formulate a model of a one-dimensional crystal that allows for a realisation of the spatial Thouless pumping and incorporates driving terms featuring an adiabatic phase.
   (b) Find the parameter regimes such that the tunnelling between sites of both the spatial and the temporal lattices is sufficient for particle transport.
   (c) Study the pumping dynamics by tracking the spatially and temporally localised Wannier functions.
2. Propose a realisation of a topologically nontrivial eight-dimensional quantum system. The following tasks were carried out:
   (a) Formulate a model of a particle in a driven one-dimensional crystal that incorporates two adiabatic phases and contains topologically nontrivial quasienergy bands.
   (b) Obtain a corresponding tight-binding Hamiltonian $\hat{H}_{\mathrm{TB}}$ and decompose it into two parts describing, respectively, the spatial and the temporal lattices.
   (c) Confirm that each of the obtained Hamiltonians describes topologically nontrivial systems by simulating Thouless pumping.
   (d) Find parameter regimes such that when two copies of $\hat{H}_{\mathrm{TB}}$ are combined, the resulting (quasi)energy spectrum remains gapped.
3. Develop a method for perturbative calculation of quasienergy spectra for the case of resonant driving. The following tasks were carried out:
   (a) Study the structure of the quasienergy operator in the extended Floquet–Hilbert space and find a transformation that isolates the degeneracies caused by the resonant driving.

(b) Derive the perturbative expansion for the transformed quasienergy operator.

(c) Test the accuracy of the theory by applying it to a resonantly driven many-body quantum system.

4. Propose a method for stabilising tightly localised vortices in multicomponent Bose–Einstein condensates and study their properties. The following tasks were carried out:

   (a) Formulate an optical setup that allows for the creation of vortices in multicomponent Bose–Einstein condensates.

   (b) Study the resulting stationary states of the condensate.

   (c) Find the regimes such that the ground state contains a localised vortex in one of the components.

   (d) Probe the superfluid properties of the system by using the localised vortex as an impurity stirring the condensate, and find the critical superfluid velocity.

Scientific novelty and relevance

The thesis presents the following novel developments:

1. Exploration of topological phenomena in the temporal dimension and in dimensions beyond three (Chapters 2 and 3). The Thouless pumping along the temporal dimension is demonstrated using a specific quantum system realisable using ultracold atoms in optical lattices. Two-dimensional pumping along the spatial and the temporal axes is studied, which is directly related to the four-dimensional quantum Hall effect. The analysis is extended to incorporate two physical spatial dimensions, resulting in an effectively eight-dimensional topologically nontrivial system. Analysis of the system is facilitated by rewriting the system Hamiltonian in a tight-binding form, thereby putting space, time, and the additional synthetic dimensions on an equal footing. The exploitation of the time as an additional dimension and, more generally, emulation of high-dimensional systems in low-dimensional settings is seen as an important step towards learning to use the synthetic dimensions for practical purposes [58–61, 49, 62, 63]. The temporal Thouless pumping — proposed and studied for the first time by the author and co-workers in Ref. [P1] and described in Chapter 2 — has since been realised in a classical system in Ref. [64].

2. Extended degenerate perturbation theory for the Floquet–Hilbert space enabling more efficient construction of effective Hamiltonians for reson-

antly driven systems (Chapter 4). This is especially relevant for many-body quantum systems, where resonances are inevitable due to the dense energy spectrum. Calculation of effective Hamiltonians is essential for the analysis of many intriguing dynamical quantum many-body effects such as prethermalisation [65–70], localisation [71–75], as well as emergence of discrete time crystals [76, 32, 33, 77–81] and topological states [18, 20, 19, 28, 82].

3. Investigation of optically created vortices in a trapped multicomponent Bose–Einstein condensate (Chapter 5). Creation of tightly localised vortices in one of the components is presented using an optical setup. The external driving allows for the stabilisation of unusual vortex configurations that are not topologically stable. A localised vortex can be moved around the trap, thereby stirring the other component. This can be used to probe the superfluid nature of the condensate using a novel type of impurity — one that is rotating around its axis. Both general studies of vortices in the condensates [83–90] and movement of impurities therein [91–99] stand as central topics in the field of Bose–Einstein condensation.

Statements of the thesis

1. An adiabatic variation of the phase of the periodic driving acting on particles in a periodic potential (for example, ultracold atoms in an optical lattice) manifests itself in the topological pumping in the temporal dimension.

2. Spatial and temporal periodicity of a quantum system, unified in the framework of time-space crystalline structures, allows one to realise a topologically nontrivial eight-dimensional system using only two physical spatial dimensions — without the use of internal quantum states.

3. The developed extended degenerate perturbation theory for the Floquet–Hilbert space surpasses the conventional degenerate perturbation theory in terms of accuracy while requiring less computational effort than the exact approach, thus providing a practical method for calculating quasienergy spectra of periodically and resonantly driven quantum many-body systems.

4. The interaction of multicomponent Bose–Einstein condensates with Laguerre–Gaussian beams allows for the stabilisation of tightly localised vortices, which can be created in a controllable manner.

Part I

Topological phenomena in time-space crystalline structures

CHAPTER 1

Topological aspects of the quantum Hall effect

The present chapter serves as an introduction of the main topological concepts used throughout the thesis. This brief review mostly concerns the integer quantum Hall effect, which highlights the implications of topology on the properties of quantum gases.

1.1 The integer quantum Hall effect

Consider a gas of electrons confined in a two-dimensional (2D) sample placed in a magnetic field $\boldsymbol{B}$ perpendicular to its surface. As in the classical Hall experiment, one is to apply a voltage drop in the x-direction and measure the resulting Hall voltage in the y-direction, as shown in Fig. 1.1. In such a setup, the quantities of central interest are the resistivity and conductivity tensors. Specifically, the Ohm's law $\rho \boldsymbol{j} = \boldsymbol{E}$ is expressed in components as

$$\begin{pmatrix} \rho_{xx} & \rho_{xy} \\ -\rho_{xy} & \rho_{yy} \end{pmatrix} \begin{pmatrix} j_x \\ j_y \end{pmatrix} = \begin{pmatrix} E_x \\ E_y \end{pmatrix}, \tag{1.1}$$

where $\boldsymbol{j}$ is the current density, ρ is the resistivity tensor, and $\boldsymbol{E}$ is the electric field in the sample [100, 101]. In the framework of the classical Drude theory [102, 101], the motion of an electron inside the sample is described by the equation

$$m\frac{\mathrm{d}\boldsymbol{v}}{\mathrm{d}t} = -e\boldsymbol{E} - e\boldsymbol{v} \times \boldsymbol{B} - \frac{m}{\tau}\boldsymbol{v}, \tag{1.2}$$

where m and $\boldsymbol{v}$ are the electron's mass and velocity, respectively, and e is the elementary charge. The scattering of electrons is accounted for by the mean free time τ. The electric current density is then given by $\boldsymbol{j} = -e\varrho\boldsymbol{v}$, where ϱ is

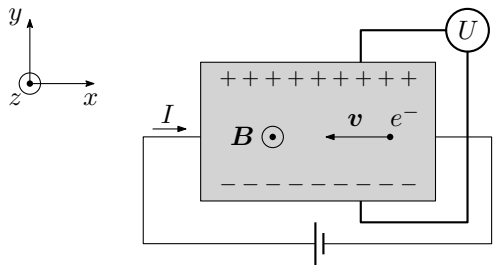

Figure 1.1: A basic setup of the Hall-effect experiment.

the electron density. It follows immediately that in the steady state (such that $\frac{\mathrm{d}\boldsymbol{v}}{\mathrm{d}t} = 0$) the longitudinal resistivity reads

$$\rho_{xx} = \frac{m}{e^2 \varrho \tau}, \tag{1.3}$$

while the transverse resistivity is given by

$$\rho_{xy} = \frac{B_z}{e\varrho}. \tag{1.4}$$

The non-zero value of the latter quantity is responsible for the classical Hall effect. At the most elementary level, one may assume that $j_y = 0$ in the steady state, yielding the transverse electric field

$$E_y = \frac{B_z}{e\varrho} j_x. \tag{1.5}$$

Integrating (along y) over the width of the sample w, we find the well-known relation

$$U_{\mathrm{H}} = \frac{B_z}{e\varrho} I, \tag{1.6}$$

where $U_{\mathrm{H}} = -E_y w$ is the Hall voltage and I is the current along the sample.

Thus, the classical prediction is that ρ_{xx} is independent of the strength of the magnetic field, while ρ_{xy} depends linearly on B_z. However, experiments using semiconducting heterostructure devices [103] have revealed that in strong magnetic fields ($> 1\,\mathrm{T}$) and at low temperatures (mK regime), ρ_{xy} depends on B_z in a step-like fashion, as shown in Fig. 1.2. Moreover, when ρ_{xy} reaches a plateau, the longitudinal resistivity ρ_{xx} vanishes, leading to dissipationless flow of current (for a related recent experiment see, e.g., Ref. [104]). Authors of the original experiment [3] have recognised that the value of ρ_{xy} on the plateau is given by the simple expression

$$\rho_{xy} = \frac{2\pi\hbar}{e^2} \frac{1}{c}, \tag{1.7}$$

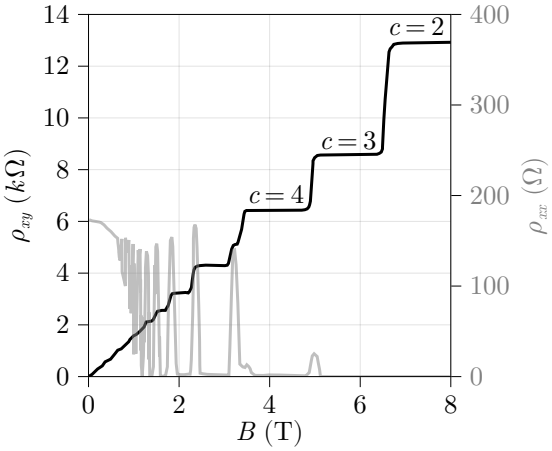

Figure 1.2: Experimental data of measurements of ρ_{xy} and ρ_{xx}, adapted from Ref. [105]. The values of c [see Eq. (1.7)] for some of the plateaus are indicated.

where c is an integer. Remarkably, the resistivity of the sample is quantised and is given in terms of fundamental constants, with no dependency on the properties of the sample.

Shortly after the experimental observation, a full quantum-mechanical treatment of the problem has been performed [4] using the linear response theory for the 2D non-interacting electron gas moving in a periodic (crystal) potential in the presence of an external magnetic field. In modern terminology, the result is stated as follows [106, 101]. First, let us consider a gas of noninteracting electrons in a periodic potential without the magnetic field. At zero temperature, the ground state is constructed by consecutively filling the energy bands, starting from the lowest one. The conductivity tensor[1)], characterising the response of the system to an external electric field, can be calculated using the current–current correlation function. The Hall conductivity $\sigma_{\mathrm{H}} \equiv -\sigma_{xy}$ reads

$$\sigma_{\mathrm{H}} = \frac{e^2}{2\pi\hbar} \sum_{n \in \text{filled}} \nu_1^{(n)}, \tag{1.8}$$

where the summation is over the filled bands. The quantities being summed are the so-called *first Chern numbers*, which are integer-valued topological invariants characterising the energy bands. The first Chern number of the nth energy band is given by

$$\nu_1^{(n)} = \frac{1}{2\pi} \int_{T^2} \mathrm{d}^2 k \, \Omega^{(n)}_{k_x k_y}(\boldsymbol{k}), \tag{1.9}$$

[1)] The conductivity tensor σ is the inverse of the resistivity tensor ρ, so that $\sigma_{xy} = \frac{-\rho_{xy}}{\rho_{xx}^2 + \rho_{xy}^2}$. On a plateau, $\rho_{xx} = 0$ leading to $\sigma_{xy} = -\frac{1}{\rho_{xy}}$.

where the integrand is the *Berry curvature*

$$\Omega^{(n)}_{k_x k_y}(\boldsymbol{k}) = \partial_{k_x} A^{(n)}_{k_y}(\boldsymbol{k}) - \partial_{k_y} A^{(n)}_{k_x}(\boldsymbol{k}) \tag{1.10}$$

defined in terms of the *Berry connection*

$$A^{(n)}_{k_i}(\boldsymbol{k}) = -\mathrm{i}\langle u^{(n)}_{\boldsymbol{k}} | \partial_{k_i} u^{(n)}_{\boldsymbol{k}} \rangle. \tag{1.11}$$

Here $|u^{(n)}_{\boldsymbol{k}}\rangle$ is the cell-periodic part of the Bloch state-vector, while $\boldsymbol{k}$ denotes the 2D quasimomentum lying in the Brillouin zone $0 < k_x, k_y < 2\pi/a$, with a being the period of the potential. The Brillouin zone is thus a two-torus (T^2). We also adopt the notation $|\partial_{k_i} u^{(n)}_{\boldsymbol{k}}\rangle \equiv \partial_{k_i} |u^{(n)}_{\boldsymbol{k}}\rangle$.

Importantly, σ_{H} is odd under time reversal, meaning that a nonzero value of σ_{H} can be obtained only if the Hamiltonian of the system breaks the time reversal symmetry [107, 108]. The external magnetic field, present in the quantum Hall experiments, plays precisely the role of breaking this symmetry, leading to nonzero Hall response. In a magnetic field, the spectrum of a 2D electron consists of equidistant Landau levels separated by $\hbar\omega_{\mathrm{c}}$, where $\omega_{\mathrm{c}} = eB/m$ is the cyclotron frequency. Each level has a macroscopically large degeneracy of $\mathcal{N} = eBS/2\pi\hbar$ states, where S is the area to which the electron's motion is restricted [109, 101]. Upon imposing a periodic potential

$$U(x, y) = 2U_0 \left(\cos\frac{2\pi x}{a} + \cos\frac{2\pi y}{a} \right), \tag{1.12}$$

one finds that, in the weak-field limit ($U_0 \ll \hbar\omega_{\mathrm{c}}$), the energy spectrum can only be calculated if the magnetic flux $\Phi = Ba^2$ piercing an elementary lattice cell can be expressed as a rational number: $\Phi = \frac{p}{q}\Phi_0$, where $\Phi_0 = 2\pi\hbar/e$ is the flux quantum, while p and q are coprime integers [110, 111, 4]. In this case, each Landau level broadens and splits into p subbands, leading to a peculiar fractal structure of the energy spectrum when plotted as a function of Φ_0/Φ, as shown in Fig. 1.3. The equations (1.8)–(1.11) are then directly applicable for each subband with the following modification: the quasimomenta now lie in a magnetic Brillouin zone such that $0 < k_x < 2\pi/qa$ and $0 < k_y < 2\pi/a$, while the Bloch modes in the coordinate representation, $u^{(r)}_{\boldsymbol{k}}(\boldsymbol{x}) = \langle \boldsymbol{x} | u^{(r)}_{\boldsymbol{k}} \rangle$, are now defined in a magnetic unit cell $0 < x < qa$ and $0 < y < a$. However, in this case the Chern number $\nu^{(r)}_1$ for the rth subband ($r = 1, \ldots, p$) can be more easily calculated from the Diophantine equation [4]

$$r = s_r q + t_r p, \qquad |s_r| < \frac{p}{2}, \tag{1.13}$$

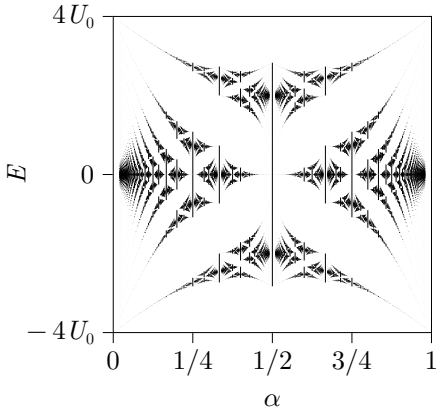

Figure 1.3: Hofstadter's butterfly [110] — the energy spectrum of a particle in a magnetic field with a simultaneously imposed periodic potential. The problem contains a duality leading to a double interpretation of the spectrum [111, 4, 112, 113]: Assuming the parameter α on the abscissa is the inverse magnetic flux Φ_0/Φ, the spectrum shows the splitting of a Landau level in the presence of a weak periodic potential, $U_0 \ll \hbar\omega_c$. Alternatively, taking the parameter α to represent the magnetic flux Φ/Φ_0, the figure displays the splitting of the tight-binding Bloch band caused by a weak magnetic field ($U_0 \gg \hbar\omega_c$). The displayed spectrum is calculated at a set of rational values $\alpha = p/q$, with $1 \leq p < q \leq 49$. For each value of α, exactly q subbands separated by gaps emerge (however, for q even, the subbands touch at $E = 0$ [111]).

having unique integer solutions[2)] (s_r, t_r). The Chern numbers are then given by $\nu_1^{(r)} = t_r - t_{r-1}$ (with $t_0 = 0$), while the integers t_r yield the Hall conductivities (1.8) for r filled subbands since $t_r = \sum_{i=1}^{r} \nu_1^{(i)}$. Solving Eq. (1.13) for $r = p$, we find that the sum of the Chern numbers of all subbands constituting a Landau level is equal to one: $t_p = 1$. Each fully filled Landau level thus contributes a Chern number of one, explaining the relation (1.7) — since $c = \sum_{n\in\text{filled}} \nu_1^{(n)}$, this number is simply the number of fully filled Landau levels.

In the pioneering experiments [3, 105], the splitting of the Landau levels into subbands could not be observed — even though the periodic potential broadens the levels, the resulting bandwidths are too small to be detected. The total bandwidth is suppressed by the factor of order $\mathrm{e}^{-\Phi_0/\Phi}$ (see, e.g., Refs. [112, 114]; this factor is normalised away in Fig. 1.3), and for a lattice constant of 2 Å and magnetic field of 10 T one finds $\Phi_0/\Phi \sim 10^4$. Observation of the fractal spectrum therefore requires creating structures with increased lattice constant. This has been achieved in Ref. [115] using patterned semiconductor heterostructures with periodicity of ~ 100 nm, allowing for reaching $\Phi_0/\Phi \sim 0.5$ and detecting the large gaps between the subbands in the vicinity of

[2)] There are no solutions when $r = p/2$ with p even, consistent with the fact that the middle subbands touch and close the gap at $E = 0$ (see Fig. 1.3).

$\alpha = 1/2$ (see Fig. 1.3). Another observation of the spectrum has been reported in Ref. [113] with the help of graphene sheets, realising the so-called moiré lattice with a periodicity of $a \sim 15\,\mathrm{nm}$.

In the opposite case of a strong periodic field ($U_0 \gg \hbar\omega_\mathrm{c}$), one can concentrate on the tight-binding limit described by the Hamiltonian of the form

$$\hat{H} = \sum_{\langle ij \rangle} J_{ij} \hat{a}_i^\dagger \hat{a}_j, \tag{1.14}$$

where $\hat{a}_i^\dagger$ and $\hat{a}_i$ are creation and annihilation operators acting on the ith lattice site, J_{ij} is the tunnelling strength, and summation is performed over all nearest neighbours (a 2D square lattice is assumed in what follows). The energy dispersion relation (with no magnetic field present) of the corresponding Bloch band then follows as

$$E(k_x, k_y) = 2U_0(\cos k_x a + \cos k_y a), \tag{1.15}$$

where we assumed $J_{ij} = U_0$. In the presence of a magnetic flux per plaquette equal to $\Phi = \frac{p}{q}\Phi_0$, the Bloch band splits into q subbands, again yielding a fractal energy spectrum [110]. It has exactly the same appearance as shown in Fig. 1.3, this time plotted as a function of Φ/Φ_0. The Hall conductivity can likewise be found from the Diophantine equation (1.13), except that t_r, rather than s_r, is constrained according to $|t_r| < q/2$, and $r = 1, \ldots, q$ [4]. Solving this modified equation for $r = q$, we find that the sum of the Chern numbers of all subbands constituting the Bloch band vanishes: $t_q = 0$.

The physics of the tight-binding limit have been experimentally simulated using ultracold atoms in optical lattices, with the effect of the magnetic field realised via an artificial gauge field [116, 14, 15]. Such an approach allows one to engineer the flux Φ directly (rather than tuning a and B), which is encoded in the phase of the complex tunnelling strengths J_{ij}. In these experiments, the ratio Φ/Φ_0 can be tuned in the full range from 0 to 1; the value of $\Phi/\Phi_0 = 1/4$ has been realised in the experiment of Ref. [16], and the Chern number of the lowest subband has been measured.

We note in passing that the appearance of a fractal spectrum in physical systems does not necessarily require the presence of a magnetic field, either real or synthetic one. For example, as shown in Ref. [117], a simple one-dimensional tight-binding lattice model with uniform and real hopping strengths and modulated onsite energies $V_j = V\cos(2\pi\alpha j)$ leads to an energy spectrum similar to the Hofstadter one when plotted as a function of the rational parameter α.

So far, we have considered the case when a number of Landau levels (or the constituent subbands) are fully filled. However, the extended plateaus in

Fig. 1.2 clearly show that each quantised value of ρ_{xy} persists over a wide range of magnetic fields, i.e., even when the filling of the levels is varied. This feature can be explained by disorder present in the system [103, 101]. Disorder broadens the Landau levels, but also results in the emergence of two kinds of states: localised ones, which do not contribute to conductivity, and extended ones, which do contribute. Suppose now that the lowest Landau level is fully filled, resulting in $\rho_{xy} = 2\pi\hbar/e^2$, and we begin filling the second level[3)]. We have to start filling the states in the lower 'tail' of the second Landau level, which, however, correspond to localised states and therefore do not contribute to conductivity and do not change the value of ρ_{xy}. Only when we fill all the localised states in the tail and start populating the extended states does the value of ρ_{xy} start to change. It should be noted, however, that effects other than disorder can also give rise to the plateaus, and the full picture is considerably more complicated [118, 119].

1.2 The relevance of topology

Let us now discuss the mathematical structure of Eqs. (1.9)–(1.11). The Berry connection (1.11) corresponds to a one-form (we omit the band index n)

$$A = -\mathrm{i}\,\langle u_{\boldsymbol{k}} | \mathrm{d}u_{\boldsymbol{k}} \rangle \tag{1.16}$$

defining a connection on the principal fibre bundle[4)] $P(M, \mathrm{U}(1))$, where the base manifold M is a two-torus in k-space [120]. Here d is the exterior derivative operator in k-space, so that $|\mathrm{d}u_{\boldsymbol{k}}\rangle = |\partial_{k_i} u_{\boldsymbol{k}}\rangle \mathrm{d}k^i$; henceforth we adopt the repeated indices summation convention. The curvature two-form is then given by $\Omega = \mathrm{d}A$ and the first Chern number is expressed as

$$\nu_1 = \frac{1}{2\pi} \int_M \Omega. \tag{1.17}$$

This formulation closely resembles the description of electromagnetism, provided we identify A with the electromagnetic gauge potential one-form and Ω with the electromagnetic field two-form.

[3)] In the semiconductor-based experiments, this can be accomplished by decreasing B, thus reducing the degeneracy of the lowest Landau level and hence transferring electrons to the second level. Alternatively, one can directly increase the number of carriers in the sample, as has been done in the original experiment [3] by changing the gate voltage in a MOSFET device.

[4)] To specify the bundle, we add that the *total space* is the manifold of states $\mathrm{e}^{\mathrm{i}\varphi}|u_{\boldsymbol{k}}\rangle$ with $\varphi \in [0, 2\pi)$ and $\boldsymbol{k} \in M$; the *projection* is given by $\pi(\mathrm{e}^{\mathrm{i}\varphi}|u_{\boldsymbol{k}}\rangle) = \boldsymbol{k}$; the *fibre at* $\boldsymbol{k}$ is the manifold of states $\mathrm{e}^{\mathrm{i}\varphi}|u_{\boldsymbol{k}}\rangle$ with $\varphi \in [0, 2\pi)$; the *typical fibre* F is topologically a unit circle S^1; the *structure group* G is U(1). Since F is isomorphic to G, we are dealing with a *principal* fibre bundle. A specific choice of φ for every $\boldsymbol{k}$, described by a function $\varphi(\boldsymbol{k})$, corresponds to fixing the gauge and provides a *section* on M.

Notably, $\int_M \Omega = \int_{\partial M} A$ by Stokes theorem (where ∂M is the boundary of M), which seems to imply $\nu_1 = 0$ when M is a closed surface, since such a surface has no boundary ($\partial M = \emptyset$) [120]. A famous 'counter-example' is provided by Dirac's magnetic monopole characterised, by convention, by the field two-form[5] $\Omega = \frac{g}{4\pi} \mathrm{d}\cos\theta \wedge \mathrm{d}\varphi$, where g is the 'magnetic charge' [121]. A direct evaluation of the integral (1.17) over a sphere S^2 yields[6] $\nu_1 = g/2\pi$, which is not identically zero. Moreover, since this integral is the Chern number, the quantity $g/2\pi$ has to be quantised (in units of the magnetic charge, since this is the dimension of our Ω). The failure of the Stokes theorem is explained by recalling that it is valid only if A is well-defined everywhere in M. In the usual problems in electromagnetism, the gauge potential A can indeed be defined globally, implying trivial topology of the associated fibre bundle. In case of the field created by the Dirac monopole, the gauge potential A cannot be well-defined globally and we are forced to introduce at least two potentials. For example, we can use $A_{\mathrm{S}} = \frac{g}{4\pi}(\cos\theta - 1)\mathrm{d}\varphi$, which is well-defined everywhere except the south pole ($\theta = \pi$), and $A_{\mathrm{N}} = \frac{g}{4\pi}(\cos\theta + 1)\mathrm{d}\varphi$, which is well-defined everywhere except the north pole ($\theta = 0$). The two potentials have to be related by a gauge transformation: $A_{\mathrm{N}} = A_{\mathrm{S}} + \mathrm{d}f$ corresponding to the transformation of the wave function $\psi \to \psi \mathrm{e}^{\mathrm{i}\frac{e}{\hbar}f(\boldsymbol{r})}$. The evaluation of the integral in (1.17) in terms of A then proceeds by splitting the integral over S^2 into a surface area S_{N} surrounding the north pole and the rest if the sphere:

$$\begin{aligned} \int_M \Omega &= \int_{(S^2 - S_{\mathrm{N}})} \Omega + \int_{S_{\mathrm{N}}} \Omega = \int_{\partial(S^2 - S_{\mathrm{N}})} A_{\mathrm{S}} + \int_{\partial S_{\mathrm{N}}} A_{\mathrm{N}} \\ &= \int_{\partial S_{\mathrm{N}}} (A_{\mathrm{N}} - A_{\mathrm{S}}) = \int_{\partial S_{\mathrm{N}}} \mathrm{d}f. \end{aligned} \tag{1.18}$$

Here the gauge potentials are well-defined in their respective integration domains, allowing one to use the Stokes theorem. To compute the final integral, we note that the single-valuedness of the wave function requires that the change of the phase factor $\frac{e}{\hbar}f$ accumulated along a closed path be equal to an integer multiple of 2π. Thus,

$$\nu_1 = \frac{1}{2\pi} \int_{\partial S_{\mathrm{N}}} \mathrm{d}f = \frac{\hbar}{e} n, \quad n \in \mathbb{Z}, \tag{1.19}$$

explicitly showing the quantisation of the Chern number. Combined with our

[5] Such an expression implies the magnetic field $\boldsymbol{B} = \frac{g}{4\pi r^2}\boldsymbol{e}_r$, where $\boldsymbol{e}_r$ is the unit vector in the radial direction. The magnetic charge therefore has the unit of weber in the convention used here.

[6] The fibre bundle relevant for the problem of a magnetic monopole is also a principal U(1) bundle. This time the base manifold is the Euclidean space with the origin excluded: $M = \mathbb{R}^3 \backslash \{0\}$. However, this space is *of the same homotopy type* as S^2, which allows us to set $M = S^2$ as far as the calculation of the Chern number is concerned [120].

previous result ($\nu_1 = g/2\pi$) this leads to Dirac's charge quantisation condition $g = \frac{2\pi\hbar}{e}n$. Alternatively, assuming g is known, this allows one to find n.

Crucially, the result (1.19) does not depend on the specific functional dependencies of A_S and A_N since the calculation ultimately amounts to an integration of $\mathrm{d}f$ around the singular point (the north pole in the gauge chosen above). Therefore, the value of ν_1 will remain unchanged under arbitrary deformation of Ω provided the number of singular points remains unchanged.

The quantum Hall effect is likewise a manifestation of nontrivial topology of the fibre bundle in question. Namely, the nonzero Chern number indicates that the connection (1.16) cannot be well-defined for all points in the BZ simultaneously [106]. An important consequence of the topological nature of the effect is its robustness against perturbations: The value of the Chern number depends on the eigenstates but not the eigenenergies; hence even if the spectrum of the Hamiltonian changes, the Hall conductance remains the same [122]. The only restriction on the change of the Hamiltonian is that the energy band under consideration remains separated from the other bands by a gap [107].

1.3 Topological pumping

The non-trivial topology of the bands also manifests itself in the phenomenon of the *quantised particle transport*, also known as Thouless, topological, or adiabatic pumping [123, 124]. Let us consider a 1D quantum particle described by $\hat{H} = \frac{\hat{p}^2}{2m} + V$ localised in a single site of a periodic potential

$$V(x) = V_\mathrm{S}\cos^2(sx) + V_\mathrm{L}\cos^2(x + \varphi_x). \tag{1.20}$$

Here s is an integer controlling the number of sites per unit cell of a lattice; the case $s = 2$ is shown in Fig. 1.4(a). By adiabatically changing the phase φ_x from 0 to π, it is possible to transport the particle by one period of the lattice. More generally, the displacement (in units of the lattice period) per one pumping cycle of a particle in the nth band of the lattice is given by the first Chern number [125–127]:

$$\nu_1^{(n)} = \frac{1}{2\pi}\int_0^{2\pi}\mathrm{d}k_x\int_0^{\pi}\mathrm{d}\varphi_x\,\Omega^{(n)}_{k_x\varphi_x}(k_x,\varphi_x). \tag{1.21}$$

Here $\Omega^{(n)}_{k_x\varphi_x}(k_x,\varphi_x)$ is the Berry curvature calculated according to (1.10), with φ_x playing the role of k_y. Explicitly, plugging (1.11) into (1.10) with the said identification, one obtains

$$\Omega^{(n)}_{k_x\varphi_x} = 2\Im\langle\partial_{k_x}u^{(n)}_{k_x,\varphi_x}|\partial_{\varphi_x}u^{(n)}_{k_x,\varphi_x}\rangle. \tag{1.22}$$

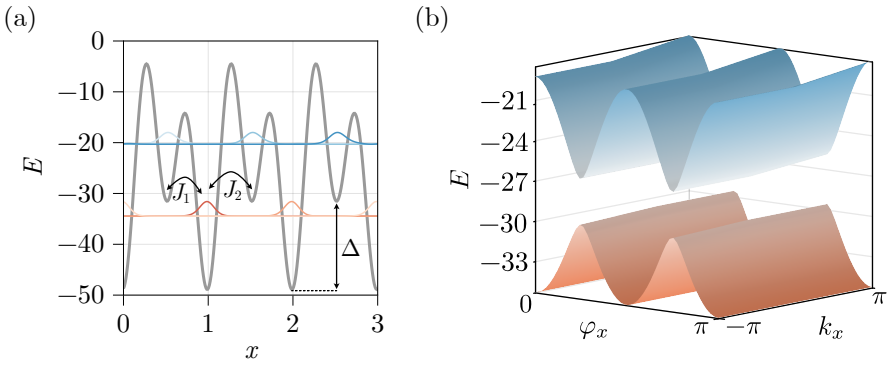

Figure 1.4: Illustration of the spatial Thouless pumping. (a) Wannier functions (shades of blue and red) of the two energy bands localised in the sites of the potential (1.20), shown in grey, at a fixed value of φ_x. A total of 3 cells is shown, each containing $s = 2$ sites. (b) Energy bands as functions of the pumping phase φ_x and quasimomentum k_x.

Notably, if the phase φ_x is varied adiabatically, it can be considered to be a periodic parameter of the Hamiltonian and treated as the quasimomentum. Consequently, the same arguments for the quantisation of the double integral (1.21) remain valid. Likewise, Eq. (1.21) is valid as long as the energy band remains separated from the neighbouring bands by a gap for all k_x and φ_x [an example is shown in Fig. 1.4(b)], and the resulting displacement is insensitive to deformations of the bands as long as the gap remains open.

The present continuous model can be mapped to a tight-binding description, revealing a connection to another topological invariant. Using the Bloch wave functions of the energy band of interest, one can construct the Wannier functions $w_{i\varphi_x}(x)$ localised at each ith site of the lattice. Then, the tight-binding Hamiltonian is obtained according to

$$\hat{H}_{\mathrm{TB}}(\varphi_x) = \sum_{\langle ij \rangle} J_{ij}(\varphi_x) \hat{c}_i^\dagger \hat{c}_j, \qquad J_{ij}(\varphi_x) = \langle w_{i\varphi_x} | \hat{H}(\varphi_x) | w_{j\varphi_x} \rangle, \tag{1.23}$$

where the summation is over all nearest-neighbour sites, with longer range couplings disregarded. In the present case of a lattice having two sites per cell, we can introduce the operators $\hat{a}^\dagger$ and $\hat{b}^\dagger$ creating particles at the respective sites and rewrite $\hat{H}_{\mathrm{TB}}$ in the form of a Rice–Mele Hamiltonian [128]

$$\begin{aligned} \hat{H}_{\mathrm{TB}}(\varphi_x) = &- \sum_i [J_1(\varphi_x) \hat{b}_i^\dagger \hat{a}_i + J_2(\varphi_x) \hat{a}_{i+1}^\dagger \hat{b}_i + \mathrm{H.c.}] \\ &+ \sum_i \Delta(\varphi_x) (\hat{a}_i^\dagger \hat{a}_i - \hat{b}_i^\dagger \hat{b}_i). \end{aligned} \tag{1.24}$$

Here, the sums run over the lattice cells. The intuitive meaning of parameters J_1, J_2, and Δ is depicted in Fig. 1.4(a). In the Rice–Mele picture, the displacement per pumping cycle is given by the *winding number* (with respect to the origin) of the curve $\xi(\varphi_x)$ traced in the course of a pumping cycle in the plane of parameters $J_1 - J_2$ and Δ [126, 127]. Once again we emphasise that only the winding number rather than the specific shape of $\xi(\varphi_x)$ controls the displacement, leading to the insensitivity of the effect to perturbations.

The Thouless pumping has been realised experimentally using optical lattices loaded with ultracold fermions [126] and bosons [127], confirming the validity of the above equations.

1.4 Higher Chern numbers

The identification of the adiabatic phase φ_x in the pumping protocol with the quasimomentum suggests the possibility of simulating higher-dimensional systems. For example, a topological pump in a 2D spatial lattice is characterised by two quasimomenta k_x, k_y and two phases φ_x, φ_y. Interpreting the latter two as quasimomenta of additional synthetic dimensions (let us call the corresponding axes v and w, respectively), we can effectively simulate a 4D crystalline structure and study possible responses. First, we note that in the usual quantum Hall effect, observed in 2D systems [that is, $(2+1)$-dimensional spacetime], the response of the system in terms of the electric current density can be expressed as [122, 106]

$$j^\mu \propto \nu_1 \epsilon^{\mu\rho\lambda} \partial_\rho A_\lambda, \tag{1.25}$$

where the greek indices run from 0 to 2, $\epsilon^{\mu\rho\lambda}$ is the totally anti-symmetric symbol, and A_λ is a component of the electromagnetic gauge field. Meanwhile, in a 4D system [$(4+1)$-dimensional spacetime], the response to external fields generalises to [122, 106]

$$j^\mu \propto \nu_2 \epsilon^{\mu\rho\lambda\sigma\tau} \partial_\rho A_\lambda \partial_\sigma A_\tau, \tag{1.26}$$

where the indices run from 0 to 4. As in the ordinary 3D case, the electromagnetic field tensor is defined as $F_{\mu\nu} = \partial_\mu A_\nu - \partial_\nu A_\mu$, the electric field along the i-axis is given by $E_i = F_{0i}$, and the magnetic field perpendicular to the jk plane is $B_{jk} = F_{jk}$ (here, the latin indices run from 1 to 4). In terms of the fields, the above expression takes the form

$$j^l \propto \nu_2 \epsilon^{lijk} B_{ij} E_k. \tag{1.27}$$

Crucially, the response is quantised, and for the (effective) 4D system it is characterised by the second Chern number ν_2. For instance, this means that the conduction along the x-axis will be quantised if one applies an electric field along the synthetic axis w and a magnetic field perpendicular to the vy plane. This has been confirmed in an experiment realising 2D Thouless pumping in a 2D photonic wave guide array [129]: the 'electric field' E_w is realised using an adiabatic phase φ_y, while the 'magnetic field' B_{vy} is created by ensuring that the on-site energies of the 2D real-space lattice which the model is mapped to are modulated along y. Similar effects emerging in an effective 4D system have been experimentally explored in Ref. [130] using ultracold atoms.

To introduce the second Chern number, let us consider the Hamiltonian

$$\hat{H}^{(xy)}(\boldsymbol{R}) = \hat{H}^{(x)}(k_x, \varphi_x) + \hat{H}^{(y)}(k_y, \varphi_y), \tag{1.28}$$

where the parameters of $\hat{H}^{(xy)}$ are gathered into a formal vector

$$\boldsymbol{R} = (k_x, \varphi_x, k_y, \varphi_y), \tag{1.29}$$

and the two terms describe 1D lattice systems, featuring periodic potentials such as the one given in Eq. (1.20). The eigenstates of $\hat{H}^{(xy)}$ are given by the tensor products of the eigenstates of $\hat{H}^{(x)}$ and $\hat{H}^{(y)}$:

$$|u^{(l)}_{\boldsymbol{R}}\rangle = |u^{(m)}_{k_x,\varphi_x}\rangle \otimes |u^{(n)}_{k_y,\varphi_y}\rangle. \tag{1.30}$$

Such an eigenstate corresponds to the eigenvalue $E^{(l)}(\boldsymbol{R})$ given by the sum of the eigenvalues corresponding to the states $|u^{(m)}_{k_x,\varphi_x}\rangle$ and $|u^{(n)}_{k_y,\varphi_y}\rangle$:

$$E^{(l)}(\boldsymbol{R}) = E^{(m)}(k_x, \varphi_x) + E^{(n)}(k_y, \varphi_y). \tag{1.31}$$

The superscripts indicate band indices; the spectrum of $\hat{H}^{(xy)}$ is therefore also assumed to be banded. Moreover, let us assume that the lowest band results from combining only the lowest band of $\hat{H}^{(x)}$ and the lowest band of $\hat{H}^{(y)}$. In this case, the resulting band will be non-degenerate in the sense that a given set of parameters $\boldsymbol{R}$ will uniquely determine the energy $E^{(1)}(\boldsymbol{R})$. (This will not be the case if, for example, the lowest band of $\hat{H}^{(xy)}$ originates from a combination of the lowest band of $\hat{H}^{(x)}$ and two lowest bands of $\hat{H}^{(y)}$.) The second Chern number is then given by [59]

$$\nu_2 = \frac{1}{(2\pi)^2} \int \frac{1}{2!} \Omega \wedge \Omega, \tag{1.32}$$

where the curvature $\Omega = \mathrm{d}A$ with the connection

$$A = -\mathrm{i}\,\langle u_{\boldsymbol{R}} | \mathrm{d} u_{\boldsymbol{R}} \rangle\,. \tag{1.33}$$

Explicitly, the resulting components of the curvature $\Omega = \frac{1}{2!}\Omega_{ij}\mathrm{d}x^i \wedge \mathrm{d}x^j$ are

$$\Omega_{ij} = 2\Im\,\langle \partial_i u_{\boldsymbol{R}} | \partial_j u_{\boldsymbol{R}} \rangle\,, \tag{1.34}$$

where $\partial_i \equiv \partial_{R_i}$. We note in passing that in the degenerate case, one has to work with a non-Abelian (i.e., matrix-valued) connection $\hat{A}$ having components $A^{ab} = -\mathrm{i}\,\langle u^a_{\boldsymbol{R}} | \mathrm{d} u^b_{\boldsymbol{R}} \rangle$, where the indices a and b enumerate the degenerate states. The curvature is then given by $\hat{\Omega} = \mathrm{d}\hat{A} + \hat{A} \wedge \hat{A}$ [120].

Let us show that when the total system is separable as in Eq. (1.28), the second Chern number of a nondegenerate band is given by the product of the first Chern numbers of the constituent bands. Noting the antisymmetry $\Omega_{ij}(\boldsymbol{R}) = -\Omega_{ji}(\boldsymbol{R})$, we find that the unique elements of Ω_{ij} are given by

$$\begin{aligned}
\Omega_{12} &= 2\Im\,\langle \partial_{k_x} u_{k_x,\varphi_x} | \partial_{\varphi_x} u_{k_x,\varphi_x} \rangle\,\langle u_{k_y,\varphi_y} | u_{k_y,\varphi_y} \rangle = \Omega_{k_x\varphi_x}\,,\\
\Omega_{13} &= 2\Im\,\langle \partial_{k_x} u_{k_x,\varphi_x} | u_{k_x,\varphi_x} \rangle\,\langle u_{k_y,\varphi_y} | \partial_{k_y} u_{k_y,\varphi_y} \rangle = 0,\\
\Omega_{14} &= 2\Im\,\langle \partial_{k_x} u_{k_x,\varphi_x} | u_{k_x,\varphi_x} \rangle\,\langle u_{k_y,\varphi_y} | \partial_{\varphi_y} u_{k_y,\varphi_y} \rangle = 0,\\
\Omega_{23} &= 2\Im\,\langle u_{k_x,\varphi_x} | \partial_{\varphi_x} u_{k_x,\varphi_x} \rangle\,\langle \partial_{k_y} u_{k_y,\varphi_y} | u_{k_y,\varphi_y} \rangle = 0,\\
\Omega_{24} &= 2\Im\,\langle \partial_{\varphi_x} u_{k_x,\varphi_x} | u_{k_x,\varphi_x} \rangle\,\langle u_{k_y,\varphi_y} | \partial_{\varphi_y} u_{k_y,\varphi_y} \rangle = 0,\\
\Omega_{34} &= 2\Im\,\langle u_{k_x,\varphi_x} | u_{k_x,\varphi_x} \rangle\,\langle \partial_{k_y} u_{k_y,\varphi_y} | \partial_{k_y} u_{k_y,\varphi_y} \rangle = \Omega_{k_y\varphi_y}\,.
\end{aligned} \tag{1.35}$$

In the first and the final lines we recognised that the results are equal to the corresponding Berry curvatures of the bands of the 1D Hamiltonians [see Eq. (1.22)]. To prove the remaining zero equalities, consider Ω_{13} as an example. Applying ∂_{k_x} to both sides of the equality $\langle u_{k_x,\varphi_x} | u_{k_x,\varphi_x} \rangle = 1$ one finds

$$2\Re\,\langle \partial_{k_x} u_{k_x,\varphi_x} | u_{k_x,\varphi_x} \rangle = 0. \tag{1.36}$$

Therefore, the term $\langle \partial_{k_x} u_{k_x,\varphi_x} | u_{k_x,\varphi_x} \rangle$ is purely imaginary, and so is the term $\langle u_{k_y,\varphi_y} | \partial_{k_y} u_{k_y,\varphi_y} \rangle$. Their product, featured in Ω_{13}, is then real, leading to $\Omega_{13} = 0$.

The curvature two-form thus decomposes to a sum of the curvatures of the 1D Hamiltonians:

$$\Omega = \frac{1}{2!}\Omega_{ij}\mathrm{d}R^i \wedge \mathrm{d}R^j = \Omega_{12}\mathrm{d}R^1 \wedge \mathrm{d}R^2 + \Omega_{34}\mathrm{d}R^3 \wedge \mathrm{d}R^4. \tag{1.37}$$

Inserting this into Eq. (1.32), we get the anticipated result

$$\begin{aligned}\nu_2 &= \frac{1}{(2\pi)^2}\int \Omega_{12}\Omega_{34}\,\mathrm{d}R^1\wedge\mathrm{d}R^2\wedge\mathrm{d}R^3\wedge\mathrm{d}R^4\\ &= \frac{1}{(2\pi)^2}\int \Omega_{k_x\varphi_x}\mathrm{d}k_x\mathrm{d}\varphi_x\int \Omega_{k_y\varphi_y}\mathrm{d}k_y\mathrm{d}\varphi_y\\ &= \nu_1^{(x)}\nu_1^{(y)}.\end{aligned} \tag{1.38}$$

Remarkably, by the same topological argument mentioned in Section 1.2, the value of ν_2 is insensitive to continuous deformations of the Hamiltonian $\hat{H}^{(xy)}(\boldsymbol{R})$. Therefore, the relation (1.38) for the lowest band holds even if the Hamiltonian is not separable, provided this band represents a continuous deformation of the lowest energy band of a separable Hamiltonian [122].

CHAPTER 2

Thouless pumping in time-space crystalline structures

We begin the application of topological concepts with a theoretical exploration of the realisation of the Thouless pumping in time- and time-space crystalline structures. The concept of time-crystalline structures will be introduced and thoroughly explained. We demonstrate that an adiabatic variation of the external driving can lead to quantised particle motion in the temporal dimension. To this end, we consider adiabatic pumping of a quantum gas in a 2D time-space crystal realised by a resonantly driven optical lattice. We study three possible processes: pumping in the temporal dimension, spatial pumping, and simultaneous pumping in both dimensions. As noted in Section 1.4, a 2D Thouless pump may be used to study the 4D quantum Hall effect, and hence the setup proposed here enables one to probe 4D physics with just a driven system of a single spatial dimension.

2.1 Model

We base our demonstration of the time-space Thouless pumping on the 1D Hamiltonian of the form

$$\hat{H} = \hat{h}(\hat{p}_x, x|\varphi_x) + \xi_{\mathrm{S}}(x,t) + \xi_{\mathrm{L}}(x,t|\varphi_t). \tag{2.1}$$

The first term is the unperturbed spatial Hamiltonian,

$$\hat{h}(\hat{p}_x, x|\varphi_x) = \hat{p}_x^2 - V_{\mathrm{S}}\cos^2(2x) - V_{\mathrm{L}}\cos^2(x+\varphi_x), \tag{2.2}$$

which is typical for setups demonstrating the Thouless pumping in the real space [126, 127]. Here, $\hat{p}_x$ is the momentum operator, V_S and V_L control, respectively, the depth of the 'short' and the 'long' optical lattices, while the relative phase φ_x has to slowly scan over a period of length π to realise a pumping cycle. In this chapter, we use the recoil units for the energy $\hbar^2 k_\mathrm{L}^2/2m$ and length $1/k_\mathrm{L}$, with k_L being the wave number of the laser beams that create the optical lattice, and m being the particle mass. The unit of time is $\hbar$ divided by the energy unit.

To engineer the Thouless pumping in time, we introduce the time-dependent perturbations

$$\xi_\mathrm{S}(x,t) = \lambda_\mathrm{S} \sin^2(2x) \cos(2\omega t), \tag{2.3a}$$

$$\xi_\mathrm{L}(x,t|\varphi_t) = \lambda_\mathrm{L} \cos^2(2x) \cos(\omega t + \varphi_t). \tag{2.3b}$$

The factors λ_S and λ_L denote the overall strength of these perturbations. As we will demonstrate shortly, the time-periodic dependencies $\cos(2\omega t)$ and $\cos(\omega t + \varphi_t)$ enable us to introduce a pumping setup based on a periodic structure in the time domain. The role of the phase shift φ_t is to allow for slowly changing the relative displacement between the two emerging time lattices. In this work we choose the driving frequency $\omega = s\Omega$, where the resonance number $s = 2$, while Ω is the gap between neighbouring energy bands of $\hat{h}$ which we wish to couple by the external perturbation. The combination of perturbations oscillating as 2Ω and 4Ω allows us to create a ring of four sites (two cells with two sites per cell) in the temporal direction. To ensure sufficient hopping strength between the sites of the spatial lattice, we study highly excited states of $\hat{h}$ that occupy bands near the top of the spatial potential wells. The corresponding value of Ω is easily determined by diagonalising $\hat{h}$. Since the phase φ_x changes the spatial potential and thus the unperturbed energy spectrum, we additionally fine-tune the value of Ω (or ω directly) to keep the spatial hopping adequate for all φ_x.

We note that the temporal phase φ_t is not a parameter of the unperturbed system, but rather a parameter of the perturbation. Moreover, φ_x and φ_t change in time in the Thouless pumping protocol. In order not to destroy the time crystalline structure which is created by resonant time-periodic driving of the system, φ_x and φ_t must not change appreciably during a single period T of the driving, i.e., $T(\mathrm{d}\varphi_{x,t}/\mathrm{d}t) \ll 2\pi$.

2.2 Quasiclassical analysis of the temporal Thouless pumping

It is instructive to start with the analysis of a 1D time crystal, whereby a particle is confined to a single potential well and the spatial periodicity plays no role. We can consider our model Hamiltonian

$$H(p_x, x, t) = h(p_x, x|\varphi_x) + \xi_{\mathrm{S}}(x, t) + \xi_{\mathrm{L}}(x, t|\varphi_t) \tag{2.4}$$

as a classical entity and use the action–angle representation of the unperturbed Hamiltonian $h(I)$, with the action I and angle $\theta \in [0, 2\pi)$ constituting a pair of canonical variables [131, 132]. Specifically, the action variable is defined for a 1D time-independent Hamiltonian [$h(p_x, x|\varphi_x)$ in our case] as the integral of momentum along a periodic orbit

$$I = \frac{1}{2\pi} \oint p_x \, \mathrm{d}x. \tag{2.5}$$

The angle θ is the position variable of a particle on a periodic trajectory that changes uniformly in time, $\theta(t) = \Omega t + \theta(0)$, where the frequency of the periodic motion is determined by $\Omega = \partial h(I)/\partial I$ (while $\theta(0)$ is an arbitrarily chosen initial phase). For a time-independent system, the action I is essentially a rescaled energy (which is conserved), while θ is the phase of the periodic motion. In this case, the periodic motion of a classical particle confined to a single lattice site of the potential in h is represented in the (I, θ) phase space by straight lines $I(\theta) = \mathrm{const}$. Meanwhile, a time-dependent perturbation causes formation of 'resonant islands' (see below) that contain closed orbits in the vicinity of the resonant value of action I_s such that $\Omega = [\partial h(I)/\partial I]\big|_{I_s} = \omega/s$ where s in an integer [133]. Analysis of the motion may be simplified by transitioning to the frame moving along the resonant orbit and applying the secular approximation, whereby the oscillatory terms of the Hamiltonian are dropped. We give all the details of this calculation below.

Setting $\varphi_x = 0$ and performing a transformation to the action–angle variables, we obtain

$$H(I, \theta, t) = h(I) + \lambda_{\mathrm{S}} \cos(2\omega t) \mathcal{Q}_{\mathrm{S}}(I, \theta) + \lambda_{\mathrm{L}} \cos(\omega t + \varphi_t) \mathcal{Q}_{\mathrm{L}}(I, \theta), \tag{2.6}$$

where $\mathcal{Q}_{\mathrm{S}}(x) = \sin^2(2x)$ and $\mathcal{Q}_{\mathrm{L}}(x) = \cos^2(2x)$ [see Eq. (2.3)] — we have chosen different functions for $\mathcal{Q}_{\mathrm{S}}(x)$ and $\mathcal{Q}_{\mathrm{L}}(x)$ but one can also choose $\sin(2x)$ [or $\cos(2x)$] for both of them. The spatial Hamiltonian $h(I)$ does not depend on θ, and the θ-dependencies of the perturbations can be represented as Fourier

series

$$\mathcal{Q}_{\mathrm{S|L}}(I,\theta) = \sum_{m=-\infty}^{\infty} \mathcal{Q}_{\mathrm{S|L}}^{(m)}(I)\,\mathrm{e}^{\mathrm{i}m\theta}. \tag{2.7}$$

We choose our working point in the vicinity of a certain resonant trajectory corresponding to a given value of the action I_s and the corresponding intrinsic frequency Ω. Switching to the rotating frame according to $\Theta = \theta - \Omega t$ and averaging out the rapidly oscillating terms, we express the long perturbation as

$$\xi_{\mathrm{L}} = \frac{1}{2}\lambda_{\mathrm{L}}\left[\mathcal{Q}_{\mathrm{L}}^{(s)}(I_s)\,\mathrm{e}^{\mathrm{i}(\varphi_t - s\Theta)} + \mathrm{c.c.}\right]. \tag{2.8}$$

Writing the complex number $\mathcal{Q}_{\mathrm{L}}^{(s)}(I_s)$ in the polar form

$$\mathcal{Q}_{\mathrm{L}}^{(s)}(I_s) = A_{\mathrm{L}}\,\mathrm{e}^{\mathrm{i}\chi_{\mathrm{L}}}, \tag{2.9}$$

we cast this result into

$$\xi_{\mathrm{L}} = \lambda_{\mathrm{L}} A_{\mathrm{L}} \cos(s\Theta - \chi_{\mathrm{L}} - \varphi_t). \tag{2.10}$$

In complete analogy, the short perturbation is written as

$$\xi_{\mathrm{S}} = \lambda_{\mathrm{S}} A_{\mathrm{S}} \cos(2s\Theta - \chi_{\mathrm{S}}), \tag{2.11}$$

where $A_{\mathrm{S}}\,\mathrm{e}^{\mathrm{i}\chi_S}$ is the polar form of $\mathcal{Q}_S^{(2s)}(I_s)$.

We also expand $h(I)$ around I_s to the second order in I,

$$h(I) = h(I_s) + (I - I_s)\Omega + \frac{1}{2}h''(I_s)(I - I_s)^2. \tag{2.12}$$

Noting also that the time-dependent canonical transformation introduces an additional term $-I\Omega$, we finally derive the effective Hamiltonian

$$H_{\mathrm{eff}} = [h(I_s) - \Omega I_s] + \frac{P^2}{2M} + U_{\mathrm{eff}}, \tag{2.13}$$

with $P \equiv I - I_s$. Here we have also defined the 'effective mass' $M = 1/h''(I_s)$, which is negative, and the effective potential

$$U_{\mathrm{eff}}(\Theta) = \lambda_{\mathrm{S}} A_{\mathrm{S}} \cos(2s\Theta - \chi_{\mathrm{S}}) + \lambda_{\mathrm{L}} A_{\mathrm{L}} \cos(s\Theta - \chi_{\mathrm{L}} - \varphi_t) \tag{2.14}$$

representing a periodic potential in the moving frame. For $s = 2$, we obtain a lattice of two elementary cells, each consisting of two sites arising from the double-well structure.

In order to verify the validity of the secular approximation, we produce a map of the motion of a particle in the (I, θ) phase-space governed by the sec-

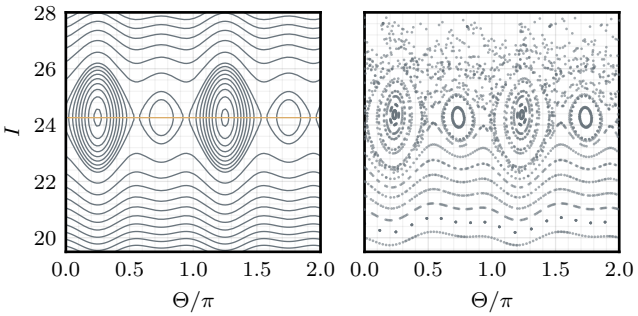

Figure 2.1: Phase-space maps of the particle motion governed by the secular effective Hamiltonian (2.13) (left panel) and the exact Hamiltonian (2.6) (right panel). The yellow line in the left panel indicates the working point $I_s = 24.3$. The map in the right panel was generated by numerically integrating the classical equations of motion resulting from the exact Hamiltonian (2.6) and registering particle's position (θ, I) stroboscopically at the intervals of the lattice driving period. The following values of parameters were used: $V_{\rm S} = 7640$, $V_{\rm L} = 2$, $\omega = 410$, $s = 2$, $\lambda_{\rm S} = 100$, $\lambda_{\rm L} = 40$, $\varphi_x = 0$, and $\varphi_t = \pi/2$.

ular effective Hamiltonian (2.13), as shown in Fig. 2.1, left panel. The right panel displays the map obtained by integrating the exact equations of motion resulting from the Hamiltonian (2.6) and by registering particle's coordinates and momenta stroboscopically at the intervals of the lattice driving period. Such a stroboscopic, rather than continuous, picture precisely corresponds to the secular approximation, which only provides the information on the dynamics averaged over the driving period. Once a point (x, p) is registered, the transformation to the (I, θ) coordinates is performed as follows. The corresponding action I is given by the action that the particle would have had if it had been found in a phase-space point (x, p) while evolving under the unperturbed Hamiltonian. Then, the angle θ is found as the phase of motion that the particle would have had if it had been found in a phase-space point (x, p) and possessing action I while evolving under the unperturbed Hamiltonian.

Comparing the two plots in Fig. 2.1, we conclude that the resonant islands where the quantum states we are interested in will be located (in the quasi-classical sense) are well reproduced in the exact picture, and hence that the secular approximation is valid for the considered strength of the perturbation (i.e., values of $\lambda_{\rm S}$ and $\lambda_{\rm L}$).

We are now in position to quantise the classical effective Hamiltonian (2.13) by changing $\Theta \to \hat{\Theta} = \Theta$ and $P \to \hat{P} = -{\rm i}\partial/\partial\Theta$:

$$\hat{H}_{\rm eff} = [h(I_s) - \Omega I_s] - \frac{1}{2M}\frac{\partial^2}{\partial\Theta^2} + U_{\rm eff}(\Theta). \tag{2.15}$$

It is immediately clear that this Hamiltonian describes a particle in a periodic

potential (with Θ being the coordinate), which stems from the time-dependent perturbation. Therefore, it is quite natural to call the resulting potential a time-crystalline structure [36].

In complete analogy with conventional space crystals, we may consider the limit of a large number of cells, $s \gg 1$ (while $\Theta \in [0, 2\pi)$). In that case, the eigenstates of Hamiltonian (2.15) are Bloch waves given by $\psi_{k_t}^{(n)}(\Theta) = \mathrm{e}^{\mathrm{i}k_t\Theta} u_{k_t}^{(n)}(\Theta)$, where k_t is the time-quasimomentum, n is the band index, and $u_{k_t}^{(n)}(\Theta) = u_{k_t}^{(n)}(\Theta + 2\pi/s)$ are cell-periodic functions [49]. We can expect the energy bands, parametrised by k_t and φ_t, to possess non-trivial topology, which can be quantified by the Chern number. It is given by Eq. (1.21) with the identifications $k_x \to k_t$ and $\varphi_x \to \varphi_t$.

To study the properties of $\hat{H}_{\mathrm{eff}}$, we proceed to its numerical diagonalisation, which is rather straightforward: In order to solve the eigenvalue problem

$$\hat{H}_{\mathrm{eff}}\psi_\beta(\Theta) = E_\beta \psi_\beta(\Theta) \tag{2.16}$$

under periodic boundary conditions, $\psi_\beta(\Theta) = \psi_\beta(\Theta + 2\pi)$, we expand the eigenfunctions in the basis of plane waves $\langle\Theta|j\rangle = \mathrm{e}^{\mathrm{i}j\Theta}/\sqrt{2\pi}$, $j \in \mathbb{Z}$, which are orthonormal on $\Theta \in [0, 2\pi)$:

$$\psi_\beta(\Theta) = \frac{1}{\sqrt{2\pi}} \sum_{j=-\infty}^{\infty} c_j^{(\beta)}\, \mathrm{e}^{\mathrm{i}j\Theta}. \tag{2.17}$$

This leads to the following matrix elements:

$$\begin{aligned}\langle j'|\hat{H}_{\mathrm{eff}}|j\rangle = &\left[h(I_s) - \Omega I_s + \frac{j^2}{2M}\right]\delta_{j',j} \\ &+ \frac{\lambda_{\mathrm{S}} A_{\mathrm{S}}}{2}(\delta_{j',j+2s}\,\mathrm{e}^{-\mathrm{i}\chi_{\mathrm{S}}} + \delta_{j',j-2s}\,\mathrm{e}^{\mathrm{i}\chi_{\mathrm{S}}}) \\ &+ \frac{\lambda_{\mathrm{L}} A_{\mathrm{L}}}{2}(\delta_{j',j+s}\,\mathrm{e}^{-\mathrm{i}(\chi_{\mathrm{L}}+\varphi_t)} + \delta_{j',j-s}\,\mathrm{e}^{\mathrm{i}(\chi_{\mathrm{L}}+\varphi_t)}).\end{aligned} \tag{2.18}$$

Another ingredient needed for the analysis are the Wannier functions, which are localised superpositions of the stationary states of $\hat{H}_{\mathrm{eff}}$. They may be found by diagonalising the position operator. In the case of a periodic system, we take this operator in the form $\mathrm{e}^{\mathrm{i}\Theta}$ [134, 128]. Its matrix elements follow as

$$\langle\psi_{\beta'}|\mathrm{e}^{\mathrm{i}\Theta}|\psi_\beta\rangle = \sum_{j=-\infty}^{\infty} c_{j+1}^{(\beta')*} c_j^{(\beta)}. \tag{2.19}$$

Numerical diagonalisation of this operator yields the coefficients $d_\beta^{(\alpha)}$ that allow

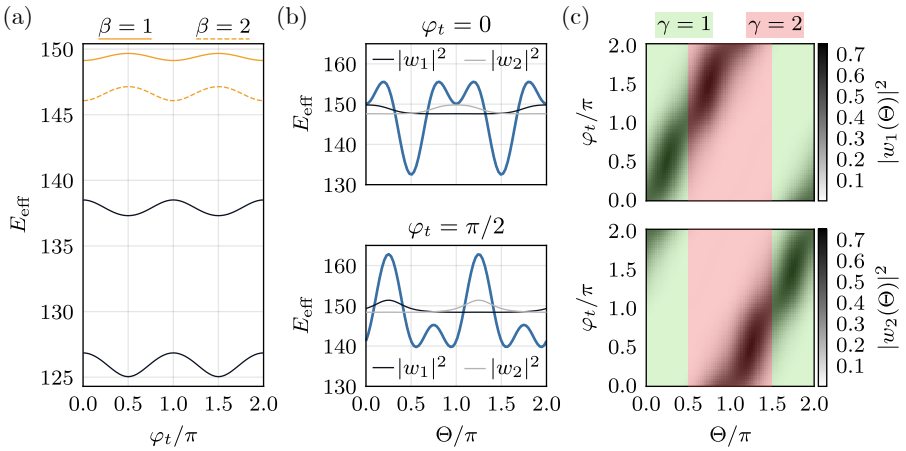

Figure 2.2: Adiabatic pumping in a two-cell time crystal simulated based on the quasiclassical approach. The values of parameters are the same as used in producing Fig. 2.1. (a) Energy levels E_β of quantised effective Hamiltonian (2.15) versus the adiabatic phase φ_t. (b) Wannier functions $|w_\alpha(\Theta)|^2$ superimposed on the effective potential (blue curves) U_{eff} at $\varphi_t = 0$ and $\varphi_t = \pi/2$. The scale of the y-axis relates to the potential. The Wannier functions are depicted in arbitrary units; they are positioned such that the flat tails mark the corresponding mean energies $\langle w_\alpha|\hat{H}_{\text{eff}}|w_\alpha\rangle$. (c) Changes of the Wannier functions $|w_\alpha(\Theta)|^2$ as φ_t scans across a complete cycle of length 2π. The shaded areas indicate the extent of the two temporal lattice cells ($\gamma = 1, 2$).

us to express the Wannier states as

$$w_\alpha(\Theta) = \sum_\beta d_\beta^{(\alpha)} \psi_\beta(\Theta). \tag{2.20}$$

Once we calculate the eigenvalues of $\hat{H}_{\text{eff}}$, we look for the highest ones since in the case of negative mass the energy spectrum is bounded from above. Four highest energy levels calculated repeatedly as the adiabatic phase φ_t is varied are shown in Fig. 2.2(a). We interpret the two highest levels ($\beta = 1, 2$) as belonging to the first energy band and the next two as constituting the second band, with the bands being separated by a gap.

We use the eigenstates ψ_1 and ψ_2 corresponding to the energy levels highlighted in orange in Fig. 2.2(a) to construct the Wannier functions w_1 and w_2, shown at $\varphi_t = 0$ and $\varphi_t = \pi/2$ in Fig. 2.2(b). These functions are vertically positioned such that the flat tails mark the corresponding mean energies $\langle w_\alpha|\hat{H}_{\text{eff}}|w_\alpha\rangle$. As we can see, the Wannier states are localised in the sites of the effective potential $U_{\text{eff}}(\Theta)$ [blue curves in Fig. 2.2(b)], which may be regarded as a crystalline structure for $s \gg 1$. Switching back to the lab frame and considering placing a detector at a fixed position $\theta = \theta_0$, we recover the time periodicity

of the potential $U_{\rm eff}(\theta_0 + \Omega t)$. Crucially, we can now interpret the dynamics of the system in terms of the time-periodic Wannier states $w_\alpha(\theta_0 + \Omega t)$: their localisation in Θ-space in the moving frame translates into localisation in time in the lab frame. Therefore, these states can be understood as being localised in the cells of a time-crystalline structure. A stationary detector placed at θ_0 in the lab frame will register periodic arrival of the two (for $s = 2$) Wannier states separated by the interval of π/Ω, corresponding to a detector scanning across Θ in the moving frame [cf. Fig. 2.2(b)]. Finally, we remark that the appreciable size of the resonant islands in Fig. 2.1 is directly related to the fact that the potential $U_{\rm eff}(\Theta)$ is strong enough to support deeply bound states.

Now let us study the changes of the Wannier functions as φ_t is varied adiabatically from 0 to 2π. Figure 2.2(b) shows that at the beginning of the cycle ($\varphi_t = 0$), state w_1 occupies the region[1)] $\Theta \in [-\pi/2, \pi/2)$, which, by convention, we will refer to as the first cell ($\gamma = 1$) of the temporal lattice. Similarly, w_2 occupies the region $\Theta \in [\pi/2, 3\pi/2)$, which we will call the second temporal cell ($\gamma = 2$). Further change of the two states is presented in Fig. 2.2(c). It is apparent that the probability densities $|w_\alpha|^2$ shift as the phase is increased. By the end of the cycle, the Wannier functions are seen to have shifted by π, with the state w_1 now occupying the second temporal cell, and w_2 occupying the first. Since the number of particles pumped through a cross-section of the lattice is given by the Chern number, the above results show that $|\nu_1| = 1$ for the studied first band of the temporal lattice. This serves as a direct confirmation of the non-trivial topology of the bands of the temporal lattice.

2.3 Quantum analysis

In the previous section we introduced the notion of a time-crystalline structure and demonstrated the Thouless pumping in a temporal direction. Our next task is to elucidate how the temporal crystalline structure emerges in a fully quantum description of the system based on the Hamiltonian (2.1). This will additionally allow us to incorporate a real-space lattice and study simultaneous pumping in time and space.

Since the perturbation $\xi_{\rm S} + \xi_{\rm L}$ is time-periodic, with the period $T = 2\pi/\omega$ [see Eqs. (2.3)], we approach the problem by introducing the quasienergy operator $\hat{Q} = \hat{H} - \mathrm{i}\partial_t$ and solving the eigenvalue problem $\hat{Q}u_n(x,t) = \varepsilon_n u_n(x,t)$ [135, 133, 17]. Here, ε_n is the quasienergy of the nth eigenstate, while $u_n(x,t)$ is the corresponding Floquet mode that respects temporal periodicity of the perturbation, i.e., $u_n(x,t) = u_n(x,t+T)$. A general solution of the Schrödinger equation can be represented as a superposition of states $\Psi_n(x,t) = \mathrm{e}^{-\mathrm{i}\varepsilon_n t}u_n(x,t)$

[1)] In this notation, it is understood that the interval $[-\pi/2, 0)$ is equivalent to $[3\pi/2, 2\pi)$.

with time-independent coefficients. In our simulations we consider a finite number of spatial cells ($N = 1$ or $N = 2$) which leads to the Hamiltonian being defined on $x \in [0, N\pi)$, and we always assume periodic boundary conditions. All the details of the diagonalisation procedure are covered in Appendix 2A.

In the following sections, we present the results of the simulations, starting with the Thouless pumping in time. Next, we consider pumping in space, which, however, is performed in a time-space crystal rather than a conventional space crystal. Finally, we study simultaneous pumping in both the temporal and the spatial dimensions.

As in Section 2.2, we will illustrate the Thouless pumping by showing how the Wannier states are transported with a change of the adiabatic parameter. We can observe pumping along temporal or spatial directions by changing φ_t or φ_x. For pumping in time, one can analyse the transport of the Wannier states that are localised in a single site of the temporal lattice and are not necessarily localised along the spatial direction. To construct such Wannier states, we will choose Floquet states which correspond to quasienergy levels with different spatial index. Note that choosing Floquet states from a given band, one obtains the Wannier states that are elements of the corresponding Hilbert subspace and are uncoupled from states belonging to any other bands.

2.3.1 Thouless pumping in time

We begin the analysis by considering time-pumping in a system of a single spatial cell ($N = 1$) which contains two sites originating from the double-well structure of the spatial potential. The relevant part of the quasienergy spectrum of $\hat{Q}$ is shown in Fig. 2.3(a). The figure displays the changes of the quasienergy levels in the course of the adiabatic pumping in the temporal dimension — the temporal phase φ_t is varied while keeping $\varphi_x = 0$. We interpret the obtained quasienergy spectrum as follows. In the limit of an infinite spatial crystal, the energy spectrum of $\hat{h}$ features series of bands separated by large gaps. Because of the double-well structure of each cell of the potential, each band consists of two subbands (a higher and a lower one), separated by a small gap, of order V_{L} at $\varphi_x = 0$. Thus, each two consecutive levels in Fig. 2.3(a) correspond, respectively, to the higher and the lower subbands of a certain spatial band. For example, the two topmost levels in Fig. 2.3(a) correspond to the subbands of the spatial band number 25 (counting from the lowest); the spatial potential supports 28 clearly formed bands in total with the chosen parameter values. From the time-crystalline structure perspective, we associate the four topmost levels in Fig. 2.3(a) with the first temporal band, and the lower four levels with the second. Note that it is natural to assign the lowest band number to the temporal band whose quasienergy is largest: A particle confined in the

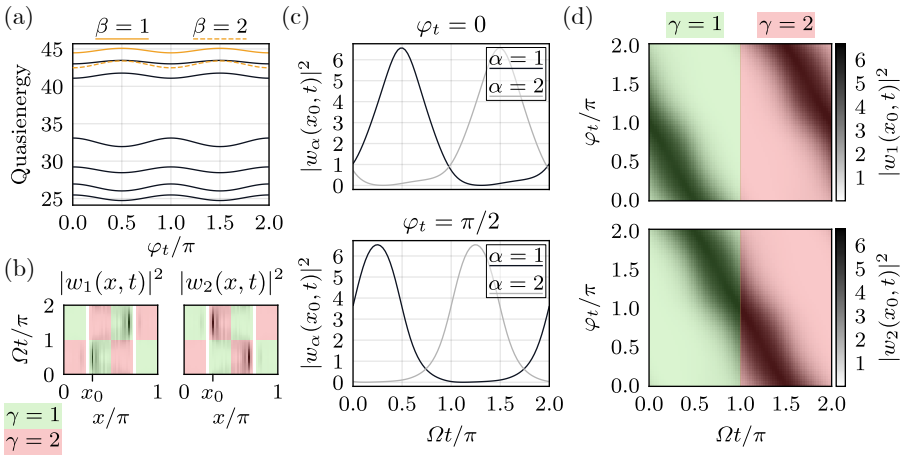

Figure 2.3: Temporal adiabatic pumping in a 2D time-space crystal with $s = 2$ temporal cells and only one ($N = 1$) spatial cell that consists of two spatial sites. The following values of parameters were used: $V_\mathrm{S} = 7640$, $V_\mathrm{L} = 2$, $\omega = 410$, $s = 2$, $\lambda_\mathrm{S} = 100$, $\lambda_\mathrm{L} = 40$ and $\varphi_x = 0$. (a) Quasienergy levels ε_β (see text for level numbering convention) of the quasienergy operator $\hat{Q}$ versus the adiabatic phase φ_t. (b) The Wannier functions $|w_\alpha(x,t)|^2$ at $\varphi_t = 0$, represented by black regions. The shaded areas (green and pink) indicate the extent of the temporal cells ($\gamma = 1, 2$). (c) Wannier functions $|w_\alpha(x_0,t)|^2$ (where $x_0 = 0.3\pi$) at $\varphi_t = 0$ and $\varphi_t = \pi/2$. (d) Change of the Wannier functions $|w_\alpha(x_0,t)|^2$ as φ_t scans across a complete cycle of length 2π. The green and pink shaded areas indicate the extent of the two temporal lattice cells ($\gamma = 1, 2$).

temporal lattice is parameterised by the effective mass which is negative (see Section 2.2), and its energy spectrum is thus bounded from above. To distinguish the quasienergy levels constituting the first temporal band, we introduce an index β. We assign the same index β to all the levels corresponding to the same spatial band: we assign $\beta = 1$ to the two topmost levels in Fig. 2.3(a) and $\beta = 2$ to the next two.

The relevant Wannier functions are spatially localised superpositions of the Floquet modes: $w_\alpha(x,t) = \sum_{\beta=1}^{2} d_\beta^{(\alpha)} u_\beta(x,t)$, where the coefficients $d_\beta^{(\alpha)}$ are found by diagonalising the position operator $\mathrm{e}^{2\mathrm{i}x/N}$ (see Appendix 2A). We will only consider the quasienergy levels of the first temporal band. This is justified by assuming that the gap between the first and the second bands is large enough so that particles loaded into the first band stay there throughout the pumping cycle. Furthermore, since we are now considering pumping in the temporal direction only, we can restrict our attention to a single site (out of two) of the spatial lattice. To obtain Wannier functions that are localised in the same spatial site, we have to mix the spatial energy levels corresponding either to the higher spatial subbands or to the lower ones. We choose to mix the levels of the higher spatial subbands by mixing the two modes $\beta = 1, 2$

whose quasienergy levels are highlighted in orange in Fig. 2.3(a). Mixing the other pair of levels (from the first temporal band) leads to analogous results and corresponds to a particle occupying the other site of the spatial lattice. The highlighted levels in Fig. 2.3(a) thus correspond to the highlighted levels in Fig. 2.2(a); the total number of levels is doubled in Fig. 2.3(a) because of the presence of the spatial lattice.

The obtained Wannier functions $w_1(x,t)$ and $w_2(x,t)$ are shown in Fig. 2.3(b) at $\varphi_t = 0$ where they are represented by black regions. In the present case we consider only one spatial cell; the two sites of this cell span the regions $x \in [0, \pi/4) \cup [3\pi/4, \pi)$ and $x \in [\pi/4, 3\pi/4)$ — note that we assume periodic boundary conditions in space. The sites are separated by white gaps in Fig. 2.3(b). Each of the spatial sites contains $s = 2$ temporal cells, which we will number with the index $\gamma = 1, 2$ and which are indicated by shaded green and pink areas.[2)] We adopt the convention that the region of time-space which is occupied by w_1 at $\varphi_t = 0$ belongs to the first temporal cell [$\gamma = 1$, green shading in Fig. 2.3(b)], while the region occupied by w_2 belongs to the second temporal cell [$\gamma = 2$, pink shading in Fig. 2.3(b)]. Note that at a different value of φ_t, the state w_1 may spread over both temporal cells or even transition to cell $\gamma = 2$, and similarly for w_2. As illustrated in Fig. 2.3(b), the Wannier functions cycle in time between the two turning points of the spatial site they are confined to, akin to classical pendula.

In space crystals we are interested in periodic distribution of particles in space at a fixed moment of time (i.e., the moment of the detection). Switching from space to time crystals, the roles of space and time are exchanged. That is, we fix position in space and ask if the probability for the detection of particles at this fixed space-point changes periodically in time [36]. To understand the emergence of a time-crystalline structure in the system analysed here, let us consider placing a detector close to the left (say) classical turning point x_0 of the spatial lattice site under consideration. We take $x_0 = 0.3\pi$ for the chosen energy regime, as indicated in Fig. 2.3(b). As shown in Fig. 2.3(c) depicting the time-periodic Wannier functions $w_\alpha(x_0, t)$ at $\varphi_t = 0$, in the time intervals (Ωt mod 2π) $\in [0, \pi)$ the detector will most likely be registering the particle whose wave function is $w_1(x_0, t)$. Meanwhile, in the intervals (Ωt mod 2π) $\in [\pi, 2\pi)$ the detector will most likely be registering the particle whose wave function is $w_2(x_0, t)$. The two time intervals can be considered to divide the time axis into cells, allowing one to introduce the notion of a time-crystalline structure. In the present case, the 'length' of the crystalline structure along the temporal axis

[2)] We reiterate the meaning of the indices α, β, γ to prevent confusion: index β numbers the Floquet modes u_β, while α numbers the Wannier functions w_α (which are superpositions of the chosen Floquet modes). Independently, index γ numbers the cells of the temporal lattice; a Wannier function w_α may in principle occupy any temporal cell.

is $2\pi/\Omega$, and the crystal is periodic in this dimension, i.e., periodic boundary conditions in time are imposed. The lower panel of Fig. 2.3(c) demonstrates additionally that at a different value of the phase, $\varphi_t = \pi/2$, the Wannier functions are shifted and they are delocalised over both cells of the temporal lattice.

Now let us turn to the Thouless pumping in the temporal dimension. To this end, we calculate the Wannier functions repeatedly as the phase φ_t is varied and produce the plots of $w_1(x_0, t)$ and $w_2(x_0, t)$ for each value of φ_t, as shown in Fig. 2.3(d). We can clearly see that w_1 is being pumped from cell $\gamma = 1$ to cell $\gamma = 2$ as the temporal phase φ_t is varied from 0 to 2π. At the same time, state w_2 adiabatically transitions from cell 2 to cell 1. To observe the pumping experimentally, one has to prepare a particle in, e.g., the state $w_1(x, t)$ and place a detector at x_0. Initially, the detector will most probably be detecting the particle in the time intervals $(\Omega t \bmod 2\pi) \in [0, \pi)$, whereas after a pumping cycle is complete the detector will be clicking in the time intervals $(\Omega t \bmod 2\pi) \in [\pi, 2\pi)$. We note in passing that one can 'invert' the pumping direction by letting φ_t vary from 0 to -2π, just as is possible in the case of the adiabatic pumping in real space.

2.3.2 Thouless pumping in space

Now let us analyse spatial-only pumping in a 2D time-space crystalline structure consisting of $N = 2$ spatial cells (and $s = 2$ temporal cells) with periodic boundary conditions. Doubling the number of spatial cells leads to a twice greater number of Floquet quasienergy levels compared to the case of $N = 1$, as shown in Fig. 2.4(a). The physical origin of the levels is the same as in the preceding discussion, and it is now immediately apparent which levels arise from the higher and the lower spatial subbands. The gap between these subbands is the smallest (but non-vanishing) at $\varphi_x = \pi/4$ and $\varphi_x = 3\pi/4$ since all wells of the spatial potential are of equal depth at these phases. Once the quasienergy spectrum is obtained, we again switch to the Wannier representation, this time introducing an additional spatial index j to number the Floquet modes and i to number the Wannier functions: $w_{i,\alpha=1}(x, t) = \sum_{j=1}^{2} d_j^{(i)} u_{j,\beta=1}(x, t)$. Since we are interested in the spatial pumping, we mix the Floquet modes bearing the same temporal index $\beta = 1$ so that the obtained Wannier functions come out delocalised over the entire temporal lattice structure, simplifying the analysis. The delocalisation in the temporal dimension and localisation in spatial dimension means physically that the particle, being confined to a single spatial site, can be detected with equal probabilities at both turning points, this being true at all times. This contrasts the situation in Section 2.3.1, where, at any given time, a particle could be detected at one turning point with a higher

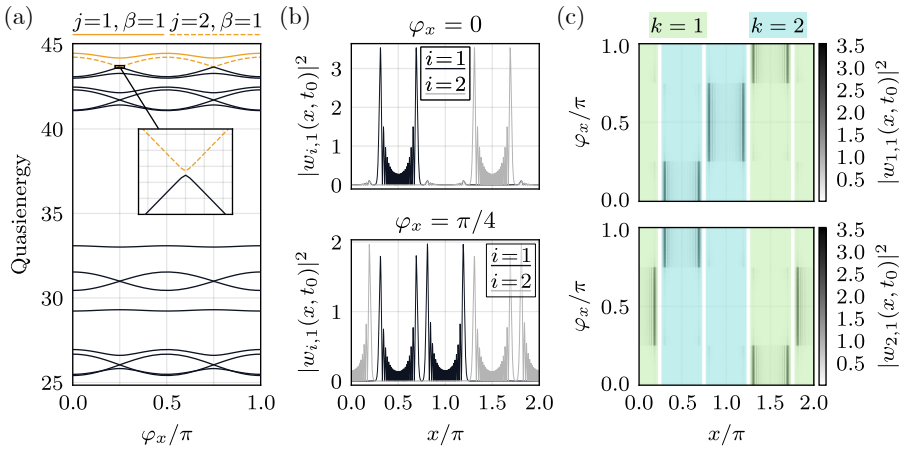

Figure 2.4: Spatial adiabatic pumping in a 2D time-space crystal with $s = 2$ temporal cells and $N = 2$ spatial cells.. The same values of parameters were used as in Fig. 2.3 except that $\varphi_t = 0$, while φ_x is varied. (a) Quasienergy levels $\varepsilon_{j,\beta}$ of the quasienergy operator $\hat{Q}$ versus the adiabatic phase φ_x. (b) Wannier functions $|w_{i,1}(x,t_0)|^2$ (where $t_0 = \pi/2\Omega$) at $\varphi_x = 0$ and $\varphi_x = \pi/4$. (c) Changes of the Wannier functions $|w_{i,1}(x,t_0)|^2$ as φ_x scans across a complete cycle of length π. The cyan and green shaded areas indicate the extent of the two spatial lattice cells ($k = 1, 2$), each consisting of two sites separated by unshaded regions.

probability than at the other, and based on this probability we could speak of the particle occupying a specific temporal cell. Note that the eigenstates of $e^{2ix/N}$ are always strongly localised in certain sites of the spatial lattice, and so are the Wannier functions $w_{i,\alpha}(x,t)$, for all t. The latter is only violated at values of φ_x close to $(2n+1)\pi/4$, $n \in \mathbb{Z}$, when the depths of all the wells of the potential become equal, leading to the Wannier functions spreading over two adjacent sites. The temporal dependence of $w_{i,\alpha}(x,t)$, on the other hand, is dictated by the temporal dependencies of the modes $u_{j,\beta}(x,t)$ that are being mixed.

The relevant quasienergy levels are highlighted in Fig. 2.4(a). Their indices are $(j = 1, \beta = 1)$ and $(j = 2, \beta = 1)$ corresponding to them occupying two different spatial cells. To analyse the pumping, we study the states $w_{1,1}(x,t_0)$ and $w_{2,1}(x,t_0)$ at a fixed detection moment $t_0 = \pi/2\Omega$. Figure 2.4(b) illustrates that, at $\varphi_x = 0$, each of these states is localised in a single site of the spatial lattice, while at $\varphi_x = \pi/4$ they occupy two sites in the process. We number the states and the cells of the spatial lattice such that $w_{1,1}$ occupies spatial cell $k = 1$, while $w_{2,1}$ occupies spatial cell $k = 2$ at the beginning of the pumping cycle (at $\varphi_x = 0$), as shown in Fig. 2.4(c). In the figure, the cyan and green shaded areas indicate the spatial extent of the spatial lattice cells, with the sites of the cells separated by unshaded gaps corresponding to the positions

of the barriers of the spatial potential. In the end of the cycle, the Wannier states end up in a cell different from the starting one, confirming that pumping does take place. It is apparent that the states remain almost insensitive to the change of the potential and are transported to a neighbouring site abruptly. However, the lower panel of Fig. 2.4(b) demonstrates that the transfer does not happen instantaneously, but rather proceeds via a stage when the Wannier states occupy both sites.

We remark that constructing the Wannier functions using the Floquet modes corresponding to the top third and fourth levels in Fig. 2.4(a) leads to pumping in the opposite direction around the circular x-axis. This is to be expected since those energy levels correspond to the lower spatial subbands, while the above results concern pumping in the higher subbands [128].

2.3.3 2D Thouless pumping

We are now ready to discuss the simultaneous temporal and spatial adiabatic pumping, demonstrated in Fig. 2.5 for the case $N = s = 2$. The adiabatic phases are varied along the trajectory $\varphi_t = 2\varphi_x$ from $\varphi_t = 0$ to $\varphi_t = 2\pi$ so that a complete pumping cycle is performed both in the temporal and in the spatial dimensions. The obtained Floquet quasienergy spectrum is shown in Fig. 2.5(a), where the legend indicates the quasienergy levels corresponding to the modes that we mix when constructing the Wannier states. The relevant modes are those of the first temporal band, among which we select those corresponding to the higher spatial subbands. As discussed in Section 2.3.2, this selection allows us to focus on the Wannier states that are transported in space to the right during the pumping process. The remaining four levels of the first temporal band constitute the Wannier functions that are being pumped to the left in space. The constructed states are expressed as $w_{i,\alpha}(x,t) = \sum_{j,\beta} d_{j,\beta}^{(i,\alpha)} u_{j,\beta}(x,t)$ and are obtained as above, by diagonalising the position operator $\mathrm{e}^{2\mathrm{i}x/N}$. Contrary to the preceding analysis, we no longer restrict our attention to a certain position x_0 or a certain detection time t_0, but rather study the two-dimensional maps of the Wannier functions $w_{i,\alpha}(x,t)$. The four Wannier states are shown in Figs. 2.5(b)–(f) at various values of the adiabatic phases, with the shaded areas dividing the whole time-space into temporal and spatial cells. The states and the cells are numbered so that initially (at $\varphi_t = 2\varphi_x = 0$) the Wannier state indices (i,α) coincide with the spatial and temporal cell numbers (k,γ). In each of the panels (b)–(f), four sites are left unoccupied by any Wannier functions — these would have been occupied by the Wannier functions constructed using the states of the lower spatial subbands, i.e., the Floquet modes corresponding to the top four black quasienergy levels in Fig. 2.5(a). We note in passing that the two Wannier functions con-

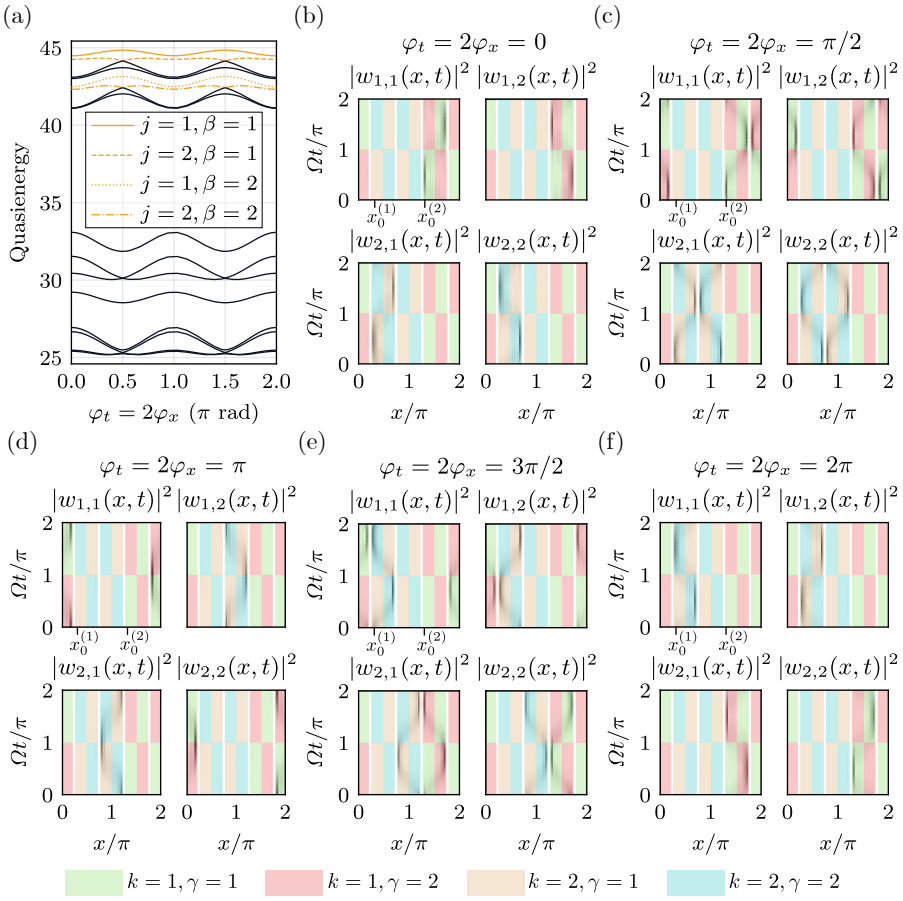

Figure 2.5: Simultaneous temporal and spatial adiabatic pumping in a 2D time-space crystal. The same values of parameters were used as in Fig. 2.3 except that both φ_t and φ_x are varied. (a) Quasienergy levels $\varepsilon_{j,\beta}$ of the quasienergy operator $\hat{Q}$ versus the adiabatic phase $\varphi_t = 2\varphi_x$. (b)–(f) The Wannier functions at $\varphi_t = 2\varphi_x = 0, \pi/2, \pi, 3\pi/2, 2\pi$. The probability densities $|w_{i,\alpha}(x,t)|^2$ are represented by black regions, while the shaded areas indicate the extent of the spatial ($k = 1, 2$) and temporal ($\gamma = 1, 2$) cells. In top-left panels in (b)–(f), $x_0^{(1)}$ and $x_0^{(2)}$ indicate the locations of two detectors discussed in the text.

structed in Section 2.3.2 using the states corresponding to only the two upper quasienergy levels appear as the sums $w_{1,1} + w_{1,2}$ and $w_{2,1} + w_{2,2}$, where $w_{i,\alpha}$ are the functions displayed in Figs. 2.5(b)–(f). Such sums exhibit spatial, but not temporal localisation.

Turning to the pumping process, in Fig. 2.5(c) we can see that the Wannier states are transported to the neighbouring spatial site (to the right) as a result of the spatial pumping, while the temporal pumping causes the states to slide down the temporal axis. At $\varphi_t = 2\varphi_x = \pi$ [see Fig. 2.5(d)], the spatial

transition is complete, whereas the time dependence of the functions is such that the functions occupy both temporal cells. Next, at $\varphi_t = 2\varphi_x = 3\pi/2$ [see Fig. 2.5(e)], the states are shown in the middle of the second spatial transition, which is completed at $\varphi_t = 2\varphi_x = 2\pi$ [see Fig. 2.5(f)]. Comparing Figs. 2.5(b) and 2.5(f), it is apparent that as a result of the pumping each state $w_{i,\alpha}$ has transitioned from cell (i, α) to cell $(i + 1 \mod N,\ \alpha + 1 \mod s)$.

Let us now give an interpretation of these results. Consider two detectors, one placed at $x_0^{(1)} = 0.3\pi$ and the other one at $x_0^{(2)} = 1.3\pi$, and a particle loaded initially into the system in the state $w_{1,1}$. At $\varphi_t = 2\varphi_x = 0$, most probably a detector placed at $x_0^{(2)}$ will be detecting the particle in the time intervals $(\Omega t \bmod 2\pi) \in [0, \pi)$, corresponding to the particle occupying the first spatial and the first temporal cells [see Fig. 2.5(b)]. In the end of the pumping cycle ($\varphi_t = 2\varphi_x = 2\pi$), the particle will most probably appear in the time intervals $(\Omega t \bmod 2\pi) \in [\pi, 2\pi)$ on a detector placed at $x_0^{(1)}$, corresponding to the particle occupying the second spatial and the second temporal cells.

2.4 Conclusions

In summary, we have shown that the quasienergy spectrum of a resonantly driven optical lattice may be interpreted as that of a crystal-like structure with the time playing the role of an additional coordinate. Using this analogy, we studied adiabatic variation of the driving protocol and demonstrated that it leads to a change of system dynamics that is a manifestation of the Thouless pumping in the temporal dimension. Finally, we have illustrated simultaneous adiabatic pumping in both spatial and temporal directions.

2.5 Appendix 2A: Diagonalisation of the quasienergy operator

In this section, we discuss the diagonalisation of the quasienergy operator

$$\hat{Q} = \hat{h} - \mathrm{i}\frac{\partial}{\partial t} + \xi_{\mathrm{S}} + \xi_{\mathrm{L}}, \tag{2.21}$$

where $\hat{h}$ is defined in Eq. (2.2), while ξ_{S} and ξ_{L} are given in Eqs. (2.3).

In order to solve the eigenvalue problem

$$\hat{Q}u_n(x,t) = \varepsilon_n u_n(x,t), \tag{2.22}$$

we first numerically obtain the eigenstates of $\hat{h}$ in the basis of plane waves $\langle x|j\rangle = \mathrm{e}^{\mathrm{i}\frac{2j}{N}x}/\sqrt{N\pi}$ orthonormal on $x \in [0, N\pi)$, where N is the number of

spatial cells. The sought eigenstates fulfil

$$\hat{h}\psi_m(x) = \epsilon_m \psi_m(x), \tag{2.23}$$

are written as

$$\psi_m(x) = \frac{1}{\sqrt{N\pi}} \sum_{j=-\infty}^{\infty} c_j^{(m)} \, \mathrm{e}^{\mathrm{i}\frac{2j}{N}x}, \tag{2.24}$$

and the coefficients $c_j^{(m)}$ that express the solution in the mth energy band are obtained by diagonalising the matrix

$$\begin{aligned} \langle j'|h|j\rangle = &\left[\left(\frac{2j}{N}\right)^2 - \frac{V_\mathrm{S}+V_\mathrm{L}}{2}\right]\delta_{j',j} \\ &- \frac{V_\mathrm{S}}{4}(\delta_{j',j+2N} + \delta_{j',j-2N}) \\ &- \frac{V_\mathrm{L}}{4}(\mathrm{e}^{2\mathrm{i}\varphi_x}\delta_{j',j+N} + \mathrm{e}^{-2\mathrm{i}\varphi_x}\delta_{j',j-N}). \end{aligned} \tag{2.25}$$

Once we have found the eigenstates of the unperturbed Hamiltonian, an additional transformation to the rotating frame provides a suitable basis consisting of functions

$$\psi'_m(x,t) = \mathrm{e}^{-\mathrm{i}\nu(m)\omega t/s}\psi_m(x). \tag{2.26}$$

Here, the function $\nu(m) = \lceil m/2N \rceil$ (where $\lceil \cdots \rceil$ is the ceiling operation) transforms the level numbers $m = 1, 2, 3, 4, 5, 6, \ldots$ into band indices

$$\nu = \underbrace{1,\ldots,1}_{2N \text{ times}}, \underbrace{2,\ldots,2}_{2N \text{ times}}, \underbrace{3,\ldots,3}_{2N \text{ times}}, \underbrace{4,\ldots,4}_{2N \text{ times}}, \ldots \tag{2.27}$$

Note that this labelling is correct when the sites of a potential cell are not too asymmetric for all φ_x. In practice, we have to keep V_L small enough so that the difference of depths of the potential wells in each cell is always smaller than the gaps between the energy bands.

We now calculate the matrix elements of $\hat{Q}$. For the diagonal part, we have

$$\langle \psi'_{m'}| \left(\hat{h} - \mathrm{i}\frac{\partial}{\partial t}\right) |\psi'_m\rangle = \left[E_m - \frac{\nu(m)\omega}{s}\right]\delta_{m',m}. \tag{2.28}$$

For the long perturbation, we obtain

$$\begin{aligned} \langle \psi'_{m'}|\xi_\mathrm{L}|\psi'_m\rangle = &\lambda_\mathrm{L}\cos(\omega t + \varphi_t)\,\mathrm{e}^{-\mathrm{i}(\omega/s)[\nu(m)-\nu(m')]t} \\ &\times \sum_{j,j'} c_{j'}^{(m')*} c_j^{(m)} \int_0^{N\pi} \frac{\mathrm{d}x}{N\pi} \mathcal{Q}_\mathrm{L}(x)\,\mathrm{e}^{\mathrm{i}(2j-2j')x}, \end{aligned} \tag{2.29}$$

where $\mathcal{Q}_{\mathrm{L}}$ is the spatial part of ξ_{L}, see Eqs. (2.3). Applying the secular approximation [133], we replace $\cos(\omega t+\varphi_t)\,\mathrm{e}^{-\mathrm{i}(\omega/s)[\nu(m)-\nu(m')]t}$ with its time-independent contribution $\frac{1}{2}(\mathrm{e}^{\mathrm{i}\varphi_t}\delta_{\nu'+s,\nu}+\mathrm{e}^{-\mathrm{i}\varphi_t}\delta_{\nu'-s,\nu})$, where $\nu'\equiv\nu(m')$. With our choice $\mathcal{Q}_{\mathrm{L}}(x)=\cos^2(2x)$, we finally obtain

$$\begin{aligned}\langle\psi'_{m'}|\xi_{\mathrm{L}}|\psi'_m\rangle = \frac{\lambda_{\mathrm{L}}}{2}(\mathrm{e}^{\mathrm{i}\varphi_t}\delta_{\nu'+s,\nu}+\mathrm{e}^{-\mathrm{i}\varphi_t}\delta_{\nu'-s,\nu})\\ \times\frac{1}{4}\sum_{j=-\infty}^{\infty}c_j^{(m)}(2c_j^{(m')*}+c_{j+2N}^{(m')*}+c_{j-2N}^{(m')*}).\end{aligned}\tag{2.30}$$

Similarly, using $\mathcal{Q}_{\mathrm{S}}(x)=\sin^2(2x)$, the matrix elements of the short perturbation follow as

$$\begin{aligned}\langle\psi'_{m'}|\xi_{\mathrm{S}}|\psi'_m\rangle = \frac{\lambda_{\mathrm{S}}}{2}(\mathrm{e}^{\mathrm{i}\varphi_t}\delta_{\nu'+2s,\nu}+\mathrm{e}^{-\mathrm{i}\varphi_t}\delta_{\nu'-2s,\nu})\\ \times\frac{1}{4}\sum_{j=-\infty}^{\infty}c_j^{(m)}(2c_j^{(m')*}-c_{j+2N}^{(m')*}-c_{j-2N}^{(m')*}).\end{aligned}\tag{2.31}$$

Having obtained the expressions (2.30) and (2.31), let us clarify the utility of using the basis functions (2.26) with the level renumbering function (2.27). First, we note that the perturbation $\cos(\omega t+\varphi_t)$ is resonant with transitions between states whose energy differ by $\omega=s\Omega$. Meanwhile, the spatial Hamiltonian $\hat{h}$ possesses narrow bands of levels, with bands separated by approximately Ω. Therefore, the perturbation couples levels belonging to bands differing in energy by $s\Omega$, while the coupling between levels of the same band can be disregarded. The level renumbering according to Eq. (2.27) groups the levels into bands, while the basis functions (2.26) effectively take into account only the couplings between the bands whose numbers differ by multiples of s. These couplings are reflected by the Kronecker deltas in Eqs. (2.30) and (2.31).

The matrix elements of $\hat{Q}$ are thus given by Eqs. (2.28), (2.30) and (2.31). We diagonalise this matrix numerically an obtain the eigenfunctions (Floquet modes) $u_n(x,t)=\sum_m b_m^{(n)}\psi'_m(x,t)$. Then, the Wannier functions are constructed by diagonalising the periodic position operator $\mathrm{e}^{\mathrm{i}\frac{2}{N}x}$ [128, 134], whose matrix elements result as

$$\langle u_{n'}(t)|\mathrm{e}^{\mathrm{i}\frac{2}{N}x}|u_n(t)\rangle=\sum_{j=-\infty}^{\infty}\sum_{m,m'}b_{m'}^{(n')*}b_m^{(n)}c_{j+1}^{(m')*}c_j^{(m)}\mathrm{e}^{\mathrm{i}[\nu(m')-\nu(m)]\omega t/s}.\tag{2.32}$$

The diagonalisation is performed at a chosen time moment t. The obtained coefficients $d_n^{(k)}$ are used to express the Wannier states as

$$w_k(x,t)=\sum_n d_n^{(k)}u_n(x,t).\tag{2.33}$$

Note that the position operator is constructed using only the relevant subspace of eigenvectors $|u_n\rangle$ that we select based on our interpretation of the quasienergy spectrum. Subsequent renumbering of these eigenvectors and the Wannier states using a pair of indices (i, α) is likewise conventional.

Our software package `TTSC.jl` implementing all relevant calculations is available on GitHub [136]. It relies on a number of software packages [137–142] developed in Julia [143].

CHAPTER 3

Eight-dimensional topological systems simulated using time-space crystalline structures

We will now take the concept of a time-space crystalline lattice further and provide a route for studying topological eight-dimensional (8D) systems that can be experimentally realised using only two physical spatial dimensions. We will start with a periodically driven 1D optical lattice with steep barriers (modelled by delta-functions) and show that it can sustain a 2D time-space lattice. The topological nature of the attained time-space crystalline structure will be once again made evident by considering adiabatic state pumping along temporal and spatial crystalline directions. Interpreting the two adiabatic phases as crystal momenta of simulated extra dimensions, we show that the energy bands of the system are characterised by nonvanishing second Chern numbers of the effective 4D lattice. Finally, we demonstrate that two such 4D systems can be combined, and the resulting energy spectrum will remain gapped. The topological properties of the obtained 8D system are then characterised by the fourth Chern number, and energy bands with nonvanishing values of the fourth Chern number are identified.

3.1 Model

The spatial part of the model Hamiltonian (2.1) underlying the analysis of Chapter 2 is straightforward to realise experimentally [127, 126, 49], but the gaps between its energy subbands are much smaller than the widths of the subbands [see Fig. 2.4(a), with the gap shown in the inset]. Consequently, if two copies of such a Hamiltonian (realised in orthogonal spatial directions) are combined as in Eq. (1.28), the resulting spectrum will not be gapped, and no

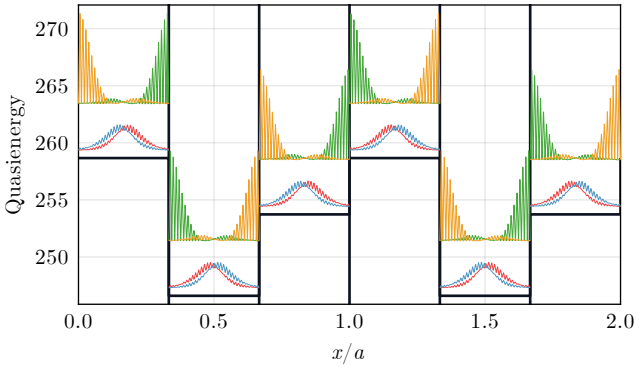

Figure 3.1: Wannier function densities $|w_\ell(x, t = 7\pi/4\Omega)|^2$ at $\varphi_x = \pi/5$, $\varphi_t = 0$, where $2\pi/\Omega$ is the period of time evolution of $w_\ell(x, t)$. The baseline of each Wannier function is shifted upwards along the quasienergy axis by the mean value of quasienergy in the corresponding state, i.e., the quantity $\langle w_\ell|\hat{Q}|w_\ell\rangle$. At the chosen value of φ_x, each Wannier function is localised almost entirely within a single site, therefore, the infinitesimal 'tails' of the functions are not shown. Black vertical lines represent the steep barriers separating the sites of the spatial lattice, while the horizontal lines depict the values of the onsite energies described by the third term in Eq. (3.1). Parameters of the model are: $N = 2$, $s = 2$, $a = 4.000$, $V = 2000$, $U = 7.000$, $\omega = 676.8$, $\lambda_S = 10.00$, $\lambda_L = 20.00$. Trailing zeros are within the numerical resolution/accuracy and are significant. The nature of the presented results, however, will not change if all the values are chosen within $\sim 10\%$ of the given ones and then ω is adjusted accordingly to ensure that the quasienergy spectrum is gapped.

topological features will emerge. Therefore, we need to consider a different model that would yield gaps which are broader than the widths of the bands.

The 1D time-dependent Hamiltonian to be considered in the present analysis again has the form (2.1), but the constituent terms are different. The unperturbed spatial Hamiltonian is taken to be

$$\hat{h} = \hat{p}_x^2 + V \sum_{n=0}^{3N} \delta(x - \tfrac{na}{3}) + U \sum_{n=1}^{3} g_n(x) \cos\Big[\varphi_x + \tfrac{2\pi(n-1)}{3}\Big]. \qquad (3.1)$$

We use the same dimensionless units as in Chapter 2. The sums describe the spatial potential — a lattice of N identical cells of length a, each consisting of three sites separated by steep delta-function barriers (see Fig. 3.1). The superlattice potential $g_n(x)$ is equal to unity in the nth site of each spatial cell and vanishes otherwise:

$$g_n(x) = \begin{cases} 1, & \frac{n}{3}a \le x \bmod a < \frac{n+1}{3}a, \\ 0, & \text{otherwise.} \end{cases} \qquad (3.2)$$

The last term of Eq. (3.1) thus modulates the onsite energies in the same way

in each cell by changing φ_x, with U controlling the modulation amplitude. Note that the modulation phase in each consecutive site is lagging with respect to its neighbour on the left by one third of a cycle. If the modulation is performed adiabatically, the Thouless pumping can be realised in the system described by $\hat{h}$. We remark that similar three-site Thouless pumping schemes have been considered in Refs. [144, 145], while the realisation of a lattice of sharp (subwavelength) optical barriers has been reported in Ref. [146].

The spatial Hamiltonian is perturbed by the terms

$$\xi_{\mathrm{S}}(x,t) = \lambda_{\mathrm{S}} \cos(\tfrac{12\pi x}{a}) \cos(2\omega t), \tag{3.3a}$$

$$\xi_{\mathrm{L}}(x,t|\varphi_t) = \lambda_{\mathrm{L}} \cos(\tfrac{6\pi x}{a}) \cos(\omega t + \varphi_t), \tag{3.3b}$$

where λ_{S} and λ_{L} control the overall strength of the perturbation. The spatial frequencies $6\pi/a$ and $12\pi/a$ ensure that all spatial sites are perturbed in the same way. The driving frequency ω is chosen so that a resonant condition is fulfilled in each spatial site. In the classical description, the resonance means that ω is very close to an integer multiple of the frequency Ω of the periodic motion of a particle in a spatial site, i.e., $\omega \approx s\Omega$, where s is integer. In the quantum description, the resonance corresponds to ω being close to an integer multiple of the gap Ω between certain bands of the Hamiltonian (3.1). In the limit $V \to \infty$ [see Eq. (3.1)] an independent time-crystalline structure is formed in each spatial site due to the resonant driving. Specifically, in the frame evolving along the resonant trajectory, the resonant dynamics of a particle can be described by $\hat{H}_{\mathrm{eff}} = \hat{\tilde{p}}_{\tilde{x}}^2 + \tilde{\lambda}_{\mathrm{S}} \cos(2s\tilde{x}) + \tilde{\lambda}_{\mathrm{L}} \cos(s\tilde{x} + \varphi_t)$ where $\tilde{x} \in [0, 2\pi)$. For example, for $s = 2$, there are two temporal cells, each consisting of two temporal sites. An adiabatic change of the phase φ_t allows for a realisation of the Thouless pumping in the time-crystalline structures. If V is finite, then tunnelling of a particle between spatial sites is possible, and the entire system forms a 2D time-space crystalline structure which, as we will show, can be described by a 2D tight-binding model.

3.2 Diagonalisation procedure and main features of the quasienergy spectrum

Analysis of the system is performed similarly to the one presented in Chapter 2. We solve the eigenvalue problem $\hat{Q}u_{n,k}(x,t) = \varepsilon_{n,k}u_{n,k}(x,t)$ for the quasienergy operator $\hat{Q} = \hat{H} - \mathrm{i}\partial_t$. We assume periodic boundary conditions for the spatial system and introduce the spatial quasimomentum k. We denote the quasienergy of the nth eigenstate by $\varepsilon_{n,k}$, while $u_{n,k}(x,t)$ is the corresponding Floquet mode that respects temporal periodicity of the perturbation:

$u_{n,k}(x,t) = u_{n,k}(x,t+2\pi/\omega)$. A general solution of the Schrödinger equation can be represented as a superposition of states $\Psi_{n,k}(x,t) = \mathrm{e}^{-\mathrm{i}\varepsilon_{n,k}t}u_{n,k}(x,t)$. In our simulations we consider a finite number of spatial cells, $N = 2$, and a finite number of temporal cells, $s = 2$. The considered values of quasimomenta are thus $k = 0$ and $k = \pi/a$, corresponding to the boundaries of the energy bands [147]. Consequently, the obtained widths of the energy bands coincide with the widths being approached in the limit $N \to \infty$.

Let us consider the diagonalisation of the quasienergy operator

$$\hat{Q}_k = \hat{H}_k - \mathrm{i}\partial_t. \tag{3.4}$$

Here, we have introduced the quasimomentum index, stemming from the spatial part of the problem. Specifically, we have

$$\hat{H}_k(x,t|\varphi_t) = \hat{h}_k(x) + \xi_{\mathrm{S}}(x,t) + \xi_{\mathrm{L}}(x,t|\varphi_t), \tag{3.5}$$

where

$$\hat{h}_k = (\hat{p}_x + k)^2 + V\sum_{n=0}^{3N}\delta(x - \tfrac{na}{3}) + U\sum_{n=0}^{2} g_n(x)\cos(\varphi_x + \tfrac{2\pi n}{3}). \tag{3.6}$$

It is a standard exercise to obtain the Bloch modes $\psi_{m,k}$ and eigenenergies $E_{m,k}$ for a delta-function Hamiltonian (3.6). The next step is to solve the eigenvalue problem

$$\hat{Q}_k v_{n,k}(x,t) = \varepsilon_{n,k} v_{n,k}(x,t). \tag{3.7}$$

The Floquet modes $u_{n,k}$ defined above as the eigenfunctions of $\hat{Q}$ are related to the functions $v_{n,k}$ according to the Bloch's theorem: $u_{n,k}(x,t) = \mathrm{e}^{\mathrm{i}kx}v_{n,k}(x,t)$.

Instead of the full diagonalisation of $\hat{Q}_k$, our aim is to obtain an effective (secular) time-independent Hamiltonian which can be more easily diagonalised. To this end we perform a time-dependent unitary transformation

$$\psi'_{m,k}(x,t) = \mathrm{e}^{-\mathrm{i}\nu(m)\omega t/s}\psi_{m,k}(x). \tag{3.8}$$

Here, the function $\nu(m) = \lceil m/3 \rceil$ (where $\lceil \cdots \rceil$ is the ceiling operation) transforms the level numbers $m = 1, 2, 3, 4, 5, 6, \ldots$ into band indices

$$\nu = 1, 1, 1, 2, 2, 2, 3, 3, 3, \ldots \tag{3.9}$$

Note that this labelling is correct as long as we keep U small enough so that the difference of depths of the sites is always smaller than the gaps between the energy bands of the unperturbed Hamiltonian.

The diagonal matrix elements of $\hat{Q}_k$ are

$$\langle\psi'_{m',k}|\left(\hat{h}_k - \mathrm{i}\frac{\partial}{\partial t}\right)|\psi'_{m,k}\rangle = \left(E_{m,k} - \frac{\nu(m)\omega}{s}\right)\delta_{m',m}. \tag{3.10}$$

For the perturbation term ξ_{L}, we obtain

$$\begin{aligned}\langle\psi'_{m',k}|\xi_{\mathrm{L}}|\psi'_{m,k}\rangle = \lambda_{\mathrm{L}}\cos(\omega t+\varphi_t)\,\mathrm{e}^{-\mathrm{i}(\omega/s)[\nu(m)-\nu(m')]t} \\ \times\int_0^a \mathrm{d}x\,\psi^*_{m',k}(x)\cos\tfrac{6\pi x}{a}\psi_{m,k}(x).\end{aligned} \tag{3.11}$$

Applying the secular approximation, we replace $\cos(\omega t+\varphi_t)\,\mathrm{e}^{-\mathrm{i}(\omega/s)[\nu(m)-\nu(m')]t}$ with its time-independent contribution $\frac{1}{2}(\mathrm{e}^{\mathrm{i}\varphi_t}\delta_{\nu'+s,\nu}+\mathrm{e}^{-\mathrm{i}\varphi_t}\delta_{\nu'-s,\nu})$, where $\nu'\equiv\nu(m')$. Similarly, we have

$$\begin{aligned}\langle\psi'_{m',k}|\xi_{\mathrm{S}}|\psi'_{m,k}\rangle = \lambda_{\mathrm{S}}\cos(2\omega t)\,\mathrm{e}^{-\mathrm{i}(\omega/s)[\nu(m)-\nu(m')]t} \\ \times\int_0^a \mathrm{d}x\,\psi^*_{m',k}(x)\cos\tfrac{12\pi x}{a}\psi_{m,k}(x),\end{aligned} \tag{3.12}$$

where we replace $\cos(2\omega t)\,\mathrm{e}^{-\mathrm{i}(\omega/s)[\nu(m)-\nu(m')]t}$ with $\frac{1}{2}(\delta_{\nu'+2s,\nu}+\delta_{\nu'-2s,\nu})$.

Figure 3.2(a) displays schematically the coupling of the eigenenergy bands of $\hat{h}_k$ induced by the perturbations. Each band of $\hat{h}_k$ consists of three subbands because each cell of the spatial potential of $\hat{h}_k$ contains three sites, but this is not detailed in the figure. As a result of the secular approximation, each level of the νth band is coupled to all the levels of bands $\nu\pm s$ (via ξ_{L}) and $\nu\pm 2s$ (via ξ_{S}); in our case, $s=2$. The driving frequency is chosen as $\omega=\Omega s$ with Ω being the energy gap between certain bands μ and $\mu+1$. In practice, however, we fine-tune ω_μ to get the optimal quasienergy spectrum. Below, we will assume the working point of $\mu=30$, which yields $E_{31}-E_{30}\approx 340$ for $a=4$. This is consistent with the result calculated for the problem of a particle in an infinitely deep potential well of width $l=a/3$: in recoil units, the energy spectrum is $E_\nu=(\nu\pi/l)^2$. This also allows one to estimate the frequency: $\Omega=E_{\mu+1}-E_\mu=(2\mu+1)\frac{\pi^2}{l^2}$. In a small neighbourhood of the μth energy band, the spectrum is close to being equidistant, therefore, transitions such as $E_{\mu-1}\leftrightarrow E_{\mu+1}$ and $E_{\mu+1}\leftrightarrow E_{\mu+3}$ are almost resonant with the frequency ω_μ.

A sketch of the quasienergy spectrum of $\hat{Q}_k$ is given in Fig. 3.2(b). The bands of $\hat{h}_k$ become grouped into overlapping pairs, and the resonant bands are the lowest. This can be seen by employing the above estimates of the energy spectrum E_ν and the resonant frequency Ω. Suppressing the k index, we find

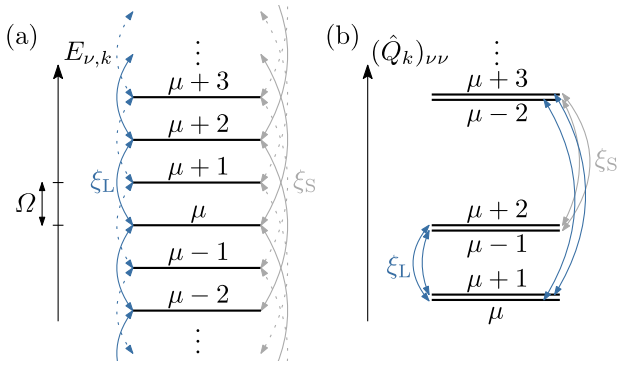

Figure 3.2: Schematic representation of the perturbation-induced band coupling (distances between bands not drawn to scale). (a) Eigenenergy bands of the unperturbed Hamiltonian $\hat{h}_k$ in the vicinity of a certain resonant band whose number is μ. Each horizontal line represents an energy band (which contains three subbands). (b) Diagonal elements of the quasienergy operator represented as coupled quasienergy levels. Only the couplings that have the most effect are shown.

from Eq. (3.10) that

$$Q_{\mu+\beta,\mu+\beta} = E_{\mu+\beta} - \Omega(\mu+\beta) = Q_{\mu,\mu} + (\beta^2-\beta)\tfrac{\pi^2}{l^2}, \tag{3.13}$$

where integer (band) index β runs from $1-\mu$ to infinity. Assuming the perturbation is small, the above expression yields the Floquet quasienergy spectrum shown in Fig. 3.2(b). The lowest are the levels $\beta = \mu$ and $\beta = \mu+1$, whose energies should coincide according to Eq. (3.13).

The actual quasienergy spectrum is shown in Fig. 3.3(a) for the case of simultaneous time-space pumping ($\varphi_x = \varphi_t$), with only the resonant bands displayed. These correspond precisely to the bands $\mu-1$ through $\mu+2$ shown schematically in Fig. 3.2(b).

Returning to the problem of finding the eigenfunctions of $\hat{Q}_k$, it remains to numerically diagonalise the obtained matrix for each k to find the coefficients $b^{(n)}_{m,k}$ of the expansion

$$v_{n,k}(x,t) = \sum_{m=1}^{\infty} b^{(n)}_{m,k}\psi'_{m,k}(x,t). \tag{3.14}$$

The described calculations are implemented in the `TTSC.jl` package [136].

3.3 Visualisation of time-space pumping using the Wannier functions

The resonant subspace of the entire Hilbert space which we are interested in consists of $3N \times 2s$ eigenstates. To analyse the pumping dynamics, we construct Wannier functions $w_\ell(x,t)$ by diagonalising the periodic position operator $\mathrm{e}^{\mathrm{i}\frac{2\pi}{Na}x}$. Diagonalisation yields the coefficients $d_{n,k}^{(\ell)}$ of the expansion

$$w_\ell(x,t) = \sum_{n,k} d_{n,k}^{(\ell)} u_{n,k}(x,t). \tag{3.15}$$

Diagonalisation has to be performed at a single fixed time moment at which the modes $u_{n,k}$ do not overlap strongly so that the resulting Wannier functions exhibit the required temporal localisation [49]. In the relevant cases we sum over all quasimomenta k, while index n runs over a selected range of modes. This way we obtain $6Ns$ Wannier functions $w_\ell(x,t)$ of the $3N \times 2s$ time-space crystalline structure which are represented by localised wave packets propagating with the period $2\pi/\Omega$ along the resonant orbits in each spatial site. These Wannier functions are shown at $t = 7\pi/4\Omega$ in Fig. 3.1, where each spatial site hosts $2s = 4$ states.

Figure 3.3(b) displays the functions w_ℓ at $\varphi_x = \varphi_t = 0$ constructed by mixing the four modes corresponding to the highest band in the spectrum in Fig. 3.3(a) (highlighted in orange). The resulting functions inherit the spatial localisation of the Floquet–Bloch modes being mixed and, consequently, are confined to a single spatial site. A detector placed at one of the turning points of any spatial site will be registering periodic arrival of a particle, and we identify this periodicity with a crystalline structure in time. The shaded regions in Fig. 3.3(b) indicate the parts of the time-space that we associate — by convention — with the four temporal sites: sites $\alpha = 1, 2$ (green and red) belong to the first temporal cell, while $\alpha = 3, 4$ (beige and blue) belong to the second. For example, a particle in the state w_1 will be passing a detector placed at $x = 0$ at time intervals $(\Omega t \bmod 2\pi) \in [0, \pi]$, meaning that it occupies the first temporal cell. In the course of the pumping, the states transition both in the spatial and in the temporal directions. At $\varphi_x = \varphi_t = \pi/3$ [see Fig. 3.3(c)], the states are localised in a single temporal site while occupying two neighbouring spatial sites. At the end of the pumping cycle, states w_1 and w_4 effectively exchange their initial occupations, as do states w_2 and w_3. Thus, having divided the time-space into temporal and spatial cells as shown in the figure, we find that at the end of a time-space pumping cycle each Wannier function occupies spatial and temporal cells different from the starting ones.

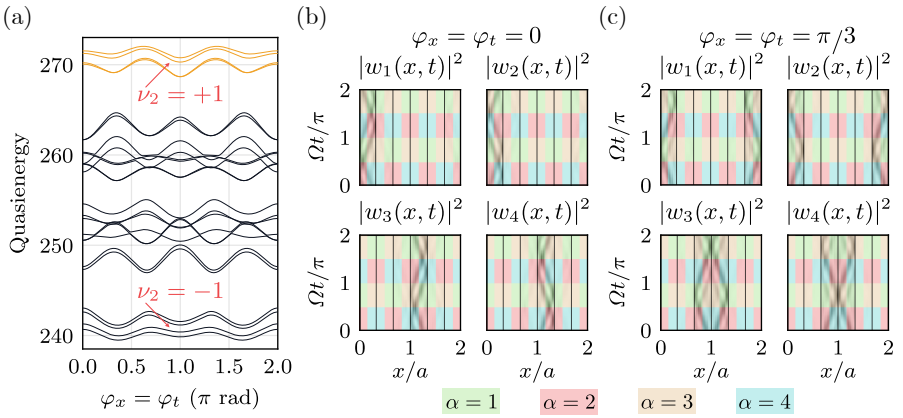

Figure 3.3: Time-space adiabatic pumping in a 2D time-space crystal with $s = 2$ temporal cells and $N = 2$ spatial cells that consists of three spatial sites. The values of parameters are the same as used in producing Fig. 3.1. (a) Quasienergy spectrum of the quasienergy operator $\hat{Q}$. (b) The Wannier functions $|w_\ell(x,t)|^2$ at $\varphi_x = \varphi_t = 0$, represented by black regions. The shaded areas indicate the extent of the temporal sites numbered by α: sites $\alpha = 1, 2$ belong to the first temporal cell, while $\alpha = 3, 4$ belong to the second. Black vertical lines separate the spatial sites. (c) Same as (b) at $\varphi_x = \varphi_t = \pi/3$.

3.4 The tight-binding picture

In the basis of the Wannier functions, the quasienergy operator restricted to the resonant subspace takes the form of the tight-binding model

$$\hat{H}_{\mathrm{TB}}(\varphi_x, \varphi_t) = \sum_{\ell',\ell} J_{\ell'\ell}(\varphi_x, \varphi_t)\hat{a}^\dagger_{\ell'}\hat{a}_\ell, \tag{3.16}$$

where operator $\hat{a}^\dagger_\ell$ creates (while $\hat{a}_\ell$ annihilates) a boson on site ℓ. Here, $\ell \in [1, 6Ns]$ enumerates all sites of the 2D time-space lattice, and it is related to the space-time index pair (j, α) as $\ell = 2s(j-1) + \alpha$, where $j \in [1, 3N]$ and $\alpha \in [1, 2s]$. The matrix elements $J_{\ell'\ell}$ are calculated as

$$J_{\ell'\ell} = \int_0^{sT} \frac{\mathrm{d}t}{sT} \langle w_{\ell'}|\hat{Q}|w_\ell\rangle, \tag{3.17}$$

where $T = 2\pi/\omega$ is the driving period. The Wannier basis is constructed repeatedly for every phase φ_x and φ_t. Each state $|w_\ell(t)\rangle$ is confined to a single spatial site, consequently, only nearest-neighbour spatial couplings are relevant. Moreover, this coupling is appreciable only at times when a given state $|w_\ell(t)\rangle$ is localised near a classical turning point (see the green and yellow states in Fig. 3.1). At these times, each of these states has only one partner which it

is coupled to. Therefore, each Wannier state is coupled to only a single state of those in the neighbouring spatial sites. Provided these partners (see like-coloured states in Fig. 3.1) are numbered with the same temporal index α, this index will not change when a state transitions to a neighbouring site (only j will change). This leads to a separable structure of the resulting time-space lattice, where 'diagonal' transitions — those which require both indices j and α to change simultaneously — are forbidden. This is an idealised picture, but one which holds with high accuracy since next-nearest-neighbour couplings are negligible, as we show below.

Let us elaborate the procedure of switching to the tight-binding description. We construct the Wannier basis functions by mixing the states corresponding to all the resonant levels of the Floquet quasienergy spectrum, i.e., all levels shown in Fig. 3.3(a). In practice, two out of four Wannier functions localised in a single spatial site come out not well-localised in the temporal dimensions. To alleviate this issue, we perform an additional unitary transformation of the two problematic Wannier functions w_a and w_b:

$$\begin{pmatrix} \tilde{w}_a \\ \tilde{w}_b \end{pmatrix} = \hat{U}(\gamma, \theta, \phi) \begin{pmatrix} w_a \\ w_b \end{pmatrix}. \tag{3.18}$$

Here, $\hat{U}(\gamma, \theta, \phi)$ is a general 2×2 unitary matrix

$$\hat{U}(\gamma, \theta, \phi) = \mathrm{e}^{\mathrm{i}\gamma \boldsymbol{n}(\theta,\phi)\boldsymbol{\sigma}}, \tag{3.19}$$

where $\gamma \in [0, 2\pi]$, $\boldsymbol{\sigma}$ is a vector of Pauli matrices, and $\boldsymbol{n}$ is a three-component unit vector parameterised by an azimuthal angle $\phi \in [0, 2\pi]$ and a polar angle $\theta \in [0, \pi]$. We optimise the angles γ, θ, and ϕ to get the least possible overlap of probability densities of $\tilde{w}_a$ and $\tilde{w}_b$. Specifically,

$$\iint \mathrm{d}x\, \mathrm{d}t \; \left| |\tilde{w}_3|^2 - |\tilde{w}_2|^2 \right| \to \max. \tag{3.20}$$

In what follows, the Wannier functions being discussed are the 'optimised' ones.

In the studied case, we obtain $3N \times 2s = 24$ Wannier functions, which we are free to number as we see fit. Figure 3.4 shows, as an example, twelve Wannier functions localised in the first, second, and sixth spatial sites. As we can see, each of them is strongly localised in a single spatial and temporal site. The numbering convention is such that the ℓth Wannier is localised in the jth spatial and the αth temporal sites, with $\ell = 2s(j-1)+\alpha$, where $j \in [1, 3N]$ and $\alpha \in [1, 2s]$. Note, however, that the temporal sites are assigned differently in the odd and even spatial sites. For example, a particle is said to occupy the first temporal site (green areas in Fig. 3.4) of an odd spatial site if it will most likely

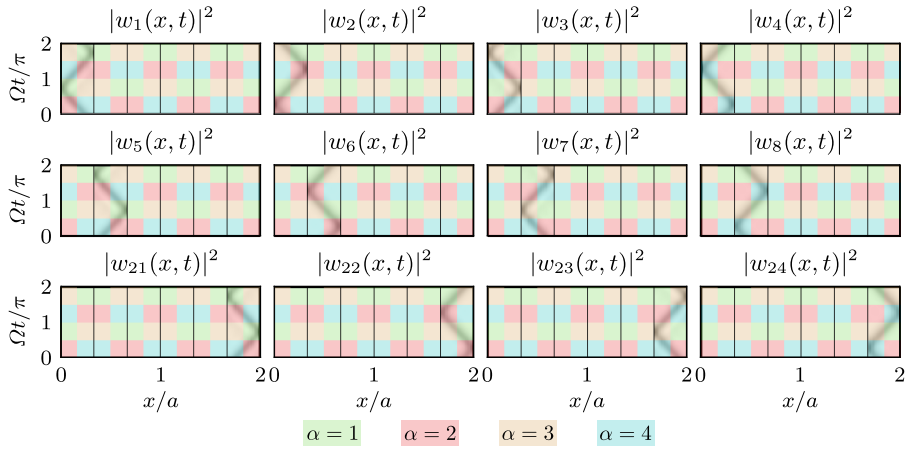

Figure 3.4: 12 (out of 24) Wannier states used as the basis functions in the tight-binding picture.

be found at the right turning point in the interval $(\Omega t \bmod 2\pi) \in [3\pi/2, 2\pi]$, see w_1 in Fig. 3.4. On the other hand, a particle occupying the first temporal site of an even spatial site will most likely be found found at the left turning point in the same interval $(\Omega t \bmod 2\pi) \in [3\pi/2, 2\pi]$, see w_5 in Fig. 3.4. Such a convention ensures the correct interpretation of the outcome of a pumping cycle, as demonstrated in Section 3.3. Moreover, it allows one to obtain a tight-binding Hamiltonian (3.16) that can be decomposed into two independent parts — the spatial Hamiltonian and the temporal one. The absolute values of the matrix elements of $\hat{H}_{\mathrm{TB}}$ calculated at $\varphi_x = \varphi_t = 0$ are presented in Fig. 3.5, where the diagonal elements have been set to zero for visual clarity. It is apparent that the resulting matrix allows for the decomposition

$$\hat{H}_{\mathrm{TB}} \approx \hat{I}^{(x)} \otimes \hat{H}^{(t)} + \hat{H}^{(x)} \otimes \hat{I}^{(t)} \equiv \hat{H}'_{\mathrm{TB}}, \tag{3.21}$$

where $\otimes$ denotes the tensor product, $\hat{H}^{(x)}$ and $\hat{H}^{(t)}$ are, respectively, the separated spatial and temporal Hamiltonians, while $\hat{I}^{(x)}$ and $\hat{I}^{(t)}$ are the identity operators acting in the spaces of, respectively, operators $\hat{H}^{(x)}$ and $\hat{H}^{(t)}$. Consequently, the eigenvalue spectrum of $\hat{H}'_{\mathrm{TB}}$ is the Minkowski sum of eigenvalue spectra of $\hat{H}^{(x)}$ and $\hat{H}^{(t)}$. We will refer to the eigenvalues of all tight-binding Hamiltonians as simply 'energies'. In our case, we take $\hat{H}^{(t)}$ to be given by the

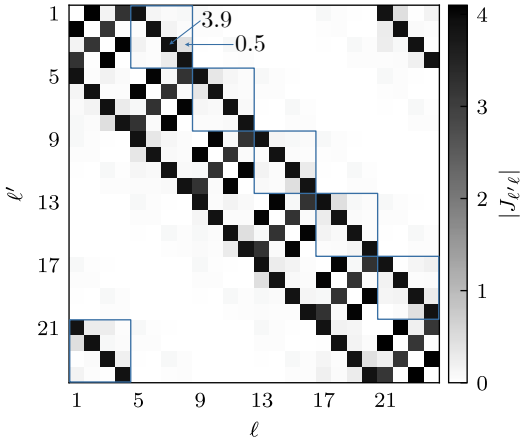

Figure 3.5: Absolute values $|J_{\ell'\ell}|$ of the matrix elements of $\hat{H}_{\mathrm{TB}}$ at $\varphi_x = \varphi_t = 0$. Diagonal elements have been set to zero for visual clarity. Values of J_{37} and J_{38} are explicitly indicated. The structure of the blue blocks is similar to the displayed one for all values of the phases φ_x and φ_t.

top left 4×4 block of $\hat{H}_{\mathrm{TB}}$, while $\hat{H}^{(x)}$ is given by

$$\hat{H}^{(x)} = \begin{pmatrix} J_{11} & |J_{15}| & 0 & 0 & 0 & |J_{15}| \\ |J_{15}| & J_{55} & |J_{15}| & 0 & 0 & 0 \\ 0 & |J_{15}| & J_{99} & |J_{15}| & 0 & 0 \\ 0 & 0 & |J_{15}| & J_{11} & |J_{15}| & 0 \\ 0 & 0 & 0 & |J_{15}| & J_{55} & |J_{15}| \\ |J_{15}| & 0 & 0 & 0 & |J_{15}| & J_{99} \end{pmatrix}. \tag{3.22}$$

For simplicity, we assume that the phases of the the tunnelling strengths have been eliminated by redefining the global phases of the basis functions. The crudest part of the separability approximation (3.21) is the dropping of the off-diagonal elements in the blue blocks (and their conjugate counterparts) highlighted in Fig. 3.5.

To extract the first Chern numbers ν_1 of the bands of Hamiltonians $\hat{H}^{(x)}$ and $\hat{H}^{(t)}$, we may calculate the pumping dynamics. To this end, we consider the periodic coordinate operator, whose elements, in coordinate representation, are given by $X_{mm} = \mathrm{e}^{\mathrm{i}\frac{2\pi}{M}m}$, where $m \in [0, M-1]$ and M is the size of the Hamiltonian under consideration ($M = 6$ for $\hat{H}^{(x)}$ and $M = 4$ for $\hat{H}^{(t)}$). Then, we diagonalise this operator in the subspace of the eigenstates of $\hat{H}^{(x)}$ or $\hat{H}^{(t)}$ corresponding to a single band of the energy spectrum. The resulting eigenfunctions of $\hat{X}$ are the Wannier functions, while the phases of the eigenvalues (scaled by $2\pi/M$) are their well-defined positions (also called the Wannier centres) [134, 128]. Black points in Fig. 3.6(a) show the dynamics of

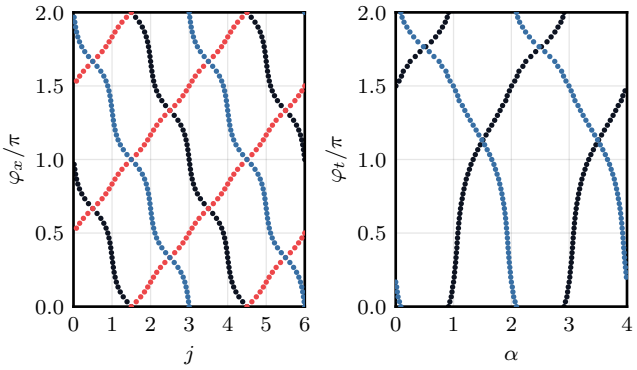

Figure 3.6: Dynamics of the Wannier centres. (a) Spatial pumping dynamics calculated based on $\hat{H}^{(x)}$. Black, red, and blue points represent, respectively, the positions of the Wannier centres calculated by mixing the eigenstates corresponding to the bottom, middle, and top bands in the spectrum of $\hat{H}^{(x)}$ [see Fig. 3.7(a)]. (b) Temporal pumping dynamics calculated based on $\hat{H}^{(t)}$. Black and blue points represent, respectively, the positions of the Wannier centres calculated by mixing the eigenstates corresponding to the bottom and top bands in the spectrum of $\hat{H}^{(t)}$ [see Fig. 3.7(b)].

the Wannier centres obtained by considering the subspace of the lowest energy band of $\hat{H}^{(x)}$. It is apparent that the states are transferred by one cell (three sites) 'to the left' during one pumping cycle. Blue points show an analogous result for the states of the highest energy band of $\hat{H}^{(x)}$, while the red points indicate a displacement by two cells per cycle in the opposite direction. The first Chern numbers of the bands are thus -1, $+2$, and -1 for the bottom, middle, and the top energy bands of $\hat{H}^{(x)}$.

The temporal pumping based on $\hat{H}^{(t)}$ is studied in Fig. 3.6(b). The black points indicate a displacement by a single cell 'to the right' per pumping cycle taking place in the bottom energy band ($\nu_1 = +1$), while the blue points show a displacement by a single cell in the opposite direction for the top energy band ($\nu_1 = -1$).

The spectra of $\hat{H}^{(x)}$ and $\hat{H}^{(t)}$ are shown in Figs. 3.7(a) and 3.7(b) together with the first Chern numbers of each band. Considering the spatial part described by $\hat{H}^{(x)}$, we treat the phase φ_x as a fictitious quasimomentum, allowing us to introduce the Berry curvature of the nth band, $\Omega^{(n)}_{k_x\varphi_x} = 2\Im\langle\partial_{k_x}\chi^{(n)}_{k_x}|\partial_{\varphi_x}\chi^{(n)}_{k_x}\rangle$, and the corresponding first Chern number $\nu_1^{(x)}$ according to (1.21). In the definition of the Berry curvature, $|\chi^{(n)}_{k_x}\rangle$ is the cell-periodic part of the Bloch eigenstate $\mathrm{e}^{\mathrm{i}k_x j}\chi^{(n)}_{k_x}(j)$ of $\hat{H}^{(x)}$ with $\chi^{(n)}_{k_x}(j+3) = \chi^{(n)}_{k_x}(j)$ where j labels spatial sites. For brevity, we suppress indication of the parametric dependence on φ_x in $\hat{H}^{(x)}$ and its eigenstates. The quasimomentum k_x is treated as a continuous quantity assuming $N \to \infty$. Let us clarify that the three subbands shown in Fig. 3.7(a) arise because there are three sites per unit

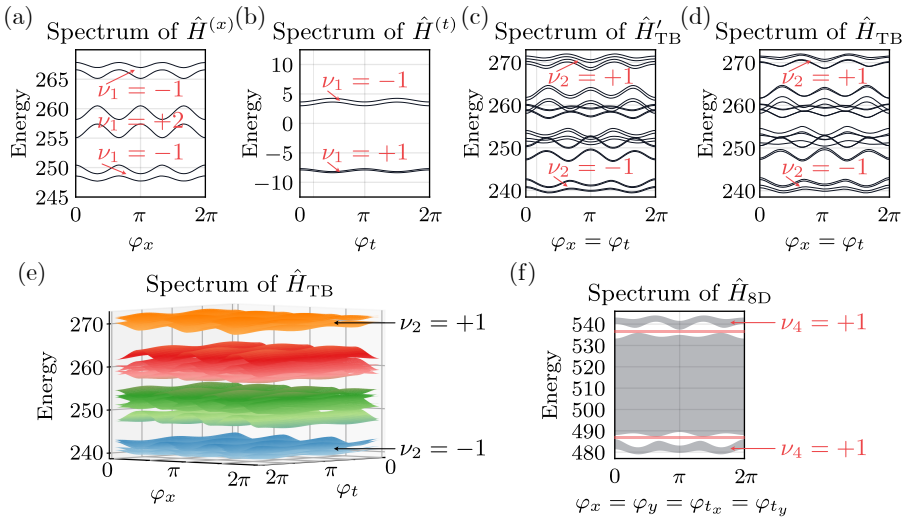

Figure 3.7: The energy spectra of derived systems. (a) Energy spectrum of the decomposed spatial Hamiltonian $\hat{H}^{(x)}$. (b) Energy spectrum of the decomposed temporal Hamiltonian $\hat{H}^{(t)}$. (c) Energy spectrum of $\hat{H}'_{\mathrm{TB}}$, equal to the Minkowski sum of the spectra in (a) and (b). A cut of the spectrum along the line $\varphi_x = \varphi_t$ is shown. (d) Energy spectrum of $\hat{H}_{\mathrm{TB}}$ along the line $\varphi_x = \varphi_t$. (e) Eigenenergy surfaces of $\hat{H}_{\mathrm{TB}}$. (f) Energy spectrum of an 8D systems obtained by combining two independent copies of the 4D systems whose spectra are shown in (e). The grey areas represent the bands, with individual levels not shown for visual clarity. The red regions indicate the gaps.

cell of the spatial lattice. Each line corresponds to a certain value of quasimomentum k_x — each subband is bounded by two lines, one corresponding to $k_x = 0$ and another to $k_x = \pi$.

In complete analogy with the spatial part of the problem, we introduce the time-quasimomentum k_t for the Hamiltonian $\hat{H}^{(t)}$, so that the eigenstates of $\hat{H}^{(t)}$ are given by $\mathrm{e}^{\mathrm{i}k_t\alpha}\tau^{(n)}_{k_t}(\alpha)$ with $\tau^{(n)}_{k_t}(\alpha+2) = \tau^{(n)}_{k_t}(\alpha)$. The first Chern numbers $\nu_1^{(t)}$ of the two bands in Fig. 3.7(b) are then calculated by integrating the Berry curvature $\Omega^{(n)}_{k_t\varphi_t}$. The two subbands shown in Fig. 3.7(b) arise because there are two sites per unit cell of the temporal lattice, and each line corresponds to a certain value of time-quasimomentum k_t.

By interpreting the phases φ_x and φ_t appearing in the Berry curvature as quasimomenta of synthetic dimension, we increase the dimensionality of the systems. Each of the Hamiltonians $\hat{H}^{(x)}$ and $\hat{H}^{(t)}$ thus describes a 2D system, while their combination, $\hat{H}'_{\mathrm{TB}}$, whose spectrum is shown in Fig. 3.7(c), describes a 4D system. The lowest and the highest bands are nondegenerate and are characterised by the second Chern numbers calculated from the Abelian Berry curvature, as explained in Section 1.4. Formally, we gather the system parameters into a vector $\boldsymbol{R} = (k_x, \varphi_x, k_t, \varphi_t)$ and calculate the curvature as

$\Omega_{ij}^{(l)}(\boldsymbol{R}) = 2\Im\langle\partial_i\xi_{k_x,k_t}^{(l)}|\partial_j\xi_{k_x,k_t}^{(l)}\rangle$ where $\partial_i \equiv \frac{\partial}{\partial R^i}$, $i = 1,2,3,4$, and $|\xi_{k_x,k_t}^{(l)}\rangle$ is the cell-periodic part of the lth band eigenstate of $\hat{H}'_{\mathrm{TB}}$. Due to the factorisation $|\xi_{k_x,k_t}^{(l)}\rangle = |\chi_{k_x}^{(m)}\rangle \otimes |\tau_{k_t}^{(n)}\rangle$, the second Chern number can be calculated according to Eq. (1.38), which in the present notation reads

$$\nu_2^{(x,t)} = \nu_1^{(x)}\nu_1^{(t)}. \tag{3.23}$$

The values of $\nu_2^{(x,t)}$ are indicated in Fig. 3.7(c).

Comparing the spectrum of $\hat{H}'_{\mathrm{TB}}$ to the spectrum of the exact tight-binding Hamiltonian $\hat{H}_{\mathrm{TB}}$, shown in Fig. 3.7(d), we note that they are nearly identical. Slight discrepancies are to be expected since in order to obtain the separable Hamiltonian we have neglected some very weak couplings in $\hat{H}_{\mathrm{TB}}$. Nevertheless, the second Chern numbers of the bands of energy spectra of $\hat{H}_{\mathrm{TB}}$ and $\hat{H}'_{\mathrm{TB}}$ are the same. This is supported by the fact that the energy spectrum of $\hat{H}_{\mathrm{TB}}$ can be obtained by adiabatically deforming the spectrum of $\hat{H}'_{\mathrm{TB}}$ without closing the gaps in process. Relatedly, we remark that the gap below the highest resonant energy band of $\hat{H}_{\mathrm{TB}}$ remains open for all values of φ_x and φ_t, as shown in Fig. 3.7(e). The same is true for the gap above the lowest band of $\hat{H}_{\mathrm{TB}}$.

3.5 Higher-dimensional extensions

Finally, let us consider an optical lattice of two orthogonal spatial dimensions, so that the full system Hamiltonian reads

$$\hat{H}_{4\mathrm{D}} = \hat{H}(x,\hat{p}_x,t|\varphi_x,\varphi_{t_x}) + \hat{H}(y,\hat{p}_y,t|\varphi_y,\varphi_{t_y}). \tag{3.24}$$

This produces a 4D time-space crystalline structure since the total Wannier functions now have four independent indices:

$$W_{\boldsymbol{j},\boldsymbol{\alpha}}(x,y,t) = w_{j_x,\alpha_x}(x,t)w_{j_y,\alpha_y}(y,t), \tag{3.25}$$

where $\boldsymbol{j} = (j_x, j_y)$ and $\boldsymbol{\alpha} = (\alpha_x, \alpha_y)$ [49]. A two-dimensional temporal structure of $2s \times 2s$ sites now emerges in each two-dimensional spatial cell; motion in the former is characterised by the temporal quasimomenta k_{t_x} and k_{t_y}. The energy spectrum of this system may be readily obtained as a Minkowski sum of two copies of spectra in Fig. 3.7(e). The result is shown in Fig. 3.7(f), where it is apparent that the highest and the lowest bands are separated from others by a gap. This holds true not only for the displayed cut of the spectrum at $\varphi_x = \varphi_y = \varphi_{t_x} = \varphi_{t_y}$, but rather for all values of the phases. The ratio of the bandwidth of the highest band to the gap below it is found to be 5%, while the ratio of the bandwidth of the lowest band to the gap above it is 2%.

The system whose spectrum is shown in Fig. 3.7(f) may thus be described by a lattice Hamiltonian

$$\hat{H}_{8\mathrm{D}} = \hat{I} \otimes \hat{H}_{\mathrm{TB}}^{(x)} + \hat{H}_{\mathrm{TB}}^{(y)} \otimes \hat{I}, \tag{3.26}$$

where $\hat{I}$ is an identity matrix of the same size as $\hat{H}_{\mathrm{TB}}$. The system parameters are the two quasimomenta k_x, k_y, the spatial phases φ_x and φ_y, and the four respective parameters of the two underlying temporal systems: k_{t_x}, k_{t_y}, φ_{t_x}, φ_{t_y}. As in the 4D case, the lowest and the highest energy bands are nondegenerate, and therefore may be characterised by the fourth Chern number of a corresponding Abelian gauge field. The theory presented in Section 1.4 can be readily generalised to 8D. Let us gather all parameters of $\hat{H}_{8\mathrm{D}}$ in the following formal vector:

$$\boldsymbol{R} = (k_x, \varphi_x, k_{t_x}, \varphi_{t_x}, k_y, \varphi_y, k_{t_y}, \varphi_{t_y}). \tag{3.27}$$

The Abelian Berry curvature is introduced using the eigenstates of a nondegenerate energy band of $\hat{H}_{8\mathrm{D}}$ as

$$\Omega_{ij}(\boldsymbol{R}) = 2\Im \left\langle \partial_i \zeta_{\boldsymbol{R}} | \partial_j \zeta_{\boldsymbol{R}} \right\rangle, \tag{3.28}$$

where index i runs from 1 through 8, and $|\zeta_{\boldsymbol{R}}\rangle$ is the cell-periodic part of an eigenstate of $\hat{H}_{8\mathrm{D}}$ of a certain band. Let $|k_x, \varphi_x, k_{t_x}, \varphi_{t_x}\rangle$ be the cell-periodic part of the eigenstate of $\hat{H}_{\mathrm{TB}}^{(x)}$ of a certain band; then (3.26) implies $|\zeta_{\boldsymbol{R}}\rangle = |k_x, \varphi_x, k_{t_x}, \varphi_{t_x}\rangle \otimes |k_y, \varphi_y, k_{t_y}, \varphi_{t_y}\rangle$.

The fourth Chern number is given by [59]

$$\nu_4 = \frac{1}{(2\pi)^4} \int \frac{1}{4!} \Omega \wedge \Omega \wedge \Omega \wedge \Omega, \tag{3.29}$$

and due to the separability of the system this expression simplifies to

$$\nu_4 = \frac{1}{(2\pi)^4} \int \Omega_{12}\Omega_{34}\Omega_{56}\Omega_{78}\, \mathrm{d}R^1 \wedge \cdots \wedge \mathrm{d}R^8 = \nu_2^{(x,t_x)} \nu_2^{(y,t_y)}. \tag{3.30}$$

The values of ν_4 are displayed in Fig. 3.7(f). This way we confirm that the highest and the lowest bands of the 8D system are characterised by nonzero fourth Chern numbers, implying the topologically nontrivial nature of the system. We note that if $\hat{H}_{8\mathrm{D}}$ is constructed using two copies of the approximate Hamiltonian $\hat{H}'_{\mathrm{TB}}$, the higher gap closes, whereas the lower one remains open.

It is apparent in Fig. 3.7(f) that the highest and the lowest bands are wider than the gaps, implying that the gaps disappear if one more copy of the spectrum in Fig. 3.7(e) is added. In that case, one ends up with a single topologically trivial band, whose Chern number is zero. Nevertheless, a time-space structure

based on a different spatial system than the one given in (3.1) may exhibit even wider gaps compared to those in Fig. 3.7(e). This would allow one to realise a 12D time-space structure by combining three copies of $\hat{H}_{\mathrm{TB}}$, each based on a separate physical dimension (x, y, and z).

3.6 Conclusions

Summarising, we have shown that the time-space crystals may be used as a platform for studying 8D systems that can be defined in a tight-binding form. We have devised a concrete, experimentally realisable driven quantum system with validated parameters that is an example of a topologically nontrivial 8D system. Remarkably, it is possible to realise systems with nontrivial topological properties and study the resulting effects in eight dimensions with the help of a properly driven 2D system and without involving any internal degrees of freedom of the particles. High-dimensional spatio-temporal crystalline structures open up possibilities for building practical devices that would be unthinkable in three dimensions. The results presented in this work pave the way towards further research in this direction.

CHAPTER 4

Extended degenerate perturbation theory for the Floquet–Hilbert space

The study of time-crystalline structures presented in Chapters 2 and 3 once again demonstrates the importance of periodically driven systems as a platform for realising unconventional physical systems. The theoretical analysis of such systems hinges on the Floquet theory, requiring one to search for the Floquet states and the quasienergy spectrum. The problems considered in Chapters 2 and 3 concern resonantly driven *single-particle* systems, which can therefore be analysed using the secular approximation. However, in interacting *many-body* systems the secular approximation becomes less effective due to the large number of couplings experienced by each state. In this chapter we tackle the many-body Floquet problem for the case of resonant driving.

To present the problem, let us state the Floquet theorem once again [135, 148, 149]: The Schrödinger equation $\mathrm{i}\partial_t|\psi(t)\rangle = \hat{H}(t)|\psi(t)\rangle$ with time-periodic (and Hermitian) Hamiltonian $\hat{H}(t+T) = \hat{H}(t)$ has solutions (*Floquet states*) possessing the property $|\psi_\alpha(t+T)\rangle = \mathrm{e}^{-\mathrm{i}\varepsilon_\alpha T}|\psi_\alpha(t)\rangle$, where ε_α are real numbers called *quasienergies* (we set $\hbar = 1$ in the present chapter). Floquet states can be written in the form $|\psi_\alpha(t)\rangle = \mathrm{e}^{-\mathrm{i}\varepsilon_\alpha t}|u_\alpha(t)\rangle$ where $|u_\alpha(t+T)\rangle = |u_\alpha(t)\rangle$ are time-periodic state vectors called *Floquet modes*. The Floquet states (and hence also the modes) form a complete orthonormal basis at each time moment. Given an arbitrary initial state $|\chi(0)\rangle$, it will evolve in time as $|\chi(t)\rangle = \sum_\alpha c_\alpha|\psi_\alpha(t)\rangle$ where $c_\alpha = \langle\psi_\alpha(0)|\chi(0)\rangle$. Notably, the coefficients c_α are time-independent — the temporal evolution of the state is encoded in the Floquet states.

The defining property of the Floquet states means that taken at time $t = 0$

they represent the eigenstates of the one-period evolution operator $\hat{U}(T)$:

$$\hat{U}(T)|\psi_\alpha(0)\rangle = \mathrm{e}^{-\mathrm{i}\varepsilon_\alpha T}|\psi_\alpha(0)\rangle. \tag{4.1}$$

The Floquet modes $|u_\alpha(0)\rangle$ satisfy an identical equation since they coincide with the Floquet states at $t = 0$. Being a unitary operator, $\hat{U}(T)$ can be expressed as $\mathrm{e}^{-\mathrm{i}\hat{H}_{\mathrm{eff}}T}$ with $\hat{H}_{\mathrm{eff}}$ Hermitian, so that

$$\mathrm{e}^{-\mathrm{i}\hat{H}_{\mathrm{eff}}T}|u_\alpha(0)\rangle = \mathrm{e}^{-\mathrm{i}\varepsilon_\alpha T}|u_\alpha(0)\rangle. \tag{4.2}$$

This equation can alternatively be written as

$$\hat{H}_{\mathrm{eff}}|u_\alpha(0)\rangle = \varepsilon_\alpha|u_\alpha(0)\rangle. \tag{4.3}$$

However, the eigenvalues ε_α of this *effective Hamiltonian* $\hat{H}_{\mathrm{eff}}$ are determined only up to an integer multiple of the driving frequency $\omega = 2\pi/T$.

To go beyond the single-period evolution, let us express the time-evolution operator as

$$\hat{U}(t) = \sum_\alpha |\psi_\alpha(t)\rangle\langle\psi_\alpha(0)| = \sum_\alpha |u_\alpha(t)\rangle\langle u_\alpha(0)|\,\mathrm{e}^{-\mathrm{i}\varepsilon_\alpha t}. \tag{4.4}$$

Using the spectral decomposition of the effective Hamiltonian

$$\hat{H}_{\mathrm{eff}} = \sum_\alpha \varepsilon_\alpha\,|u_\alpha(0)\rangle\langle u_\alpha(0)| \tag{4.5}$$

and introducing the *micromotion operator*

$$\hat{P}(t) = \sum_\alpha |u_\alpha(t)\rangle\langle u_\alpha(0)|\,, \tag{4.6}$$

one finds

$$\hat{U}(t) = \hat{P}(t)\mathrm{e}^{-\mathrm{i}\hat{H}_{\mathrm{eff}}t}. \tag{4.7}$$

Due to the periodicity of the Floquet modes, the micromotion operator reduces to an identity operator at integer multiples of the driving period, $\hat{P}(nT) = \hat{I}$, so that $\hat{U}(nT) = \mathrm{e}^{-\mathrm{i}\hat{H}_{\mathrm{eff}}nT}$.

For a better understanding of the meaning of $\hat{H}_{\mathrm{eff}}$ and $\hat{P}(t)$, consider the Schrödinger equation for a transformed state vector $|\phi(t)\rangle = \hat{S}^\dagger(t)|\psi(t)\rangle$ where $\hat{S}(t)$ is a unitary operator. Evolution of such a state vector is governed by $\mathrm{i}\partial_t|\phi(t)\rangle = \hat{H}'(t)|\phi(t)\rangle$ where

$$\hat{H}'(t) = \hat{S}^\dagger(t)\hat{H}(t)\hat{S}(t) - \mathrm{i}\hat{S}^\dagger(t)\frac{\partial\hat{S}(t)}{\partial t}. \tag{4.8}$$

If one takes $\hat{S}(t) = \hat{P}(t)$, then the transformed Hamiltonian becomes precisely the effective Hamiltonian (4.5). Formally, this means that we have transitioned to a frame where the dynamics are governed by a time-independent Hamiltonian $\hat{H}_{\text{eff}}$.

Construction of the effective Hamiltonian may be conveniently approached in the extended Floquet–Hilbert space $\mathscr{F}$, where time-dependent operators become infinite matrices that possess a block-banded structure. To switch to this space, we start by noting that the Floquet modes obey $\hat{Q}|u_\alpha(t)\rangle = \varepsilon_\alpha|u_\alpha(t)\rangle$, where $\hat{Q} = \hat{H} - \mathrm{i}\partial_t$ is the *quasienergy operator*. The Floquet modes $|u_\alpha(t)\rangle$ of the Hilbert space $\mathscr{H}$ can be regarded as the elements of the composite Floquet–Hilbert space $\mathscr{F}$ defined as the tensor product of $\mathscr{H}$ and the space of time-periodic functions $\mathscr{T}$ [148–150]. We adopt the notation $|u_\alpha\rangle\!\rangle$ for the elements of $\mathscr{F}$, where the inner product is defined as $\langle\!\langle u_\beta|u_\alpha\rangle\!\rangle = \frac{1}{T}\int_0^T \langle u_\beta(t)|u_\alpha(t)\rangle \,\mathrm{d}t$. The basis spanning $\mathscr{F}$ is given by $|\alpha m\rangle\!\rangle \Leftrightarrow |\alpha\rangle \mathrm{e}^{\mathrm{i}m\omega t}$, where $m \in \mathbb{Z}$, while states $|\alpha\rangle$ form an orthonormal basis in $\mathscr{H}$. The quasienergy operator then assumes a block-banded form:

$$\langle\!\langle \alpha' m'|\bar{Q}|\alpha m\rangle\!\rangle = \langle \alpha'|\hat{H}_{m'-m}|\alpha\rangle + \delta_{m'm}\delta_{\alpha'\alpha} m\omega \tag{4.9}$$

with the blocks containing the Fourier images $\hat{H}_m = \frac{1}{T}\int_0^T \hat{H}(t)\mathrm{e}^{\mathrm{i}m\omega t}\mathrm{d}t$. Hereafter we indicate the operators acting in $\mathscr{F}$ by overbars. The above equation can be illustrated by the following matrix:

$$\bar{Q} = \begin{pmatrix} \ddots & \vdots & \vdots & \vdots & \iddots \\ \cdots & \hat{H}_0 - \hat{I}\omega & \hat{H}_{-1} & \hat{H}_{-2} & \cdots \\ \cdots & \hat{H}_1 & \hat{H}_0 & \hat{H}_{-1} & \cdots \\ \cdots & \hat{H}_2 & \hat{H}_1 & \hat{H}_0 + \hat{I}\omega & \cdots \\ \iddots & \vdots & \vdots & \vdots & \ddots \end{pmatrix}, \tag{4.10}$$

where $\hat{I}$ is the identity operator of $\mathscr{H}$.

Finding a frame where the Hamiltonian is time-independent is equivalent to block-diagonalising $\bar{Q}$ since off-diagonal blocks account for the time dependence. According to the preceding discussion, $\bar{Q}$ can be block-diagonalised using the micromotion operator $\bar{P}$. In practice, diagonalisation is done perturbatively, starting by separating $\bar{Q}$ into the block-diagonal unperturbed part $\bar{Q}^{(0)}$ and the perturbation $\bar{V}$:

$$\bar{Q} = \bar{Q}^{(0)} + \lambda\bar{V}_{\mathrm{D}} + \lambda\bar{V}_{\mathrm{X}}. \tag{4.11}$$

The dimensionless parameter λ is introduced to track the order of the expansion. The indices 'D' and 'X' refer to the block-diagonal and block-off-diagonal

parts of a given operator, respectively:

$$\begin{aligned}\langle\!\langle \alpha' m'|\bar{O}_{\rm D}|\alpha m\rangle\!\rangle &= \langle\!\langle \alpha' m'|\bar{O}|\alpha m\rangle\!\rangle\delta_{m'm},\\ \langle\!\langle \alpha' m'|\bar{O}_{\rm X}|\alpha m\rangle\!\rangle &= \langle\!\langle \alpha' m'|\bar{O}|\alpha m\rangle\!\rangle(1-\delta_{m'm}).\end{aligned} \tag{4.12}$$

The perturbative expansion of the transformed quasienergy operator is given by

$$\bar{P}^{\dagger}\bar{Q}\bar{P} = \bar{Q}^{(0)} + \lambda(\bar{W}_{\rm D}^{(1)} + \bar{W}_{\rm X}^{(1)}) + \lambda^2(\bar{W}_{\rm D}^{(2)} + \bar{W}_{\rm X}^{(2)}) + \dots \tag{4.13}$$

The goal is to find $\bar{P}$ as a series $\bar{P} = \bar{P}^{(0)} + \lambda\bar{P}^{(1)} + \lambda^2\bar{P}^{(2)} + \dots$ that sets the off-diagonal parts $\bar{W}_{\rm X}^{(n)}$ to zero, up to a given order.

Let us introduce the operator

$$\bar{Q}_0 \Leftrightarrow -{\rm i}\partial_t, \qquad \langle\!\langle \alpha' m'|\bar{Q}_0|\alpha m\rangle\!\rangle = \delta_{m'm}\delta_{\alpha'\alpha}m\omega \tag{4.14}$$

and define an additional operator $\bar{W}_{\rm D}^{(0)}$ by writing $\bar{Q}^{(0)} = \bar{Q}_0 + \bar{W}_{\rm D}^{(0)}$. Then, the block-diagonalised operator $\bar{Q}^{(0)} + \bar{W}_{\rm D}^{(1)} + \bar{W}_{\rm D}^{(2)} + \dots$ will have the structure $\delta_{m'm}(\langle\alpha'|\hat{W}_{\rm D}^{[n]}|\alpha\rangle + \delta_{\alpha'\alpha}m\omega)$, where

$$\hat{W}_{\rm D}^{[n]} \equiv \hat{W}_{\rm D}^{(0)} + \hat{W}_{\rm D}^{(1)} + \dots + \hat{W}_{\rm D}^{(n)} \tag{4.15}$$

is the nth order approximation of the effective Hamiltonian (4.5). The eigenvalue spectrum of $\bar{Q}$ can therefore be expressed as $\varepsilon_{\alpha m} = \varepsilon_\alpha + m\omega$, reflecting the 'mod ω' indeterminancy of the quasienergies mentioned above. It follows that any interval of quasienergies of width ω carries the same physical information, and these intervals are called *Floquet zones* by analogy with the Brillouin zones.

The standard approach used for finding $\hat{W}_{\rm D}^{[n]}$ is to construct it as an expansion in powers of $1/\omega$ [151, 149, 152, 153, 28, 154, 150]. Calculation of $\hat{W}_{\rm D}^{[n]}$ in the high-frequency limit relies on the assumption that the energy spectrum of the unperturbed Hamiltonian is bounded and that its width is much less than ω. In that case, the unperturbed quasienergy operator can be split as $\bar{Q} = \bar{Q}_0 + \bar{H}$ with $\hat{H}(t) \Leftrightarrow \bar{H}$. By assumption, the elements of $\bar{H}$ are small compared to ω, therefore, $\bar{H}$ can be treated perturbatively. The expansion (4.13) then becomes an expansion in powers of $1/\omega$. However, if transitions resonant with ω are possible, then one is required to include the diagonal elements of $\bar{H}$ in the unperturbed part of the problem, but this introduces degeneracies. Specifically, if the difference $E_\beta - E_\alpha$ between two diagonal elements of $\hat{H}_0$ is equal (or is close to) $n\omega$, where n is integer, then the degeneracy $\langle\!\langle \beta(m+n)|\bar{Q}|\beta(m+n)\rangle\!\rangle = \langle\!\langle \alpha m|\bar{Q}|\alpha m\rangle\!\rangle$ makes the perturbation theory divergent. In that case, one can apply the conventional degenerate perturbation theory (DPT), whereby $\hat{W}_{\rm D}^{[n]}$ is constructed by including the couplings between

the degenerate states exactly and taking into account all remaining couplings perturbatively [155, 156]. The application of the DPT in the ordinary space $\mathscr{H}$ amounts to constructing and subsequently diagonalising a submatrix $\hat{h}_{\text{eff}}$ (which is called the effective Hamiltonian as well) describing the degenerate subspace $\mathscr{H}_1$ of the Hamiltonian $\hat{H} = \hat{H}_0 + \hat{V}$. To second order in the perturbation strength, the elements of $\hat{h}_{\text{eff}}$ are given by [109]

$$\langle \alpha' | \hat{h}_{\text{eff}} | \alpha \rangle = \langle \alpha' | \hat{H} | \alpha \rangle + \sum_{|\beta\rangle \notin \mathscr{H}_1} \frac{\langle \alpha' | \hat{V} | \beta \rangle \langle \beta | \hat{V} | \alpha \rangle}{E_\alpha - E_\beta}. \tag{4.16}$$

Here, all states $|\alpha\rangle$ and $|\alpha'\rangle$ of the degenerate subspace $\mathscr{H}_1$ are assumed to correspond to the same unperturbed energy $E_\alpha = E_{\alpha'}$, while the summation is performed over all states of $\mathscr{H}$ excluding the degenerate ones. If the states of interest are not exactly degenerate (this is known as the quasidegenerate case), then such an approach is still valid provided the summation is symmetrised as follows [157]:

$$\langle \alpha' | \hat{h}_{\text{eff}} | \alpha \rangle = \langle \alpha' | \hat{H} | \alpha \rangle + \frac{1}{2} \sum_{|\beta\rangle \notin \mathscr{H}_1} \langle \alpha' | \hat{V} | \beta \rangle \langle \beta | \hat{V} | \alpha \rangle \left(\frac{1}{E_\alpha - E_\beta} + \frac{1}{E_{\alpha'} - E_\beta} \right). \tag{4.17}$$

Properly modified, such an expression can be applied for the matrix $\bar{Q}$ to construct $\hat{H}_{\text{eff}}$. However, the accuracy of such an approach might be insufficient for systems where the degenerate states are coupled to a large number of states outside the degenerate subspace.

The aim of this chapter is to extend the degenerate perturbation theory in the Floquet–Hilbert space to obtain expressions for $\hat{W}_{\text{D}}^{[n]}$ that ensure higher accuracy of the resulting quasienergy spectrum both exactly on resonance and in its vicinity. This will be achieved by including in the degenerate subspace not only the degenerate levels of interest but rather all the states of $\mathscr{H}$. The resulting approach, which we call EDPT, parallels the van Vleck high-frequency expansion [149] provided the elements of $\bar{Q}$ are reordered so that each mth diagonal block corresponds to the mth Floquet zone. To demonstrate the validity of the obtained expressions, we apply them to the calculation of quasienergy spectra of the driven Bose–Hubbard model for a number of parameter sets. Comparison with numerically exact results shows that EDPT surpasses the conventional DPT in terms of accuracy while requiring less computational effort than the exact approach.

4.1 Degenerate perturbation theories in the extended space

The starting point of the proposed theory is the natural concept of reduced energies

$$\varepsilon_\alpha^{(0)} = E_\alpha - a\omega \in \mathrm{FZ}, \quad a \in \mathbb{Z}, \tag{4.18}$$

which are the diagonal elements E_α of $\hat{H}_0$ reduced to the chosen Floquet zone (FZ), whose width necessarily equals ω. Note that $\hat{H}_0$ is just the unperturbed Hamiltonian with, possibly, the secular contribution of the driving included. This way, an integer a is uniquely assigned to each state $|\alpha\rangle$; generally, multiple states will share the same value of a. We reserve the symbols a, a', b, and c to indicate the 'reduction numbers' of states $|\alpha\rangle$, $|\alpha'\rangle$, $|\beta\rangle$, and $|\gamma\rangle$, respectively. Next, we reorder the elements of the quasienergy operator so that its mth diagonal block contains energies reduced to the mth FZ. The diagonal elements of the resulting quasienergy operator $\bar{Q}'$ then read

$$\varepsilon_{\alpha m}^{(0)} \equiv \langle\!\langle \alpha m|\bar{Q}'|\alpha m\rangle\!\rangle = \varepsilon_\alpha^{(0)} + m\omega, \tag{4.19}$$

while all other elements are expressed as

$$\langle\!\langle \alpha' m'|\bar{Q}'|\alpha m\rangle\!\rangle = \langle\alpha'|\hat{H}_{a-a'+m'-m}|\alpha\rangle + \delta_{m'm}\delta_{\alpha'\alpha} m\omega. \tag{4.20}$$

The quasienergy matrix retains its block structure, which can be visualised as follows:

$$\bar{Q}' = \begin{pmatrix} \ddots & \vdots & \vdots & \vdots & \iddots \\ \cdots & \hat{D} - \hat{I}\omega & \hat{X}_{-1} & \hat{X}_{-2} & \cdots \\ \cdots & \hat{X}_1 & \hat{D} & \hat{X}_{-1} & \cdots \\ \cdots & \hat{X}_2 & \hat{X}_1 & \hat{D} + \hat{I}\omega & \cdots \\ \iddots & \vdots & \vdots & \vdots & \ddots \end{pmatrix}, \tag{4.21}$$

where the diagonal blocks are given by

$$\hat{D} = \begin{pmatrix} \varepsilon_\alpha^{(0)} & H_{b-a}^{\alpha\beta} & H_{c-a}^{\alpha\gamma} \\ H_{a-b}^{\beta\alpha} & \varepsilon_\beta^{(0)} & H_{c-b}^{\beta\gamma} \\ H_{a-c}^{\gamma\alpha} & H_{b-c}^{\gamma\beta} & \varepsilon_\gamma^{(0)} \end{pmatrix}, \tag{4.22}$$

while the off-diagonal ones read

$$\hat{X}_m = \begin{pmatrix} H_m^{\alpha\alpha} & H_{b-a+m}^{\alpha\beta} & H_{c-a+m}^{\alpha\gamma} \\ H_{a-b+m}^{\beta\alpha} & H_m^{\beta\beta} & H_{c-b+m}^{\beta\gamma} \\ H_{a-c+m}^{\gamma\alpha} & H_{b-c+m}^{\gamma\beta} & H_m^{\gamma\gamma} \end{pmatrix}. \tag{4.23}$$

Here the matrices $\hat{D}$ and $\hat{X}_m$ are shown for the case of a three-level system for brevity (so that the basis in the Hilbert space is spanned by $|\alpha\rangle$, $|\beta\rangle$, and $|\gamma\rangle$), and $H_m^{\alpha'\alpha} \equiv \langle\alpha'|\hat{H}_m|\alpha\rangle$. The central block $\hat{D}$ describes the states of the central ($m = 0$) FZ and their mutual couplings, which will be accounted for exactly. The off-diagonal blocks $\hat{X}_m$ describe couplings between different Floquet zones; these couplings will be taken into account perturbatively. The connection between $\bar{Q}$ in Eq. (4.10) and $\bar{Q}'$ in Eq. (4.21) is shown schematically in Fig. 4.1. To clarify further, we now give an example for a two-level system in which the diagonal elements of the undriven Hamiltonian are given by E_1 and $E_1 + \omega + \delta$ with $|\delta| \ll \omega$. Part of the infinite matrix $\bar{Q}$ can be displayed as

$$\bar{Q} = \begin{array}{c|cc|cc|c} E_1+\delta & \vdots & \vdots & \vdots & \vdots & \iddots \\ \hline \cdots & E_1 & H_0^{12} & H_{-1}^{11} & H_{-1}^{12} & \cdots \\ \cdots & H_0^{12} & E_1+\omega+\delta & H_{-1}^{12} & H_{-1}^{22} & \cdots \\ \hline \cdots & H_1^{11} & H_1^{12} & E_1+\omega & H_0^{12} & \cdots \\ \cdots & H_1^{12} & H_1^{22} & H_0^{12} & E_1+2\omega+\delta & \cdots \\ \hline \iddots & \vdots & \vdots & \vdots & \vdots & E_1+2\omega \end{array}$$

where the lines delimit the blocks. The elements $E_1 + \omega + \delta$ and $E_1 + \omega$, coupled by the elements H_{-1}^{12} and H_1^{12} of the off-diagonal blocks, are almost degenerate, and so the high-frequency expansion cannot be applied. However, in this case of a two-level system, one can simply change the definition of the diagonal blocks so that the result looks as follows:

$$\bar{Q}' = \begin{array}{cc|cc|cc} E_1+\delta & \vdots & \vdots & \vdots & \vdots & \iddots \\ \cdots & E_1 & H_0^{12} & H_{-1}^{11} & H_{-1}^{12} & \cdots \\ \hline \cdots & H_0^{12} & E_1+\omega+\delta & H_{-1}^{12} & H_{-1}^{22} & \cdots \\ \cdots & H_1^{11} & H_1^{12} & E_1+\omega & H_0^{12} & \cdots \\ \hline \cdots & H_1^{12} & H_1^{22} & H_0^{12} & E_1+2\omega+\delta & \cdots \\ \iddots & \vdots & \vdots & \vdots & \vdots & E_1+2\omega \end{array}$$

The degeneracies are now contained in the diagonal blocks, and no obstructions to the application of the usual high-frequency expansion occurs.

In the general case described by Eq. (4.20), different diagonal blocks will no longer share degenerate elements, with one possible exception in case there are states with reduced energies near both boundaries of the Floquet zones. For example, for the FZ choice $[-\frac{\omega}{2}, \frac{\omega}{2})$, this will be the case if $\varepsilon_{\pm}^{(0)} \approx \pm\frac{\omega}{2}$. The element $\varepsilon_{+}^{(0)} + m\omega$ of the mth diagonal block will then coincide with the element $\varepsilon_{-}^{(0)} + (m+1)\omega$ of the $(m+1)$st diagonal block. This issue will be discussed further in Section 4.1.3. Abstracting from it, we proceed to derive the expressions for the effective Hamiltonian.

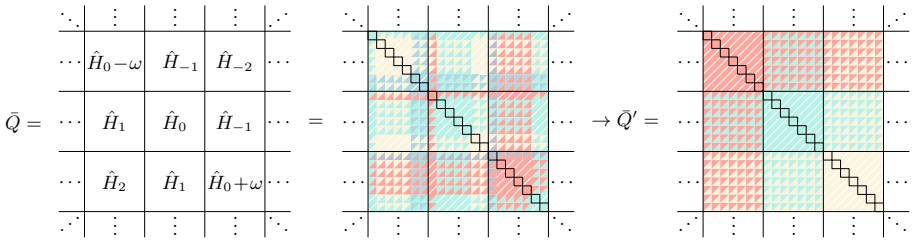

Figure 4.1: Schematic representation of $\bar{Q}$ and $\bar{Q}'$. In the first step, the diagonal elements of $\bar{Q}$ are coloured such that those lying in the same Floquet zone share the same colour. For example, the diagonal elements falling in the range $[-\frac{\omega}{2}, \frac{\omega}{2})$ are coloured red, those falling in the range $[\frac{\omega}{2}, \frac{3\omega}{2})$ are coloured blue, and so on. Additionally, each off-diagonal element (in both diagonal and off-diagonal blocks) is coloured in two tones corresponding to the colours of diagonal elements that are being coupled. In the second step, all elements are permuted so that like-coloured diagonal elements are gathered in the same blocks (while the permutation of the off-diagonal elements follows unambiguously).

4.1.1 Extended degenerate perturbation theory

In the first step, we separate $\bar{Q}'$ as in Eq. (4.11), writing

$$\bar{Q}' = \bar{Q}'^{(0)} + \lambda \bar{V}_{\mathrm{D}} + \lambda \bar{V}_{\mathrm{X}}, \tag{4.24}$$

where

$$\begin{aligned} \langle\!\langle \alpha' m' | \bar{Q}'^{(0)} | \alpha m \rangle\!\rangle &= \varepsilon^{(0)}_{\alpha m} \delta_{\alpha'\alpha} \delta_{m'm}, \\ \langle\!\langle \alpha' m' | \bar{V}_{\mathrm{D}} | \alpha m \rangle\!\rangle &= \langle \alpha' | \hat{H}_{a-a'} | \alpha \rangle (1 - \delta_{\alpha'\alpha}) \delta_{m'm}, \\ \langle\!\langle \alpha' m' | \bar{V}_{\mathrm{X}} | \alpha m \rangle\!\rangle &= \langle \alpha' | \hat{H}_{a-a'+m'-m} | \alpha \rangle (1 - \delta_{m'm}). \end{aligned} \tag{4.25}$$

The zeroth-order term of the effective Hamiltonian is therefore given by

$$\langle \alpha' | \hat{W}^{(0)}_{\mathrm{D}} | \alpha \rangle = \varepsilon^{(0)}_{\alpha} \delta_{\alpha'\alpha}. \tag{4.26}$$

In the following step, we write down the expansion $\bar{P}^\dagger \bar{Q}' \bar{P}$ of Eq. (4.13) by assuming $\bar{P} = \mathrm{e}^{\bar{G}}$, where $\bar{G}$ is an antihermitian operator that we expand in series: $\bar{G} = \lambda \bar{G}^{(1)} + \lambda^2 \bar{G}^{(2)} + \ldots$ (the zeroth-order term can be set to zero). Collecting the terms of the first order this yields

$$-[\bar{G}^{(1)}, \bar{Q}'^{(0)}] + \bar{V}_{\mathrm{D}} + \bar{V}_{\mathrm{X}} = \bar{W}^{(1)}_{\mathrm{D}} + \bar{W}^{(1)}_{\mathrm{X}}. \tag{4.27}$$

We require $\bar{G}^{(1)}$ be block-off-diagonal, so that $[\bar{G}^{(1)}, \bar{Q}'^{(0)}]$ is block-off-diagonal as well. The remaining block-diagonal terms immediately yield the first-order

term of the effective Hamiltonian according to

$$\langle\!\langle \alpha' m|\bar{W}_{\rm D}^{(1)}|\alpha m\rangle\!\rangle = \langle\!\langle \alpha' m|\bar{V}_{\rm D}|\alpha m\rangle\!\rangle, \tag{4.28}$$

or, in the space $\mathscr{H}$,

$$\langle\alpha'|\hat{W}_{\rm D}^{(1)}|\alpha\rangle = \langle\alpha'|\hat{H}_{a-a'}|\alpha\rangle(1-\delta_{\alpha'\alpha}). \tag{4.29}$$

The first order of the theory thus corresponds to neglecting all off-diagonal blocks of $\bar{Q}'$, so that the effective Hamiltonian is given by $\hat{D}$ in Eq. (4.21). In fact, this coincides with the secular approximation used in Chapters 2 and 3. The level-renumbering functions ν used there [see Eqs. (2.27) and (3.9)] correspond to the reduction numbers of the present formulation, while the basis functions (2.26) and (3.8) select the appropriate elements of the quasienergy operator, coinciding with the central block of $\bar{Q}'$ in the present formulation.

Next, we require $\bar{W}_{\rm X}^{(1)} = 0$, obtaining the equation for the block-off-diagonal terms: $[\bar{G}^{(1)}, \bar{Q}'^{(0)}] = \bar{V}_{\rm X}$. This allows us to find $\bar{G}^{(1)}$ and proceed to the equation for the second-order terms. Continuing in the similar fashion, one obtains

$$\begin{aligned}\langle\!\langle \alpha' m|\bar{W}_{\rm D}^{(2)}|\alpha m\rangle\!\rangle = \frac{1}{2}\sum_{\beta}\sum_{n\neq m}\langle\!\langle \alpha' m|\bar{V}_{\rm X}|\beta n\rangle\!\rangle\langle\!\langle \beta n|\bar{V}_{\rm X}|\alpha m\rangle\!\rangle \\ \times\left(\frac{1}{\varepsilon_{\alpha' m}^{(0)}-\varepsilon_{\beta n}^{(0)}}+\frac{1}{\varepsilon_{\alpha m}^{(0)}-\varepsilon_{\beta n}^{(0)}}\right).\end{aligned} \tag{4.30}$$

One recognises that the resulting expressions are identical to the van Vleck high-frequency expansion [149], which is expected since $\bar{Q}'$ possesses exactly the same structure as in the usual applications of this expansion. The $\mathscr{H}$-space expressions, however, do different because the matrix elements of $\bar{V}_{\rm X}$ and the quantities $\varepsilon_{\alpha m}^{(0)}$ have a different meaning in our case. The second-order term of the effective Hamiltonian results as

$$\begin{aligned}\langle\alpha'|\hat{W}_{\rm D}^{(2)}|\alpha\rangle = \frac{1}{2}\sum_{\beta}\sum_{n\neq 0}\langle\alpha'|\hat{H}_{-(a'-b+n)}\,|\beta\rangle\langle\beta|\,\hat{H}_{a-b+n}|\alpha\rangle \\ \times\left(\frac{1}{\varepsilon_{\alpha'}^{(0)}-\varepsilon_{\beta}^{(0)}-n\omega}+\frac{1}{\varepsilon_{\alpha}^{(0)}-\varepsilon_{\beta}^{(0)}-n\omega}\right).\end{aligned} \tag{4.31}$$

Expressions for the third-order terms of the effective Hamiltonian are provided in Appendix 4A.

The formula (4.30) could alternatively be obtained by a direct application of the conventional DPT as given by Eq. (4.17), provided one assumes that all of the states $|\alpha m\rangle\!\rangle$ of a given block ($m = 0$, say) constitute the degenerate

subspace. The condition $n \neq m$ in the summation over the intermediate states $|\beta n\rangle\!\rangle$ in Eq. (4.30) corresponds precisely to the skipping of states belonging to the degenerate subspace. We will refer to Eqs. (4.26), (4.29), and (4.31) as the results of the extended degenerate perturbation theory (EDPT) since the degenerate subspace is extended to include all levels in a Floquet zone.

4.1.2 Conventional degenerate perturbation theory

For comparison, let us consider the conventional DPT, whereby the degenerate subspace of $\mathscr{F}$ consists only of the states that are exactly (or nearly) degenerate. We start by dividing $\mathscr{H}$ into two subspaces, $\mathscr{H}_0$ and $\mathscr{H}_1$, so that $\mathscr{H}_1$ contains the states sharing the same value of reduced energy of interest, $\varepsilon_*^{(0)}$, while $\mathscr{H}_0$ contains the remaining states. That is, for each state $|\alpha\rangle$,

$$|\alpha\rangle \in \begin{cases} \mathscr{H}_1, & \varepsilon_\alpha^{(0)} = \varepsilon_*^{(0)}, \\ \mathscr{H}_0, & \varepsilon_\alpha^{(0)} \neq \varepsilon_*^{(0)}. \end{cases} \tag{4.32}$$

Consequently, we partition each diagonal block of $\bar{Q}'$ into two subblocks — one containing the states belonging to $\mathscr{H}_0$, and one containing the states of $\mathscr{H}_1$. The couplings between these subblocks are then considered to constitute the off-diagonal blocks of $\bar{Q}'$, and are therefore treated as a perturbation. This means that the definition of diagonal and off-diagonal blocks is changed from the one given in Eq. (4.25) to

$$\begin{aligned} \langle\!\langle \alpha' m' | \bar{O}_{\mathrm{D}} | \alpha m \rangle\!\rangle &= \langle\!\langle \alpha' m | \bar{O} | \alpha m \rangle\!\rangle \delta_{m'm} \delta_{A'A}, \\ \langle\!\langle \alpha' m' | \bar{O}_{\mathrm{X}} | \alpha m \rangle\!\rangle &= \langle\!\langle \alpha' m' | \bar{O} | \alpha m \rangle\!\rangle (1 - \delta_{m'm} \delta_{A'A}). \end{aligned} \tag{4.33}$$

Here, $|\alpha\rangle \in \mathscr{H}_A$ and $|\alpha'\rangle \in \mathscr{H}_{A'}$ (with A and A' being either 0 or 1) so that the Kronecker delta $\delta_{A'A}$ is unity if both states $|\alpha'\rangle$ and $|\alpha\rangle$ belong to the same subspace — either degenerate or not — and zero if they belong to different subspaces. With these definitions, and $\langle\!\langle \alpha' m' | \bar{V} | \alpha m \rangle\!\rangle = \langle \alpha' | \hat{V}_{a-a'+m'-m} | \alpha \rangle$ as before, one finds

$$\langle \alpha' | \hat{w}_{\mathrm{D}}^{(0)} | \alpha \rangle = \varepsilon_\alpha^{(0)} \delta_{\alpha'\alpha} \tag{4.34}$$

in the zeroth order,

$$\langle \alpha' | \hat{w}_{\mathrm{D}}^{(1)} | \alpha \rangle = \delta_{A'A} \langle \alpha' | \hat{H}_{a-a'} | \alpha \rangle (1 - \delta_{\alpha'\alpha}) \tag{4.35}$$

in the first, and

$$\langle\alpha'|\hat{w}_{\mathrm{D}}^{(2)}|\alpha\rangle = \frac{1}{2}\delta_{A'A}\sum_{\beta}\sum_{n\neq 0 \text{ if } B=A}\langle\alpha'|\hat{H}_{-(a'-b+n)}\,|\beta\rangle\langle\beta|\,\hat{H}_{a-b+n}|\alpha\rangle \times\left(\frac{1}{\varepsilon_{\alpha'}^{(0)}-\varepsilon_{\beta}^{(0)}-n\omega}+\frac{1}{\varepsilon_{\alpha}^{(0)}-\varepsilon_{\beta}^{(0)}-n\omega}\right) \tag{4.36}$$

in the second. In the last expression, B is the number of subspace (0 or 1) which $|\beta\rangle$ belongs to, i.e., $|\beta\rangle \in \mathscr{H}_B$. In the second sum, the index n runs from $-\infty$ to ∞, skipping the value $n = 0$ if $B = A$. The terms of the effective Hamiltonian constructed using DPT are denoted here by $\hat{w}^{(n)}$, and they are composed of two uncoupled blocks. In fact, when using DPT, one is only interested in the block describing the degenerate subspace, and it can be diagonalised separately from the other block. Together, Eqs. (4.34)–(4.36) correspond to the DPT formula (4.17) given for the space $\mathscr{H}$.

Notably, construction of $\hat{w}_{\mathrm{D}}^{[2]}$ is not equivalent to simply neglecting in $\hat{W}_{\mathrm{D}}^{(2)}$ the couplings between the blocks $\mathscr{H}_0$ and $\mathscr{H}_1$. Considering two states $|\alpha'\rangle$ and $|\alpha\rangle$ of the degenerate subspace, one has $\langle\alpha'|\hat{w}_{\mathrm{D}}^{(2)}|\alpha\rangle \neq \langle\alpha'|\hat{W}_{\mathrm{D}}^{(2)}|\alpha\rangle$. This point will be discussed further in Section 4.2.2.

The above formalism also allows one to construct schemes that are intermediate between DPT and EDPT. Instead of including in $\mathscr{H}_1$ only the states whose reduced energies are equal to the reduced energy of interest $\varepsilon_*^{(0)}$, one can include all states in a certain interval $[\varepsilon_*^{(0)} - \Delta\varepsilon/2, \varepsilon_*^{(0)} + \Delta\varepsilon/2]$ (with $\Delta\varepsilon < \omega$). The size of $\mathscr{H}_1$ will then increase, resulting in larger numerical effort required to calculate the eigenvalues, but these should approximate the exact values more accurately. The choice $\Delta\varepsilon = \omega$ corresponds to EDPT, whereby all states are assigned to $\mathscr{H}_1$. We will not, however, consider the accuracy of these intermediate schemes further in this work, instead focusing on the two limiting cases, DPT and EDPT.

4.1.3 Convergence condition

It follows that the necessary condition for the convergence of the expansion (4.13) is

$$r \equiv \frac{|\langle\alpha'|\hat{H}_{a-a'-n}|\alpha\rangle|}{|\varepsilon_{\alpha'}^{(0)}-\varepsilon_{\alpha}^{(0)}-n\omega|} \ll 1, \tag{4.37}$$

which has to be satisfied for all states $|\alpha\rangle$, $|\alpha'\rangle$ and all integers n, except the resonant cases excluded in the summation in Eq. (4.31) (EDPT case) or Eq. (4.36) (DPT case). As long as the numerator does not vanish, this condition might be violated for $|\varepsilon_{\alpha'}^{(0)} - \varepsilon_{\alpha}^{(0)}| \approx \omega$, which is possible if the reduced energies of the two states $|\alpha'\rangle$ and $|\alpha\rangle$ are on the opposite boundaries of the FZ. A simple

resolution is to shift the FZ in a such way so that there are no levels near one or both boundaries. However, if the reduced energies $\varepsilon_\alpha^{(0)}$ fill the FZ densely, then the problem cannot be circumvented. The EDPT will be applicable in those cases only if the couplings between states on the boundary of the FZ can be disregarded. On the other hand, in case of DPT this issue does not arise for the states of the degenerate subspace if one centres the FZ around $\varepsilon_*^{(0)}$. Since $|\alpha\rangle$ and $|\alpha'\rangle$ enumerate only the states of the degenerate subspace, the absolute values of denominators in Eq. (4.36) are no smaller than $\omega/2$. However, the problem appears in the DPT case as well once the third-order term, provided in Appendix 4A, is included since it contains differences between the reduced energies of the nondegenerate subspace.

We reiterate that in the limit $\omega \to \infty$ (so that all diagonal elements E_α are in the same FZ) the EDPT essentially coincides with the usual van Vleck high-frequency expansion. The only difference is that the latter method assumes that the unperturbed quasienergy operator is simply $\bar{Q}_0$ (4.14), while in the EDPT case each diagonal block also contains the diagonal elements of $\hat{H}_0$. As the frequency is lowered towards the resonant case, this transfer of diagonal elements becomes essential, but it causes divergence of the usual expansion. On the other hand, it may be the case that the couplings between the diagonal blocks can still be considered small, and perturbative treatment could in principle be possible. The reshuffling of elements used in EDPT solves the problem of degeneracies and allows for subsequent perturbative treatment as long as the condition (4.37) holds. The EDPT can therefore be also considered as an extension of the usual van Vleck expansion to lower frequencies.

4.2 Applications

To check the validity of the presented theories, we will compare the quasienergy spectra obtained by diagonalising $\hat{W}_{\mathrm{D}}^{[3]}$ and $\hat{w}_{\mathrm{D}}^{[3]}$ with the numerically exact ones. The exact spectra were obtained by diagonalising the single-period evolution operator $\hat{U}(T)$ — its eigenvalues are $\mathrm{e}^{-\mathrm{i}\varepsilon_\alpha T}$, and the eigenvectors are the Floquet modes $|u_\alpha(0)\rangle$. The operator $\hat{U}(T)$ was constructed using the general decomposition $\hat{U}(T) = \sum_\alpha |\alpha(T)\rangle\langle\alpha(0)|$, where states $|\alpha(0)\rangle$ form an arbitrary orthonormal basis in $\mathscr{H}$, and while states $|\alpha(T)\rangle$ were obtained by propagating the Schrödinger equation for a single period [17]. The theory will be applied to a driven Bose–Hubbard system, defined in Section 4.2.1.

4.2.1 Driven Bose–Hubbard model

The driven Bose–Hubbard model is defined by the Hamiltonian [158]

$$\hat{H}'(t) = -J \sum_{\langle ij \rangle} \hat{a}_i^\dagger \hat{a}_j + \frac{U}{2} \sum_j \hat{n}_j(\hat{n}_j - 1) + \sum_j \hat{n}_j x_j F \cos \omega t, \tag{4.38}$$

where J, U, and F control the strengths of, respectively, the nearest-neighbour hopping, the on-site interaction, and the external driving (we study monochromatic driving of frequency ω). The first sum runs over nearest-neighbour pairs, while the remaining ones run over all lattice sites. In the last sum, x_j is the x-coordinate of site j, in units of the lattice constant. A gauge transformation (4.8) with $\hat{S}(t) = \exp\left(-\mathrm{i}\frac{F}{\omega} \sin \omega t \sum_j x_j \hat{n}_j\right)$ shows that the effect of the driving amounts to a renormalisation of the hopping strength [159, 160]:

$$\hat{H}(t) = -J \sum_{\langle ij \rangle} \mathrm{e}^{\mathrm{i}\frac{F}{\omega}(x_i - x_j)\sin \omega t} \hat{a}_i^\dagger \hat{a}_j + \frac{U}{2} \sum_j \hat{n}_j(\hat{n}_j - 1). \tag{4.39}$$

The Fourier image of the resulting Hamiltonian is given by

$$\hat{H}_m = -J \sum_{\langle ij \rangle} J_m\left(\frac{F(x_i - x_j)}{\omega}\right) \hat{a}_i^\dagger \hat{a}_j, \tag{4.40}$$

where $J_m(x)$ denotes the Bessel function of the first kind of order m.

We will use the Fock basis $|\alpha\rangle$ to refer to the elements of $\hat{H}(t)$, denoting the diagonal ones by $E_\alpha = \langle \alpha | \hat{H}_0 | \alpha \rangle$. An example of the distribution of diagonal elements E_α is displayed in Fig. 4.2(a). The presence of degenerate elements does not require extra care — these degeneracies will directly translate into degeneracies in the first-order term (4.29) of the effective Hamiltonian. The effective Hamiltonian, once obtained perturbatively, will be diagonalised exactly (numerically). On the other hand, the possibility of resonant transitions requires the application of degenerate perturbation theory in $\mathscr{F}$. Since the diagonal elements E_α are given by integer multiples of U, resonant transitions become possible when the condition $pU = q\omega$, where $\{p, q\} \in \mathbb{Z}$, is satisfied. This translates into degeneracies in $\mathscr{F}$, as depicted in Fig. 4.2(b) showing the diagonal elements $\varepsilon^{(0)}_{\alpha m}$ [see Eq. (4.19)] for $3U = 2\omega$. In the figure, black horizontal lines delimit the FZ chosen as $[-\frac{\omega}{2}, \frac{\omega}{2})$, and the values of a are displayed.

The analysis of accuracy of DPT and EDPT will be performed by choosing the driving strength F and the frequency ω, and calculating the quasienergies as the parameter U is varied. We will focus our attention on the quasienergy of the 'driven Mott-insulator (MI) state', a name we will use for the Floquet mode having the largest overlap with MI state (denoted as $|\mathrm{MI}\rangle$). For $U \gg J$, $|\mathrm{MI}\rangle$

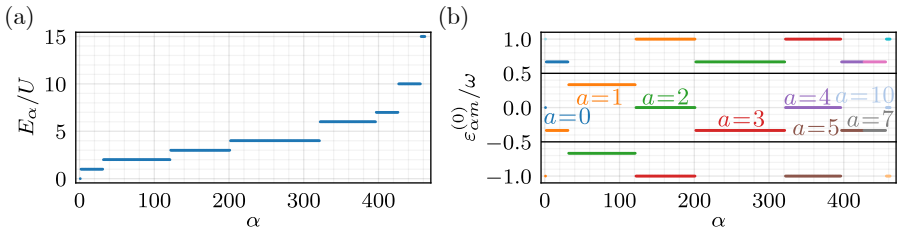

Figure 4.2: Diagonal elements of $\hat{H}_0$ and $\bar{Q}'$ for a BH system on a 1×6 lattice assuming $\omega/J = 20$, $U = \frac{2}{3}\omega$. (a) Diagonal elements $E_\alpha = \langle\alpha|\hat{H}_0|\alpha\rangle$. Note the existence of a zero-energy state ($E_1 = 0$), which is the Mott-insulator state (when $U \gg J$). (b) Diagonal elements $\varepsilon^{(0)}_{\alpha m} = \langle\!\langle \alpha m|\bar{Q}'|\alpha m\rangle\!\rangle$ in the vicinity of zero. The values of m are: $m = 0$ for the levels in the central FZ $[-\frac{\omega}{2}, \frac{\omega}{2})$, $m = -1$ for the levels in the zone below, and $m = 1$ for the levels in the zone above.

is the ground state of the undriven system, corresponding to $E = 0$. Therefore, we centre the FZ around $\varepsilon^{(0)}_* = 0$ by choosing the interval $[-\frac{\omega}{2}, \frac{\omega}{2})$.

We note that the interesting features of the quasienergy spectra — the anticrossings indicatory of resonant processes — will appear at certain values of the ratio U/ω. From the definition (4.18) with $E_\alpha = k_\alpha U$ where k_α is integer, it follows that the denominator in Eq. (4.37), $\omega|(\varepsilon^{(0)}_{\alpha'} - \varepsilon^{(0)}_\alpha)/\omega - n|$, grows linearly in ω for fixed U/ω. Therefore, the accuracy of the perturbation theory in the vicinity of resonances is expected to increase with increasing ω, although this reasoning does not take into account the dependence on ω of the coupling strength [i.e., the numerator in Eq. (4.37)].

Finally, let us clarify that DPT can be applied not only exactly on resonance (when the degenerate energies of interest exactly coincide), but also in its vicinity. For example, we can calculate the quasienergies for U in the vicinity of $\frac{2}{3}\omega$ by including in $\mathscr{H}_1$ the same states as those constituting $\mathscr{H}_1$ when U exactly equals $\frac{2}{3}\omega$. Similarly, the same reduction numbers [see Eq. (4.18)] as those obtained exactly on resonance are used even when U does not exactly equal $\frac{2}{3}\omega$.

4.2.2 Study case 1: One-dimensional lattice

We begin the assessment of accuracy of the perturbation theories with the study of a BH system defined on a periodic 1×8 lattice containing 8 bosons; we set $F/\omega = 2$ and $\omega/J = 20$. The plots in Fig. 4.3(a) display the quasienergies of ten Floquet modes having the largest overlap with the MI state for $U \in [0, 1.5\omega]$. The quasienergies of the driven MI state are highlighted in red. The left plot displays the exact result, while the right one shows the results obtained using third-order EDPT. As explained above, the DPT approach is only applicable in the vicinity of resonances, and cannot be directly used to calculate the

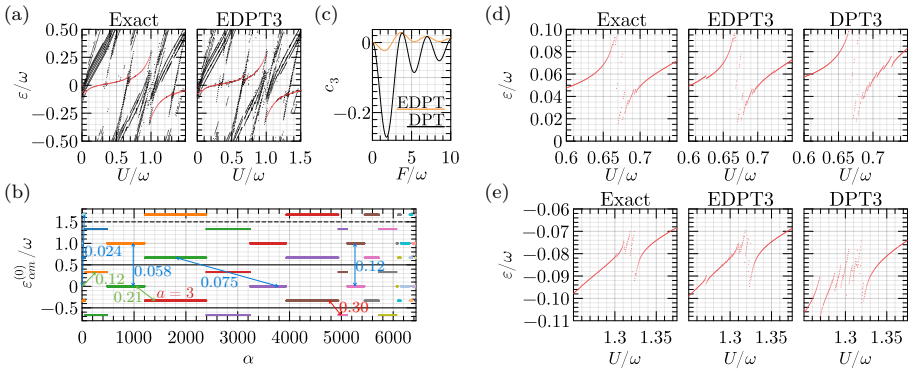

Figure 4.3: Assessment of accuracy of DPT and EDPT for an eight-particle BH system on a 1×8 lattice with $F/\omega = 2$, $\omega/J = 20$. (a) Quasienergy spectrum for $U \in [0, 1.5\omega]$. Quasienergies of ten Floquet modes having the largest overlap with the MI state are displayed; quasienergies of the mode with the maximum overlap are highlighted in red. (b) Diagonal elements of $\bar{Q}'$ at $U = \frac{2}{3}\omega$. Black horizontal lines indicate the boundaries of the FZs. Red and blue arrows with numbers show the largest relative coupling strengths r (4.37) corresponding to coupling with states outside the central FZ. For example, for the states $|\alpha 0\rangle\rangle$ of the central FZ with $\alpha \in [478, 1205]$, the largest relative coupling strength of $r = 0.058$ is found as a result of the coupling with one of the states $|\alpha 1\rangle\rangle$. Green arrows with numbers show the largest coupling strengths r corresponding to coupling with states inside the central FZ. Only some of the couplings are indicated. (c) Coupling element $c_3 \equiv \langle 3|\hat{W}_{\mathrm{D}}^{(2)}|\mathrm{MI}\rangle$ calculated at $U = \frac{2}{3}\omega$ using DPT and EDPT versus F/ω. (d) Quasienergies of the driven MI state in the vicinity of $U = \frac{2}{3}\omega$. (e) Quasienergies of the driven MI state in the vicinity of $U = \frac{4}{3}\omega$.

quasienergies for such a wide range of U. The most pronounced anticrossing seen at $U \approx \omega$ corresponds to first-order creation of particle–hole excitations in the MI state, whereby a particle is annihilated at a certain site and created at its neighbouring site [155]. At $U = \omega$, transitions between all levels of the system become resonant, therefore, all diagonal elements of $\bar{Q}'$ in the given diagonal block share the same value. Consequently, the actual distribution of quasienergies is almost entirely captured by the first-order effective Hamiltonian (4.29). Additionally, DPT becomes equivalent to EDPT since all levels of the system are included in the degenerate subspace. The second- and third-order terms of $\hat{W}_{\mathrm{D}}$ provide a slight improvement and yield results in agreement with the exact ones, as shown in Fig. 4.3(a). Notably, the EDPT results remain sufficiently accurate away from resonances as well. Exactly on the resonance $U = \omega$, the largest value of the coupling ratio (4.37) is $r_{\max} = 0.12$, which is one of the largest values that can be considered to satisfy the condition (4.37). Therefore, for smaller values of ω (and the same value of F/ω), the EDPT is not expected to yield reliable results near the resonance $U = \omega$.

To assess the accuracy of the methods on a finer scale, we inspect the

quasienergy of the driven MI state in the vicinity of $U = \frac{2}{3}\omega$, as shown in Fig. 4.3(d). The obtained anticrossing is a result of the second-order process whereby two particles of an MI state hop to the site of their common neighbour, producing a triply occupied site and resulting in a state of energy $E = 3U$. This process has been analysed in Ref. [155] using the DPT approach. Plugging the expressions (4.40) into Eq. (4.36) one finds that for the resonance condition $3U = q\omega$, the element $c_3 \equiv \langle 3|\hat{w}_{\mathrm{D}}^{(2)}|\mathrm{MI}\rangle$ vanishes for q odd ($|3\rangle$ denotes any one of the states with a triply occupied site reachable starting from $|\mathrm{MI}\rangle$ in two hops). Meanwhile, for $q = 2$, the strongest coupling is observed for $F/\omega \approx 2$. The quasienergy of the driven MI state is indeed calculated correctly using DPT, as shown in Fig. 4.3(d). However, as U is tuned away from resonance, the EDPT yields more accurate results.

As noted in Section 4.1.2, the EDPT and DPT approaches are not equivalent, therefore, the value of c_3 depends on which method is used to construct the effective Hamiltonian. These values are compared in Fig. 4.3(c) for $U = \frac{2}{3}\omega$ and a range of coupling strengths F/ω. The curves are quite different in nature: for example, at $F/\omega \approx 3.4$ the DPT curve crosses the zero, while the EDPT curve approaches a local maximum. Vanishing coupling indicates disappearance of the corresponding anticrossing in the quasienergy spectrum [155], which is indeed the case for $F/\omega \approx 3.4$, as confirmed by an exact calculation (not shown). Thus, even though EDPT yields quasienergies with higher accuracy than DPT, the matrix elements of $\hat{W}_{\mathrm{D}}$ constructed using EDPT do not have such a straightforward interpretation compared to the case when DPT is used. Another difference between EDPT and DPT concerns the higher-order terms of the effective Hamiltonian. In the DPT case, the third-order term $\hat{w}_{\mathrm{D}}^{(3)}$ gives an insignificant correction to the second-order theory at $U = \frac{2}{3}\omega$. The additional processes appearing in the third-order are the creation of a state featuring three doubly occupied sites (the corresponding matrix element is $\eta = 9.2$ times smaller than c_3) and the process of creating a state with a triply occupied site in three hops ($\eta = 25$). In the EDPT case, on the other hand, inclusion of the third-order term $\hat{W}_{\mathrm{D}}^{(3)}$ gives a substantial improvement in terms of accuracy.

It is instructive to consider the values of the coupling ratios (4.37) for EDPT. Exactly on resonance $U = \frac{2}{3}\omega$, we find $r_{\max} = 0.30$, which is quite large. However, this value comes from the coupling of a state corresponding to $\varepsilon_{\alpha m}^{(0)} = -\frac{1}{3}\omega$ with a state corresponding to $\varepsilon_{\alpha' m'}^{(0)} = -\frac{2}{3}\omega$, therefore, this coupling does not directly influence the driven MI state, whose reduced energy is $\varepsilon_{*}^{(0)} = 0$. The said coupling is indicated in red in Fig. 4.3(b) depicting the diagonal elements of $\bar{Q}'$ at $U = \frac{2}{3}\omega$. On the other hand, all of the degenerate states sharing the value $\varepsilon_{*}^{(0)} = 0$ are coupled weakly to states outside the central FZ, as indicated by the blue numbers in Fig. 4.3(b) (see figure caption for

details). This explains the fact that accurate results have been obtained using EDPT despite the condition (4.37) not being satisfied. We remind that the couplings between the states in the central FZ [see green arrows with numbers in Fig. 4.3(b)] are taken into account exactly in the EDPT framework. Meanwhile, the couplings of degenerate states with the nondegenerate ones are treated perturbatively in the DPT, which explains why the reported DPT results are less accurate even exactly on resonance.

Let us also discuss the origin of the discontinuity at $U = \frac{5}{8}\omega$ in the EDPT results seen in Fig. 4.3(d). For definiteness, consider the group of levels characterised by $\varepsilon_\alpha^{(0)} = -\frac{1}{3}\omega$ and reduction number $a = 3$, appearing in red in Fig. 4.3(b), where $U = \frac{2}{3}\omega$ is assumed. These are the levels arising from the unperturbed states of energy $E = 4U$. As U decreases, these levels shift downwards, reaching the lower FZ boundary when U attains the value of $\frac{5}{8}\omega$. Decreasing U still further makes this particular group of levels leave the FZ, and another one (appearing in green in the figure) enters from above. However, the reduction number for the levels of the latter group is $a = 2$. Since the reduction number directly influences the strength of coupling with other levels, the coupling with the states under consideration changes abruptly as U crosses the value of $\frac{5}{8}\omega$. Although processes such as this one reduce the accuracy of the EDPT, their impact is not that noticeable if the states of actual interest are not strongly coupled to the states crossing the boundaries of FZ. This is certainly the case presently: Our main focus is on the driven MI state, which is not directly coupled to the $4U$ states. Consequently, the artifactual discontinuity in Fig. 4.3(d) is an order of magnitude narrower than the width of the anticrossing that is of actual interest.

The last case for this parameter set is studied in Fig. 4.3(e) that displays the quasienergy of the driven MI state in the vicinity of $U = \frac{4}{3}\omega$. The anticrossing is again a manifestation of the second-order process producing a triply occupied site. Despite the width of the anticrossing making up only $\sim 2\%$ of the width of the FZ, it can be calculated accurately using perturbation theory. Again, EDPT is more accurate than DPT, although the former one yields a number of false anticrossings.

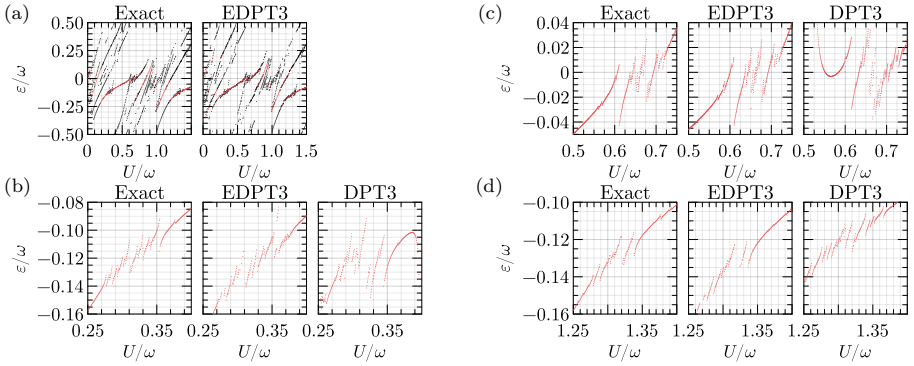

Figure 4.4: Assessment of accuracy of DPT and EDPT for an eight-particle BH system on a 2×4 lattice with $F/\omega = 2$, $\omega/J = 20$. (a) Quasienergy spectrum for $U \in [0, 1.5\omega]$. Quasienergies of five Floquet modes having the largest overlap with the MI state are displayed; quasienergies of the mode with the maximum overlap are highlighted in red. (b) Quasienergies of the driven MI state in the vicinity of $U = \frac{1}{3}\omega$. (c) Quasienergies of the driven MI state in the vicinity of $U = \frac{2}{3}\omega$. (d) Quasienergies of the driven MI state in the vicinity of $U = \frac{4}{3}\omega$.

4.2.3 Study case 2: Two-dimensional lattice

We now turn to a BH system described by the same parameter values ($F/\omega = 2$, $\omega/J = 20$), but this time on a 2×4 lattice periodic in the x-direction (we direct the x-axis along the longer dimension of the lattice). The quasienergy spectrum calculated for $U \in [0, 1.5\omega]$ is shown in Fig. 4.4(a). We notice that the curve of the driven MI state undergoes many more anticrossings compared to the above case of a one-dimensional lattice, indicating richer system dynamics. The EDPT results are less accurate here, featuring erroneous and noticeable discontinuities. Nevertheless, the quasienergies can be considered calculated qualitatively correctly in the vicinity of the main anticrossing at $U = \omega$.

According to Eq. (4.39), driving renormalises the hopping strength only for hopping along the x-axis. As a result, the DPT theory no longer predicts that c_3 vanishes for all F when $U = \frac{m}{3}\omega$ with m odd. Indeed, Fig. 4.4(b) confirms that numerous anticrossings appear in the vicinity of $U = \frac{1}{3}\omega$. Their presence is predicted by both EDPT and DPT, albeit the exact results are matched only qualitatively. Meanwhile, in the cases $U = \frac{2}{3}\omega$ and $U = \frac{4}{3}\omega$ the EDPT ensures higher accuracy, providing a considerable improvement over DPT [see Figs. 4.4(c) and (d)].

Finally, we consider the results obtained for the case of a higher driving frequency: $\omega/J = 30$. As expected, the accuracy of the perturbation theory is higher in this case, which is confirmed by the plots in Fig. 4.5. Figure 4.5(a) shows that EDPT yields accurate results on a large scale, capturing all the essential features of the exact quasienergy spectrum. The close-up views

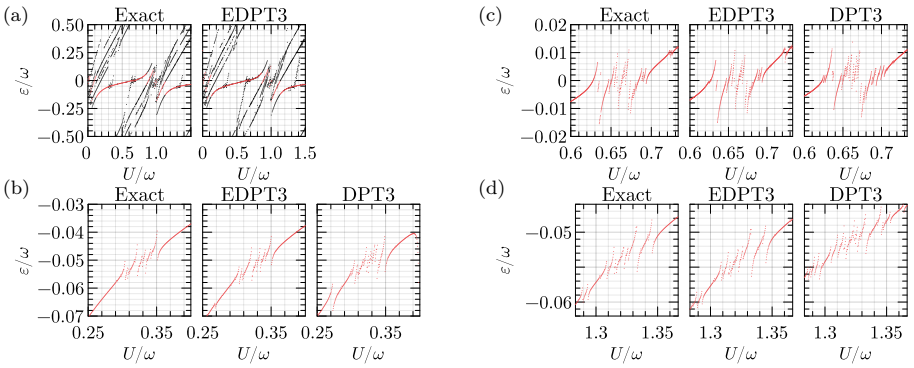

Figure 4.5: Same as in Fig. 4.4 for $\omega/J = 30$.

of the spectrum in the vicinity of $U = \frac{1}{3}\omega$, $U = \frac{2}{3}\omega$ and $U = \frac{4}{3}\omega$, shown in Figs. 4.5(b), (c), and (d), respectively, display that EDPT is capable of providing quantitatively correct results in this regime. The DPT is certainly applicable as well, although the accuracy is lower.

4.2.4 Computational cost of the methods

Concluding the discussion of accuracy of the considered methods, let us compare the associated computational costs. Calculation of quasienergies using both DPT and EDPT comes down to a Hermitian matrix diagonalisation. In the EDPT case, one is required to diagonalise the matrix whose size is given by the total number of states of the unperturbed systems. In the studied eight-particle systems, there are $N = 6435$ such states. In the DPT case, the size is given by the number of states sharing the same value of reduced energy $\varepsilon_*^{(0)}$. For example, on a 2×4 lattice and at $U = \frac{2}{3}\omega$, there are 2017 states sharing the value of $\varepsilon_*^{(0)} = 0$ [cf. Fig. 4.3(b)]. Both methods thus suffer from exponential growth of the required computation resources, which can only be alleviated by limiting the number of states taken into consideration.

The numerically exact calculation of the quasienergies via the single-period evolution operator $\hat{U}(T)$ requires performing a (unitary) $N \times N$ matrix diagonalisation, similarly to the the EDPT case. However, the construction of $\hat{U}(T)$ additionally requires propagating the Schrödinger equation for one period of the drive N times (for each basis state as the initial condition). Although the specific time required to solve the differential equations depends on multiple factors (such as the solver, required tolerance, and hardware), in our experience [161] the exact calculation of the quasienergies for a single value of U took 2.5–6 times longer than the EDPT calculation and, importantly, required ~ 15 times more memory (see Appendix 4B for details).

4.3 Conclusions

Let us now summarise the results. We have provided an extension of the conventional degenerate perturbation theory that improves the accuracy of the calculation of quasienergy spectra of periodically driven systems. Application of the theory to the driven Bose–Hubbard system has shown that third-order EDPT yields results matching the exact ones on a quantitative level. While the exact applicability criterion is difficult to formulate, the simple condition (4.37) together with the provided example calculations may serve as a basis for predicting the expected accuracy. Generally, the accuracy is expected to improve with increasing driving frequency.

Along the way, we have also studied the application of the conventional DPT. It has an advantage that the matrix elements of the resulting effective Hamiltonian $\hat{w}_{\mathrm{D}}^{[n]}$ admit a straightforward interpretation. Specifically, it enables one to make qualitative predictions about the possible appearance of the anticrossings in the quasienergy spectrum, and the matrix elements of $\hat{w}_{\mathrm{D}}^{[n]}$ may be used to estimate the relative probabilities of various resonant excitation processes [155, 156, 149]. On the other hand, since $\hat{w}_{\mathrm{D}}^{[n]}$ consists of two decoupled blocks (describing the spaces $\mathscr{H}_0$ and $\mathscr{H}_1$, cf. Section 4.1.2), which is clearly a bold approximation, it might not capture important properties of the system, such as the existence of a Floquet dynamical symmetry [162–164]. In this respect, the effective Hamiltonian $\hat{W}_{\mathrm{D}}^{[n]}$ provided by EDPT is expected to be more useful: existence of an operator $\hat{A}$ such that $[\hat{W}_{\mathrm{D}}^{[n]}, \hat{A}] = g\hat{A}$ with g a real number would imply the existence of a dynamical symmetry in the effective system [162, 165], to the nth order of the perturbation theory. This might help in exploring the platforms for constructing discrete time crystals.

The performed analysis has shown that the accuracy of the quasienergies obtained using DPT is considerably lower than that of EDPT. Moreover, while DPT is applicable only in the vicinity of resonances, EDPT remains equally useful if the driving is not resonant. The advantages of EDPT, however, come at the expense of increased numerical effort since the resulting effective Hamiltonian is of the same size as the unperturbed one. For large systems, its diagonalisation becomes prohibitively costly, and one might need to reduce the number of considered states by excluding highly-excited ones, for example. Another option is to adopt a scheme intermediate between DPT and EDPT so that only some of the couplings between the states in the FZ are treated exactly, and others are taken into account perturbatively. The required formalism has been presently provided.

4.4 Appendix 4A: Third-order expressions for the effective Hamiltonian

Here, we provide the third-order expressions for the effective Hamiltonians. In the DPT framework, one obtains

$$
\begin{aligned}
\langle\alpha'|\hat{w}_{\mathrm{D}}^{(3)}|\alpha\rangle = \frac{1}{2}\delta_{A'A}\sum_{\beta,\gamma}\sum_{p\neq 0 \text{ if } C=A}\Bigg[&\delta_{AB}\frac{1}{\varepsilon_\beta-\varepsilon_\gamma-p\omega}\\
\times\Bigg(&\frac{\langle\alpha'|\hat{H}_{b-a'}|\beta\rangle\langle\beta|\hat{H}_{c-b-p}|\gamma\rangle\langle\gamma|\hat{H}_{a-c+p}|\alpha\rangle}{\varepsilon_\gamma-\varepsilon_{\alpha'}+p\omega}\\
&+\frac{\langle\alpha'|\hat{H}_{c-a'-p}|\gamma\rangle\langle\gamma|\hat{H}_{b-c+p}|\beta\rangle\langle\beta|\hat{H}_{a-b}|\alpha\rangle}{\varepsilon_\gamma-\varepsilon_\alpha+p\omega}\Bigg)\\
+\delta_{BC}&\langle\alpha'|\hat{H}_{b-a'-p}|\beta\rangle\langle\beta|\hat{H}_{c-b}|\gamma\rangle\langle\gamma|\hat{H}_{a-c+p}|\alpha\rangle\\
\times\Bigg(&\frac{1}{(\varepsilon_{\alpha'}-\varepsilon_\beta-p\omega)(\varepsilon_{\alpha'}-\varepsilon_\gamma-p\omega)}+\frac{1}{(\varepsilon_\alpha-\varepsilon_\beta-p\omega)(\varepsilon_\alpha-\varepsilon_\gamma-p\omega)}\Bigg)\Bigg]\\
-\frac{1}{12}\delta_{A'A}\sum_{\beta\gamma}\sum_{p\neq 0 \text{ if } A=B}\sum_{\substack{q\neq p \text{ if } B=C\\ q\neq 0 \text{ if } C=A}}&\langle\alpha'|\hat{H}_{b-a'-p}|\beta\rangle\langle\beta|\hat{H}_{c-b+p-q}|\gamma\rangle\langle\gamma|\hat{H}_{a-c+q}|\alpha\rangle\\
\times\Bigg[&\frac{3}{\varepsilon_\beta-\varepsilon_\alpha+p\omega}\left(\frac{1}{\varepsilon_\alpha-\varepsilon_\gamma-q\omega}+\frac{1}{\varepsilon_\beta-\varepsilon_\gamma+(p-q)\omega}\right)\\
&+\frac{3}{\varepsilon_{\alpha'}-\varepsilon_\gamma-q\omega}\left(\frac{1}{\varepsilon_\beta-\varepsilon_\gamma+(p-q)\omega}+\frac{1}{\varepsilon_\beta-\varepsilon_{\alpha'}+p\omega}\right)\\
&+\frac{1}{\varepsilon_\beta-\varepsilon_\gamma+(p-q)\omega}\left(\frac{1}{\varepsilon_\beta-\varepsilon_{\alpha'}+p\omega}+\frac{1}{\varepsilon_\alpha-\varepsilon_\gamma-q\omega}\right)\\
&+\frac{2}{(\varepsilon_\alpha-\varepsilon_\gamma-q\omega)(\varepsilon_\beta-\varepsilon_{\alpha'}+p\omega)}\Bigg].
\end{aligned}
\tag{4.41}
$$

Integers A, A', B, and C indicate which subspaces the states belong to: $|\alpha\rangle \in \mathscr{H}_A$, $|\alpha'\rangle \in \mathscr{H}_{A'}$, $|\beta\rangle \in \mathscr{H}_B$, $|\gamma\rangle \in \mathscr{H}_C$. In the EDPT framework, all states are assigned to the same subspace, therefore, in that case one should put $A = A' = B = C$ in the above equation.

4.5 Appendix 4B: Benchmarks of the methods

In this Appendix we provide benchmarks of the methods and additional technical details.

The scaling of the computational time and required memory with the system size is shown in Fig. 4.6. The performed calculations correspond to those presented in Fig. 4.3 at a single point of $U = \frac{2}{3}\omega$, for lattice sizes $N = 5$ through 10 (with unit filling). The data is depicted on a semi-logarithmic scale, together with an exponential fit $y = 10^{kN} + y_0$; the coefficients k are provided in the legends. It is apparent that the EDPT provides a noticeable advantage in terms of calculation times compared to the exact approach and requires more than an order of magnitude less memory. The memory requirements for DPT are similar to those of EDPT because we were constructing the effective Hamiltonian $\hat{w}_{\mathrm{D}}^{[3]}$ for both the degenerate and nondegenerate subspaces, although we were diagonalising only the block corresponding to the degenerate space.

In practice, one often needs to repeat the calculation of quasienergies for a range of one or more system parameters, as was done in our analysis. The loop scanning over the parameters can be easily parallelised on a multicore machine or a cluster, but the memory requirements might put a limit on the number of processes that can be run in parallel. For example, the exact calculation shown in Fig. 4.4(a), where ~ 300 values of U were scanned, was performed using only 21 of 64 cores of an AMD 2990WX CPU because that already used almost all

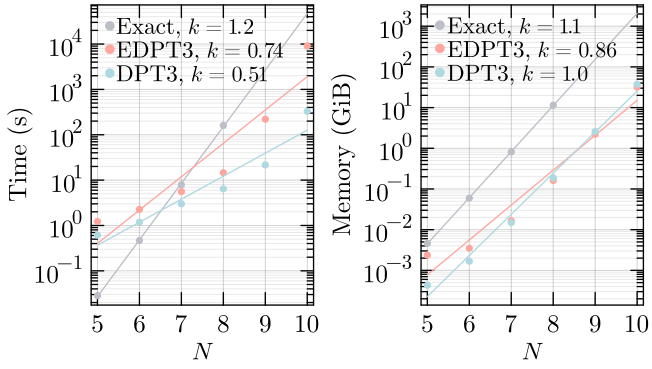

Figure 4.6: Scaling of computation time and required memory with the system size. The code [161] was benchmarked on a Mac mini computer with Apple M2 Pro chip (8 performance cores variant) and 32 GB RAM. The exact calculations for systems with $N > 8$ were not performed as the memory requirements exceeded resources available on the test machine. The reported memory utilisation was measured as the total amount of memory allocated during the calculation. This was chosen as a reproducible criterion that reflects the scaling behaviour. The actual amount of memory required is highly dependent on the implementation details.

available RAM space (121 GB out of 128 GB). The execution time was 6 hours. Meanwhile, EDPT3 allowed us to utilise all 64 cores while requiring 22 GB RAM in total; the calculation finished in 50 minutes.

The software package `FloquetSystems.jl` implementing all relevant calculations is available on GitHub [161]. A number of software packages [137, 138, 166] developed in Julia [143] was used.

Part II

Topological phenomena in Bose–Einstein condensates

CHAPTER 5

Light-induced localised vortices in multicomponent Bose–Einstein condensates

In this chapter, we explore the manifestation of topology in interacting quantum gases — the Bose–Einstein condensates (BECs). A BEC forms when a dilute gas of bosonic atoms is cooled below a critical temperature, leading to a macroscopic occupation of the ground state. On the mean-field level of treatment, the system can be described by a macroscopic wave function $\Psi(\boldsymbol{r}, t)$ whose evolution is governed by a time-dependent Gross–Pitaevskii equation (GPE)

$$\mathrm{i}\hbar\frac{\partial}{\partial t}\Psi = \left(-\frac{\hbar^2}{2m}\Delta + V + g|\Psi|^2\right)\Psi, \tag{5.1}$$

where $V(\boldsymbol{r})$ is a trapping potential, while g characterises the particle interaction strength and is related to the s-wave scattering length a_s as $g = 4\pi\hbar^2 a_\mathrm{s}/m$ [167, 168]. The wave function Ψ (normalised to the total number of atoms in the condensate, $\int |\Psi|^2 \,\mathrm{d}^3 r = N$) describes the collective order in the atomic system and thus plays the role of an order parameter. Writing it in terms of the modulus and phase as

$$\Psi(\boldsymbol{r}, t) = \sqrt{n(\boldsymbol{r}, t)}\mathrm{e}^{\mathrm{i}\phi(\boldsymbol{r}, t)}, \tag{5.2}$$

one can define the velocity field of the condensate as

$$\boldsymbol{v}(\boldsymbol{r}, t) = \frac{\hbar}{m}\nabla\phi(\boldsymbol{r}, t). \tag{5.3}$$

With this definition, the condensate wave function satisfies the continuity equation $\frac{\partial n}{\partial t} + \nabla(n\boldsymbol{v}) = 0$, which follows from Eq. (5.1), and thus reflects the actual

movement of atoms.

In the following discussion, we will concentrate on the stationary configurations of the condensates. The GPE (5.1) possesses stationary solutions of the form

$$\Psi(\boldsymbol{r},t) = \mathrm{e}^{-\mathrm{i}\mu t/\hbar}\psi(\boldsymbol{r}) = \mathrm{e}^{-\mathrm{i}\mu t/\hbar}\sqrt{n(\boldsymbol{r})}\mathrm{e}^{\mathrm{i}\phi(\boldsymbol{r})}, \tag{5.4}$$

where μ is the chemical potential. Notably, the velocity field may be nonzero in the stationary state, provided there is a nonvanishing gradient of the phase, as follows from Eq. (5.3).

Since the phase is defined up to an integer multiple of 2π, it follows that the integral of the velocity field around an arbitrary closed contour is quantised:

$$\oint \boldsymbol{v}\,\mathrm{d}\boldsymbol{\tau} = \frac{\hbar}{m}\oint \mathrm{d}\phi = 2\pi\ell\frac{\hbar}{m}, \qquad \ell \in \mathbb{Z}, \tag{5.5}$$

thereby restricting the allowed motion of atoms. Application of the Stokes theorem seems to imply than only the value $\ell = 0$ is allowed since $\nabla \times \nabla\phi = 0$. However, nonzero values of ℓ can in fact be realised if ϕ contains a singularity. A prime example is given by the vortex configuration, described in cylindrical coordinates $\boldsymbol{r} = (\rho, \varphi, z)$ by the phase profile $\phi(\boldsymbol{r}) = \ell\varphi$, $\varphi \in [0, 2\pi)$. In this case, the phase of the wave function is undefined on the line $\rho = 0$; while we can assign an arbitrary fixed value for ϕ on this line, such an assignment would render ϕ discontinuous. Meanwhile, the velocity field reads

$$\boldsymbol{v}(\boldsymbol{r}) = \frac{\hbar}{m}\frac{\ell}{\rho}\boldsymbol{e}_\varphi, \tag{5.6}$$

where $\boldsymbol{e}_\varphi$ is the unit vector in the azimuthal direction. It follows that $\boldsymbol{v}$ grows without bound as $\rho \to 0$, and its curl may be expressed as

$$\nabla \times \boldsymbol{v} = 2\pi\ell\frac{\hbar}{m}\delta^{(2)}(\boldsymbol{r})\boldsymbol{e}_z, \tag{5.7}$$

where $\delta^{(2)}(\boldsymbol{r})$ is the 2D delta-function and $\boldsymbol{e}_z$ is a unit vector in the z-direction. Clearly, for ψ to be well-defined and for the kinetic energy of the condensate to remain bounded, one must have $\psi = 0$ on the singular vortex line.

A vortex line is an example of a *topological defect* — a singularity of the order parameter that cannot be eliminated without introducing singularities at arbitrarily large distances from the original defect [50]. For example, let us consider a vortex configuration with $\ell = 1$ and contemplate deforming the function $\phi(\boldsymbol{r})$ so as to achieve $\phi(\boldsymbol{r}) = \text{const}$, which is equivalent to a vortex-free configuration with $\ell = 0$. We can try achieving this by reducing the value of ϕ towards zero everywhere. Formally, we can describe this process by the function $\phi(\boldsymbol{r}|t) = (1-t)\varphi$ which interpolates between the two cases as the parameter

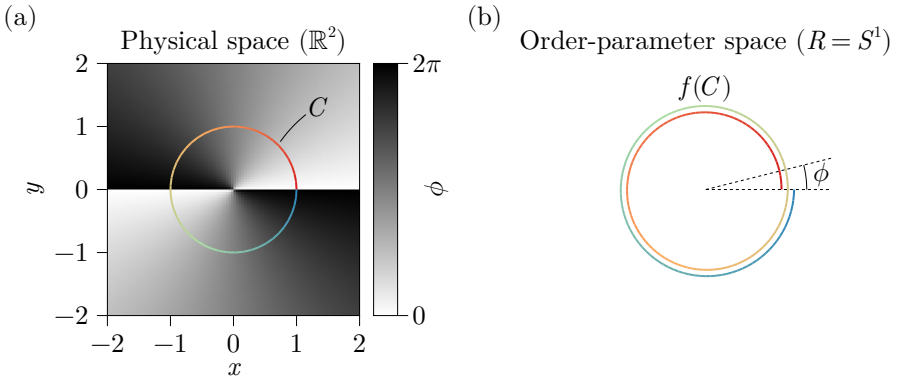

Figure 5.1: (a) A contour $C = S^1$ surrounding a point defect in 2D physical space (x, y), where the order parameter $e^{i\phi(x,y)}$ is defined. The case of $\phi(x, y) = 2\varphi$ is displayed. (b) Mapping of the contour C into a loop $f(C)$ in the order-parameter space R, which is also topologically S^1. The red and blue 'ends' of the loop should be identified.

t changes from 0 to 1. For intermediate values of t, the function $\phi(\boldsymbol{r}|t)$, and hence also the order parameter $\psi \sim e^{i\phi}$, becomes discontinuous at $\varphi = 0$ for all ρ and z. A BEC could possibly pass through this configuration by having the order parameter vanish identically at those singular points, as it does on the vortex line. However, this is associated with additional variation of the order parameter in space, and hence with additional energy of the state. The configurations corresponding to different values of ℓ are therefore separated by an energy barrier.

The above argument can be made more precise using the language of homotopy theory. First, we introduce the notion of *surrounding* the defect by an n-sphere such that

$$n = d - d' - 1, \tag{5.8}$$

where d is the dimensionality of the physical space in which the order parameter is defined, and d' is the dimensionality of the defect [169, 120]. In the case of a vortex line ($d' = 1$) in a 3D BEC ($d = 3$), one finds that the defect is surrounded by a circle S^1, and the same is true for a quasi-2D BEC, in which the vortex line becomes a singular point ($d' = 0$). Next, we consider the values of the phase factor $e^{i\phi}$ to constitute the *order-parameter space* R and study the mapping of the values of the order parameter on the surrounding n-sphere into the space R. For both 3D and 2D BEC, we find that the values of the order parameter $e^{i\ell\varphi}$ along the surrounding loop S^1 are mapped to a loop of winding number ℓ in the order-parameter space. This is illustrated in Fig. 5.1 for $\ell = 2$. The mappings — or simply the resulting loops in the order-parameter space — that can be continuously deformed into each other are said to be *homotopic*,

and they belong to the same *homotopy class*. By a proper definition of the composition law of homotopy classes[1)], they are made to form a *homotopy group*. Presently, we are concerned with the mappings of a loop S^1 into R, and these are described by the first homotopy group $\pi_1(R)$. The latter provides a characterisation of the defect, reflecting its stability and the 'composition law for defects'. Since R in the BEC example is isomorphic to S^1, the group of interest is $\pi_1(S^1)$. A detailed calculation [120] shows that $\pi_1(S^1) \cong \mathbb{Z}$, which, being a nontrivial group, guarantees the stability of vortices. This means that the loop surrounding a vortex is characterised by an integer — the winding number ℓ of the corresponding loop in R. Such a loop cannot be continuously deformed into one with a different value of ℓ, implying that the corresponding structure surrounded by S^1 in the physical space likewise cannot be eliminated by a continuous change of the order parameter. Remarkably, the winding number does not depend on the distance from the vortex line at which the surrounding loop S^1 is taken, implying that the presence of the vortex can be detected in the medium arbitrarily far from its core, and therefore removing the vortex would require disturbing the medium at arbitrarily remote points.

The group structure of $\pi_1(S^1)$ directly reflects the fact that two vortices characterised by vorticities ℓ_1 and ℓ_2 can be combined to produce a vortex of vorticity $\ell = \ell_1 + \ell_2$. The circle surrounding such a pair of vortices will be mapped to a loop of winding number ℓ, implying that at long distances from the vortices, the order parameter assumes the form that it would have, had there been a single vortex of vorticity ℓ. A direct manifestation of this combination law is provided by the experiments demonstrating annihilation of pairs of vortices of opposite vorticities [85]. Likewise, a vortex having a winding number ℓ can split into a number of vortices characterised by winding numbers ℓ_i provided that $\ell = \sum_i \ell_i$. In fact, this underlies the dynamical instability of vortices with higher winding numbers — the energy of a vortex is proportional to ℓ^2, so that splitting is energetically favourable (this holds true for condensates uniform in the bulk, but the situation is more involved in trapped rotating BECs [170]).

In the preceding discussion we have assumed that the physical space in which the order parameter is defined has no boundaries. This is, of course, not the case in real applications, and the presence of a boundary creates the possibility of removing the vortex (without introducing singularities) by moving its core towards the boundary, clearing the order parameter of the singularity.

[1)] The composition law of homotopy classes is defined as follows [102, 120]. First, we define the composition $f \circ g$ of loops f and g as the loop obtained by first traversing f and then g, starting and ending at a point that the two loops are assumed to have in common. Next, let $[f]$ denote the homotopy class to which the loop f belongs. The composition of classes $[f]$ and $[g]$ is then defined as $[f] \circ [g] = [f \circ g]$.

The reverse process is exactly the mechanism of the appearance of vortices in trapped BECs [171, 172].

The above analysis may be generalised to mixtures of BECs. Current experimental techniques allow for producing BECs of two atom species, e.g., mixing ^{87}Rb with ^{41}K [173] or with ^{133}Cs [174]. Alternatively, a mixture of atoms in several hyperfine states can be produced — by using optical rather than magnetic trapping, so that the projection of the spin of the atoms is not fixed, constituting an additional degree of freedom. Examples include trapping the states of different F-manifolds, such as the states $|F = 1, m_F = -1\rangle$ and $|F = 2, m_F = 2\rangle$ [175], or producing a spinor condensate by trapping the three states of the $F = 1$ manifold [176].

The BEC mixtures are described by a multicomponent order parameter $|\psi(\boldsymbol{r})\rangle$, leading to the emergence of topological structures not possible in scalar BECs. One such example is a *coreless vortex*, which refers to the structure in which one component is in a vortex state, with its core filled by the atoms of the second, vortex-free component [177–181]. A coreless vortex may be described by the order parameter [182, 2, 183]

$$|\psi(\boldsymbol{r})\rangle = \sqrt{n(\boldsymbol{r})} \begin{pmatrix} \cos\frac{\alpha(\rho)}{2} \\ \mathrm{e}^{\mathrm{i}s\varphi} \sin\frac{\alpha(\rho)}{2} \end{pmatrix}, \tag{5.9}$$

where $s \in \mathbb{Z}$, while $\alpha(\rho)$ is a monotonically increasing function subject to the boundary conditions

$$\alpha(0) = 0, \qquad \alpha(\infty) = \pi. \tag{5.10}$$

The second component of $|\psi(\boldsymbol{r})\rangle$ is in a vortex state, but its core is nonsingular since the density of the second component vanishes identically at the origin. The total density $n(\boldsymbol{r})$, however, need not vanish at $\rho = 0$. The order parameter assigns a Bloch vector to every point in space, so that the order-parameter space is a two-sphere S^2. The contour surrounding the line defect in the physical space is a circle S^1 as before. The properties of the defect are captured by the homotopy group that, however, is a trivial group[2)]: $\pi_1(S^2) \cong 0$ [50]. This means that the coreless-vortex configuration can be continuously deformed into a vortex-free configuration, implying that the vortex can disappear in the course of the evolution of the condensate. Explicitly, this can be achieved by reducing the value of $\alpha(\rho)$ to zero at each point in space. The condensate can thus 'get rid' of the vorticity by rotating the spinors (5.9) at each point in space towards

[2)] Heuristically, this result follows from the fact that any loop on a surface of a sphere can be continuously deformed to a point, and this is the case even for nonzero winding numbers s. For example, consider the circle S^1 surrounding the vortex at a distance ρ from its core such that $\alpha(\rho) = \pi/2$. This contour gets mapped to a loop encircling the equator of the Bloch sphere in the order-parameter space s times. It can then be deformed to a point by sliding the loop to one of the poles.

the spin-up orientation. Note that in this discussion we allow the function $\alpha(\rho)$ to change arbitrarily, without requiring the boundary conditions (5.10) to remain valid.

Despite not being topologically stable, the configuration (5.9) has attracted much attention due to its relation to the superfluid flow of the A-phase of ^{3}He. The order parameter of the latter is characterised by an orthonormal triad $(\boldsymbol{m}_1(\boldsymbol{r}), \boldsymbol{m}_2(\boldsymbol{r}), \boldsymbol{l}(\boldsymbol{r}))$ assigned to each point in space. Remarkably, the Bloch-vector field (or the average spin field) corresponding to the configuration (5.9) possesses exactly the same Cartesian components as does the $\boldsymbol{l}(\boldsymbol{r})$ field of ^{3}He in the so-called Anderson–Toulouse–Chechetkin (ATC) vortex state [184, 2]. Explicitly, we have

$$\begin{aligned} \boldsymbol{l}(\boldsymbol{r}) &= \frac{\langle\psi(\boldsymbol{r})|\hat{\boldsymbol{\sigma}}|\psi(\boldsymbol{r})\rangle}{\langle\psi(\boldsymbol{r})|\psi(\boldsymbol{r})\rangle} \\ &= \boldsymbol{e}_x \sin\alpha(\rho)\cos s\varphi + \boldsymbol{e}_y \sin\alpha(\rho)\sin s\varphi + \boldsymbol{e}_z \cos\alpha(\rho), \end{aligned} \tag{5.11}$$

where $\hat{\boldsymbol{\sigma}}$ is a vector of Pauli matrices. For $s = 1$, the above reduces to the ATC case characterised by $\boldsymbol{l}(\boldsymbol{r}) = \boldsymbol{e}_\rho \sin\alpha(\rho) + \boldsymbol{e}_z \cos\alpha(\rho)$, and it is shown in Fig. 5.2. The $\boldsymbol{l}$-field allows one to calculate the curl of the superfluid velocity for ^{3}He-A, which is given by the Mermin–Ho relation [2]

$$\nabla \times \boldsymbol{v} = \frac{\hbar}{4m}\epsilon_{ijk} l_i (\nabla l_j \times \nabla l_k) = \frac{\hbar}{2m}[\boldsymbol{l} \cdot (\partial_x \boldsymbol{l} \times \partial_y \boldsymbol{l})]\boldsymbol{e}_z. \tag{5.12}$$

In general, and in the case of the ATC vortex in particular, this quantity is nonzero and nonsingular, contrary to the case of the conventional superfluid vortex [cf. Eq. (5.7)]. The superfluid velocity itself is given by (for $s = 1$) [2]

$$\boldsymbol{v} = \frac{\hbar}{2m\rho}[1 - \cos\alpha(\rho)]\boldsymbol{e}_\varphi, \tag{5.13}$$

which approaches zero[3)] in the limit $\rho \to 0$ rather than diverging as in a conventional vortex.

Mathematically, the explicit form of the $\boldsymbol{l}$-field (5.11) represents the compactification of the 2D Euclidean plane (parametrised by ρ and φ) to a two-sphere. The resulting field describes the topological structure known as a *2D skyrmion*, and it is associated with a topological quantum number (charge) [183, 2]

$$Q = \frac{1}{4\pi}\int \boldsymbol{l} \cdot (\partial_x \boldsymbol{l} \times \partial_y \boldsymbol{l})\,\mathrm{d}x\mathrm{d}y = -\frac{s}{2}\cos\alpha(\rho)\Big|_{\rho=0}^{\rho=\infty} = s. \tag{5.14}$$

Here the integration was performed over the whole Euclidean plane $\mathbb{R}^2$. The

[3)] It is assumed that $\alpha(\rho)$ approaches zero in the limit $\rho \to 0$ faster than $\sqrt{\rho}$, i.e., $\alpha(\rho) \approx \rho^b$ with $b > \frac{1}{2}$.

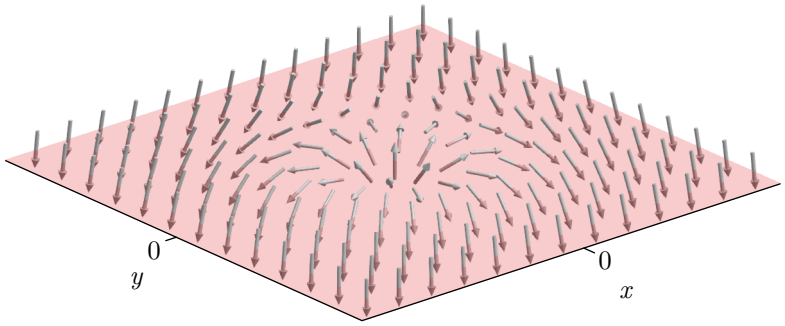

Figure 5.2: Vector field $\boldsymbol{l}(\boldsymbol{r})$ of the $s = 1$ skyrmion (5.11) in the xy plane. In an infinite and continuous picture one would see that each possible orientation of the vector $\boldsymbol{l}$ appears exactly s times.

value of this integral indicates how many times the vector $\boldsymbol{l}$ wraps around the Bloch sphere. Comparing with Eq. (5.12), we find that the circulation of $\boldsymbol{v}$ taken along the contour at infinity is related to the charge of the skyrmion by

$$\oint \boldsymbol{v}\,\mathrm{d}\boldsymbol{\tau} = 4\pi Q\frac{\hbar}{2m} \tag{5.15}$$

and is therefore quantised. We note, however, that the circulation depends in a continuous fashion on the area enclosed by the contour. For this reason vortices obeying the Mermin–Ho relation (5.12) are called continuous vortices. Another important type of a continuous vortex, known as the Mermin–Ho vortex or a *meron*, can be constructed by changing the boundary condition at infinity to $\alpha(\infty) = \pi/2$ [2, 120]. The topological charge of such a vortex is $Q = s/2$ reflecting the fact that the vector $\boldsymbol{l}$ sweeps over half the Bloch sphere.

In the framework of homotopy theory, the 2D skyrmion is characterised by the second homotopy group $\pi_2(R)$, describing the mappings of two-spheres (or compactified 2D planes) into the order-parameter space. The standard result $\pi_2(S^2) \cong \mathbb{Z}$ reflects the fact that these structures can be classified by integer-valued indices, which are precisely the topological charges (5.14). However, the compactification that is involved means that the boundary conditions play a prominent role [185]. Namely, if the boundary conditions (5.10) are held fixed, the skyrmion structure is topologically stable — it cannot be continuously deformed into a configuration with a different value of Q.

In the following we will consider the situation whereby the coordinates $\boldsymbol{r}$ on which the order parameter depends are regarded as adiabatic parameters belonging to some manifold M. In the case of the spinor (5.9) we can consider M to be the Euclidean plane $\mathbb{R}^2$. Due to the freedom of choice of the (coordinate-dependent) phase of $|\psi\rangle$, we are led to a description of the problem in terms

of a U(1) principal fibre bundle, which was already encountered in the study of the quantum Hall effect and the problem of the magnetic monopole (see Chapter 1). Specifically, the states $c|\psi(\boldsymbol{r})\rangle$ with all possible values of the complex phase factor c make up a fibre at a point $\boldsymbol{r} \in M$. Interestingly, we can make the bundle topologically nontrivial by identifying all points at infinity, which is in fact realised by the mapping (5.11): all points $\rho \to \infty$ are mapped to the south pole of the Bloch sphere. With this identification, $M = \mathbb{R}^2 \cup \{\infty\} \cong S^2$ becomes closed, and the bundle may be characterised by the Chern numbers. The Berry connection is given by $\boldsymbol{A} = -\mathrm{i}\,\langle\psi|\nabla\psi\rangle$ and the Berry curvature is $\Omega_{xy} = \partial_x A_y - \partial_y A_x$. The latter can be expressed in terms of $\boldsymbol{l}$ as follows: $\Omega_{xy} = \frac{1}{2}\boldsymbol{l} \cdot (\partial_x \boldsymbol{l} \times \partial_y \boldsymbol{l})$. The charge of the skyrmion Q in (5.14) is therefore precisely the first Chern number of the bundle: $Q = \frac{1}{2\pi}\int \Omega_{xy}\mathrm{d}x\mathrm{d}y \equiv \nu_1$, cf. Eq. (1.9). A nonzero value of ν_1 indicates non-existence of a well-defined global gauge for $|\psi\rangle$; this is the case for the spinor exhibited in Eq. (5.9) — it is singular at $\rho = \infty$ because φ is undefined there as all points at infinity have been identified. By changing the gauge so that $|\psi\rangle \to \mathrm{e}^{-\mathrm{i}s\varphi}|\psi\rangle$, this singularity can be transferred to the origin ($\rho = 0$), but no transformation can remove it. These ideas have been explored in the context of the so-called *optical flux lattices* [186, 187], in which the Bloch vector of a two-component spinor exhibits skyrmion-like structures in each unit cell of the lattice. The base manifold M relevant for those two-dimensional problems is the two-torus, which is closed with no compactification required. Similarly, Q gives the Chern number (Hall conductivity) for a two-dimensional two-level system described by the quasimomentum-space Hamiltonian $\hat{H}(\boldsymbol{k}) = E(\boldsymbol{k}) + \boldsymbol{l}(\boldsymbol{k})\hat{\boldsymbol{\sigma}}$, with the integration in Eq. (5.14) then taking place over the two-torus in k-space [188, 189, 27].

Yet another important feature of the mapping (5.11) emerges in the case when α is an independent variable representing the polar angle of a point in the 3D physical space, rather than a function of ρ. Then, Eq. (5.11) provides a mapping of a two-sphere in the physical space (parametrised by φ and α) to the one in the order-parameter space (parametrised by the direction of $\boldsymbol{l}$), with the former 'covering' the latter s times. This covering is expressed as $\pi_2(S^2) \cong \mathbb{Z}$ and reflects the stability of such a point defect (surrounded, according to Eq. (5.8), by a two-sphere, hence the usage of the second homotopy group π_2) [185]. For $s = 1$, the vector $\boldsymbol{l}$ points radially in every point in space, and this configuration is known as a *hedgehog* or a monopole by analogy with the magnetic monopole discussed in Section 1.2. Monopoles in antiferromagnetic BECs have been investigated in Ref. [190] and realised experimentally in Ref. [191] with the help of a synthetic magnetic field. Furthermore, in Ref. [192] the realisation of a non-Abelian monopole has been reported — an analogue of

a magnetic monopole in synthetic 5D space generating a non-Abelian (Yang–Mills) gauge field and characterised by the second Chern number[4)].

In the rest of this chapter, we will study the generalisation of the order parameter (5.9) such that both components will be allowed to have a vortex factor $e^{i\ell_i\varphi}$. Moreover, the function $\alpha(\rho)$ will be fixed externally, so that the mechanism of removing the vortex discussed above will not be possible. This will lead to coreless vortex that is stable, owning to the fact that the populations of the two components are fixed. In other words, the components are decoupled, leading to the order-parameter space being given by $R = S^1 \times S^1$. The corresponding homotopy group is $\pi_1(R) \cong \mathbb{Z} \times \mathbb{Z}$, reflecting the fact that the state is characterised by two independent integers — the vorticities of each component. We will also consider the configuration of an 'inverted' coreless vortex, whereby the vortex component is tightly localised in a region surrounded by the non-rotating component. By adjusting the external parameters, this state can be made to become the ground state of the system, ensuring its stability.

Rather than postulating the form of the condensate wave function, we will present an optical setup that generates the desired states. The setup is based on the so-called Λ-type coupling configuration, which creates an internal dark state that is immune to decay via spontaneous emission. The properties of this state can be used to realise atom control at subwavelength resolution [193, 194], create optical lattices featuring barriers of subwavelength width [195, 146, 196], and make narrow structures in the BEC [197]. The Λ-systems have also been used to create vortices in BEC via time-dependent transfer of population between the atomic internal states by applying Raman-type schemes [198–201]. Presently, we will make use of the ability to control the system via the coupling laser beams to show that the created localised vortices can be robustly moved around the trap. As long as the beam movement speed is below the speed of sound, the vortex follows the beams without notably disturbing the non-rotating component. To quantify this effect, we will consider moving the vortex in circular paths, thereby stirring the other component with a localised impurity. By examining the resulting heating, we will determine the critical velocity of the superfluid flow below which the vortex moves without dissipation.

[4)] The relevant base manifold is four-dimensional.

5.1 Model

5.1.1 Single-particle Hamiltonian of the system

We consider a general three-level atomic system arranged in a Λ-type configuration of the atom–light coupling shown in Fig. 5.3 [9, 10, 202, 203, 193–195, 204]. Two co-propagating light beams provide the position-dependent couplings between the atomic internal states. The beams are characterised by the Rabi frequencies:

$$\begin{aligned} \Omega_1(\boldsymbol{r}) &= \Omega_0 \left(\frac{\rho}{a}\right)^s \mathrm{e}^{-\rho^2/w_0^2}\, \mathrm{e}^{\mathrm{i}k_z z + \mathrm{i}s\varphi}, \\ \Omega_2(\boldsymbol{r}) &= \Omega_0\, \mathrm{e}^{-\rho^2/w_0^2}\, \mathrm{e}^{\mathrm{i}k_z z}, \end{aligned} \tag{5.16}$$

where w_0 is the beam waist (the same for both beams), Ω_0 is the amplitude of the Rabi frequencies, and k_z is the wave number for the paraxial propagation of the light beams in the z direction. The parameter a, having dimension of length, controls the subwavelength nature of the setup. The beam characterised by the Rabi frequency Ω_1 couples the atomic internal states $|1\rangle$ and $|3\rangle$ and represents a Laguerre–Gaussian mode LG_0^s with a vorticity (winding number) $s > 0$ [205, 206, 198, 200, 207–211]. On the other hand, the atomic states $|2\rangle$ and $|3\rangle$ are coupled by a Gaussian beam characterised by the Rabi frequency Ω_2. Both beams co-propagate along the z-axis [10, 203, 202], oscillating at frequencies ω_1 and ω_2, respectively.

On a single-particle level, the dynamics of an atom is governed by the Hamiltonian

$$\hat{H}(\boldsymbol{r}) = -\frac{\hbar^2}{2m}\Delta + V(\boldsymbol{r}) + \hat{H}_0(\boldsymbol{r}). \tag{5.17}$$

The kinetic energy term and the trapping potential $V(\boldsymbol{r})$ (assumed to be the same for the atomic internal states $|1\rangle$, $|2\rangle$ and $|3\rangle$) act as identity operators in the space of atom's internal states. Transitions between the latter states are described by the internal-space Hamiltonian

$$\begin{aligned} \hat{H}_0(\boldsymbol{r}) = {} & \epsilon\, |2\rangle\langle 2| + (-\delta - \mathrm{i}\tfrac{\Gamma}{2})\, |3\rangle\langle 3| \\ & + \hbar[\Omega_1(\boldsymbol{r})\, |3\rangle\langle 1| + \Omega_2(\boldsymbol{r})\, |3\rangle\langle 2| + \text{H.c.}]. \end{aligned} \tag{5.18}$$

The temporal dependence of this Hamiltonian has been eliminated by transitioning to the rotating frame and adopting the rotating wave approximation [212]. Two parameters emerge as a result, including the single-photon detuning $-\delta = E_3 - E_1 - \hbar\Omega_1$ and the two-photon detuning $\epsilon = E_2 - E_1 + \hbar\Omega_2 - \hbar\Omega_1$; here E_i denotes the energy of the ith energy level (see Fig. 5.3). Furthermore, we have introduced the spontaneous decay rate Γ for the excited state $|3\rangle$ represented through the imaginary part of the excited-state energy. In the following,

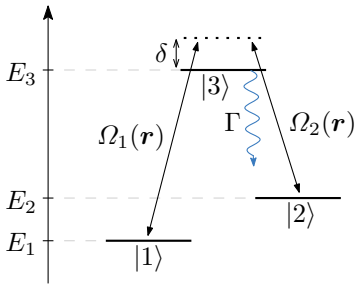

Figure 5.3: Schematic representation of the relevant energy levels of the Λ scheme of the atom–light coupling.

we consider the two-photon resonance, for which $\epsilon = 0$.

It is instructive to consider the states $|\chi(\boldsymbol{r})\rangle$ representing the eigenstates of the internal-space Hamiltonian (5.18), such that $\hat{H}_0(\boldsymbol{r})|\chi(\boldsymbol{r})\rangle = \varepsilon_\chi(\boldsymbol{r})|\chi(\boldsymbol{r})\rangle$, with $\boldsymbol{r}$ treated parametrically. Of special interest is the 'dark' eigenstate of $\hat{H}_0$, given by

$$|\mathrm{D}(\boldsymbol{r})\rangle = \frac{|1\rangle - \zeta(\boldsymbol{r})|2\rangle}{\sqrt{1+|\zeta(\boldsymbol{r})|^2}}, \tag{5.19}$$

where

$$\zeta(\boldsymbol{r}) = \frac{\Omega_1(\boldsymbol{r})}{\Omega_2(\boldsymbol{r})} = \left(\frac{\rho}{a}\right)^s \mathrm{e}^{\mathrm{i}s\varphi}. \tag{5.20}$$

The dark state is characterised by zero eigenenergy. Having no contribution from the lossy excited state $|3\rangle$, the dark state has an infinite lifetime as far as the evolution under $\hat{H}_0$ is concerned. For $\delta = \Gamma = 0$, the remaining two eigenstates of the internal-space Hamiltonian are given by

$$|\pm\rangle = \frac{|\mathrm{B}\rangle \pm |3\rangle}{\sqrt{2}}, \quad \text{where} \quad |\mathrm{B}\rangle = \frac{\zeta^*|1\rangle + |2\rangle}{\sqrt{1+|\zeta|^2}}, \tag{5.21}$$

with

$$\hat{H}_0|\pm\rangle = \pm\hbar\Omega|\pm\rangle \quad \text{and} \quad \Omega = \sqrt{|\Omega_1^2| + |\Omega_2^2|}. \tag{5.22}$$

In Eq. (5.21), $|\mathrm{B}\rangle$ is the so-called bright state, representing a superposition of atomic states orthogonal to the dark state $|\mathrm{D}\rangle$. Later we will consider the adiabatic motion of atoms in the dark-state manifold, which is relevant if the total Rabi frequency Ω is much larger than the characteristic kinetic energy of the atomic centre of mass motion.

To make contact with the above discussion of the order parameter (5.9) for the coreless vortex, let us rewrite the dark state (5.19) as

$$|\mathrm{D}(\boldsymbol{r})\rangle = \cos\frac{\alpha(\rho)}{2}|1\rangle - \mathrm{e}^{\mathrm{i}s\varphi}\sin\frac{\alpha(\rho)}{2}|2\rangle. \tag{5.23}$$

Here we have defined the angle function $\alpha(\rho)$ such that

$$\cos\frac{\alpha(\rho)}{2}=\frac{1}{\sqrt{1+\left(\frac{\rho}{a}\right)^{2s}}},\qquad \sin\frac{\alpha(\rho)}{2}=\frac{\left(\frac{\rho}{a}\right)^{s}}{\sqrt{1+\left(\frac{\rho}{a}\right)^{2s}}}. \tag{5.24}$$

It satisfies the boundary conditions $\alpha(0)=0$ and $\alpha(\infty)=\pi$.

5.1.2 Dynamics of the BEC

Now let us consider the equations for an atomic BEC interacting with the laser fields. We start with the Schrödinger equation for the full state vector $|\Phi(\boldsymbol{r})\rangle$ of a single atom

$$\mathrm{i}\hbar\frac{\partial}{\partial t}|\Phi(\boldsymbol{r})\rangle=\hat{H}(\boldsymbol{r})|\Phi(\boldsymbol{r})\rangle \tag{5.25}$$

and use the expansion

$$|\Phi(\boldsymbol{r})\rangle=\sum_{i=1}^{3}\Phi_i(\boldsymbol{r})|i\rangle. \tag{5.26}$$

Here $|i\rangle$ are the bare atomic states featured in the definition of $\hat{H}_0$ in Eq. (5.18). To account for the interaction between the atoms, we use the Gross–Pitaevskii approach for the multicomponent BECs [167]. In practice, this amounts to supplementing the Schrödinger equations for $\Phi_i(\boldsymbol{r})$ with the nonlinear terms, thereby promoting the single-particle wave functions to the wave functions of the components of the condensate [202]. This way we arrive at

$$\begin{aligned}
\mathrm{i}\hbar\frac{\partial}{\partial t}\Phi_1&=\left(-\frac{\hbar^2}{2m}\Delta+V+g_{11}|\Phi_1|^2+g_{12}|\Phi_2|^2\right)\Phi_1+\hbar\Omega_1^*\Phi_3,\\
\mathrm{i}\hbar\frac{\partial}{\partial t}\Phi_2&=\left(-\frac{\hbar^2}{2m}\Delta+V+g_{12}|\Phi_1|^2+g_{22}|\Phi_2|^2\right)\Phi_2+\hbar\Omega_2^*\Phi_3,\\
\mathrm{i}\hbar\frac{\partial}{\partial t}\Phi_3&=\left(-\frac{\hbar^2}{2m}\Delta+V-\delta-\mathrm{i}\frac{\Gamma}{2}\right)\Phi_3+\hbar\Omega_1\Phi_1+\hbar\Omega_2\Phi_2.
\end{aligned} \tag{5.27}$$

For atoms adiabatically following the dark state, the population of the excited state $|3\rangle$ described by the wave function Φ_3 is small at all times, so atom collisions are not taken into account in the equation for Φ_3. The coefficients g_{ij} describing interaction between the atoms in the corresponding internal states are related to the s-wave scattering lengths a_{ij} as $g_{ij}=4\pi\hbar^2a_{ij}/m$. The multicomponent wave function of the BEC is normalised to the total number of atoms, $\sum_{i=1}^{3}\int|\Phi_i|^2\,\mathrm{d}^3r=N$. We will also use parameters η_i to quantify the relative population of each component:

$$\eta_i=\frac{1}{N}\int|\Phi_i|^2\,\mathrm{d}^3r. \tag{5.28}$$

We remark that the system of equations (5.27) can alternatively be derived starting from the Heisenberg equations $\mathrm{i}\hbar\frac{\partial}{\partial t}\hat{\Phi}_i(\boldsymbol{r},t) = [\hat{\Phi}_i(\boldsymbol{r},t), \hat{\mathcal{H}}]$ for the field operators $\hat{\Phi}_i(\boldsymbol{r},t)$ in the Heisenberg picture (with $\hat{\mathcal{H}}$ being the second-quantised Hamiltonian containing the two-body interaction term) and replacing $\hat{\Phi}_i(\boldsymbol{r},t)$ with $\Phi_i(\boldsymbol{r},t)$ in the final expressions [167].

To obtain an equation for the evolution of atoms adiabatically following the dark state, we introduce the following superpositions of Φ_1 and Φ_2 describing the wave functions for atoms in the dark and bright states introduced in the previous Section 5.1.1:

$$\begin{aligned}\Phi_{\mathrm{D}} &= \frac{1}{\sqrt{1+|\zeta|^2}}(\Phi_1 - \zeta^*\Phi_2),\\ \Phi_{\mathrm{B}} &= \frac{1}{\sqrt{1+|\zeta|^2}}(\zeta\Phi_1 + \Phi_2).\end{aligned} \tag{5.29}$$

Inserting these definitions into Eq. (5.27), we obtain a set of equations for Φ_{D}, Φ_{B} and Φ_3, in which the dark-state and bright-state wave functions Φ_{D} and Φ_{B} are coupled via non-adiabatic terms. Under the adiabatic assumption of slow centre-of-mass motion for atoms in the dark internal states, justified for the systems to be considered, and the assumption of equal nonlinear couplings ($g_{11} = g_{12} = g_{22} = g$), we reach the dark-state GPE [202]

$$\mathrm{i}\hbar\frac{\partial}{\partial t}\Phi_{\mathrm{D}} = \frac{1}{2m}(-\mathrm{i}\hbar\nabla - \boldsymbol{A})^2\Phi_{\mathrm{D}} + (U+V)\Phi_{\mathrm{D}} + g|\Phi_{\mathrm{D}}|^2\Phi_{\mathrm{D}}. \tag{5.30}$$

It is worth noting that, although Φ_{D} is the solution to a nonlinear mean-field equation for a BEC, the term 'dark-state wave function' remains appropriate. This state contains no atoms in the internal state $|3\rangle$, and, provided the adiabatic approximation holds, this remains true at all times, since the equation for Φ_{D} is fully decoupled from those for Φ_{B} and Φ_3. In contrast, the equation for the 'bright-state BEC' Φ_{B} is coupled to Φ_3, allowing atoms in Φ_{B} to transition into $|3\rangle$ and decay.

Reduction to the dark-state manifold results in the appearance of geometric vector and scalar potentials $\boldsymbol{A}(\boldsymbol{r})$ and $U(\boldsymbol{r})$ in the dynamical equation (5.30), emerging due to the position-dependence of the atom–light coupling. They are given by [203, 202, 120]

$$\begin{aligned}\boldsymbol{A}(\boldsymbol{r}) &= \mathrm{i}\hbar\,\langle \mathrm{D}(\boldsymbol{r})|\nabla\mathrm{D}(\boldsymbol{r})\rangle\,,\\ U(\boldsymbol{r}) &= \frac{\hbar^2}{2m}\left(\langle\nabla\mathrm{D}(\boldsymbol{r})|\nabla\mathrm{D}(\boldsymbol{r})\rangle + \langle \mathrm{D}(\boldsymbol{r})|\nabla\mathrm{D}(\boldsymbol{r})\rangle^2\right).\end{aligned} \tag{5.31}$$

For the beams given by Eq. (5.16) the geometric gauge potentials do not depend

on z and read

$$\begin{aligned} \boldsymbol{A} &= -\frac{\hbar s}{a}\frac{\left(\frac{\rho}{a}\right)^{2s-1}}{1+\left(\frac{\rho}{a}\right)^{2s}}\boldsymbol{e}_{\varphi}, \\ U &= \frac{1}{m}\left(\frac{\hbar s}{a}\right)^{2}\frac{\left(\frac{\rho}{a}\right)^{2s-2}}{\left[1+\left(\frac{\rho}{a}\right)^{2s}\right]^{2}}. \end{aligned} \tag{5.32}$$

The artificial magnetic field resulting from the geometric potential $\boldsymbol{A}$ is

$$\boldsymbol{B} = \nabla \times \boldsymbol{A} = -\frac{2m}{\hbar}U\boldsymbol{e}_{z}. \tag{5.33}$$

In the present configuration, the effective magnetic field is thus proportional to the scalar potential.

As already noted, the dark state $|\mathrm{D}(\boldsymbol{r})\rangle$ depends on the coordinate as a parameter, and the base manifold $M \ni \boldsymbol{r}$ of the relevant U(1) fibre bundle is the 3D Euclidean space. However, we will be considering systems of finite spatial extent, namely, those confined in a cylinder. Therefore, M is a solid cylinder, which is contractible, and hence the fibre bundle in question is trivial [120]. This ensures that there exists a single globally well-defined state $|\mathrm{D}(\boldsymbol{r})\rangle$ (representing a *section* of the bundle) and globally well-defined connection $\boldsymbol{A}$, as explicitly exhibited in Eqs. (5.23) and (5.32), respectively.

Once a solution of Eq. (5.30) is found, one can return to the wave functions Φ_1 and Φ_2 of the internal-state basis according to

$$\begin{aligned} \Phi_1 &= \frac{1}{\sqrt{1+|\zeta|^2}}\Phi_{\mathrm{D}}, \\ \Phi_2 &= -\frac{\zeta}{\sqrt{1+|\zeta|^2}}\Phi_{\mathrm{D}}. \end{aligned} \tag{5.34}$$

This follows from Eq. (5.29) with $\Phi_{\mathrm{B}} = 0$, since for adiabatic atomic motion in the dark state, described by Eq. (5.30), the system is almost completely in the dark state with a negligible population of the bright and excited states.

In this way, when the atoms forming the BEC are in the dark state, the components Φ_1 and Φ_2 are related to each other via Eq. (5.34), in which the component Φ_2 has an extra factor $\zeta = \Omega_1/\Omega_2$. This factor is proportional to $\mathrm{e}^{\mathrm{i}s\varphi}$, as the Rabi frequency Ω_1 has a vortex with a winding number s. As a result, at least one of the components Φ_1 or Φ_2 should have a vortex when the BEC atoms are in the dark state. Explicitly, inserting the wave functions (5.34) into the state vector (5.26), taking $\Phi_3 = 0$, and using the notation of

Eq. (5.23) we find the expression for the full system state vector

$$|\Phi(\boldsymbol{r},t)\rangle = \Phi_{\mathrm{D}}(\boldsymbol{r},t)|\mathrm{D}(\boldsymbol{r})\rangle. \tag{5.35}$$

In the following, we will focus on the stationary solutions of the form $\Phi(\boldsymbol{r},t) = f(\rho)\mathrm{e}^{\mathrm{i}\ell\varphi}\mathrm{e}^{-\mathrm{i}\mu t/\hbar}$, where μ is the chemical potential of the system. Therefore, the stationary dark state is described by

$$|\Phi(\boldsymbol{r})\rangle = f(\rho)\left(\mathrm{e}^{\mathrm{i}\ell_1\varphi}\cos\frac{\alpha(\rho)}{2}|1\rangle - \mathrm{e}^{\mathrm{i}\ell_2\varphi}\sin\frac{\alpha(\rho)}{2}|2\rangle\right), \tag{5.36}$$

where we introduced the vorticities of the two components according to $\ell_1 = \ell$ and $\ell_2 = \ell + s$. The obtained state has precisely the form of the order parameter (5.9) hosting a coreless vortex, which is now generalised to both components having vortex factors. However, as already noted, the function $\alpha(\rho)$ is fixed externally by the choice of the coupling beams, therefore, the populations of the components cannot change in the course of the evolution (as long as the system remains in the dark state). This leads to the stability of the vortex structures to be discussed, which are thus stabilised by the external driving.

5.1.3 Trap geometry and parameter values

As the geometric vector and scalar potentials $\boldsymbol{A}$ and U of Eq. (5.32), corresponding to the light beams (5.16), do not depend on z, we can consider the two-dimensional motion of dark-state atoms in the xy plane for fixed z. Specifically, for a cylindrically symmetric setup of interest, in the dark-state GPE (5.30) we can separate the variables as $\Phi_{\mathrm{D}}(\rho,\varphi,z,t) = \Phi_{\mathrm{D}}^{(2)}(\rho,\varphi,t)Z(z)$ and take $Z(z) = 1/\sqrt{d}$, thereby using the Thomas–Fermi approximation for the atomic motion in the z-direction extended over the distance d. The resulting equation for $\Phi_{\mathrm{D}}^{(2)}(\rho,\varphi,t)$ has the same form as Eq. (5.30) but the interaction strength changes as $g \to g/d$. A similar procedure can be performed for the exact system (5.27), yielding accurate results in the adiabatic regime.

In our numerical simulations we consider a BEC cloud of $N = 5\times10^4$ atoms confined in a cylindrical trap [213] of the radius R and the extent d along the z-axis with $R = d = 15.0\,\mu\mathrm{m}$. The states $|1\rangle$ and $|2\rangle$ are taken to be two hyperfine levels of ^{87}Rb: $|1\rangle = |F=1, m_F=-1\rangle$ and $|2\rangle = |F=2, m_F=1\rangle$, while state $|3\rangle$ is the $5\,^2\mathrm{P}_{\frac{3}{2}}$ state, whose decay rate is $\Gamma = 38.1\,\mathrm{MHz}$ [214]. The scattering lengths are [215]: $a_{11} = 100a_0$, $a_{12} = 98.0a_0$, $a_{22} = 95.4a_0$, where a_0 is the Bohr radius. The assumption of equal scattering lengths, used in deriving the dark-state GPE, is thus justified for this system.

The typical values of the Rabi frequencies used in Λ-scheme experiments range from $\sim 10\,\mathrm{MHz}$ to $\sim 1\,\mathrm{GHz}$. Our calculations show that the dark-state

GPE yields very accurate results [compared to the solution of the full system of GPEs (5.27)] already at $\Omega_0 = 1\,\mathrm{MHz}$, meaning that the lowest states of the dark-state manifold indeed become effectively decoupled from the states of the $|\pm\rangle$ manifolds. Generally, the non-adiabatic coupling may be disregarded provided $U/\hbar \ll \Omega(\boldsymbol{r})$ for all $\boldsymbol{r}$ [202, 203, 195], where $\Omega \equiv \Omega(\boldsymbol{r})$ is the total Rabi frequency given by Eq. (5.22). For $s = 1$, the maximum of U is located at the origin, while Ω attains its minimal value there (we neglect the beam-waist term $\mathrm{e}^{-\rho^2/w_0^2}$ in the present reasoning), equal to $\Omega(\boldsymbol{r} = 0) = \Omega_0$. However, even for the lowest value of a considered in this work ($a = 0.3\,\mu\mathrm{m}$), one finds $U/\hbar = 8\,\mathrm{kHz}$, which is orders of magnitude smaller than the typical value of Ω_0. Furthermore, although generally including the decay rate of $|3\rangle$ improves the validity of the dark-state description [195, 204, 196], in the regime in question we obtained equally accurate results even for $\Gamma = 0$ — again because Ω_0 is very large compared to U. Finally, we mention the effect of the detuning δ. Non-zero positive values of δ shift the manifold of the $|-\rangle$ states down in energy, further reducing the coupling with the states of the $|\mathrm{D}\rangle$ manifold. On the other hand, the states of the $|+\rangle$ manifold are then also shifted to lower energies, and this enhances the coupling with the $|\mathrm{D}\rangle$-manifold states. Thus, the dark-state GPE is expected to be valid for some intermediate values of δ. For example, we have found that for $\Omega_0 \sim 10\,\mathrm{MHz}$, values of δ from 0 to up to $\sim 10\Omega_0/a^s$ lead to good agreement between the dark-state analysis and the full treatment. Meanwhile, negative values of δ shift to higher energies the manifold of $|-\rangle$ states. This facilitates coupling between the $|-\rangle$ and $|\mathrm{D}\rangle$ states, reducing the accuracy of the dark-state description.

In all our calculations we used $\Omega_0 = 20.0\,\mathrm{MHz}$ and $\delta = 10\Omega_0/a^s$, where the parameter a characterises the Rabi frequency of the vortex light beam in Eq. (5.16). The beam-waist term $\mathrm{e}^{-\rho^2/w_0^2}$ can be set to unity assuming the waist is much larger than the radial extent of the cloud. Moreover, the term $\mathrm{e}^{-\rho^2/w_0^2}$ plays no role in the adiabatic dynamics of atoms in the dark state, since it drops out of the relative Rabi frequency ζ given by Eq. (5.20). However, we did include this term in the exact numerical calculations by setting $w_0 = 2R$ — while the results were the same, this provided a slight speed-up for the calculations.

Henceforth we adopt the dimensionless units, measuring length in units of R, energy in units of kinetic energy $E_R = \hbar^2/2mR^2$ corresponding to the momentum $k_R = 1/R$, and time in units of $\hbar/E_R$. In these units the radial coordinate ρ varies from 0 to 1. We refer the reader to Appendix 5A for additional details on the units and the dimensionless form of the equations used for numerical calculations.

5.2 Stationary vortex solutions

5.2.1 Approximate analysis of motion of dark-state atoms

To gain physical insight into the expected structure of the possible stationary states of the system undergoing the 2D motion, it is instructive to consider the dark-state GPE (5.30) first. To find stationary solutions, we put $\Phi_{\mathrm{D}}(\boldsymbol{r},t) = \mathrm{e}^{-\mathrm{i}\mu t}\psi(\boldsymbol{r})$ and further separate the variables due to the cylindrical symmetry of the system:

$$\psi(\rho,\varphi) = f(\rho)\mathrm{e}^{\mathrm{i}\ell\varphi} \tag{5.37}$$

with $f(\rho)$ being real and ℓ being integer. In the specific case of the geometric potentials given in Eq. (5.32), this leads to the equation of the Bessel type (with an additional nonlinear term):

$$\rho^2\partial_\rho^2 f + \rho\partial_\rho f + [(\mu - U - gf^2)\rho^2 - (\ell - \rho A_\varphi)^2]f = 0. \tag{5.38}$$

Here the external trapping potential term is not written explicitly, but it controls the boundary conditions: $f(1) = 0$.

To allow for an analytical treatment, in the following Sections 5.2.1.1 and 5.2.1.2 we will neglect the interaction term by setting $g = 0$. Our numerical calculations confirm that the conclusions obtained regarding the value of ℓ of the ground-state wave function remain valid in the presence of interactions. We will analyse two limiting regimes for the solutions of Eq. (5.38) with $g = 0$. The regimes are defined by the distance a describing the extent of the geometric scalar potential U and the effective magnetic field $\boldsymbol{B}$ given by Eqs. (5.32)–(5.33).

5.2.1.1 Large a

First, we consider the case when the distance a is large compared to the system radius R, so that $\rho \ll a$. Then, according to Eq. (5.32), for $\ell \neq 0$ one can neglect the term $\rho A_\varphi \approx -(\rho/a)^{2s}\, s$ in comparison with ℓ in Eq. (5.38), whereas for $\ell = 0$ this term may be disregarded because $A_\varphi^2 \ll \mu$. In a similar way, the geometric scalar potential U is small in comparison with μ and thus can also be neglected. In such a situation, the solutions satisfying the boundary condition are the properly scaled Bessel functions of the first kind J_ℓ. From the sequence of zeros of J_ℓ we find that the ground state corresponds to $\ell = 0$, and the degenerate pair of the lowest excited states corresponds to $\ell = \pm 1$. Explicitly, the chemical potential $\mu^{(\ell)}$ (the eigenenergy) of the ground state is given by $\mu^{(0)} = (j_{0,1})^2$, where $j_{\ell,n}$ is the nth root of the Bessel function $J_\ell(x)$. The corresponding wave function $\psi^{(\ell)}$ is given by $\psi^{(0)}(\rho,\varphi) = f^{(0)}(\rho) = CJ_0(\rho j_{0,1})$,

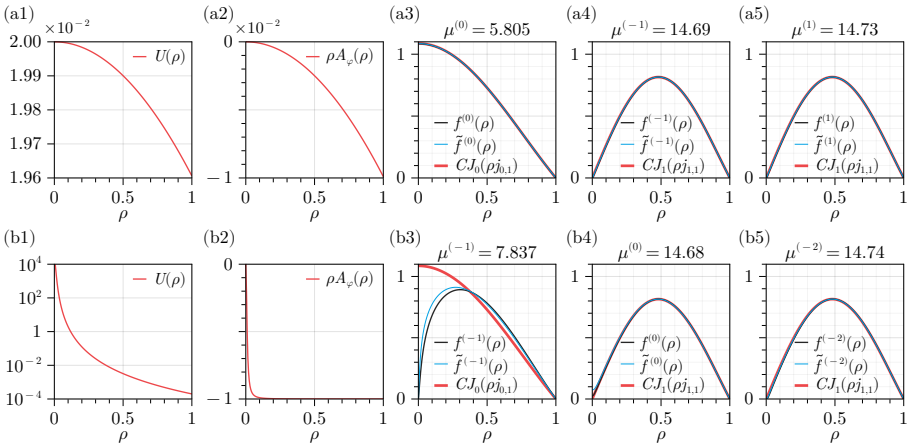

Figure 5.4: The potentials U, ρA_φ and the solutions of Eq. (5.38). Panels (a1)–(a5) show, respectively, the curves U, ρA_φ, and three solutions of Eq. (5.38) (with $g = 0$) for $s = 1$ and $a = 10$. In panels (a3)–(a5), curves $\tilde{f}^{(\ell)}(\rho)$ depict the solution obtained under an additional assumption $U = 0$. Panels (b1)–(b5) show the same as panels (a1)–(a5) for $s = 1$ and $a = 0.01$. The depicted wave functions are normalised such that $\int_S |\psi^{(\ell)}(\rho, \varphi)|^2 \mathrm{d}S = 2\pi \int_0^1 [f^{(\ell)}(\rho)]^2 \rho \, \mathrm{d}\rho = 1$.

with C being a normalisation constant.

These findings are illustrated in Figs. 5.4(a1)–(a5), corresponding to $a = 10$, $s = 1$. Figures 5.4(a1)–(a2) display the curves of $U(\rho)$ and $\rho A_\varphi(\rho)$. It is apparent that the two functions are low in magnitude compared to the chemical potential and can be disregarded as noted above. Indeed, numerically solving Eq. (5.38) (with U and ρA_φ included) we find that the chemical potential of the ground state is $\mu^{(0)} = 5.805$, close to the limiting value $(j_{0,1})^2 \approx 5.783$. The solution $f^{(0)}(\rho)$ also matches the limiting solution $J_0(\rho j_{0,1})$, as shown in Fig. 5.4(a3). The blue curve additionally shows the solution $\tilde{f}^{(0)}(\rho)$ obtained from Eq. (5.38) with U disregarded, confirming that the scalar potential has almost no impact on the solution. Finally, Figs. 5.4(a4)–(a5) display the excited states corresponding to $\ell = \pm 1$; the degeneracy is slightly lifted by the ρA_φ term.

To draw conclusions regarding the motion of atoms, we have to return to the wave functions of the two components given in Eq. (5.34). Substituting the ground state solution $\Phi_\mathrm{D}^{(0)} = \mathrm{e}^{-\mathrm{i}\mu t}\psi^{(0)}$, we find that in the ground state, $\Phi_1^{(0)}$ is vortex-free and is localised near the origin (with a maximum at $\rho = 0$), while $\Phi_2^{(0)}$ describes a vortex having zero density at the origin and rotating around the first component with vorticity equal to $\ell_2 = \ell + s = +1$. It should be noted that, according to Eq. (5.34), the vorticities of the components always differ by s units. Therefore, at least one of the two components will necessarily be in a vortex state as long as the spatial part of Φ_D is of the form (5.37). As we have

just demonstrated, even if $\ell = 0$, then Φ_1 is vortex-free, while Φ_2 has vorticity equal to s.

5.2.1.2 Small a

Now let us consider the case when the distance a is small compared to the system radius, $a \ll R$. In that case, one has $\rho \gg a$ for most of the area occupied by the condensate, except for a small area close to the centre, $\rho \lessapprox a$ in which the geometric scalar and vector potentials are concentrated. For $\rho \gg a$, it follows from Eq. (5.32) that $\rho A_\varphi(\rho) \to -s$. The ground-state solution can be found by choosing ℓ such that $\ell + s = 0$; the solution will again be given by J_0. Thus, for $\rho \gg a$ the ground state wave function is given by $\psi^{(-s)}(\rho, \varphi) = CJ_0(\rho j_{0,1})\mathrm{e}^{-\mathrm{i}s\varphi}$. However, close to the origin, where $\rho \lessapprox a$, the radial part of the solution will have a different form. Indeed, ℓ is now fixed to $-s$, and we can neglect the term ρA_φ. The solution in the region $\rho \ll a$ is then given by J_s, attaining a zero at the origin as a vortex solution should. Meanwhile, the two lowest excited states will come in a degenerate pair having the radial dependence J_1 in the region $\rho \gg a$ and corresponding to $\ell + s = \pm 1$. Close to the origin ($\rho \ll a$), they will have the radial dependencies $J_{\pm 1-s}$. These results are illustrated in Figs. 5.4(b1)–(b5) for the case where $a = 0.01$, $s = 1$. In Fig. 5.4(b1), it is apparent that the maximum value of U greatly exceeds that of the chemical potential. However, the presence of the potential does not appreciably influence the resulting wave functions due to the potential being localised at the origin. Figure 5.4(b2) displays the curve ρA_φ, which has a value close to $s = -1$ in most of space occupied by the condensate. In agreement with the preceding arguments, the state with the lowest chemical potential is obtained for $\ell = -1$ [see Fig. 5.4(b3)]. Away from the origin, the wave function tends to J_0, while at the origin it attains a zero. Further reducing a increases the steepness of the wave function near the origin and enhances the match with J_0 (not shown). The degenerate pair of the lowest excited states is shown in Figs. 5.4(b4)–(b5). These wave functions mostly follow the shape of J_1 except for the small portion of space near the origin where the condition $\rho \gg a$ no longer holds. There, the state with $\ell = +1 - s = 0$ has the form of a J_0 function, while the $\ell = -1 - s = -2$ state has the shape of J_2.

Thus, if parameter a is small enough so that the condition $\rho \gg a$ holds in most of space occupied by the condensate, the dark-state solution of the lowest energy will be the one corresponding to $\ell = -s$. In this limit the gradient of the phase ϕ of wave function equals $-\boldsymbol{e}_\varphi s/\rho$, thereby canceling the contribution of vector potential $\boldsymbol{A}$ to the velocity field: $\boldsymbol{v} \propto \nabla\phi - \boldsymbol{A} \to 0$. As a result, Φ_1 will be in a vortex state, while Φ_2 will be vortex-free.

5.2.2 Full treatment

We will now turn to the solutions of the full coupled GPEs (5.27), including the atom–atom interactions, and study the structure of the lowest-energy states of the dark-state manifold. To obtain the numerical solutions, we employed the method of imaginary-time evolution: one makes a change $t \to -\mathrm{i}\tau$ and propagates the equations in time τ until convergence is reached, starting from a certain trial wave function. The algorithm will then converge to the lowest-energy state provided it has nonzero overlap with the trial wave function. To enable convergence to the states of the dark-state manifold, we used the solution of Eq. (5.30) as the trial function for solving coupled GPEs (5.27). In turn, the trial wave functions required to solve Eq. (5.30) were constructed by solving this equation using the Thomas–Fermi approximation and multiplying the solution by a phase factor $\mathrm{e}^{\mathrm{i}\ell\varphi}$ with a chosen value of ℓ. Since states of the form (5.37) with different ℓ are orthogonal, the trial wave function of this form converges to a state with the same value of ℓ. This allowed us to obtain stationary solutions of different vorticities. The ground state can then be found by ordering the states based on the value of the energy per particle E. The population of each component was calculated from the obtained solutions rather than being enforced. Additional numerical details are provided in Appendix 5A.

In a stationary state, the wave functions of the components have the form $\Phi_i(\boldsymbol{r}, t) = \mathrm{e}^{-\mathrm{i}\mu t}\psi_i(\boldsymbol{r})$. Below, we show the results obtained using full three-level calculation so as to take into account the different scattering lengths. If they are taken to be equal, then the results match the dark-state calculations based on solving Eq. (5.30) or Eq. (5.38) (the resulting total chemical potentials agree with at least three-digit accuracy).

We start by setting $s = 1$ and $a = 0.5$. Such a value of a corresponds to an intermediate regime whereby the term ρA_φ is not small (compared to unity) and cannot be approximated by $-s$, as one can see in the bottom panel of Fig. 5.5(a). Numerical calculations show that ground state is the one corresponding to an $\ell = 0$ solution of the dark-state GPE (5.30). As noted above, this corresponds to Φ_1 being vortex-free and Φ_2 being in a vortex state. Such a solution is shown in Fig. 5.5(b). It is apparent that the first component fills the core of the second component, a situation known to stabilise vortices with vorticities higher than $\ell = 1$ [89, 88]. Notably, which of the components acquires vorticity is determined by the inequivalent coupling fields Ω_1 and Ω_2 rather than the intrinsic properties of the two states (the scattering lengths). The total density of the BEC, shown in grey in Fig. 5.5(b), indicates that the condensate as a whole does not have a pronounced density dip at the origin, meaning that the core of the vortex is 'completely' filled.

Two lowest excited states are shown in Figs. 5.5(c)–(d). Their energies

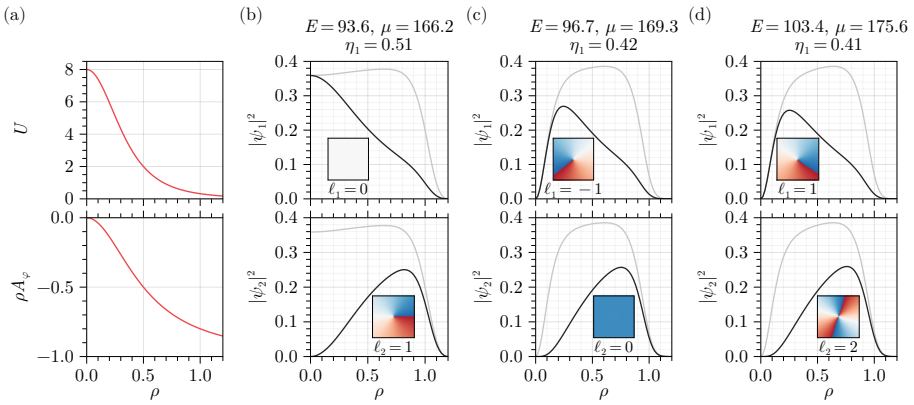

Figure 5.5: The potentials U and ρA_φ, as well as the solutions of Eqs. (5.27) for $s = 1$ and $a = 0.5$. (a) Potentials U and ρA_φ. (b), (c), and (d) show, respectively, three lowest-energy solutions of Eqs. (5.27); wave function normalisation is $\sum_{i=1}^{3} \int_S |\psi_i|^2 \, \mathrm{d}S = 1$. The black lines in the top and bottom panels show, respectively, the radial cuts of the densities $|\psi_1|^2$ and $|\psi_2|^2$ of the first and the second component. The grey lines show the total density. The values of the density of the third component are vanishingly small in all cases (calculation yields values no larger than 10^{-7}) and are therefore not shown. For the same reason, the relative occupation of the second component can be taken to be $\eta_2 = 1 - \eta_1$. The vorticities ℓ_i of the two components are displayed together with the insets showing the two-dimensional phase profiles in the xy-plane. The value of the phase is colour-coded as follows: dark blue $= -\pi$, white $= 0$, dark red $= \pi$.

per particle are 96.7 and 103.4 units, respectively, showing that the term ρA_φ has lifted the degeneracy. Notably, the 'interaction potentials' $g_{ij}|\Phi_k|^2$ do not depend on the vorticities of the components and, therefore, do not lift the degeneracy. In the first excited state, the first component is in a vortex state, rotating in the direction opposite to the direction of the vector field $\boldsymbol{A}$, while the second component is vortex-free. The vortex on the first component mostly occupies the space at the centre of the second component. Such an approximate phase separation is in line with the criterion $g_{12}^2 > g_{11}g_{22}$ [216, 217] that, however, does not take into account the kinetic energy [218], which is especially important in the present setting. In the second excited state, vorticities of the two components are given by $\ell_1 = 1$ and $\ell_2 = 2$, while the spatial profiles are almost the same as those of the respective components of the first excited state. In both cases, the components contribute to a nearly uniform total density of the cloud in the bulk.

Let us now study the regime where the distance a is much smaller that the system radius R, namely, $a = 0.02$. In this case the condition $\rho \gg a$ holds in most of the space, and ρA_φ tends to $-s$ already in the vicinity of the origin [see Fig. 5.6(a), bottom panel]. The ground state now corresponds to the $\ell = -s = -1$ solution of the dark-state GPE (5.30). This means that Φ_1

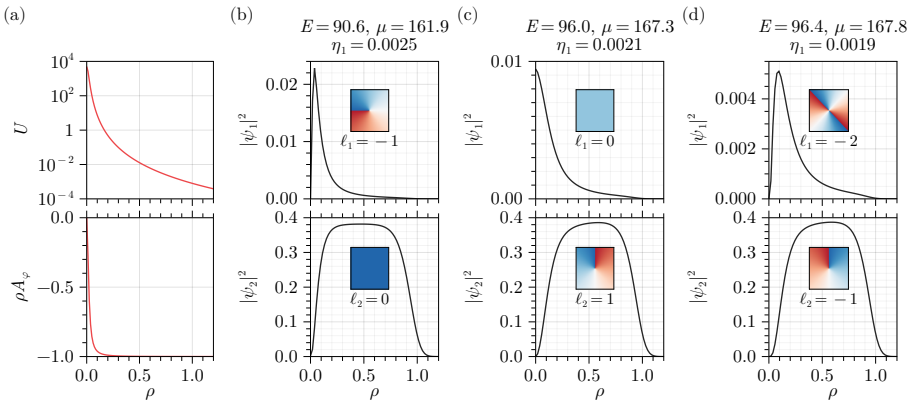

Figure 5.6: Same as Fig. 5.5 for $s = 1$ and $a = 0.02$. The total densities are not explicitly shown since they would appear to largely coincide with $|\psi_2|^2$ due to the highly imbalanced occupation of the two components.

is a vortex state, and it occupies a small region of space near the origin [see Fig. 5.6(b)]. Specifically, the density of the first component is concentrated in a region of the order of the healing length ξ_2 of the second component. Assuming all atoms are in the second component, we have (in dimensionless units) $\xi_2 = \sqrt{S/g_{22}} = 0.086$, where we approximately took $S = \pi$ for the occupied area. The localised nature of the vortex results from the $\frac{1}{\sqrt{1+|\zeta|^2}}$ term in the expression for Φ_1 (5.34), which effectively cuts the vortex off when $\rho \gg a$. Another consequence is the small resulting population of the first component, which in the present case is $\eta_1 = 0.25\%$. Thus, decreasing the a parameter localises the vortex more tightly, but also reduces the population of the first component. The second component occupies the space surrounding the first component and has zero vorticity.

The first excited state, on the other hand, has the typical structure whereby the non-rotating component fills the core of the rotating one [see Fig. 5.6(c)]. The almost-degenerate partner of this state is shown in Fig. 5.6(d). These two states correspond, respectively, to the $\ell = 0$ and $\ell = -2$ solutions of the dark-state GPE (5.30). The degeneracy results from the fact that the kinetic energy is the same, whether the cloud does not rotate ($\ell = 0$) or rotates in the direction opposite to the $\boldsymbol{A}$ field but with twice the speed ($\ell = -2$).

Localised vortices with vorticities higher than one can be analogously created by using beams with $s > 1$. The results for the case $s = 2$ are presented in Fig. 5.7. Choosing $a = 0.1$ already yields the potential ρA_φ tending to $-s$ in most of space [see Fig. 5.7(a)]. This leads to a ground state with the first component having vorticity $\ell_1 = -2$ and the second being vortex-free: $\ell_2 = \ell_1 + s = 0$. The vortex has a density maximum farther from origin com-

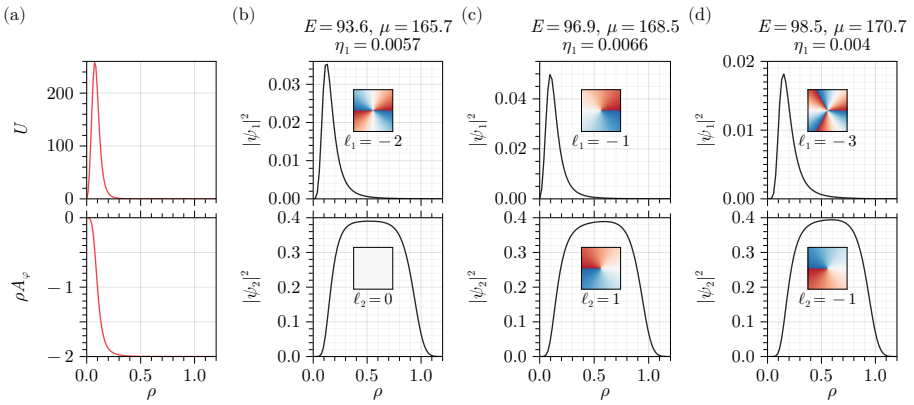

Figure 5.7: Same as Fig. 5.6 for $s = 2$ and $a = 0.1$.

pared to the $\ell_1 = -1$ vortex in Fig. 5.6(b) due, in part, to the former having the form of J_2 and thus rising less sharply compared to J_1. The degree of localisation can be increased by reducing a, but the number of atoms in the vortex component will then decrease. The lowest excited states [see Figs. 5.7(c)–(d)] also contain localised vortices in the first component.

It is worth noting that the density profiles of both components remain essentially unchanged as g_{12} is reduced into the miscible regime, $g_{12}^2 < g_{11}g_{22}$, provided the coupling constants g_{ij} are of similar magnitude. In particular, the densities shown in Figs. 5.6(b) and 5.7(b) remain virtually unaffected. This invariance is expected, as the localised-vortex configuration is sustained by the external laser beams rather than particle interactions, as demonstrated in Section 5.2.1, where interactions are entirely neglected.

5.3 Moving the vortex

To demonstrate the stability of the localised lowest-energy vortex states and show the high level of available control, we consider changing the position of the vortex by moving the laser beams. A similar protocol has been considered in [219], however, that work considered moving a vortex created by a phase-imprinting technique. Our approach is more robust because the laser beams create a pinned vortex which cannot break free.

We focus on the regime $s = 1$, $a = 0.02$ studied in Fig. 5.6 but this time consider an off-axis vortex created by centring the laser beams at $(x, y) = (0.5, 0)$. Once the state is prepared, the transverse profiles of the laser beams Ω_1 and Ω_2 start moving counterclockwise on a circular path around the origin at a constant tangential speed v. Figure 5.8 shows the wave functions obtained after completing one full circle. In Fig. 5.8(a) corresponding to $v_1 = 150\,\mu$m/s

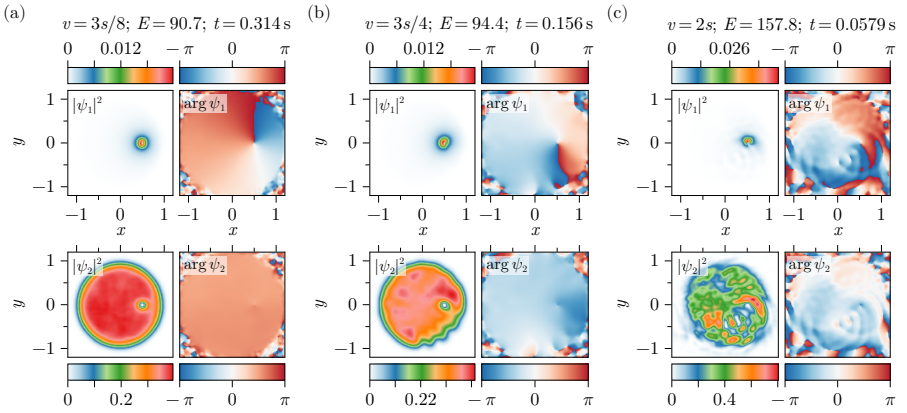

Figure 5.8: Wave functions of components 1 and 2 after completing one circular sweep of the laser beams around the origin. The tangential beam movement speed is (a) $v_1 = 3v_s/8 = 150\,\mu$m/s, (b) $v_2 = 3v_s/4 = 300\,\mu$m/s, and (c) $v_3 = 2v_s = 800\,\mu$m/s. In all three cases the relative population of the first component is $\eta_1 \approx 0.0025$, while the third component is essentially unpopulated.

(time to complete the circle is $t = 0.314\,\mathrm{s}$), it is apparent that the vortex of the first component has retained its structure, and the density of the second component has not been strongly distorted. The value of E has increased by only 3% of the energy (per particle) gap between the ground state and the first excited one. Here the velocity is chosen to be lower than the speed of sound in the second component, which equals to $v_s = \hbar/(m\xi_2\sqrt{2}) = 400\,\mu$m/s. Moving the vortex at twice the speed, $v_2 = 2v_1$, results in setting the whole of the second component in circular motion. The distortion of the density is apparent in Fig. 5.8(b).

Finally, the case of supersonic movement is studied in Fig. 5.8(c) corresponding to the movement speed $v_3 = 2v_s$. The density profiles of both components are strongly distorted and the energy is increased 1.5 times. Nevertheless, the first component retains its signature phase profile, and no additional vortices are created in the second component in the process. Let us stress that in all three cases, the third component remained essentially unpopulated, and the total norm of the wave functions was conserved on the level of the numerical accuracy used, meaning that, in practice, no loss of atoms took place.

It is also instructive to use the localised vortex in the first component as a probe for the critical superfluid velocity v_c of the second component. In this case, the vortex acts as an impurity that can move without resistance provided its speed remains below v_c. According to Landau's criterion, the phononic excitation spectrum of the condensate sets the critical velocity equal to the sound velocity [168]. However, both experimental results [91, 92, 94, 95] and detailed theoretical studies [96–98] indicate that v_c is typically lower,

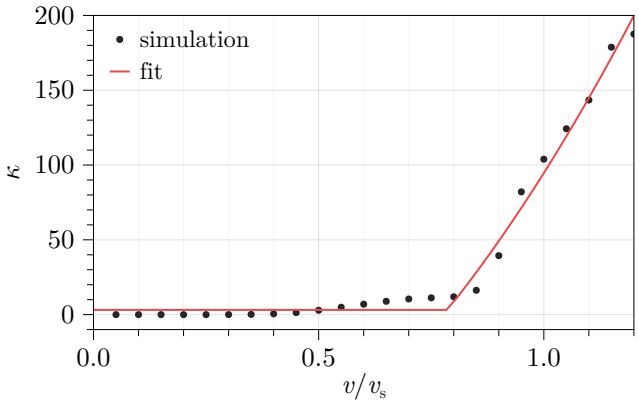

Figure 5.9: Condensate heating rate as a function of the movement speed of the beams.

depending on factors such as impurity size [94], the nature of the impurity potential (attractive or repulsive) [96], and the impurity trajectory (linear or circular) [96, 98]. To measure v_c in our system, we repeat the circular trajectory simulations, moving the beams for a fixed duration of 0.1 s. We monitor the total energy per particle, $E(t)$, and fit it with a linear function to obtain the heating rate $\kappa = \mathrm{d}E/\mathrm{d}t$. Since the first component's population is much smaller than that of the second, $E(t)$ primarily reflects the energy of the atoms in the second component. The results for velocities from $0.1v_s$ to $1.2v_s$ are shown in Fig. 5.9, revealing a clear threshold behaviour where κ increases rapidly once the velocity exceeds a certain value.

We quantify this threshold by fitting the data to

$$\kappa(v) = \kappa_0 + b \max(v^2 - v_c^2, 0), \tag{5.39}$$

where κ_0, b, and v_c are fit parameters. This form is suitable for 2D systems [93] and has proven effective in experimental analyses [94, 97]. The least-squares fit shown in Fig. 5.9 yields $v_c = 0.8v_s$, which is lower than the sound velocity, consistent with the above observations. The precise dissipation mechanisms, however, warrant further study.

5.4 Conclusions

In summary, we have studied the interaction of a two-component BEC mixture with the light fields in a Λ-type configuration and investigated the stationary states of the dark-state manifold. The angular momentum of $s\hbar$ per photon carried by one of the two fields leads to either one or both components being in a vortex state, with their vorticities differing by s units. In the regime $a \ll R$, the structure of the stationary states is dictated by the vector potential term. In this limit, $\boldsymbol{A}$ tends to $-\frac{s}{\rho}\boldsymbol{e}_\varphi$ and its contribution to the velocity field (and hence to the kinetic energy) can be cancelled if the dark state is described by a wave function $f(\rho)\mathrm{e}^{-\mathrm{i}s\varphi}$. We have demonstrated that the lowest-energy state of the dark-state manifold indeed has this form. In this case, the first component (the one interacting with the LG beam) contains a vortex of vorticity s, while the second component is vortex-free. The core of the former vortex coincides with the centre of the beams, while the density profile of the vortex demonstrates a strong degree of localisation as the density falls off as $[1+(\rho/a)^2]^{-1/2}$ away from the vortex core. Such a vortex can be moved around the trap by moving the laser beams. Provided the movement speed is less than approximately half the speed of sound in the second component, the shape of the vortex retains its structure during the movement, and the density of the second component does not get distorted. More specifically, moving the vortex at a speed below the critical value of about $0.8v_\mathrm{s}$ causes almost no heating of the condensate, indicating its superfluid nature.

5.5 Appendix 5A: Dimensionless units and numerical details

For our numerical calculations we used dimensionless units, measuring length in units of cylindrical trap radius R, energy in units of $E_R = \hbar^2/2mR^2$, and time in units of $\hbar/E_R$. In these units, the system of equations (5.27) becomes

$$\begin{aligned}
\mathrm{i}\frac{\partial}{\partial t}\Phi_1 &= \left(-\Delta + V + g_{11}|\Phi_1|^2 + g_{12}|\Phi_2|^2\right)\Phi_1 + \Omega_1^*\Phi_3,\\
\mathrm{i}\frac{\partial}{\partial t}\Phi_2 &= \left(-\Delta + V + g_{12}|\Phi_1|^2 + g_{22}|\Phi_2|^2\right)\Phi_2 + \Omega_2^*\Phi_3,\\
\mathrm{i}\frac{\partial}{\partial t}\Phi_3 &= \left(-\Delta + V - \delta - \mathrm{i}\frac{\Gamma}{2}\right)\Phi_3 + \Omega_1\Phi_1 + \Omega_2\Phi_2.
\end{aligned} \tag{5.40}$$

Our calculations were carried out in the dark-state regime, where the amplitudes of Φ_3 were vanishingly small. Consequently, the non-Hermitian nature of the dynamics arising from the imaginary decay term Γ was effectively negligible, allowing us to adopt the conventional normalisation used for Hermitian

systems, $\sum_{i=1}^{3}\int|\Phi_i|^2\,\mathrm{d}^3r=1$ (the sum can equally be taken over Φ_1 and Φ_2 only). Furthermore, the energies and chemical potentials of the stationary states had vanishingly small imaginary parts, implying that the wave function norm remained essentially constant over time. We note that in our numerical calculations, the wave functions were normalised to unity rather than to the total particle number.

We take $R=15.0\,\mu$m and the mass of an ^{87}Rb atom $m=1.443\times10^{-25}\,$kg. The amplitudes of the Rabi frequencies Ω_1 and Ω_2 are expressed in terms of Ω_0 [see Eq. (5.16)] whose value is $\Omega_0=\frac{20.0\,\mathrm{MHz}}{E_R/\hbar}=1.23\times10^7$; the decay rate is $\Gamma=\frac{38.1\,\mathrm{MHz}}{E_R/\hbar}=2.35\times10^7$, and the detuning is $\delta=10\Omega_0/a^s$. The interaction strengths are characterised by $g_{ij}=8\pi a_{ij}N/d$, where division by the cylindrical trap height d appears as a result of reduction to the 2D equations (see Section 5.1.3). We take $d=R$, $N=5\times10^4$, $a_{11}=100a_0$, $a_{12}=98.0a_0$, and $a_{22}=95.4a_0$, where a_0 is the Bohr radius. This results in $g_{11}=443$, $g_{12}=434$, $g_{22}=423$.

The radial profile of the cylindrical trap was modelled by a logistic function

$$V(\rho)=\frac{V_0}{1+V_0\mathrm{e}^{-b(\rho-\rho_0)}} \tag{5.41}$$

with $V_0=1000$, $b=17$, $\rho_0=0.7$, ensuring a steep rise at $\rho\approx1$ [89]. The computational grid contained 129 points in each dimension, spanning the interval $\rho\in[-1.2,1.2]$.

The dark-state GPE in dimensionless units becomes

$$\mathrm{i}\frac{\partial}{\partial t}\Phi_\mathrm{D}=(-\mathrm{i}\nabla-\boldsymbol{A})^2\Phi_\mathrm{D}+(U+V)\Phi_\mathrm{D}+g|\Phi_\mathrm{D}|^2\Phi_\mathrm{D}, \tag{5.42}$$

while the components of the artificial gauge field are given by

$$\begin{aligned}\boldsymbol{A}&=-\frac{s}{a}\frac{\left(\frac{\rho}{a}\right)^{2s-1}}{1+\left(\frac{\rho}{a}\right)^{2s}}\boldsymbol{e}_\varphi,\\ U&=2\left(\frac{s}{a}\right)^2\frac{\left(\frac{\rho}{a}\right)^{2s-2}}{[1+\left(\frac{\rho}{a}\right)^{2s}]^2}.\end{aligned} \tag{5.43}$$

We remind that the dark-state GPE is obtained under the assumption of equal inter- and intracomponent scattering lengths; in our calculations we used $g=g_{11}=443$.

The solutions Φ_D of the dark-state GPE (5.42) were obtained using the imaginary-time evolution algorithm. The trial wave functions were constructed by solving the equation using the Thomas–Fermi approximation and multiplying the solution by a phase factor $\mathrm{e}^{\mathrm{i}\ell\varphi}$ with a chosen value of ℓ. Since states (5.37) with different ℓ's are orthogonal, the trial wave function of this form con-

verges to a state with the same value of ℓ. To solve the GPE system (5.40), we used the following trial functions: Φ_3 was simply set to zero, while Φ_1 and Φ_2 were obtained from the corresponding dark-state solution Φ_D using Eq. (5.34).

The chemical potential was calculated from the stationary solution of the system (5.40) using

$$\mu = \sum_{i,j} \int \Phi_i^* (D_{ij} + F_{ij}) \Phi_j \, \mathrm{d}^2 r \tag{5.44}$$

where

$$\hat{D} = \begin{pmatrix} -\Delta + V & 0 & \Omega_1^* \\ 0 & -\Delta + V & \Omega_2^* \\ \Omega_1 & \Omega_2 & -\Delta + V - \delta - \mathrm{i}\frac{\Gamma}{2} \end{pmatrix} \tag{5.45}$$

and

$$\hat{F} = \begin{pmatrix} g_{11}|\Phi_1|^2 + g_{12}|\Phi_2|^2 & 0 & 0 \\ 0 & g_{12}|\Phi_1|^2 + g_{22}|\Phi_2|^2 & 0 \\ 0 & 0 & 0 \end{pmatrix}. \tag{5.46}$$

Meanwhile, the energy per particle E is given by Eq. (5.44) with $F_{ij} \to \frac{1}{2} F_{ij}$.

Calculations have been performed using the `GPELab` software package [220, 221].

References

[1] F. D. M. Haldane, Nobel Lecture: Topological quantum matter, Rev. Mod. Phys. **89**, 040502 (2017).

[2] G. E. Volovik, *The universe in a helium droplet* (Oxford University Press, 2009).

[3] K. V. Klitzing, G. Dorda and M. Pepper, New method for high-accuracy determination of the fine-structure constant based on quantized Hall resistance, Phys. Rev. Lett. **45**, 494–497 (1980).

[4] D. J. Thouless, M. Kohmoto, M. P. Nightingale and M. den Nijs, Quantized Hall conductance in a two-dimensional periodic potential, Phys. Rev. Lett. **49**, 405–408 (1982).

[5] J. E. Avron, R. Seiler and B. Simon, Homotopy and quantization in condensed matter physics, Phys. Rev. Lett. **51**, 51–53 (1983).

[6] I. Bloch, J. Dalibard and W. Zwerger, Many-body physics with ultracold gases, Rev. Mod. Phys. **80**, 885–964 (2008), arXiv:0704.3011.

[7] T. D. Stanescu, V. Galitski and S. Das Sarma, Topological states in two-dimensional optical lattices, Phys. Rev. A **82**, 013608 (2010), arXiv:0912.3559.

[8] N. Goldman, J. C. Budich and P. Zoller, Topological quantum matter with ultracold gases in optical lattices, Nat. Phys. **12**, 639–645 (2016), arXiv:1607.03902.

[9] R. Dum and M. Olshanii, Gauge structures in atom-laser interaction: Bloch oscillations in a dark lattice, Phys. Rev. Lett. **76**, 1788–1791 (1996).

[10] G. Juzeliūnas and P. Öhberg, Slow light in degenerate Fermi gases, Phys. Rev. Lett. **93**, 033602 (2004), arXiv:cond-mat/0402317.

[11] J. Ruseckas, G. Juzeliūnas, P. Öhberg and M. Fleischhauer, Non-Abelian gauge potentials for ultracold atoms with degenerate dark states, Phys. Rev. Lett. **95**, 010404 (2005), arXiv:cond-mat/0503187.

[12] Y.-J. Lin, R. L. Compton, K. Jiménez-García, J. V. Porto and I. B. Spielman, Synthetic magnetic fields for ultracold neutral atoms, Nature **462**, 628–632 (2009), arXiv:1007.0294.

[13] A. S. Sørensen, E. Demler and M. D. Lukin, Fractional quantum Hall states of atoms in optical lattices, Phys. Rev. Lett. **94**, 086803 (2005), arXiv:cond-mat/0405079.

[14] M. Aidelsburger, M. Atala, M. Lohse, J. T. Barreiro, B. Paredes and I. Bloch, Realization of the Hofstadter Hamiltonian with ultracold atoms in optical lattices, Phys. Rev. Lett. **111**, 185301 (2013), arXiv:1308.0321.

[15] H. Miyake, G. A. Siviloglou, C. J. Kennedy, W. C. Burton and W. Ketterle, Realizing the Harper Hamiltonian with laser-assisted tunneling in optical lattices, Phys. Rev. Lett. **111**, 185302 (2013), arXiv:1308.1431.

[16] M. Aidelsburger, M. Lohse, C. Schweizer, M. Atala, J. T. Barreiro, S. Nascimbène, N. R. Cooper, I. Bloch and N. Goldman, Measuring the Chern number of Hofstadter bands with ultracold bosonic atoms, Nat. Phys. **11**, 162–166 (2015), arXiv:1407.4205.

[17] M. Holthaus, Floquet engineering with quasienergy bands of periodically driven optical lattices, J. Phys. B: At. Mol. Opt. Phys. **49**, 013001 (2015), arXiv:1510.09042.

[18] T. Kitagawa, E. Berg, M. Rudner and E. Demler, Topological characterization of periodically driven quantum systems, Phys. Rev. B **82**, 235114 (2010), arXiv:1010.6126.

[19] G. Jotzu, M. Messer, R. Desbuquois, M. Lebrat, T. Uehlinger, D. Greif and T. Esslinger, Experimental realization of the topological Haldane model with ultracold fermions, Nature **515**, 237–240 (2014), arXiv:1406.7874.

[20] A. G. Grushin, Gómez-León and T. Neupert, Floquet fractional Chern insulators, Phys. Rev. Lett. **112**, 156801 (2014), arXiv:1309.3571.

[21] E. Anisimovas, G. Žlabys, B. M. Anderson, G. Juzeliūnas and A. Eckardt, Role of real-space micromotion for bosonic and fermionic Floquet fractional Chern insulators, Phys. Rev. B **91**, 245135 (2015), arXiv:1504.03583.

[22] M. Rodriguez-Vega and B. Seradjeh, Universal fluctuations of Floquet topological invariants at low frequencies, Phys. Rev. Lett. **121**, 036402 (2018), arXiv:1706.05303.

[23] P. Liang, M. Marthaler and L. Guo, Floquet many-body engineering: topology and many-body physics in phase space lattices, New J. Phys. **20**, 023043 (2018), arXiv:1710.09716.

[24] C. Weitenberg and J. Simonet, Tailoring quantum gases by Floquet engineering, Nat. Phys. **17**, 1342–1348 (2021), arXiv:2102.07009.

[25] M. Račiūnas, G. Žlabys, A. Eckardt and E. Anisimovas, Modified interactions in a Floquet topological system on a square lattice and their impact on a bosonic fractional Chern insulator state, Phys. Rev. A **93**, 043618 (2016), arXiv:1602.06784.

[26] M. Račiūnas, F. N. Ünal, E. Anisimovas and A. Eckardt, Creating, probing, and manipulating fractionally charged excitations of fractional Chern insulators in optical lattices, Phys. Rev. A **98**, 063621 (2018), arXiv:1804.02002.

[27] N. H. Lindner, G. Refael and V. Galitski, Floquet topological insulator in semiconductor quantum wells, Nat. Phys. **7**, 490–495 (2011).

[28] T. Mikami, S. Kitamura, K. Yasuda, N. Tsuji, T. Oka and H. Aoki, Brillouin-Wigner theory for high-frequency expansion in periodically driven systems: Application to Floquet topological insulators, Phys. Rev. B **93**, 144307 (2016), arXiv:1511.00755.

[29] M. S. Rudner, N. H. Lindner, E. Berg and M. Levin, Anomalous edge states and the bulk-edge correspondence for periodically driven two-dimensional systems, Phys. Rev. X **3**, 031005 (2013).

[30] M. S. Rudner and N. H. Lindner, Band structure engineering and non-equilibrium dynamics in Floquet topological insulators, Nat. Rev. Phys. **2**, 229–244 (2020).

[31] K. Wintersperger, C. Braun, F. N. Ünal, A. Eckardt, M. D. Liberto, N. Goldman, I. Bloch and M. Aidelsburger, Realization of an anomalous Floquet topological system with ultracold atoms, Nat. Phys. **16**, 1058–1063 (2020), arXiv:2002.09840.

[32] D. V. Else, B. Bauer and C. Nayak, Floquet time crystals, Phys. Rev. Lett. **117**, 090402 (2016), arXiv:1603.08001.

[33] N. Y. Yao, A. C. Potter, I.-D. Potirniche and A. Vishwanath, Discrete time crystals: rigidity, criticality, and realizations, Phys. Rev. Lett. **118**, 030401 (2017), arXiv:1608.02589.

[34] K. Sacha and J. Zakrzewski, Time crystals: a review, Rep. Prog. Phys. **81**, 016401 (2018), arXiv:1704.03735.

[35] L. Guo and P. Liang, Condensed matter physics in time crystals, New J. Phys. **22**, 075003 (2020), arXiv:2005.03138.

[36] K. Sacha, *Time crystals* (Springer, 2020).

[37] P. Hannaford and K. Sacha, Condensed matter physics in big discrete time crystals, AAPPS Bulletin **32**, 12 (2022), arXiv:2202.05544.

[38] L. Guo, M. Marthaler and G. Schön, Phase space crystals: a new way to create a quasienergy band structure, Phys. Rev. Lett. **111**, 205303 (2013), arXiv:1305.1800.

[39] K. Sacha, Anderson localization and Mott insulator phase in the time domain, Sci. Rep. **5**, 10787 (2015), arXiv:1502.02507.

[40] L. Guo, M. Liu and M. Marthaler, Effective long-distance interaction from short-distance interaction in a periodically driven one-dimensional classical system, Phys. Rev. A **93**, 053616 (2016), arXiv:1503.03096.

[41] L. Guo and M. Marthaler, Synthesizing lattice structures in phase space, New J. Phys. **18**, 023006 (2016), arXiv:1410.3795.

[42] M. Mierzejewski, K. Giergiel and K. Sacha, Many-body localization caused by temporal disorder, Phys. Rev. B **96**, 140201 (2017), arXiv:1706.09791.

[43] D. Delande, L. Morales-Molina and K. Sacha, Three-dimensional localized-delocalized Anderson transition in the time domain, Phys. Rev. Lett. **119**, 230404 (2017), arXiv:1702.03591.

[44] K. Giergiel, A. Miroszewski and K. Sacha, Time crystal platform: From quasicrystal structures in time to systems with exotic interactions, Phys. Rev. Lett. **120**, 140401 (2018), arXiv:1710.10087.

[45] E. Lustig, Y. Sharabi and M. Segev, Topological aspects of photonic time crystals, Optica **5**, 1390–1395 (2018).

[46] K. Giergiel, A. Dauphin, M. Lewenstein, J. Zakrzewski and K. Sacha, Topological time crystals, New J. Phys. **21**, 052003 (2019), arXiv:1806.10536.

[47] Y. Peng and G. Refael, Topological energy conversion through the bulk or the boundary of driven systems, Phys. Rev. B **97**, 134303 (2018), arXiv:1801.05811.

[48] Y. Peng and G. Refael, Time-quasiperiodic topological superconductors with Majorana multiplexing, Phys. Rev. B **98**, 220509 (2018), arXiv:1805.01896.

[49] G. Žlabys, C.-h. Fan, E. Anisimovas and K. Sacha, Six-dimensional time-space crystalline structures, Phys. Rev. B **103**, L100301 (2021), arXiv:2012.02783.

[50] N. D. Mermin, The topological theory of defects in ordered media, Rev. Mod. Phys. **51**, 591–648 (1979).

[51] A. L. Fetter and A. A. Svidzinsky, Vortices in a trapped dilute Bose-Einstein condensate, J. Phys.: Condens. Matter **13**, R135–R194 (2001), arXiv:cond-mat/0102003.

[52] M. Tsubota, M. Kobayashi and H. Takeuchi, Quantum hydrodynamics, Phys. Rep. **522**, 191–238 (2013), arXiv:1208.0422.

[53] M. T. Reeves, K. Goddard-Lee, G. Gauthier, O. R. Stockdale, H. Salman, T. Edmonds, X. Yu, A. S. Bradley, M. Baker, H. Rubinsztein-Dunlop, M. J. Davis and T. W. Neely, Turbulent relaxation to equilibrium in a two-dimensional quantum vortex gas, Phys. Rev. X **12**, 011031 (2022), arXiv:2010.10049.

[54] K. Harada, T. Matsuda, J. Bonevich, M. Igarashi, S. Kondo, G. Pozzi, U. Kawabe and A. Tonomura, Real-time observation of vortex lattices in a superconductor by electron microscopy, Nature **360**, 51–53 (1992).

[55] E. Poli, T. Bland, S. J. M. White, M. J. Mark, F. Ferlaino, S. Trabucco and M. Mannarelli, Glitches in rotating supersolids, Phys. Rev. Lett. **131**, 223401 (2023), arXiv:2306.09698.

[56] G. Marmorini, S. Yasui and M. Nitta, Pulsar glitches from quantum vortex networks, Sci. Rep. **14**, 7857 (2024).

[57] P. Magierski, A. Barresi, A. Makowski, D. Pęcak and G. Wlazłowski, Quantum vortices in fermionic superfluids: from ultracold atoms to neutron stars., Eur. Phys. J. A **60**, 186 (2024), arXiv:2406.14158.

[58] T. Ozawa and H. M. Price, Topological quantum matter in synthetic dimensions, Nat. Rev. Phys. **1**, 349–357 (2019), arXiv:1910.00376.

[59] I. Petrides, H. M. Price and O. Zilberberg, Six-dimensional quantum Hall effect and three-dimensional topological pumps, Phys. Rev. B **98**, 125431 (2018), arXiv:1804.01871.

[60] C. H. Lee, Y. Wang, Y. Chen and X. Zhang, Electromagnetic response of quantum Hall systems in dimensions five and six and beyond, Phys. Rev. B **98**, 094434 (2018), arXiv:1803.07047.

[61] H. M. Price, Four-dimensional topological lattices through connectivity, Phys. Rev. B **101**, 205141 (2020), arXiv:1806.05263.

[62] Y.-Q. Zhu, Z. Zheng, G. Palumbo and Z. D. Wang, Topological electromagnetic effects and higher second Chern numbers in four-dimensional gapped phases, Phys. Rev. Lett. **129**, 196602 (2022), arXiv:2203.16153.

[63] J. Argüello-Luengo, U. Bhattacharya, A. Celi, R. W. Chhajlany, T. Grass, M. Płodzień, D. Rakshit, T. Salamon, P. Stornati, L. Tarruell and M. Lewenstein, Synthetic dimensions for topological and quantum phases, Commun. Phys. **7**, 143 (2024).

[64] T. Simula, N. Kjærgaard and T. Pfau, Topological transport of a classical droplet in a lattice of time, Nat. Sci. **4**, 10.1002/ntls.20240022 (2024), arXiv:2403.06500.

[65] M. Bukov, S. Gopalakrishnan, M. Knap and E. Demler, Prethermal Floquet steady states and instabilities in the periodically driven, weakly interacting Bose-Hubbard model, Phys. Rev. Lett. **115**, 205301 (2015), arXiv:1507.01946.

[66] D. A. Abanin, W. De Roeck, W. W. Ho and F. Huveneers, Effective Hamiltonians, prethermalization, and slow energy absorption in periodically driven many-body systems, Phys. Rev. B **95**, 014112 (2017), arXiv:1510.03405.

[67] K. Singh, C. J. Fujiwara, Z. A. Geiger, E. Q. Simmons, M. Lipatov, A. Cao, P. Dotti, S. V. Rajagopal, R. Senaratne, T. Shimasaki, M. Heyl, A. Eckardt and D. M. Weld, Quantifying and controlling prethermal nonergodicity in interacting Floquet matter, Phys. Rev. X **9**, 041021 (2019), arXiv:1809.05554.

[68] A. Rubio-Abadal, M. Ippoliti, S. Hollerith, D. Wei, J. Rui, S. L. Sondhi, V. Khemani, C. Gross and I. Bloch, Floquet prethermalization in a Bose-Hubbard system, Phys. Rev. X **10**, 021044 (2020), arXiv:2001.08226.

[69] C. Fleckenstein and M. Bukov, Prethermalization and thermalization in periodically driven many-body systems away from the high-frequency limit, Phys. Rev. B **103**, L140302 (2021), arXiv:2012.10405.

[70] W. W. Ho, T. Mori, D. A. Abanin and E. G. Dalla Torre, Quantum and classical Floquet prethermalization, Ann. Phys. **454**, 169297 (2023), arXiv:2212.00041.

[71] D. H. Dunlap and V. M. Kenkre, Dynamic localization of a charged particle moving under the influence of an electric field, Phys. Rev. B **34**, 3625–3633 (1986).

[72] A. Eckardt, M. Holthaus, H. Lignier, A. Zenesini, D. Ciampini, O. Morsch and E. Arimondo, Exploring dynamic localization with a Bose-Einstein condensate, Phys. Rev. A **79**, 013611 (2009), arXiv:0812.1997.

[73] A. Kosior, J. Major, M. Płodzień and J. Zakrzewski, Controlling disorder with periodically modulated interactions, Phys. Rev. A **92**, 023606 (2015), arXiv:1502.02453.

[74] P. Bordia, H. Lüschen, U. Schneider, M. Knap and I. Bloch, Periodically driving a many-body localized quantum system, Nat. Phys. **13**, 460–464 (2017), arXiv:1607.07868.

[75] D. A. Abanin, E. Altman, I. Bloch and M. Serbyn, Colloquium: Many-body localization, thermalization, and entanglement, Rev. Mod. Phys. **91**, 021001 (2019), arXiv:1804.11065.

[76] K. Sacha, Modeling spontaneous breaking of time-translation symmetry, Phys. Rev. A **91**, 033617 (2015).

[77] J. Zhang, P. W. Hess, A. Kyprianidis, P. Becker, A. Lee, J. Smith, G. Pagano, I.-D. Potirniche, A. C. Potter, A. Vishwanath, N. Y. Yao and C. Monroe, Observation of a discrete time crystal, Nature **543**, 217–220 (2017), arXiv:1609.08684.

[78] S. Choi, J. Choi, R. Landig, G. Kucsko, H. Zhou, J. Isoya, F. Jelezko, S. Onoda, H. Sumiya, V. Khemani, C. von Keyserlingk, N. Y. Yao, E. Demler and M. D. Lukin, Observation of discrete time-crystalline order in a disordered dipolar many-body system, Nature **543**, 221–225 (2017), arXiv:1610.08057.

[79] A. Kosior and K. Sacha, Dynamical quantum phase transitions in discrete time crystals, Phys. Rev. A **97**, 053621 (2018), arXiv:1712.05588.

[80] D. V. Else, C. Monroe, C. Nayak and N. Y. Yao, Discrete time crystals, Annu. Rev. Condens. Matter Phys. **11**, 467–499 (2020), arXiv:1905.13232.

[81] K. Giergiel, A. Kuroś, A. Kosior and K. Sacha, Inseparable time-crystal geometries on the Möbius strip, Phys. Rev. Lett. **127**, 263003 (2021).

[82] H. M. Price, T. Ozawa and N. Goldman, Synthetic dimensions for cold atoms from shaking a harmonic trap, Phys. Rev. A **95**, 023607 (2017), arXiv:1605.09310.

[83] N. Lo Gullo, S. McEndoo, T. Busch and M. Paternostro, Vortex entanglement in Bose-Einstein condensates coupled to Laguerre-Gauss beams, Phys. Rev. A **81**, 053625 (2010), arXiv:0912.1305.

[84] S. K. Adhikari, Stable controllable giant vortex in a trapped Bose–Einstein condensate, Laser Phys. Lett. **16**, 085501 (2019), arXiv:1906.11108.

[85] W. J. Kwon, G. Del Pace, K. Xhani, L. Galantucci, A. Muzi Falconi, M. Inguscio, F. Scazza and G. Roati, Sound emission and annihilations in a programmable quantum vortex collider, Nature **600**, 64–69 (2021), arXiv:2105.15180.

[86] S. Das, K. Mukherjee and S. Majumder, Vortex formation and quantum turbulence with rotating paddle potentials in a two-dimensional binary Bose-Einstein condensate, Phys. Rev. A **106**, 023306 (2022), arXiv:2202.04531.

[87] L. Klaus, T. Bland, E. Poli, C. Politi, G. Lamporesi, E. Casotti, R. N. Bisset, M. J. Mark and F. Ferlaino, Observation of vortices and vortex stripes in a dipolar condensate, Nat. Phys. **18**, 1453–1458 (2022), arXiv:2206.12265.

[88] A. Richaud, G. Lamporesi, M. Capone and A. Recati, Mass-driven vortex collisions in flat superfluids, Phys. Rev. A **107**, 053317 (2023), arXiv:2209.00493.

[89] S. Patrick, A. Gupta, R. Gregory and C. F. Barenghi, Stability of quantized vortices in two-component condensates, Phys. Rev. Res. **5**, 033201 (2023).

[90] D. Kuiri, T. Mithun and B. Dey, Controlling vortex lattice structure of binary Bose-Einstein condensates via disorder-induced vortex pinning, Phys. Rev. A **109**, 063333 (2024), arXiv:2406.00757.

[91] C. Raman, M. Köhl, R. Onofrio, D. S. Durfee, C. E. Kuklewicz, Z. Hadzibabic and W. Ketterle, Evidence for a critical velocity in a Bose-Einstein condensed gas, Phys. Rev. Lett. **83**, 2502–2505 (1999), arXiv:cond-mat/9909109.

[92] R. Onofrio, C. Raman, J. M. Vogels, J. R. Abo-Shaeer, A. P. Chikkatur and W. Ketterle, Observation of superfluid flow in a Bose-Einstein condensed gas, Phys. Rev. Lett. **85**, 2228–2231 (2000), arXiv:cond-mat/0006111.

[93] G. E. Astrakharchik and L. P. Pitaevskii, Motion of a heavy impurity through a Bose-Einstein condensate, Phys. Rev. A **70**, 013608 (2004), arXiv:cond-mat/0307247.

[94] R. Desbuquois, L. Chomaz, T. Yefsah, J. Léonard, J. Beugnon, C. Weitenberg and J. Dalibard, Superfluid behaviour of a two-dimensional Bose gas, Nat. Phys. **8**, 645–648 (2012), arXiv:1205.4536.

[95] W. Weimer, K. Morgener, V. P. Singh, J. Siegl, K. Hueck, N. Luick, L. Mathey and H. Moritz, Critical velocity in the BEC-BCS Crossover, Phys. Rev. Lett. **114**, 095301 (2015), arXiv:1408.5239.

[96] V. P. Singh, W. Weimer, K. Morgener, J. Siegl, K. Hueck, N. Luick, H. Moritz and L. Mathey, Probing superfluidity of Bose-Einstein condensates via laser stirring, Phys. Rev. A **93**, 023634 (2016), arXiv:1509.02168.

[97] V. P. Singh, C. Weitenberg, J. Dalibard and L. Mathey, Superfluidity and relaxation dynamics of a laser-stirred two-dimensional Bose gas, Phys. Rev. A **95**, 043631 (2017), arXiv:1703.02024.

[98] H. Kiehn, V. P. Singh and L. Mathey, Superfluidity of a laser-stirred Bose-Einstein condensate, Phys. Rev. A **105**, 043317 (2022), arXiv:2110.14634.

[99] K. Sasaki, N. Suzuki and H. Saito, Bénard–von Kármán vortex street in a Bose-Einstein condensate, Phys. Rev. Lett. **104**, 150404 (2010), arXiv:1002.2058.

[100] H. Aoki, Quantised Hall effect, Rep. Prog. Phys. **50**, 655–730 (1987).

[101] D. Tong, *Lectures on the quantum Hall effect* (2016), arXiv:1606.06687.

[102] N. W. Ashcroft and N. D. Mermin, *Solid state physics* (Saunders College Publishing, 1976).

[103] B. Jeckelmann and B. Jeanneret, The quantum Hall effect as an electrical resistance standard, Rep. Prog. Phys. **64**, 1603–1655 (2001).

[104] G. M. Ferguson, R. Xiao, A. R. Richardella, D. Low, N. Samarth and K. C. Nowack, Direct visualization of electronic transport in a quantum anomalous Hall insulator, Nat. Mater. **22**, 1100–1105 (2023).

[105] M. A. Paalanen, D. C. Tsui and A. C. Gossard, Quantized Hall effect at low temperatures, Phys. Rev. B **25**, 5566–5569 (1982).

[106] B. A. Bernevig, *Topological insulators and topological superconductors* (Princeton University Press, 2013).

[107] Y. Avron, R. Seiler and B. Shapiro, Generic properties of quantum Hall Hamiltonians for finite systems, Nuclear Physics B **265**, 364–374 (1986).

[108] F. D. M. Haldane, Model for a quantum Hall effect without Landau levels: condensed-matter realization of the "parity anomaly", Phys. Rev. Lett. **61**, 2015–2018 (1988).

[109] L. D. Landau and E. M. Lifshitz, *Quantum mechanics: Non-relativistic theory*, 3rd ed. (Pergamon, 1977).

[110] D. R. Hofstadter, Energy levels and wave functions of Bloch electrons in rational and irrational magnetic fields, Phys. Rev. B **14**, 2239–2249 (1976).

[111] G. H. Wannier, A result not dependent on rationality for Bloch electrons in a magnetic field, Phys. Status Solidi B **88**, 757–765 (1978).

[112] A. H. MacDonald, Landau-level subband structure of electrons on a square lattice, Phys. Rev. B **28**, 6713–6717 (1983).

[113] C. R. Dean, L. Wang, P. Maher, C. Forsythe, F. Ghahari, Y. Gao, J. Katoch, M. Ishigami, P. Moon, M. Koshino, T. Taniguchi, K. Watanabe, K. L. Shepard, J. Hone and P. Kim, Hofstadter's butterfly and the fractal quantum Hall effect in moiré superlattices, Nature **497**, 598–602 (2013), arXiv:1212.4783.

[114] D. Springsguth, R. Ketzmerick and T. Geisel, Hall conductance of Bloch electrons in a magnetic field, Phys. Rev. B **56**, 2036–2043 (1997), arXiv:cond-mat/9705208.

[115] C. Albrecht, J. H. Smet, K. Von Klitzing, D. Weiss, V. Umansky and H. Schweizer, Evidence of Hofstadter's fractal energy spectrum in the quantized Hall conductance, Phys. Rev. Lett. **86**, 147–150 (2001).

[116] M. Aidelsburger, M. Atala, S. Nascimbène, S. Trotzky, Y.-A. Chen and I. Bloch, Experimental realization of strong effective magnetic fields in an optical lattice, Phys. Rev. Lett. **107**, 255301 (2011), arXiv:1110.5314.

[117] L.-J. Lang, X. Cai and S. Chen, Edge states and topological phases in one-dimensional optical superlattices, Phys. Rev. Lett. **108**, 220401 (2012), arXiv:1110.6120.

[118] J. Weis and K. Von Klitzing, Metrology and microscopic picture of the integer quantum Hall effect, Phil. Trans. R. Soc. A. **369**, 3954–3974 (2011).

[119] K.-S. Kim and S. A. Kivelson, The quantum Hall effect in the absence of disorder, npj Quantum Mater. **6**, 22 (2021), arXiv:2009.14203.

[120] M. Nakahara, *Geometry, topology and physics*, 2nd ed. (CRC Press, 2003).

[121] A. Zee, *Quantum field theory in a nutshell*, 2nd ed. (Princeton University Press, 2010).

[122] X.-L. Qi, T. L. Hughes and S.-C. Zhang, Topological field theory of time-reversal invariant insulators, Phys. Rev. B **78**, 195424 (2008), arXiv:0802.3537.

[123] D. J. Thouless, Quantization of particle transport, Phys. Rev. B **27**, 6083–6087 (1983).

[124] Q. Niu, D. J. Thouless and Y.-S. Wu, Quantized Hall conductance as a topological invariant, Phys. Rev. B **31**, 3372–3377 (1985).

[125] L. Wang, M. Troyer and X. Dai, Topological charge pumping in a one-dimensional optical lattice, Phys. Rev. Lett. **111**, 026802 (2013), arXiv:1301.7435.

[126] S. Nakajima, T. Tomita, S. Taie, T. Ichinose, H. Ozawa, L. Wang, M. Troyer and Y. Takahashi, Topological Thouless pumping of ultracold fermions, Nat. Phys. **12**, 296–300 (2016), arXiv:1507.02223.

[127] M. Lohse, C. Schweizer, O. Zilberberg, M. Aidelsburger and I. Bloch, A Thouless quantum pump with ultracold bosonic atoms in an optical superlattice, Nat. Phys. **12**, 350–354 (2016), arXiv:1507.02225.

[128] J. K. Asbóth, L. Oroszlány and A. P. Pályi, *A short course on topological insulators* (Springer, 2016), arXiv:1509.02295.

[129] O. Zilberberg, S. Huang, J. Guglielmon, M. Wang, K. P. Chen, Y. E. Kraus and M. C. Rechtsman, Photonic topological boundary pumping as a probe of 4D quantum Hall physics, Nature **553**, 59–62 (2018), arXiv:1705.08361.

[130] M. Lohse, C. Schweizer, H. M. Price, O. Zilberberg and I. Bloch, Exploring 4D quantum Hall physics with a 2D topological charge pump, Nature **553**, 55–58 (2018), arXiv:1705.08371.

[131] L. D. Landau and E. M. Lifshitz, *Mechanics*, 3rd ed. (Butterworth-Heinemann, 1976).

[132] A. Lichtenberg and M. Lieberman, *Regular and chaotic dynamics*, 2nd ed. (Springer-Verlag, 1992).

[133] A. Buchleitner, D. Delande and J. Zakrzewski, Non-dispersive wave packets in periodically driven quantum systems, Phys. Rep. **368**, 409–547 (2002), arXiv:quant-ph/0210033.

[134] A. A. Aligia and G. Ortiz, Quantum mechanical position operator and localization in extended systems, Phys. Rev. Lett. **82**, 2560–2563 (1999), arXiv:cond-mat/9810348.

[135] J. H. Shirley, Solution of the Schrödinger equation with a Hamiltonian periodic in time, Phys. Rev. **138**, B979–B987 (1965).

[136] Y. Braver, *TTSC.jl: Simulations of topological time-space crystals*, https://github.com/yakovbraver/TTSC.jl.

[137] C. Rackauckas and Q. Nie, DifferentialEquations.jl – a performant and feature-rich ecosystem for solving differential equations in Julia, J. Open Res. Software **5**, 15 (2017).

[138] C. Rackauckas and Q. Nie, Confederated modular differential equation APIs for accelerated algorithm development and benchmarking, Adv. Eng. Software **132**, 1–6 (2019), arXiv:1807.06430.

[139] W. Kahan and R.-C. Li, Composition constants for raising the orders of unconventional schemes for ordinary differential equations, Math. Comp. **66**, 1089–1099 (1997).

[140] R. I. McLachlan and P. Atela, The accuracy of symplectic integrators, Nonlinearity **5**, 541–562 (1992).

[141] P. K. Mogensen and A. N. Riseth, Optim: A mathematical optimization package for Julia, J. Open Source Software **3**, 615 (2018).

[142] D. P. Sanders and L. Benet, *JuliaIntervals/IntervalArithmetic.jl: V0.20.8*, Zenodo, 2022.

[143] J. Bezanson, A. Edelman, S. Karpinski and V. B. Shah, Julia: a fresh approach to numerical computing, SIAM Rev. **59**, 65–98 (2017), arXiv:1411.1607.

[144] J. Tangpanitanon, V. M. Bastidas, S. Al-Assam, P. Roushan, D. Jaksch and D. G. Angelakis, Topological pumping of photons in nonlinear resonator arrays, Phys. Rev. Lett. **117**, 213603 (2016), arXiv:1607.04050.

[145] T. Haug, R. Dumke, L.-C. Kwek and L. Amico, Topological pumping in Aharonov–Bohm rings, Communs. Phys. **2**, 127 (2019), arXiv:1810.08525.

[146] Y. Wang, S. Subhankar, P. Bienias, M. Łącki, T.-C. Tsui, M. A. Baranov, A. V. Gorshkov, P. Zoller, J. V. Porto and S. L. Rolston, Dark state optical lattice with a subwavelength spatial structure, Phys. Rev. Lett. **120**, 083601 (2018), arXiv:1712.00655.

[147] E. M. Lifshitz and L. P. Pitaevskii, *Statistical physics, part 2* (Butterworth-Heinemann, 1980).

[148] H. Sambe, Steady states and quasienergies of a quantum-mechanical system in an oscillating field, Phys. Rev. A **7**, 2203–2213 (1973).

[149] A. Eckardt and E. Anisimovas, High-frequency approximation for periodically driven quantum systems from a Floquet-space perspective, New J. Phys. **17**, 093039 (2015), arXiv:1502.06477.

[150] M. Rodriguez-Vega, M. Lentz and B. Seradjeh, Floquet perturbation theory: formalism and application to low-frequency limit, New J. Phys. **20**, 093022 (2018), arXiv:1805.01190.

[151] S. Rahav, I. Gilary and S. Fishman, Effective Hamiltonians for periodically driven systems, Phys. Rev. A **68**, 013820 (2003), arXiv:nlin/0301033.

[152] M. Bukov, L. D'Alessio and A. Polkovnikov, Universal high-frequency behavior of periodically driven systems: From dynamical stabilization to Floquet engineering, Adv. Phys. **64**, 139–226 (2015), arXiv:1407.4803.

[153] A. P. Itin and M. I. Katsnelson, Effective Hamiltonians for rapidly driven many-body lattice systems: Induced exchange interactions and density-dependent hoppings, Phys. Rev. Lett. **115**, 075301 (2015), arXiv:1401.0402.

[154] V. Novičenko, E. Anisimovas and G. Juzeliūnas, Floquet analysis of a quantum system with modulated periodic driving, Phys. Rev. A **95**, 023615 (2017).

[155] A. Eckardt and M. Holthaus, Avoided-level-crossing spectroscopy with dressed matter waves, Phys. Rev. Lett. **101**, 245302 (2008), arXiv:0809.1032.

[156] M. Weinberg, C. Ölschläger, C. Sträter, S. Prelle, A. Eckardt, K. Sengstock and J. Simonet, Multiphoton interband excitations of quantum gases in driven optical lattices, Phys. Rev. A **92**, 043621 (2015), arXiv:1505.02657.

[157] F. Neese, L. Lang and V. G. Chilkuri, Effective Hamiltonians in chemistry, in *Topology, entanglement, and strong correlations*, edited by E. Pavarini and E. Koch (Forschungszentrum Jülich, 2020).

[158] A. Eckardt, C. Weiss and M. Holthaus, Superfluid-insulator transition in a periodically driven optical lattice, Phys. Rev. Lett. **95**, 260404 (2005), arXiv:cond-mat/0601020.

[159] A. Eckardt, Colloquium: Atomic quantum gases in periodically driven optical lattices, Rev. Mod. Phys. **89**, 011004 (2017), arXiv:1606.08041.

[160] V. Novičenko and G. Juzeliūnas, Non-Abelian geometric phases in periodically driven systems, Phys. Rev. A **100**, 012127 (2019), arXiv:1811.06045.

[161] Y. Braver, *FloquetSystems.jl: A package for studying quantum Floquet systems*, https://github.com/yakovbraver/FloquetSystems.jl.

[162] K. Chinzei and T. N. Ikeda, Time crystals protected by Floquet dynamical symmetry in Hubbard models, Phys. Rev. Lett. **125**, 060601 (2020), arXiv:2003.13315.

[163] S. Sarkar and Y. Dubi, Signatures of discrete time-crystallinity in transport through an open Fermionic chain, Commun. Phys. **5**, 155 (2022), arXiv:2107.04214.

[164] S. Sarkar and Y. Dubi, Emergence and dynamical stability of a charge time-crystal in a current-carrying quantum dot simulator, Nano Lett. **22**, 4445–4451 (2022), arXiv:2205.06441.

[165] B. Buča, J. Tindall and D. Jaksch, Non-stationary coherent quantum many-body dynamics through dissipation, Nat. Commun. **10**, 1730 (2019), arXiv:1804.06744.

[166] C. Tsitouras, Runge–Kutta pairs of order 5(4) satisfying only the first column simplifying assumption, Comput. Math. Appl. **62**, 770–775 (2011).

[167] L. P. Pitaevskii and S. Stringari, *Bose–Einstein condensation and superfluidity* (Oxford University Press, 2016).

[168] C. J. Pethick and H. Smith, *Bose–Einstein condensation in dilute gases*, 2nd ed. (Cambridge University Press, 2008).

[169] G. Toulouse and M. Kléman, Principles of a classification of defects in ordered media, J. Physique Lett. **37**, 149–151 (1976).

[170] E. Lundh, Multiply quantized vortices in trapped Bose-Einstein condensates, Phys. Rev. A **65**, 043604 (2002), arXiv:cond-mat/0103272.

[171] D. A. Butts and D. S. Rokhsar, Predicted signatures of rotating Bose–Einstein condensates, Nature **397**, 327–329 (1999).

[172] B. Damski, K. Sacha and J. Zakrzewski, Stirring a Bose–Einstein condensate, J. Phys. B: At. Mol. Opt. Phys. **35**, 4051–4057 (2002), arXiv:cond-mat/0205478.

[173] G. Modugno, M. Modugno, F. Riboli, G. Roati and M. Inguscio, Two atomic species superfluid, Phys. Rev. Lett. **89**, 190404 (2002), arXiv:cond-mat/0205485.

[174] D. J. McCarron, H. W. Cho, D. L. Jenkin, M. P. Köppinger and S. L. Cornish, Dual-species Bose-Einstein condensate of ^{87}Rb and ^{133}Cs, Phys. Rev. A **84**, 011603 (2011), arXiv:1102.1576.

[175] C. J. Myatt, E. A. Burt, R. W. Ghrist, E. A. Cornell and C. E. Wieman, Production of two overlapping Bose-Einstein condensates by sympathetic cooling, Phys. Rev. Lett. **78**, 586–589 (1997).

[176] J. Stenger, S. Inouye, D. M. Stamper-Kurn, H.-J. Miesner, A. P. Chikkatur and W. Ketterle, Spin domains in ground-state Bose–Einstein condensates, Nature **396**, 345–348 (1998), arXiv:cond-mat/9901072.

[177] T.-L. Ho, Spinor Bose condensates in optical traps, Phys. Rev. Lett. **81**, 742–745 (1998), arXiv:cond-mat/9803231.

[178] J. E. Williams and M. J. Holland, Preparing topological states of a Bose–Einstein condensate, Nature **401**, 568–572 (1999), arXiv:cond-mat/9909163.

[179] M. R. Matthews, B. P. Anderson, P. C. Haljan, D. S. Hall, C. E. Wieman and E. A. Cornell, Vortices in a Bose-Einstein Condensate, Phys. Rev. Lett. **83**, 2498–2501 (1999), arXiv:cond-mat/9908209.

[180] K.-P. Marzlin, W. Zhang and B. C. Sanders, Creation of skyrmions in a spinor Bose-Einstein condensate, Phys. Rev. A **62**, 013602 (2000), arXiv:cond-mat/0003273.

[181] A. E. Leanhardt, Y. Shin, D. Kielpinski, D. E. Pritchard and W. Ketterle, Coreless vortex formation in a spinor Bose-Einstein condensate, Phys. Rev. Lett. **90**, 140403 (2003), arXiv:cond-mat/0212539.

[182] U. Leonhardt and G. E. Volovik, How to create an Alice string (half-quantum vortex) in a vector Bose-Einstein condensate, JETP Lett. **72**, 46–48 (2000), arXiv:cond-mat/0003428.

[183] J. H. Han, *Skyrmions in condensed matter* (Springer, 2017).

[184] D. Vollhardt and P. Wölfle, *The superfluid phases of helium 3* (Taylor and Francis, 1990).

[185] Y. Kawaguchi and M. Ueda, Spinor Bose–Einstein condensates, Phys. Rep. **520**, 253–381 (2012), arXiv:1001.2072.

[186] N. R. Cooper, Optical flux lattices for ultracold atomic gases, Phys. Rev. Lett. **106**, 175301 (2011), arXiv:1101.2382.

[187] G. Juzeliūnas and I. B. Spielman, Flux lattices reformulated, New J. Phys. **14**, 123022 (2012), arXiv:1207.2657.

[188] G. E. Volovik, An analog of the quantum Hall effect in a superfluid ^{3}He film, Sov. Phys. JETP **67**, 1804–1811 (1988).

[189] X.-L. Qi, Y.-S. Wu and S.-C. Zhang, Topological quantization of the spin Hall effect in two-dimensional paramagnetic semiconductors, Phys. Rev. B **74**, 085308 (2006), arXiv:cond-mat/0505308.

[190] H. T. C. Stoof, E. Vliegen and U. Al Khawaja, Monopoles in an antiferromagnetic Bose-Einstein condensate, Phys. Rev. Lett. **87**, 120407 (2001), arXiv:cond-mat/0103194.

[191] M. W. Ray, E. Ruokokoski, S. Kandel, M. Möttönen and D. S. Hall, Observation of Dirac monopoles in a synthetic magnetic field, Nature **505**, 657–660 (2014), arXiv:1408.3133.

[192] S. Sugawa, F. Salces-Carcoba, A. R. Perry, Y. Yue and I. B. Spielman, Second Chern number of a quantum-simulated non-Abelian Yang monopole, Science **360**, 1429–1434 (2018), arXiv:1610.06228.

[193] G. Juzeliūnas, J. Ruseckas, P. Öhberg and M. Fleischhauer, Formation of solitons in atomic Bose–Einstein condensates by dark-state adiabatic passage, Lith. J. Phys. **47**, 351–360 (2007), arXiv:0710.1702.

[194] A. V. Gorshkov, L. Jiang, M. Greiner, P. Zoller and M. D. Lukin, Coherent quantum optical control with subwavelength resolution, Phys. Rev. Lett. **100**, 093005 (2008), arXiv:0706.3879.

[195] M. Łącki, M. A. Baranov, H. Pichler and P. Zoller, Nanoscale "Dark State" optical potentials for cold atoms, Phys. Rev. Lett. **117**, 233001 (2016), arXiv:1607.07338.

[196] E. Gvozdiovas, I. B. Spielman and G. Juzeliūnas, Interference-induced anisotropy in a two-dimensional dark-state optical lattice, Phys. Rev. A **107**, 033328 (2023), arXiv:2304.00302.

[197] H. R. Hamedi, G. Žlabys, V. Ahufinger, T. Halfmann, J. Mompart and G. Juzeliūnas, Spatially strongly confined atomic excitation via a two dimensional stimulated Raman adiabatic passage, Opt. Express **30**, 13915 (2022), arXiv:2111.03750.

[198] G. Nandi, R. Walser and W. P. Schleich, Vortex creation in a trapped Bose-Einstein condensate by stimulated Raman adiabatic passage, Phys. Rev. A **69**, 063606 (2004).

[199] Z. Dutton and J. Ruostekoski, Transfer and storage of vortex states in light and matter waves, Phys. Rev. Lett. **93**, 193602 (2004), arXiv:cond-mat/0405159.

[200] K. T. Kapale and J. P. Dowling, Vortex phase qubit: Generating arbitrary, counterrotating, coherent superpositions in Bose-Einstein condensates via optical angular momentum beams, Phys. Rev. Lett. **95**, 173601 (2005), arXiv:quant-ph/0504130.

[201] S. Thanvanthri, K. T. Kapale and J. P. Dowling, Arbitrary coherent superpositions of quantized vortices in Bose-Einstein condensates via orbital angular momentum of light, Phys. Rev. A **77**, 053825 (2008), arXiv:0803.2725.

[202] G. Juzeliūnas, P. Öhberg, J. Ruseckas and A. Klein, Effective magnetic fields in degenerate atomic gases induced by light beams with orbital angular momenta, Phys. Rev. A **71**, 053614 (2005), arXiv:cond-mat/0412015.

[203] G Juzeliūnas, J Ruseckas and P Öhberg, Effective magnetic fields induced by EIT in ultra-cold atomic gases, J. Phys. B: At. Mol. Opt. Phys. **38**, 4171–4183 (2005), arXiv:quant-ph/0511087.

[204] F. Jendrzejewski, S. Eckel, T. G. Tiecke, G. Juzeliūnas, G. K. Campbell, L. Jiang and A. V. Gorshkov, Subwavelength-width optical tunnel junctions for ultracold atoms, Phys. Rev. A **94**, 063422 (2016), arXiv:1609.01285.

[205] K.-P. Marzlin, W. Zhang and E. M. Wright, Vortex coupler for atomic Bose-Einstein condensates, Phys. Rev. Lett. **79**, 4728–4731 (1997), arXiv:cond-mat/9708198.

[206] R. Dum, J. I. Cirac, M. Lewenstein and P. Zoller, Creation of dark solitons and vortices in Bose-Einstein condensates, Phys. Rev. Lett. **80**, 2972–2975 (1998), arXiv:cond-mat/9710238.

[207] G. Juzeliūnas and P. Öhberg, Creation of an effective magnetic field in ultracold atomic gases using electromagnetically induced transparency, Opt. Spectrosc. **99**, 357 (2005).

[208] M. F. Andersen, C. Ryu, P. Cladé, V. Natarajan, A. Vaziri, K. Helmerson and W. D. Phillips, Quantized rotation of atoms from photons with orbital angular momentum, Phys. Rev. Lett. **97**, 170406 (2006), arXiv:quant-ph/0607171.

[209] K. C. Wright, L. S. Leslie and N. P. Bigelow, Optical control of the internal and external angular momentum of a Bose-Einstein condensate, Phys. Rev. A **77**, 041601 (2008).

[210] K. C. Wright, L. S. Leslie, A. Hansen and N. P. Bigelow, Sculpting the vortex state of a spinor BEC, Phys. Rev. Lett. **102**, 030405 (2009), arXiv:0812.0973.

[211] K. Mukherjee, S. Bandyopadhyay, D. Angom, A. M. Martin and S. Majumder, Dynamics of the creation of a rotating Bose–Einstein condensation by two photon Raman transition using a Laguerre–Gaussian laser pulse, Atoms **9**, 14 (2021).

[212] M. O. Scully and M. S. Zubairy, *Quantum Optics* (Cambridge University Press, 1997).

[213] A. L. Gaunt, T. F. Schmidutz, I. Gotlibovych, R. P. Smith and Z. Hadzibabic, Bose-Einstein condensation of atoms in a uniform potential, Phys. Rev. Lett. **110**, 200406 (2013), arXiv:1212.4453.

[214] R. F. Gutterres, C. Amiot, A. Fioretti, C. Gabbanini, M. Mazzoni and O. Dulieu, Determination of the ^{87}Rb $5p$ state dipole matrix element and radiative lifetime from the photoassociation spectroscopy of the Rb_2 $0_g^-(P_{3/2})$ long-range state, Phys. Rev. A **66**, 024502 (2002).

[215] M. Egorov, B. Opanchuk, P. Drummond, B. V. Hall, P. Hannaford and A. I. Sidorov, Measurement of s-wave scattering lengths in a two-component Bose-Einstein condensate, Phys. Rev. A **87**, 053614 (2013), arXiv:1204.1591.

[216] P. Ao and S. T. Chui, Binary Bose-Einstein condensate mixtures in weakly and strongly segregated phases, Phys. Rev. A **58**, 4836–4840 (1998), arXiv:cond-mat/9809195.

[217] E. Timmermans, Phase separation of Bose-Einstein condensates, Phys. Rev. Lett. **81**, 5718–5721 (1998), arXiv:cond-mat/9709301.

[218] L. Wen, W. M. Liu, Y. Cai, J. M. Zhang and J. Hu, Controlling phase separation of a two-component Bose-Einstein condensate by confinement, Phys. Rev. A **85**, 043602 (2012), arXiv:1204.1256.

[219] X. Di, Y.-H. Nie and T. Yang, Manipulating vortices with a rotating laser beam in Bose–Einstein condensates, Laser Phys. **33**, 085501 (2023).

[220] X. Antoine and R. Duboscq, GPELab, a Matlab toolbox to solve Gross-Pitaevskii equations I: Computation of stationary solutions, Comput. Phys. Commun. **185**, 2969–2991 (2014).

[221] X. Antoine and R. Duboscq, GPELab, a Matlab toolbox to solve Gross-Pitaevskii equations II: Dynamics and stochastic simulations, Comput. Phys. Commun. **193**, 95–117 (2015).

List of publications and conference contributions

This thesis is based on the following four scientific works:

[P1] **Y. Braver**, C.-h. Fan, G. Žlabys, E. Anisimovas and K. Sacha, Two-dimensional Thouless pumping in time-space crystalline structures, Phys. Rev. B **106**, 144301 (2022).

[P2] **Y. Braver**, E. Anisimovas and K. Sacha, Eight-dimensional topological systems simulated using time-space crystalline structures, Phys. Rev. B **108**, L020303 (2023).

[P3] **Y. Braver** and E. Anisimovas, Extended degenerate perturbation theory for the Floquet–Hilbert space, Phys. Rev. A **110**, 023315 (2024).

[P4] **Y. Braver**, D. Burba, S. S. Nair, G. Žlabys, E. Anisimovas, Th. Busch and G. Juzeliūnas, Light-induced localized vortices in multicomponent Bose-Einstein condensates, Phys. Rev. A **112**, 033301 (2025).

In all of these works, the author substantially contributed to every aspect of the research, including development of the theoretical ideas, performing analytical and numerical calculations, analysing the results, and writing the manuscripts.

Author of the thesis has also co-authored six other scientific works:

[P1*] A. Gelzinis, **Y. Braver**, J. Chmeliov and L. Valkunas, Decay- and evolution-associated spectra of time-resolved fluorescence of LHCII aggregates, Lith. J. Phys. **58**, 295–306 (2018).

[P2*] **Y. Braver**, A. Gelzinis, J. Chmeliov and L. Valkunas, Application of decay- and evolution-associated spectra for molecular systems with spectral shifts or inherent inhomogeneities, Chem. Phys. **525**, 110403 (2019).

[P3*] **Y. Braver**, L. Valkunas and A. Gelzinis, Benchmarking the forward–backward trajectory solution of the quantum-classical Liouville equation, J. Chem. Phys. **152**, 214116 (2020).

[P4*] **Y. Braver**, L. Valkunas and A. Gelzinis, Derivation of the stationary fluorescence spectrum formula for molecular systems from the perspective of quantum electrodynamics, Lith. J. Phys. **61**, 110–123 (2021).

[P5*] **Y. Braver**, L. Valkunas and A. Gelzinis, Quantum–classical approach for calculations of absorption and fluorescence: Principles and applications, J. Chem. Theory Comput., **17**, 7157–7168 (2021).

[P6*] **Y. Braver**, L. Valkunas and A. Gelzinis, Stark absorption and Stark fluorescence spectroscopies: Theory and simulations, J. Chem. Phys., **155**, 244101 (2021).

The results of the thesis have been presented at the following scientific conferences:

[C1] **Y. Braver**, C.-h. Fan, G. Žlabys, E. Anisimovas and K. Sacha, High-dimensional time-space crystalline structures and their topological properties, *14th European Conference on Atoms Molecules and Photons*, Vilnius, Lithuania (2022).

[C2] **Y. Braver**, E. Anisimovas and K. Sacha, High-dimensional topological pumping in time-space crystalline structures, *66th International Open Readings Conference for Students of Physics and Natural Sciences*, Vilnius, Lithuania (2023).

[C3] **Y. Braver**, E. Anisimovas and K. Sacha, Construction of eight-dimensional topological systems based on time-space crystalline structures, *Humboldt Kolleg on Synthetic Quantum Matter*, Vilnius, Lithuania (2023).

[C4] **Y. Braver**, E. Anisimovas and K. Sacha, Time-space crystalline structures with properties of eight-dimensional topological systems, *Time Crystals Conference 2023*, Kraków, Poland (2023).

[C5] **Y. Braver** and E. Anisimovas, High-frequency approximation for periodically driven quantum systems in the vicinity of resonances, *67th International Open Readings Conference for Students of Physics and Natural Sciences*, Vilnius, Lithuania (2024).

[C6] **Y. Braver** and E. Anisimovas, Extended degenerate perturbation theory for the Floquet–Hilbert space, *Non-equilibrium Many-body Physics Beyond the Floquet Paradigm*, Dresden, Germany (2024).

[C7] **Y. Braver**, D. Burba, G. Žlabys, E. Anisimovas, Th. Busch and G. Juzeliūnas, Stationary vortex states in two-component Bose–Einstein condensates, *The 29th Central European Workshop on Quantum Optics*, Vilnius, Lithuania (2025).

[C8] **Y. Braver**, D. Burba, G. Žlabys, E. Anisimovas, Th. Busch and G. Juzeliūnas, Stationary vortex states of two-component Bose–Einstein condensates interacting with laser fields, *Workshop on Unconventional Optical Lattices*, Vilnius, Lithuania (2025).

[C9] **Y. Braver**, D. Burba, G. Žlabys, E. Anisimovas, Th. Busch and G. Juzeliūnas, Optical creation and manipulation of localised vortices in two-component Bose–Einstein condensates, *15th European Conference on Atoms, Molecules and Photons*, Innsbruck, Austria (2025).

Curriculum Vitae

Education

2021–2025 **PhD studies**, Vilnius University.

2019–2021 **Master's Degree in Physics**, Vilnius University.
Theoretical Physics and Astrophysics study programme.
Graduated with highest honours (*magna cum laude*).

2015–2019 **Bachelor's Degree in Physics**, Vilnius University.
Computing Physics and Modelling study programme.
Graduated with highest honours (*magna cum laude*).

Research Experience

Jan 2023–present **Junior Researcher**, Institute of Theoretical Physics and Astronomy, Vilnius University (Vilnius, Lithuania).

Sept 2024–Nov 2024 **Research Intern**, Quantum Systems Unit, Okinawa Institute of Science and Technology Graduate University (Okinawa, Japan).

July 2021–Sept 2021 **Junior Researcher**, Department of Molecular Compound Physics, Center for Physical Sciences and Technology (Vilnius, Lithuania).

July 2019–June 2021 **Engineer**, Department of Molecular Compound Physics, Center for Physical Sciences and Technology (Vilnius, Lithuania).

Nov 2017–June 2019 **Technician**, Department of Molecular Compound Physics, Center for Physical Sciences and Technology (Vilnius, Lithuania).

Open Source Projects

FloquetSystems **Maintainer**, Hosted on GitHub.
A package for studying quantum Floquet systems.

TTSC **Maintainer**, Hosted on GitHub.
Simulations of topological time-space crystals.

QuaCla **Maintainer**, Hosted on GitLab.
Quantum-classical simulations of excitonic molecular aggregates.

Honours and Awards

2022–2023 and 2024–2025 **Promotional scholarship for PhD students**, issued by the Research Council of Lithuania, for the academic years 2022–2023 and 2024–2025.

2022 **Winner of the competition of scientific works of university students, organised by the Lithuanian Academy of Science**, prize awarded for the work 'Stark absorption and Stark fluorescence spectroscopies: Theory and simulations'.

2020–2021 **Antanas Stulginskis presidential scholarship** for the academic year 2020–2021.

2019 **Dr. Remi Gaška scholarship** 'For the best bachelor's final thesis', a one-off scholarship.

Santrauka (Summary in Lithuanian)

Įvadas

Universalių fizikos principų paieškos jau seniai remiasi simetrija ir tvermės dėsniais, siekiant klasifikuoti ir suprasti skirtingas medžiagos būsenas. Tačiau pastaraisiais dešimtmečiais tapo aišku, kad kitas organizavimo principas – topologija – vaidina pagrindinį vaidmenį formuojant kvantinius reiškinius [1, 2]. Skirtingai nuo geometrinių savybių, kurios gali kisti tolydžiai, topologinės charakteristikos išlieka nekintančios esant tolydžioms deformacijoms, todėl jos yra patikimi fizinių sistemų klasifikatoriai. Tai turi didelę reikšmę kvantinei teorijai, kur *topologiniai invariantai* lemia kvantinių būsenų ir medžiagos fazių stabilumą.

Ryškus pavyzdys yra kvantinis Holo efektas [3], kuriame Holo laidumas yra kvantuojamas sveikaisiais e^2/h (elementarusis krūvis kvadratu, dalintas iš Planko konstantos) kartotiniais, kur kiekvienas sveikasis skaičius atitinka sveikąjį skaičių topologinių invariantų, vadinamų *Černo skaičiais* [4, 5], sumą. Įdomu tai, kad šiuo atveju topologija užtikrina makroskopinio, o ne mikroskopinio dydžio (pvz., vieno atomo energijos) kvantavimą. Išreikšdama globalias banginių funkcijų ir hamiltoniano savybes, topologija suteikia galingą būdą, kaip klasifikuoti ir prognozuoti egzotines medžiagos fazes, kurios dažnai negali būti numatytos įprastiniais metodais.

Ypač universalią platformą topologiniams efektams tirti siūlo labai šaltos atominės dujos optinėse gardelėse [6], kur sistemos savybes galima modifikuoti ir tirti itin tiksliai valdant parametrus [7, 8]. Optinės gardelės ir sintetiniai kalibraciniai laukai [9–12] leidžia modeliuoti juostines struktūras su reguliuojama topologija [13, 14, 16], o pažangios aptikimo technologijos suteikia prieigą prie kvantinių būsenų geometrinių ir topologinių savybių. Paminėtina, kad labai šaltų atomų eksperimentai nėra ribojami kietojo kūno medžiagoms būdingų priemaišų ar gardelės defektų, todėl jie tinka topologiniams reiškiniams tirti švariomis ir reguliuojamomis sąlygomis.

Be statinių sistemų, išorinio žadinimo vaidmuo atvėrė naujas galimybes to-

pologinių fazių kūrimui. Periodinis žadinimas, formalizuotas Flokė teorija, suteikia galimybę dinamiškai modifikuoti juostines struktūras [17] ir kurti efektyvinius hamiltonianus, turinčius netrivialias topologines savybes [18–24]. Šis metodas, vadinamas *Flokė inžinerija*, leido realizuoti tokias fazes kaip Flokė trupmeniniai Černo izoliatoriai [20, 25, 26], Flokė topologiniai izoliatoriai [27, 28] ir anomalūs Flokė topologiniai izoliatoriai [29–31]; pastarieji neturi statinių atitikmenų. Be to, periodinio judėjimo ir simetrijos pažeidimo sąveika lėmė *diskrečiųjų laiko kristalų* atradimą – tai medžiagos fazė, kurioje savaime pažeidžiama išorinė diskrečioji laiko transliacijos simetrija sukuriant simetriją su ilgesniu periodu [32, 33]. Naujausi laiko kristalų tyrimai [34–37] apima ir *laiko kristalinių struktūrų* – uždarų kvantinių sistemų, kurias valdo periodiniai išoriniai signalai, – tyrimus, siekiant pasinaudoti sukeltu reguliariu periodiniu pasikartojimu laike. Tokiu būdu laikas įgyja papildomos koordinatės savybes. Tokiais atvejais laiko periodinė struktūra iš tiesų yra suteikta išoriškai; nereikia pasikliauti palankiu dalelių sąveikos vaidmeniu jos savaiminiam susidarymui. Nepaisant to, periodinio reguliarumo pasireiškimas laike yra ne mažiau intriguojantis dėl atsiveriančių galimybių imituoti įprastas erdviškai periodines kietojo kūno sistemas ir kondensuotosios medžiagos fizikos reiškinius. Sistemingi tyrimai lėmė vis didėjantį fazių, atkurtų arba apibendrintų laiko srityje, sąrašą: Andersono lokalizuotos ir daugiadalelinės lokalizuotos būsenos, Moto izoliatoriaus būsena, taip pat topologines fazės [38–48]. Dar vienas išplėtimas buvo pasiūlytas naudojant laiko-erdvės kristalines struktūras [49], kurios sujungia periodiškumą laike ir erdvėje. Sintetinių dimensijų įvedimu požiūriu šios laiko-erdvės gardelės atveria kelią potencialiam dimensijų skaičiaus padvigubinimui.

Kita turtinga topologijos apraiška kvantinėje fizikoje kyla iš *topologinių defektų*. Jie atsiranda, kai tvarkos parametro, apibūdinančio sistemos būseną, tolydumas yra nesuderinamas su būsenos topologinėmis savybėmis. Šių defektų negalima pašalinti lokaliais trikdžiais, nes jų egzistavimas yra susijęs su globalia tvarkos parametro erdvės struktūra. Kondensuotųjų medžiagų sistemose topologiniai defektai pasireiškia įvairiomis formomis feromagnetuose, kristaluose ir supertakiuose skysčiuose [50, 2]. Supertakiuose skysčiuose ir atominių Bozė ir Einšteino kondensatų kontekste esminiai topologiniai defektai yra sūkuriai, kuriems būdinga kvantuota cirkuliacija ir tvarkos parametro fazės singuliarumas [51]. Sūkurių tyrimas turi plačią reikšmę – nuo kvantinės turbulencijos [52, 53] iki ryšių su superlaidumu [54] ir neutroninių žvaigždžių struktūra [55–57].

Ši trumpa srities apžvalga išryškina daugybę paradigmų, susijusių su dabartiniu skirtingų medžiagos būsenų supratimu. Šio darbo tikslas – pagilinti šį supratimą, nustatant ryšius tarp jų ir naudojant topologiją kaip vienijantį principą. Darbe nagrinėsime topologinių reiškinių pasireiškimą Flokė fazėse

– laiko-erdvės kristalinėse struktūrose – išaiškindami laiko vaidmenį sintetinių matmenų sistemose. Taip pat nagrinėsime netipinių, stipriai lokalizuotų sūkurių savybes Bozė ir Einšteino kondensatuose, kurie, nors ir nėra topologiškai stabilūs, bus stabilizuojami išoriniu žadinimu.

Pagrindiniai tikslai

Šiuo darbu siekiama keturių konkrečių tikslų:

1. Realizuoti topologinį transportą laiko-erdvės kristalinėse struktūrose. Tikslui pasiekti buvo įvykdytos šios užduotys:
   (a) Suformuluoti vienmačio kristalo modelį, kuris leistų realizuoti erdvinį topologinį transportą ir įskaitytų periodinį žadinimą su adiabatine faze.
   (b) Rasti parametrų režimus, kad tuneliavimas tarp erdvinės ir laikinės gardelės narvelių būtų pakankamai stiprus dalelių pernašai.
   (c) Ištirti transporto dinamiką sekant erdvėje ir laike lokalizuotas Vanjė funkcijas.
2. Pasiūlyti topologiškai netrivialios aštuonių dimensijų kvantinės sistemos realizaciją. Tikslui pasiekti buvo įvykdytos šios užduotys:
   (a) Suformuluoti dalelės modelį žadinamame vienmačiame kristale, kuris apimtų dvi adiabatines fazes ir turėtų topologiškai netrivialias kvazienergijos juostas.
   (b) Gauti atitinkamą stipraus ryšio hamiltonianą $\hat{H}_{\mathrm{TB}}$ ir suskaidyti jį į dvi dalis, atitinkamai apibūdinančias erdvinę ir laikinę gardelę.
   (c) Patikrinti, kad kiekvienas iš gautų hamiltonianų apibūdintų topologiškai netrivialias sistemas, modeliuojant topologinį transportą.
   (d) Rasti parametrų režimus, kad sujungus dvi $\hat{H}_{\mathrm{TB}}$ kopijas, gautas (kvazi)energijos spektras turėtų draustinius tarpus.
3. Sukurti perturbacinį kvazienergijos spektrų skaičiavimo metodą rezonansinio žadinimo atveju. Tikslui pasiekti buvo įvykdytos šios užduotys:
   (a) Ištirti kvazienergijos operatoriaus struktūrą išplėstinėje Flokė ir Hilberto erdvėje ir rasti transformaciją, kuri išskiria rezonansinio žadinimo sukeltus išsigimimus.
   (b) Išvesti transformuoto kvazienergijos operatoriaus perturbacinį skleidinį.
   (c) Patikrinti teorijos tikslumą pritaikant ją rezonansiniu būdu žadinamai daugiadalelinei kvantinei sistemai.

4. Pasiūlyti metodą, leidžiantį stabilizuoti lokalizuotus sūkurius kelių komponenčių Bozė ir Einšteino kondensatuose, ir ištirti jų savybes. Tikslui pasiekti buvo įvykdytos šios užduotys:

   (a) Suformuluoti optinę sistemą, kuri leistų sukurti sūkurius kelių komponenčių Bozė ir Einšteino kondensatuose.

   (b) Ištirti stacionarias kondensato būsenas.

   (c) Rasti režimus, kuriuose pagrindinėje būsenoje vienoje iš komponenčių yra lokalizuotas sūkurys.

   (d) Ištirti sistemos supertakumo savybes, naudojant lokalizuotą sūkurį kaip priemaišą, maišančią kondensatą, ir rasti kritinį supertakumo greitį.

Mokslinis naujumas ir aktualumas

Disertacijoje pristatomi šie naujoviniai tyrimai:

1. Topologinių reiškinių tyrimas laikinėje dimensijoje ir daugiau nei trijose dimensijose. Topologinis transportas laikinėje dimensijoje demonstruojamas naudojant konkrečią kvantinę sistemą, realizuojamą naudojant labai šaltus atomus optinėse gardelėse. Tiriamas dvimatis transportas erdvinėje ir laikinėje ašyse, kuris yra tiesiogiai susijęs su keturmačiu kvantiniu Holo efektu. Analizė išplečiama, įtraukiant du fizinius erdvinius matmenis, gaunant efektyvinę aštuonių matmenų topologiškai netrivialią sistemą. Sistemos analizė palengvinama perrašant sistemos hamiltonianą į stipriojo ryšio formą, tokiu būdu sujungiant erdvę, laiką ir papildomas sintetines dimensijas į vientisą aprašymą. Laiko, kaip papildomos dimensijos, panaudojimas ir daugiamačių sistemų modeliavimas laikomas svarbiu žingsniu siekiant išnaudoti sintetines dimensijas praktiniams tikslams [58–61, 49, 62]. Topologinis transportas laikinėje dimensijoje – pirmą kartą pasiūlytas ir išstudijuotas Autoriaus su kolegomis darbe [P1] ir pristatytas šioje disertacijoje – buvo vėliau realizuotas klasikinėje sistemoje darbe [64].

2. Išplėstinė išsigimusi perturbacijos teorija Flokė ir Hilberto erdvėje, leidžianti efektyviau konstruoti efektyvinius hamiltonianus rezonansiškai žadinamoms sistemoms. Tai ypač aktualu daugiadalelinių kvantinių sistemų analizei, kur rezonansai neišvengiami dėl tankaus energijos spektro. Efektyvinių hamiltonianų skaičiavimas yra būtinas analizuojant daugelį intriguojančių dinaminių kvantinių daugiadalelinių efektų, tokių kaip prieštermalizacija [65–70], lokalizacija [71–75], taip pat diskrečiųjų lai-

ko kristalų [76, 32, 33, 77–81] ir topologinių būsenų [18, 20, 19, 28, 82] susidarymas.

3. Optiškai sukurtų sūkurių tyrimas kelių komponenčių Bozė ir Einšteino kondensate. Pateikiamas stipriai lokalizuotų sūkurių susidarymo vienoje iš komponenčių būdas naudojant optinę konfigūraciją. Išorinis žadinimas leidžia stabilizuoti netipines sūkurių konfigūracijas, kurios savaime nėra topologiškai stabilios. Lokalizuotas sūkurys gali būti judinamas aplink gaudyklę, taip maišant kitą komponentę. Tai gali būti naudojama kondensato supertakumo pobūdžiui tirti naudojant naujo tipo priemaišą – besisukančią aplink savo ašį. Tiek bendrieji sūkurių tyrimai kondensatuose [83–90], tiek priemaišų judėjimas juose [91–99] yra esminės tyrimų kryptys Bozė ir Einšteino kondensacijos srityje.

Ginamieji teiginiai

1. Adiabatinis periodinio žadinimo fazės kitimas dalelėms esant periodiniame erdviniame potenciale (pavyzdžiui, labai šaltieji atomai optinėje gardelėje) pasireiškia topologiniu transportu laikinėje dimensijoje.

2. Kvantinės sistemos erdvinis ir laikinis periodiškumas, suvienytas naudojant laiko-erdvės kristalinių struktūrų teoriją, leidžia realizuoti topologiškai netrivialią aštuonių dimensijų sistemą, naudojant tik dvi fizines erdvines dimensijas – nenaudojant vidinių kvantinių būsenų.

3. Sukurta išplėstinė išsigimusi perturbacijos teorija Flokė ir Hilberto erdvėje pranoksta įprastą išsigimusią perturbacijų teoriją tikslumu, tuo pačiu reikalaudama mažiau skaitinių resursų nei tikslus sprendimas, suteikiant praktišką metodą periodiškai ir rezonansiškai žadinamų kvantinių daugiadalelinių sistemų kvazienergijos spektrų skaičiavimui.

4. Kelių komponenčių Bozė ir Einšteino kondensatų sąveika su Lagero ir Gauso pluoštais leidžia valdomu būdu sukurti ir stabilizuoti stipriai lokalizuotus sūkurius.

Topologinis transportas laiko-erdvės kristalinėse struktūrose

Topologinių sąvokų taikymą pradedame teoriniu topologinio transporto realizacijos laiko ir laiko-erdvės kristalinėse struktūrose tyrimu. Pademonstruosime, kad adiabatinis išorinio žadinimo kitimas gali sukelti kvantinį dalelių judėjimą laiko dimensijoje. Šiuo tikslu nagrinėjame kvantinių dujų adiabatinį transportą dvimatėje (2D) laiko-erdvės kristalinėje struktūroje, realizuojamoje rezonansiniu būdu žadinamoje optinėje gardelėje. Nagrinėjame tris galimus procesus: transportą laiko dimensijoje, erdvinį transportą ir transportą abiejose dimensijose vienu metu. Dvimatis topologinis transportas gali būti naudojamas keturmačiam (4D) kvantiniam Holo efektui tirti, todėl siūloma konfigūracija leidžia tirti fizikinius reiškinius keturiose dimensijose naudojant vienos erdvinės dimensijos žadinamą sistemą.

Laiko-erdvės topologinis transportas demonstruojamas naudojant 1D hamiltonianą pavidalu

$$\hat{H} = \hat{h}(\hat{p}_x, x|\varphi_x) + \xi_{\mathrm{S}}(x,t) + \xi_{\mathrm{L}}(x,t|\varphi_t). \tag{S1}$$

Pirmasis narys yra nesutrikdytas erdvinis hamiltonianas

$$\hat{h}(\hat{p}_x, x|\varphi_x) = \hat{p}_x^2 - V_{\mathrm{S}}\cos^2(2x) - V_{\mathrm{L}}\cos^2(x+\varphi_x), \tag{S2}$$

tipiškai naudojamas demonstruojant topologinį transportą realioje erdvėje [126, 127]. Čia $\hat{p}_x$ yra impulso operatorius, V_{S} ir V_{L} kontroliuoja, „trumpos“ ir „ilgos“ optinių gardelių gylius, o santykinė fazė φ_x realizuoja vieną transporto ciklą kintama ilgio π periodu. Formulėje (S2) ilgis matuojamas $1/k_{\mathrm{L}}$ vienetai, čia k_{L} yra lazerio, kuriančio gardelę, banginis skaičius, o energija matuojama $\hbar^2 k_{\mathrm{L}}^2/2m$ vienetais, čia m yra dalelės masė. Laiko vienetas yra redukuota Planko konstanta $\hbar$, dalinta iš energijos vieneto.

Topologinis transportas laikinėje dimensijoje realizuojamas naudojant šitokį žadinimą:

$$\xi_{\mathrm{S}}(x,t) = \lambda_{\mathrm{S}}\sin^2(2x)\cos(2\omega t), \tag{S3a}$$

$$\xi_{\mathrm{L}}(x,t|\varphi_t) = \lambda_{\mathrm{L}}\cos^2(2x)\cos(\omega t + \varphi_t). \tag{S3b}$$

Čia λ_{S} ir λ_{L} kontroliuoja žadinimo stiprumus, o fazė φ_t leidžia lėtai keisti santykinį poslinkį tarp laikinės gardelės narvelių. Žadinimo dažnis pasirenkamas pavidalu $\omega = s\Omega$ su rezonansiniu skaičiumi $s = 2$, o Ω yra energijos tarpas tarp gretimų hamiltoniano $\hat{h}$ energijos juostų, kurias siekiama sukabinti išoriniu žadinimu. Trikdžiai, osciliuojantys dažniais 2Ω ir 4Ω, leidžia sukurti keturių

mazgų žiedinę gardelę (sudarytą iš dviejų narvelių su dviem mazgais kiekvienas) laikinėje dimensijoje. Siekdami užtikrinti pakankamą šuolio stiprumą tarp erdvinės gardelės mazgų, tiriame aukštai sužadintas $\hat{h}$ būsenas, kurios užima juostas netoli erdvinio potencialo duobių viršaus. Atitinkamą Ω reikšmę lengva nustatyti diagonalizuojant $\hat{h}$. Kadangi fazė φ_x keičia erdvinį potencialą ir tokiu būdu neperturbuotą energijos spektrą, papildomai sureguliuojame Ω (arba tiesiogiai ω) reikšmę, kad erdvinio tuneliavimo stiprumas būtų pakankamas visiems φ_x.

Kadangi trikdis $\xi_\mathrm{S}+\xi_\mathrm{L}$ yra periodinis laike (periodas $T=2\pi/\omega$), uždavinys sprendžiamas įvedant kvazienergijos operatorių $\hat{Q}=\hat{H}-\mathrm{i}\partial_t$ ir sprendžiant tikrinių verčių uždavinį $\hat{Q}u_n(x,t)=\varepsilon_n u_n(x,t)$ [135, 133, 17]. Čia ε_n yra n-osios tikrinės būsenos kvazienergija, o $u_n(x,t)$ yra atitinkama Flokė moda – periodinė funkcija $u_n(x,t)=u_n(x,t+T)$. Bendrasis Šriodingerio lygties sprendinys gali būti išreikštas per funkcijų $\Psi_n(x,t)=\mathrm{e}^{-\mathrm{i}\varepsilon_n t}u_n(x,t)$ superpozicija su nepriklausančiais nuo laiko koeficientais. Skaitinis uždavinio sprendimas yra realizuotas `TTSC.jl` pakete [136].

Vienu metu atliekamas laikinis ir erdvinis topologinis transportas 2D laiko-erdvės kristalinėje struktūroje yra pademonstruotas S1 pav. atveju, kai $s=2$, o erdvinių narvelių skaičius taip pat yra $N=2$. Adiabatinės fazės varijuojamos pagal trajektoriją $\varphi_t=2\varphi_x$ nuo $\varphi_t=0$ iki $\varphi_t=2\pi$, tam kad būtų įveiktas vienas transportavimo ciklas laikinėje ir erdvinėje dimensijose. Gautas Flokė kvazienergijų spektras parodytas S1(a) pav.; legendoje pažymėti lygmenys, atitinkantys Flokė modas, kurių superpozicija buvo panaudota Vanjė funkcijų skaičiavimui. Tai leidžia ištirti Vanjė būsenas, kurios yra transportuojamos fizinėje erdvėje „į dešinę“. Likusieji keturi lygmenys (pirmos laikinės juostos) atitinka Vanjė funkcijas, kurios yra transportuojamos priešinga kryptimi. Sukonstruotos būsenos yra išreiškiamos kaip $w_{i,\alpha}(x,t)=\sum_{j,\beta}d_{j,\beta}^{(i,\alpha)}u_{j,\beta}(x,t)$ ir yra randamos diagonalizuojant pozicijos operatorių $\mathrm{e}^{2\mathrm{i}x/N}$ [128, 134]. Keturios gautos Vanjė funkcijos parodytos S1(b)–(f) pav. esant skirtingoms adiabatinės fazės vertėms. Užtušuoti plotai nurodo erdvinius ($k=1,2$) ir laikinius ($\gamma=1,2$) narvelius. Būsenos ir narveliai yra sunumeruotos taip, kad pradiniame etape (kai $\varphi_t=2\varphi_x=0$) Vanjė funkcijų indeksai (i,α) sutaptų su erdvinių ir laikinių narvelių indeksais (k,γ).

Analizuodami transportavimo procesą, S1(c) pav. matome, kad Vanjė būsenos yra transportuojamos į gretimus erdvinius narvelius (į dešinę) erdvinio transportavimo dėka, o laikinis transportavimas sukelia būsenų slydimą laikine ašimi žemyn. Kai $\varphi_t=2\varphi_x=\pi$ [žr. S1(d) pav.], būsenos yra pilnai perėjusios į gretimą erdvinį narvelį, o funkcijų laikinė priklausomybė yra tokia, kad funkcijos užima abu laikinius narvelius. Toliau, kai $\varphi_t=2\varphi_x=3\pi/2$ [žr. S1(e) pav.], būsenos yra parodytos erdvinio perėjimo viduryje, kuris pilnai užsibaigia kai

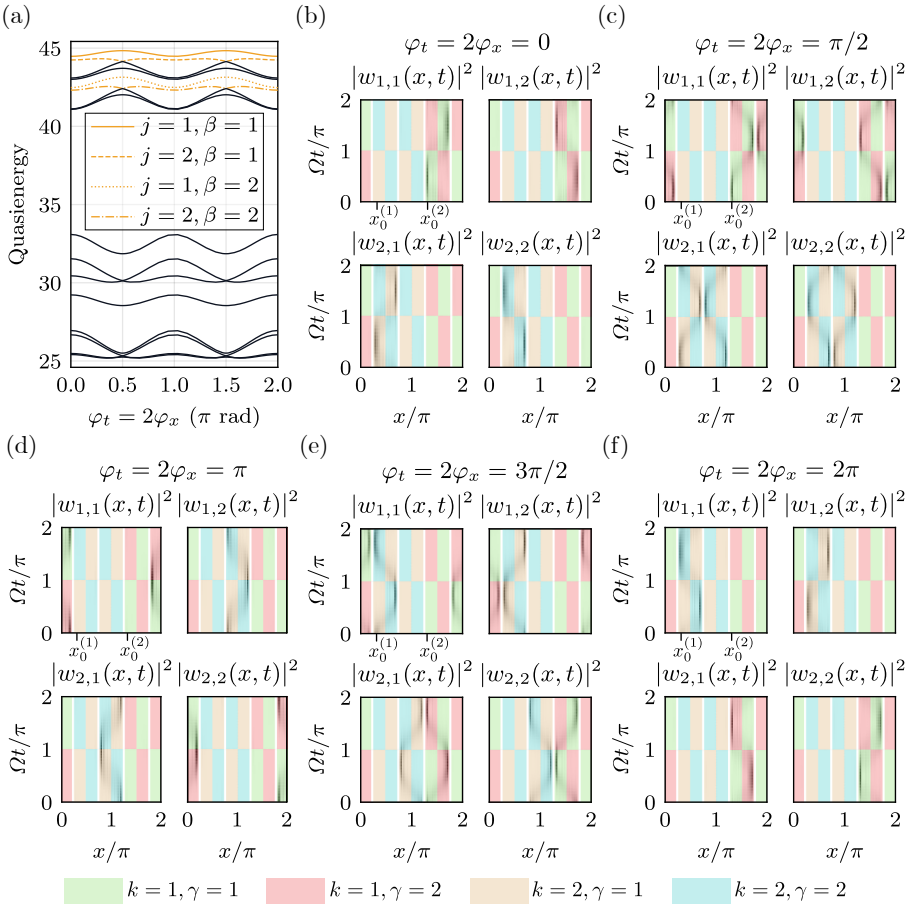

S1 pav.: Vienu metu atliekamas laikinis ir erdvinis topologinis transportas 2D laiko-erdvės kristalinėje struktūroje. Parametrų vertės yra: $V_\mathrm{S} = 7640$, $V_\mathrm{L} = 2$, $\omega = 410$, $s = 2$, $\lambda_\mathrm{S} = 100$, $\lambda_\mathrm{L} = 40$. (a) Kvazienergijų $\varepsilon_{j,\beta}$ priklausomybė nuo adiabatinės fazės išilgai trajektorijos $\varphi_t = 2\varphi_x$. (b)–(f) Vanjė funkcijos kai $\varphi_t = 2\varphi_x = 0, \pi/2, \pi, 3\pi/2, 2\pi$. Tikimybės tankiai $|w_{i,\alpha}(x,t)|^2$ atvaizduojami juoda spalva, o užtušuoti plotai nurodo erdvinius ($k = 1, 2$) ir laikinius ($\gamma = 1, 2$) narvelius. Koordinatės $x_0^{(1)}$ ir $x_0^{(2)}$ nurodo dviejų detektorių padėtis, minimas tekste.

$\varphi_t = 2\varphi_x = 2\pi$ [žr. S1(f) pav.]. Lygindami S1(b) pav. ir S1(f) pav., matome, kad transporto rezultate funkcijos $w_{i,\alpha}$ perėjo iš narvelio (i, α) į narvelį $(i + 1 \mod N,\ \alpha + 1 \mod s)$.

Dabar nurodysime šių rezultatų interpretaciją. Įsivaizduokime du detektorius – vieną nustatytą ties $x_0^{(1)} = 0.3\pi$ ir kitą – ties $x_0^{(2)} = 1.3\pi$. Tegul dalelė eksperimento pradžioje yra būsenoje $w_{1,1}$. Kai $\varphi_t = 2\varphi_x = 0$, detektorius, nustatytas ties $x_0^{(2)}$, su didžiausia tikimybe registruos dalelę laiko intervaluose $(\Omega t \mod 2\pi) \in [0, \pi)$, kas atitinka tą faktą, kad dalelė užima pirmąjį erdvinį narvelį ir pirmąjį laikinį narvelį [žr. S1(b) pav.]. Transportavimo ciklo pabai-

goje (kai $\varphi_t = 2\varphi_x = 2\pi$), dalelė su didžiausia tikimybe bus registruojama laiko intervaluose $(\Omega t \bmod 2\pi) \in [\pi, 2\pi)$ detektoriumi, esančiu ties $x_0^{(1)}$. Tai nurodo, kad dalelė užima antrąjį erdvinį narvelį ir antrąjį laikinį narvelį.

Išvados

Apibendrinant, parodėme, kad rezonansiškai žadinamos optinės gardelės kvazienergijos spektras gali būti interpretuojamas kaip kristalinės struktūros spektras, kur laikas atlieka papildomos koordinatės vaidmenį. Remdamiesi šia analogija, tyrėme adiabatinį žadinimo kitimą ir parodėme, kad jis lemia sistemos dinamikos pokytį, kuris yra topologinio transporto pasireiškimas laiko dimensijoje. Šį faktą iliustravome modeliuodami vienalaikį adiabatinį transportavimą erdvine ir laiko kryptimis.

Aštuonmatės topologinės sistemos, modeliuojamos naudojantis laiko-erdvės kristalinėmis struktūromis

Dabar toliau plėtosime laiko-erdvės kristalinės gardelės koncepciją ir pateiksime būdą, kaip tirti topologines aštuonių dimensijų (8D) sistemas, kurias galima eksperimentiškai realizuoti naudojant tik dvi fizines erdvines dimensijas. Pradėsime nuo periodiškai žadinamos vienmatės optinės gardelės su stačiais barjerais (modeliuojamais delta funkcijomis) ir parodysime, kad ji gali išlaikyti dvimatę laiko-erdvės kristalinę gardelę. Gautos laiko-erdvės kristalinės struktūros topologinis pobūdis dar kartą paaiškės nagrinėjant adiabatinį būsenų transportą laiko ir erdvės kristalinėmis kryptimis. Interpretuodami dvi adiabatines fazes kaip sintetinių papildomų dimensijų kvaziimpulsus, parodysime, kad sistemos energijos juostas apibūdina nenykstantys antrieji efektyviosios 4D gardelės Černo skaičiai. Galiausiai parodysime, kad dvi tokias 4D sistemas galima sujungti į vieną sistemą, išlaikant energijų spektre draustinį tarpą. Gautos 8D sistemos topologinės savybės apibūdinamos ketvirtuoju Černo skaičiumi ir identifikuojamos energijos juostos su nenykstančiomis ketvirtojo Černo skaičiaus reikšmėmis.

Erdvinė modelinio hamiltoniano (S1) dalis yra nesunkiai realizuojama eksperimentiškai [127, 126], tačiau tarpai tarp šio hamiltoniano energijos pajuosčių yra daug mažesni nei pajuosčių pločiai. Todėl, jei dvi tokio hamiltoniano kopijos (realizuotos ortogonaliose erdvinėse kryptyse) sujungiamos į vieną sistemą, gautame spektre nebus tarpų ir neatsiras jokių topologinių ypatybių. Todėl turime apsvarstyti kitą modelį, kuris leistų gauti tarpus, platesnius nei pajuostų pločiai.

Vienmatis, nuo laiko priklausantis hamiltonianas, kurį nagrinėsime šiame skyriuje, vėl bus (S1) pavidalo, tačiau kiekvienas narys bus kitoks. Neperturbuotas erdvinis hamiltonianas pasirenkamas pavidalu

$$\hat{h} = \hat{p}_x^2 + V \sum_{n=0}^{3N} \delta(x - \tfrac{na}{3}) + U \sum_{n=1}^{3} g_n(x) \cos\Big[\varphi_x + \tfrac{2\pi(n-1)}{3}\Big]. \tag{S4}$$

Šios sumos apibūdina erdvinį potencialą – N identiškų narvelių, kurių ilgis a, gardelę, kurių kiekvienas susideda iš trijų mazgų, atskirtų stačiais delta funkcijos barjerais. Supergardelės potencialas $g_n(x)$ lygus vienetui kiekviename n-ojo erdvinio narvelio mazge, o kitur lygus nuliui:

$$g_n(x) = \begin{cases} 1, & \frac{n}{3}a \le x \bmod a < \frac{n+1}{3}a, \\ 0, & \text{kitaip.} \end{cases} \tag{S5}$$

Taigi, paskutinis lygties (S4) narys moduliuoja (keičiant φ_x) mazgo ener-

gijas kiekviename narvelyje tokiu pačiu būdu, o U kontroliuoja moduliacijos amplitudę. Kiekviename sekančiame mazge moduliacijos fazė atsilieka nuo fazės kairiajame kaimyniniame narvelyje. Jei moduliacija atliekama adiabatiškai, topologinis transportas gali būti realizuotas sistemoje, aprašomojoje hamiltonianu (S4). Aštrių (mažesnio už bangos ilgį pločio) optinių barjerų realizavimas ir taip pat topologinis transportas trijų mazgų per narvelį gardelėje jau buvo tirti literatūroje [195, 144, 145].

Erdvinis hamiltonianas yra žadinamas nariais

$$\xi_{\mathrm{S}}(x,t) = \lambda_{\mathrm{S}} \cos(\tfrac{12\pi x}{a}) \cos(2\omega t), \tag{S6a}$$

$$\xi_{\mathrm{L}}(x,t|\varphi_t) = \lambda_{\mathrm{L}} \cos(\tfrac{6\pi x}{a}) \cos(\omega t + \varphi_t), \tag{S6b}$$

čia λ_{S} ir λ_{L} kontroliuoja bendrą perturbacijos stiprumą. Erdviniai dažniai $6\pi/a$ ir $12\pi/a$ užtikrina, kad visi erdviniai mazgai būtų perturbuojami vienodai. Žadinimo dažnis ω parenkamas taip, kad kiekviename erdviniame mazge būtų įvykdyta rezonansinė sąlyga. Klasikiniame aprašyme rezonansas reiškia, kad ω yra labai artimas dalelės periodinio judėjimo potenciale dažnio Ω sveikojo skaičiaus kartotiniui, t.y. $\omega \approx s\Omega$, čia s yra sveikasis skaičius. Kvantiniame aprašyme rezonansas atitinka dažnį ω, esantį artimą tarpo Ω tarp tam tikrų Hamiltoniano (S4) juostų sveikojo skaičiaus kartotiniui. Riboje $V \to \infty$ [žr. lygtį (S4)] kiekviename erdviniame mazge dėl rezonansinio žadinimo poveikio susidaro nepriklausoma laiko kristalinė struktūra. Tiksliau sakant, rezonansine trajektorija besivystančioje sistemoje dalelės rezonansinę dinamiką galima apibūdinti taip: $\hat{H}_{\mathrm{eff}} = \hat{\tilde{p}}_{\tilde{x}}^2 + \tilde{\lambda}_{\mathrm{S}} \cos(2s\tilde{x}) + \tilde{\lambda}_{\mathrm{L}} \cos(s\tilde{x} + \varphi_t)$ su $\tilde{x} \in [0, 2\pi)$. Pavyzdžiui, kai $s = 2$, turime du laikinius kristalinius narvelius, kurių kiekvienas susideda iš dviejų laikinių mazgų. Adiabatinės fazės φ_t kitimas leidžia realizuoti topologinį transportą laiko-kristalinėje struktūroje. Jei V yra baigtinis, dalelės tuneliavimas tarp erdvinių mazgų tampa įmanomu, o visa sistema sudaro 2D laiko-erdvės kristalinę struktūrą, kurią, kaip parodysime, galima apibūdinti 2D stipraus ryšio modeliu.

Vanjė funkcijų bazėje kvazienergijos operatorius $\hat{Q} = \hat{H} - \mathrm{i}\partial_t$ įgyja pavidalą

$$\hat{H}_{\mathrm{TB}}(\varphi_x, \varphi_t) = \sum_{\ell',\ell} J_{\ell'\ell}(\varphi_x, \varphi_t) \hat{a}_{\ell'}^\dagger \hat{a}_\ell, \tag{S7}$$

čia operatorius $\hat{a}_\ell^\dagger$ sukuria (o $\hat{a}_\ell$ sunaikina) bozoną gardelės mazge ℓ. Indeksas $\ell \in [1, 6Ns]$ numeruoja 2D laiko-erdvės gardelės mazgus. Matriciniai elementai $J_{\ell'\ell}$ skaičiuojami pagal

$$J_{\ell'\ell} = \int_0^{sT} \frac{\mathrm{d}t}{sT} \langle w_{\ell'} | \hat{Q} | w_\ell \rangle, \tag{S8}$$

čia $T = 2\pi/\omega$ yra žadinimo periodas.

Hamiltonianas (S7) gali būti apytiksliai suskaidytas į dvi nepriklausomas dalis — erdvinę ir laikinę:

$$\hat{H}_{\mathrm{TB}} \approx \hat{I}^{(x)} \otimes \hat{H}^{(t)} + \hat{H}^{(x)} \otimes \hat{I}^{(t)} \equiv \hat{H}'_{\mathrm{TB}}, \tag{S9}$$

čia $\otimes$ žymi tenzorinę sandaugą, $\hat{H}^{(x)}$ ir $\hat{H}^{(t)}$ yra, atitinkamai, erdvinis ir laikinis hamiltonianas, o $\hat{I}^{(x)}$ ir $\hat{I}^{(t)}$ yra vienetiniai operatoriai, veikiantys operatorių $\hat{H}^{(x)}$ ir $\hat{H}^{(t)}$ erdvėse. Hamiltoniano $\hat{H}'_{\mathrm{TB}}$ tikrinių verčių spektras yra Minkovskio suma tikrinių verčių spektrų hamiltonianų $\hat{H}^{(x)}$ ir $\hat{H}^{(t)}$. Paprastumo dėlei visų stipraus ryšio hamiltonianų tikrines vertes vadinsime energijomis.

Hamiltonianų $\hat{H}^{(x)}$ ir $\hat{H}^{(t)}$ spektrai parodyti S2(a) ir S2(b) pav. kartu su juostų Černo skaičiais. Nagrinėdami erdvinę uždavinio dalį, aprašomą hamiltonianu $\hat{H}^{(x)}$, fazę φ_x galime interpretuoti kaip kvaziimpulsą. Tai leidžia įvesti n-osios juostos Berio kreivumą $\Omega_{k_x\varphi_x} = 2\Im \langle \partial_{k_x} \chi_{n,k_x} | \partial_{\varphi_x} \chi_{n,k_x} \rangle$ ir atitinkamą pirmąjį Černo skaičių

$$\nu_1^{(x)} = \frac{1}{2\pi} \int_0^{2\pi} \mathrm{d}k_x \int_0^{\pi} \mathrm{d}\varphi_x \, \Omega_{k_x\varphi_x}(k_x, \varphi_x). \tag{S10}$$

Berio kreivumo apibrėžime, $|\chi_{n,k_x}\rangle$ žymi hamiltoniano $\hat{H}^{(x)}$ Blocho funkcijos $\mathrm{e}^{\mathrm{i}k_x j}\chi_{n,k_x}(j)$ periodinę dalį, su sąlyga $\chi_{n,k_x}(j+3) = \chi_{n,k_x}(j)$, čia j numeruoja erdvinius narvelius. Pagal analogiją su erdvine dalimi, įvedamas laikinis kvaziimpulsas k_t hamiltonianui $\hat{H}^{(t)}$, kurio tikrinės funkcijos gali būti išreikštos kaip $\mathrm{e}^{\mathrm{i}k_t\alpha}\tau_{n,k_t}(\alpha)$ su $\tau_{n,k_t}(\alpha+2) = \tau_{n,k_t}(\alpha)$. Atitinkamai, pirmieji Černo skaičiai $\nu_1^{(t)}$, parodyti S2(b) pav., apibrėžiami per Berio kreivumo $\Omega_{k_t\varphi_t}$ integralą.

Interpretuodami Berio kreivumų formulėse figūruojančias fazes φ_x ir φ_t kaip fiktyvių dimensijų kvaziimpulsus, mes galime padidinti sistemos dimensiškumą. Tuomet kiekvienas iš hamiltonianu $\hat{H}^{(x)}$ ir $\hat{H}^{(t)}$ aprašo 2D sistemą, o jų kombinacija $\hat{H}'_{\mathrm{TB}}$, kurios spektras parodytas S2(c) pav., aprašo 4D sistemą. Žemiausioji ir aukščiausioji juostos yra neišsigimusios ir yra aprašomos antruoju Černo skaičiumi, skaičiuojamu iš abelinio Berio kreivumo. Formaliai, sistemos parametrai gali būti surinkti į vektorių $\boldsymbol{R} = (k_x, \varphi_x, k_t, \varphi_t)$, o kreivumas apskaičiuotas kaip $\Omega_{\mu\nu}(\boldsymbol{R}) = 2\Im \langle \partial_\mu \xi_{n,k_x,k_t} | \partial_\nu \xi_{n,k_x,k_t} \rangle$, čia $\partial_\mu \equiv \frac{\partial}{\partial R^\mu}$, $\mu = 1,2,3,4$, o $|\xi_{n,k_x,k_t}\rangle$ yra periodinė dalis n-osios hamiltoniano $\hat{H}'_{\mathrm{TB}}$ energijos juostos Blocho funkcijos. Išraiška (S9) lemią faktorizavimą $|\xi_{n,k_x,k_t}\rangle = |\chi_{n,k_x}\rangle \otimes |\tau_{n,k_t}\rangle$, todėl antrasis Černo skaičius yra

$$\nu_2^{(x,t)} = \nu_1^{(x)} \nu_1^{(t)}. \tag{S11}$$

Vertės $\nu_2^{(x,t)}$ yra nurodytos S2(c) pav.

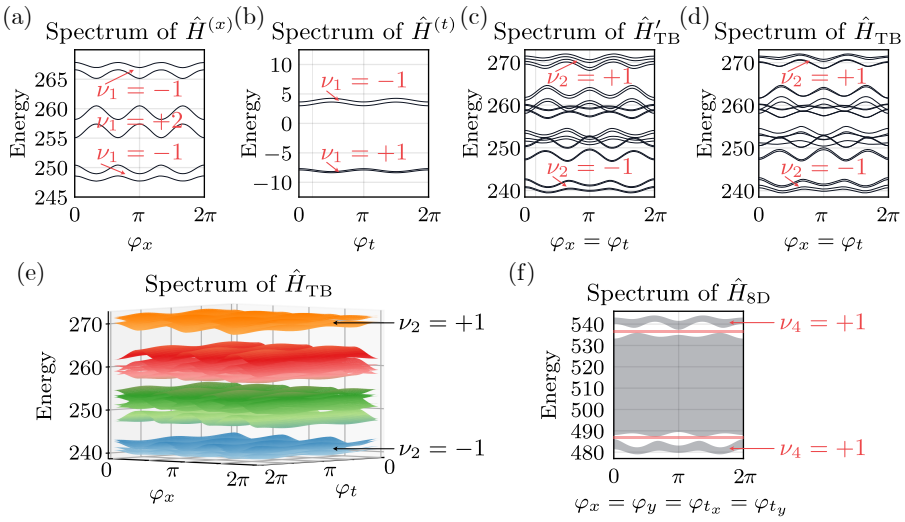

S2 pav.: Sistemų energijos spektrai. (a) Erdvinio hamiltoniano $\hat{H}^{(x)}$ spektras. (b) Laikinio hamiltoniano $\hat{H}^{(t)}$ spektras. (c) Hamiltoniano $\hat{H}'_{\mathrm{TB}}$ spektras, lygus Minkovskio sumai spektrų, parodytų (a) ir (b) dalyse. Parodytas spektro pjūvis išilgai linijos $\varphi_x = \varphi_t$. (d) Hamiltoniano $\hat{H}_{\mathrm{TB}}$ energijos spektras išilgai linijos $\varphi_x = \varphi_t$. (e) Hamiltoniano $\hat{H}_{\mathrm{TB}}$ energijos juostos. (f) Aštuonmatės sistemos energijos spektras, gautas sudėjus dvi nepriklausomas 4D sistemas, kurių spektrai parodyti (e) dalyje. Pilki plotai atitinka energijų juostas (atskiri lygmenys nėra parodyti), o raudoni plotai nurodo draustinius tarpus.

Lygindami $\hat{H}'_{\mathrm{TB}}$ spektrą su tikslaus stipriojo ryšio hamiltoniano $\hat{H}_{\mathrm{TB}}$ spektru, parodytu S2(d) pav., pastebime, kad jie yra beveik identiški. Nedideli neatitikimai yra tikėtini, nes norėdami gauti atskiriamą hamiltonianą, mes nepaisėme kai kurių labai silpnų sąveikų tiksliame hamiltoniane. Nepaisant to, $\hat{H}_{\mathrm{TB}}$ ir $\hat{H}'_{\mathrm{TB}}$ energijos juostų antrieji Černo skaičiai yra vienodi. Tai patvirtina faktas, kad $\hat{H}_{\mathrm{TB}}$ energijos spektrą galima gauti adiabatiškai deformuojant $\hat{H}'_{\mathrm{TB}}$ spektrą neuždarant draustinio tarpo. Taip pat pastebėsime, kad tarpas žemiau aukščiausios $\hat{H}_{\mathrm{TB}}$ energijos juostos išlieka atviras visoms φ_x ir φ_t reikšmėms, kaip parodyta S2(e) pav. Tas pats galioja ir tarpui virš žemiausios $\hat{H}_{\mathrm{TB}}$ juostos.

Pagaliau, panagrinėkime optinę gardelę, sukurtą dviejose ortogonaliose erdvinėse dimensijose taip, kad sistema būtų aprašoma hamiltonianu

$$\hat{H}_{4\mathrm{D}} = \hat{H}(x, \hat{p}_x, t|\varphi_x, \varphi_{t_x}) + \hat{H}(y, \hat{p}_y, t|\varphi_y, \varphi_{t_y}). \tag{S12}$$

Tai sukuria 4D laiko-erdvės kristalinę struktūrą, kadangi Vanjė funkcijos dabar turės keturis nepriklausomus indeksus:

$$W_{\boldsymbol{j},\boldsymbol{\alpha}}(x, y, t) = w_{j_x,\alpha_x}(x, t) w_{j_y,\alpha_y}(y, t), \tag{S13}$$

čia $\boldsymbol{j} = (j_x, j_y)$ ir $\boldsymbol{\alpha} = (\alpha_x, \alpha_y)$ [49]. Dvimatė laikinė struktūra sudaryta iš $2s \times 2s$ mazgų gaunama kiekviename dvimačiame erdviniame narvelyje; judėjimas laikiniuose narveliuose yra charakterizuojamas laikiniai kvaziimpulsais k_{t_x} ir k_{t_y}. Šios sistemos energijos spektrą galima lengvai gauti kaip dviejų S2(e) pav. pavaizduotų spektrų kopijų Minkovskio sumą. Rezultatas parodytas S2(f) pav., kur akivaizdu, kad aukščiausią ir žemiausią juostas nuo kitų skiria tarpai. Tai galioja ne tik parodytam spektro pjūviui ties $\varphi_x = \varphi_y = \varphi_{t_x} = \varphi_{t_y}$, bet visoms fazės vertėms. Aukščiausios juostos pločio ir tarpo žemiau jos santykis yra 5%, o žemiausios juostos pločio ir tarpo virš jos santykis yra 2%.

Sistema, kurios spektras parodytas S2(f) pav., gali būti aprašyta hamiltonianu

$$\hat{H}_{8\mathrm{D}} = \hat{I} \otimes \hat{H}_{\mathrm{TB}}^{(x)} + \hat{H}_{\mathrm{TB}}^{(y)} \otimes \hat{I}, \tag{S14}$$

čia $\hat{I}$ yra vienetinė matrica to paties dydžio kaip ir $\hat{H}_{\mathrm{TB}}$. Sistemos parametrai yra du kvaziimpulsai k_x, k_y, erdvinės fazės φ_x bei φ_y, ir keturi atitinkami dviejų laikinių sistemų parametrai: k_{t_x}, k_{t_y}, φ_{t_x}, φ_{t_y}. Kaip ir 4D atveju, žemiausioji ir aukščiausioji juostos yra neišsigimusios, todėl gali būti charakterizuojamos ketvirtuoju Černo skaičiumi, skaičiuojamu iš atitinkamo abelinio Berio kreivumo. Surinkime hamiltoniano $\hat{H}_{8\mathrm{D}}$ parametrus į vektorių

$$\boldsymbol{R} = (k_x, \varphi_x, k_{t_x}, \varphi_{t_x}, k_y, \varphi_y, k_{t_y}, \varphi_{t_y}). \tag{S15}$$

Abelinis Berio kreivumas yra skaičiuojamas naudojant neišsigimusios $\hat{H}_{8\mathrm{D}}$ energijos juostos tikrines būsenas pagal formulę

$$\Omega_{\mu\nu}(\boldsymbol{R}) = 2\Im \left\langle \partial_\mu \zeta_{\boldsymbol{R}} | \partial_\nu \zeta_{\boldsymbol{R}} \right\rangle, \tag{S16}$$

čia $\partial_\mu \equiv \frac{\partial}{\partial R^\mu}$, indeksas μ prabėga vertes nuo 1 iki 8, o $|\zeta_{\boldsymbol{R}}\rangle$ yra periodinė tikrinės būsenos dalis. Tegul $|k_x, \varphi_x, k_{t_x}, \varphi_{t_x}\rangle$ yra periodinė dalis hamiltoniano $\hat{H}_{\mathrm{TB}}^{(x)}$ tikrinės būsenos, atitinkančios tam tikrą energijos juostą; tada (S14) lemia $|\zeta_{\boldsymbol{R}}\rangle = |k_x, \varphi_x, k_{t_x}, \varphi_{t_x}\rangle \otimes |k_y, \varphi_y, k_{t_y}, \varphi_{t_y}\rangle$.

Ketvirtasis Černo skaičius gali būti išreikštas per Berio kreivumo dviformas kaip [59]

$$\nu_4 = \frac{1}{(2\pi)^4} \int \frac{1}{4!} \Omega \wedge \Omega \wedge \Omega \wedge \Omega, \tag{S17}$$

ir dėl sistemos atskiriamumo ši išraiška supaprastėja iki

$$\nu_4 = \frac{1}{(2\pi)^4} \int \Omega_{12}\Omega_{34}\Omega_{56}\Omega_{78}\, \mathrm{d}R^1 \wedge \cdots \wedge \mathrm{d}R^8 = \nu_2^{(x,t_x)} \nu_2^{(y,t_y)}. \tag{S18}$$

Reikšmės ν_4 pateiktos S2(f) pav. Tokiu būdu patvirtiname, kad aukščiausia ir žemiausia 8D sistemos juostos pasižymi nenuliniais ketvirtaisiais Černo skaičiais, o tai rodo topologiškai netrivialų sistemos pobūdį. Pastebėsime, kad jei

$\hat{H}_{8\mathrm{D}}$ sukonstruojamas naudojant dvi apytikslio Hamiltono $\hat{H}'_{\mathrm{TB}}$ kopijas, aukštesnis tarpas užsidaro, o apatinis lieka atviras.

Paveiksle S2(f) matyti, kad aukščiausia ir žemiausia juostos yra platesnės už tarpus, o tai reiškia, kad tarpai išnyksta, jei pridedama dar viena S2(e) pav. pateikto spektro kopija. Nepaisant to, laiko-erdvės struktūra, pagrįsta kita erdvine sistema nei aprašoma (S4) lygtimi, gali turėti dar platesnius tarpus lyginant su pateiktais S2(e) pav. Tai leistų realizuoti 12D laiko-erdvės struktūrą, sujungiant tris $\hat{H}_{\mathrm{TB}}$ kopijas, kurių kiekviena realizuota atskiroje fizinėje dimensijoje (x, y ir z).

Išvados

Apibendrinant, parodėme, kad laiko-erdvės kristalai gali būti naudojami kaip platforma tiriant 8D sistemas, kurias galima apibrėžti stipraus ryšio modeliu. Sukūrėme konkrečią, eksperimentiškai realizuojamą žadinamą kvantinę sistemą, kuri yra topologiškai netrivialios 8D sistemos pavyzdys. Įdomu tai, kad tinkamai žadinamos 2D sistemos pagalba ir neįtraukiant jokių dalelių vidinių laisvės laipsnių, įmanoma realizuoti sistemas su netrivialiomis topologinėmis savybėmis ir tirti gaunamus efektus aštuoniuose matmenyse. Daugiamatės laiko-erdvės kristalinės struktūros atveria galimybes kurti praktiškus įrenginius, kurie būtų neįsivaizduojami trijuose matmenyse. Šiame darbe pateikti rezultatai atveria kelią tolesniems tyrimams šia kryptimi.

Išplėstinė išsigimusi perturbacijos teorija Flokė ir Hilberto erdvėje

Laiko kristalinių struktūrų tyrimas, pateiktas praeituose skyriuose, dar kartą parodo periodiškai žadinamų sistemų, kaip platformos neįprastoms fizikinėms sistemoms realizuoti, svarbą. Teorinė tokių sistemų analizė remiasi Flokė teorija. Praeituose skyriuose buvo nagrinėjamos rezonansiškai žadinamomis viendalelinės sistemos, todėl jas galima buvo analizuoti naudojant sekuliariąją aproksimaciją. Šiame gi skyriuje plėtosime metodą, skirtą rezonansiškai žadinamoms daugiadalelinėms sistemoms tirti. Konkrečiai, pristatysime būdą, kaip sukonstruoti efektyvinį Hamiltonianą iš kvazienergijos operatoriaus tuo atveju, kai žadinimas yra rezonansinis ir lemia išsigimimus.

Efektyvinį hamiltonianą patogu konstruoti išplėstinėje Flokė ir Hilberto erdvėje, kur nuo laiko priklausantys operatoriai tampa begalinėmis matricomis, turinčiomis blokų juostų struktūrą. Norėdami pereiti prie šios erdvės, pradedame pastebėdami, kad Hilberto erdvės $\mathscr{H}$ Flokė modos $|u_\alpha(t)\rangle$ tenkina lygtį $\hat{Q}|u_\alpha(t)\rangle = \varepsilon_\alpha|u_\alpha(t)\rangle$, čia $\hat{Q} = \hat{H} - \mathrm{i}\partial_t$ yra kvazienergijos operatorius. Šios modos gali būti laikomos elementais sudėtinės Flokė ir Hilberto erdvės $\mathscr{F}$, apibrėžtos kaip erdvės $\mathscr{H}$ ir laiko periodinių funkcijų erdvės $\mathscr{T}$ tenzorinė sandauga [148–150]. Erdvės $\mathscr{F}$ elementams naudosime žymėjimą $|u_\alpha\rangle\!\rangle$, o vidinę sandaugą $\mathscr{F}$ erdvėje apibrėšime kaip $\langle\!\langle u_\beta|u_\alpha\rangle\!\rangle = \frac{1}{T}\int_0^T \langle u_\beta(t)|u_\alpha(t)\rangle\,\mathrm{d}t$. Bazė, apimanti $\mathscr{F}$, yra $|\alpha m\rangle\!\rangle \Leftrightarrow |\alpha\rangle \mathrm{e}^{\mathrm{i}m\omega t}$, čia $m \in \mathbb{Z}$, o vektoriai $|\alpha\rangle$ sudaro bazę erdvėje $\mathscr{H}$; $\omega = 2\pi/T$ yra žadinimo dažnis. Kvazienergijos operatorius tada įgauna blokų juostų struktūrą:

$$\langle\!\langle \alpha' m'|\bar{Q}|\alpha m\rangle\!\rangle = \langle\alpha'|\hat{H}_{m'-m}|\alpha\rangle + \delta_{m'm}\delta_{\alpha'\alpha} m\omega, \tag{S19}$$

o blokuose yra Furjė atvaizdai $\hat{H}_m = \frac{1}{T}\int_0^T \hat{H}(t)\mathrm{e}^{\mathrm{i}m\omega t}\mathrm{d}t$. Čia ir toliau $\mathscr{F}$ erdvės operatorius žymėsime viršutiniais brūkšneliais. Lygtį (S19) galime iliustruoti šitokia matrica

$$\bar{Q} = \begin{pmatrix} \ddots & \vdots & \vdots & \vdots & \iddots \\ \cdots & \hat{H}_0 - \hat{I}\omega & \hat{H}_{-1} & \hat{H}_{-2} & \cdots \\ \cdots & \hat{H}_1 & \hat{H}_0 & \hat{H}_{-1} & \cdots \\ \cdots & \hat{H}_2 & \hat{H}_1 & \hat{H}_0 + \hat{I}\omega & \cdots \\ \iddots & \vdots & \vdots & \vdots & \ddots \end{pmatrix}, \tag{S20}$$

čia $\hat{I}$ yra erdvės $\mathscr{H}$ vienetinis operatorius.

Efektyvinį hamiltonianą galimą rasti diagonalizuojant blokais operatorių $\bar{Q}$. Transformuoto kvazienergijos operatoriaus perturbacinis skleidinys gali būti

užrašytas pavidalu

$$\mathrm{e}^{-\bar{G}}\bar{Q}\mathrm{e}^{\bar{G}} = \bar{Q}^{(0)} + (\bar{W}_{\mathrm{D}}^{(1)} + \bar{W}_{\mathrm{X}}^{(1)}) + (\bar{W}_{\mathrm{D}}^{(2)} + \bar{W}_{\mathrm{X}}^{(2)}) + \dots \tag{S21}$$

Čia $\bar{Q}^{(0)}$ yra neperturbuota $\bar{Q}$ dalis, kurią galima užrašyti pavidalu $\bar{Q}^{(0)} = \bar{Q}_0 + \bar{W}_{\mathrm{D}}^{(0)}$ įvedus operatorių

$$\bar{Q}_0 \Leftrightarrow -\mathrm{i}\partial_t, \qquad \langle\!\langle \alpha' m' | \bar{Q}_0 | \alpha m \rangle\!\rangle = \delta_{m'm}\delta_{\alpha'\alpha} m\omega. \tag{S22}$$

Indeksai „D“ ir „X“ nurodo į diagonalinių blokų ir nediagonalinių blokų elementus:

$$\begin{aligned} \langle\!\langle \alpha' m' | \bar{O}_{\mathrm{D}} | \alpha m \rangle\!\rangle &= \langle\!\langle \alpha' m' | \bar{O} | \alpha m \rangle\!\rangle \delta_{m'm}, \\ \langle\!\langle \alpha' m' | \bar{O}_{\mathrm{X}} | \alpha m \rangle\!\rangle &= \langle\!\langle \alpha' m' | \bar{O} | \alpha m \rangle\!\rangle (1 - \delta_{m'm}). \end{aligned} \tag{S23}$$

Mūsų tikslas yra rasti unitarinį operatorių $\bar{G} = \bar{G}^{(1)} + \bar{G}^{(2)} + \dots$ tokį, kad nediagonalūs elementai $\bar{W}_{\mathrm{X}}^{(n)}$ būtų lygūs nuliui, tam tikros eilės tikslumu. Likęs diagonalinių blokų operatorius $\bar{Q}^{(0)} + \bar{W}_{\mathrm{D}}^{(1)} + \bar{W}_{\mathrm{D}}^{(2)} + \dots$ bus pavidalo $\delta_{m'm}(\langle\alpha'|\hat{W}_{\mathrm{D}}^{[n]}|\alpha\rangle + \delta_{\alpha'\alpha} m\omega)$, kur $\hat{W}_{\mathrm{D}}^{[n]} \equiv \hat{W}_{\mathrm{D}}^{(0)} + \hat{W}_{\mathrm{D}}^{(1)} + \dots + \hat{W}_{\mathrm{D}}^{(n)}$ yra ieškomas efektyvinis hamiltonianas. Operatoriaus $\bar{Q}$ tikrinių verčių spektras gali būti užrašytas kaip $\varepsilon_{\alpha m} = \varepsilon_\alpha + m\omega$. Tai reiškia, kad bet kuris ω pločio kvazienergijų intervalas perneša tą pačią fizikinę informaciją, ir šie intervalai vadinami Flokė zonomis pagal analogiją su Briliueno zonomis.

Standartinis $\hat{W}_{\mathrm{D}}^{[n]}$ paieškos būdas yra skleidinio $1/\omega$ eilute konstravimas [151, 149, 152, 153, 28, 154, 150]. Operatoriaus $\hat{W}_{\mathrm{D}}^{[n]}$ skaičiavimas aukšo dažnio riboje remiasi prielaida, kad neperturbuoto hamiltoniano spektras yra aprėžtas ir kad jo plotis yra daug mažesnis už ω. Tokiu atveju kvazienergijos operatorių galima atskirti į dalis pagal $\bar{Q} = \bar{Q}_0 + \bar{H}$ su $\hat{H}(t) \Leftrightarrow \bar{H}$. Operatoriaus $\bar{H}$ elementai laikomi mažais lyginant su ω, todėl $\bar{H}$ gali būti įskaitomas kaip perturbacija. Tuomet skleidinys (S21) tampa skleidiniu $1/\omega$ laipsniais. Tačiau jeigu yra galimi perėjimai tarp būsenų, energijų skirtumas tarp kurių yra ω, tenka įskaityti diagonalius $\bar{H}$ elementus neperturbuotoje dalyje, o tai lemia išsigimimo atsiradimą. Būtent, jeigu skirtumas $E_\beta - E_\alpha$ tarp dviejų diagonalių $\hat{H}_0$ elementų yra lygus (arba artimas) dydžiui $n\omega$ su sveikuoju n, tada išsigimimas $\langle\!\langle \beta(m+n)|\bar{Q}|\beta(m+n)\rangle\!\rangle = \langle\!\langle \alpha m|\bar{Q}|\alpha m\rangle\!\rangle$ lemia perturbacijos teorijos divergavimą. Tokiu atveju galima taikyti standartinę išsigimusią perturbacijos teoriją (DPT) – žr. [109, 157] – kuomet efektyvinis hamiltonianas yra konstruojamas įskaitant sąveiką tarp išsigimusių lygmenų tiksliai, o sąveiką su visais kitais lygmenimis – kaip trikdį [155, 156].

Šiame skyriuje kursime išplėstinę išsigimusią perturbacijos teoriją (EDPT) Flokė ir Hilberto erdvėje, kad rastume efektinio hamiltoniano $\hat{W}_{\mathrm{D}}^{[n]}$ išraiškas,

kurios užtikrina tikslesnį kvazienergijų spektro skaičiavimą esant tiksliam rezonansui ir arti jo. Pradedame nuo to, kad įvedame redukuotas energijas

$$\varepsilon_\alpha^{(0)} = E_\alpha - a\omega \in \mathrm{FZ}, \quad a \in \mathbb{Z}. \tag{S24}$$

Tai yra operatoriaus $\hat{H}_0$ diagonalieji elementai E_α, redukuoti į pasirinktą Flokė zoną (FZ), kurios plotis sudaro ω. Tokiu būdu kiekvienai būsenai $|\alpha\rangle$ priskiriamas sveikasis skaičius a; bendru atveju kelios būsenos turės tą patį skaičių a. Simbolius a, a', b, ir c toliau naudosime atitinkamai būsenų $|\alpha\rangle$, $|\alpha'\rangle$, $|\beta\rangle$, ir $|\gamma\rangle$ „redukcijos skaičiams“ žymėti. Kitame žingsnyje pertvarkome $\bar{Q}$ elementus taip, kad m-asis diagonalus blokas turėtų energijas, redukuotas į m-ąją FZ. Gaunamo kvazienergijos operatoriaus $\bar{Q}'$ diagonalieji elementai tuomet bus lygūs

$$\varepsilon_{\alpha m}^{(0)} \equiv \langle\!\langle \alpha m|\bar{Q}'|\alpha m\rangle\!\rangle = \varepsilon_\alpha^{(0)} + m\omega \tag{S25}$$

o visi kiti elementai

$$\langle\!\langle \alpha' m'|\bar{Q}'|\alpha m\rangle\!\rangle = \langle\alpha'|\hat{H}_{a-a'+m'-m}|\alpha\rangle + \delta_{m'm}\delta_{\alpha'\alpha} m\omega. \tag{S26}$$

Kvazienergijos matrica išlaiko blokinę struktūrą, kuri gali būti vizualizuota šitaip:

$$\bar{Q}' = \begin{pmatrix} \ddots & \vdots & \vdots & \vdots & \iddots \\ \cdots & \hat{D} - \hat{I}\omega & \hat{X}_{-1} & \hat{X}_{-2} & \cdots \\ \cdots & \hat{X}_1 & \hat{D} & \hat{X}_{-1} & \cdots \\ \cdots & \hat{X}_2 & \hat{X}_1 & \hat{D} + \hat{I}\omega & \cdots \\ \iddots & \vdots & \vdots & \vdots & \ddots \end{pmatrix}, \tag{S27}$$

čia diagonaliniai blokai yra

$$\hat{D} = \begin{pmatrix} \varepsilon_\alpha^{(0)} & H_{b-a}^{\alpha\beta} & H_{c-a}^{\alpha\gamma} \\ H_{a-b}^{\beta\alpha} & \varepsilon_\beta^{(0)} & H_{c-b}^{\beta\gamma} \\ H_{a-c}^{\gamma\alpha} & H_{b-c}^{\gamma\beta} & \varepsilon_\gamma^{(0)} \end{pmatrix}, \tag{S28}$$

o nediagonalūs aprašomi

$$\hat{X}_m = \begin{pmatrix} H_m^{\alpha\alpha} & H_{b-a+m}^{\alpha\beta} & H_{c-a+m}^{\alpha\gamma} \\ H_{a-b+m}^{\beta\alpha} & H_m^{\beta\beta} & H_{c-b+m}^{\beta\gamma} \\ H_{a-c+m}^{\gamma\alpha} & H_{b-c+m}^{\gamma\beta} & H_m^{\gamma\gamma} \end{pmatrix}. \tag{S29}$$

Trumpumo dėlei matricos $\hat{D}$ ir $\hat{X}_m$ parodytos trijų lygmenų sistemos atveju (atitinkamai, bazę Hilberto erdvėje sudaro būsenos $|\alpha\rangle$, $|\beta\rangle$, ir $|\gamma\rangle$) ir pažymėta $H_m^{\alpha'\alpha} \equiv \langle\alpha'|\hat{H}_m|\alpha\rangle$. Centrinis blokas $\hat{D}$ aprašo centrinės ($m = 0$) FZ būsenas

ir jų tarpusavio sąveikas, kurios bus įskaitytos tiksliai. Nediagonalieji blokai $\hat{X}_m$ aprašo sąveikas tarp skirtingų Flokė zonų; šios sąveikos bus įskaitytos perturbatyviai.

Išvedimą pradedame nuo to, kad suskaidome $\bar{Q}'$ į neperturbuotą dalį ir perturbaciją, o pastaroji turi diagonalinių blokų ir nediagonalinių blokų dalis:

$$\bar{Q}' = \bar{Q}'^{(0)} + \bar{V}_{\mathrm{D}} + \bar{V}_{\mathrm{X}}, \tag{S30}$$

čia

$$\begin{aligned} \langle\!\langle \alpha' m' | \bar{Q}'^{(0)} | \alpha m \rangle\!\rangle &= \varepsilon^{(0)}_{\alpha m} \delta_{\alpha'\alpha} \delta_{m'm}, \\ \langle\!\langle \alpha' m' | \bar{V}_{\mathrm{D}} | \alpha m \rangle\!\rangle &= \langle \alpha' | \hat{H}_{a-a'} | \alpha \rangle (1 - \delta_{\alpha'\alpha}) \delta_{m'm}, \\ \langle\!\langle \alpha' m' | \bar{V}_{\mathrm{X}} | \alpha m \rangle\!\rangle &= \langle \alpha' | \hat{H}_{a-a'+m'-m} | \alpha \rangle (1 - \delta_{m'm}). \end{aligned} \tag{S31}$$

Įstatydami $\bar{Q}'$ į (S21) lygtį ir laikydami $\bar{G} = \bar{G}^{(1)} + \bar{G}^{(2)} + \ldots$, surenkame tos pačios eilės narius. Nulinės eilės narys yra

$$\langle \alpha' | \hat{W}^{(0)}_{\mathrm{D}} | \alpha \rangle = \varepsilon^{(0)}_{\alpha} \delta_{\alpha'\alpha}. \tag{S32}$$

Pirmos eilės nariui gauname

$$\langle \alpha' | \hat{W}^{(1)}_{\mathrm{D}} | \alpha \rangle = \langle \alpha' | \hat{H}_{a-a'} | \alpha \rangle (1 - \delta_{\alpha'\alpha}), \tag{S33}$$

o antroje eilėje randame

$$\begin{aligned} \langle \alpha' | \hat{W}^{(2)}_{\mathrm{D}} | \alpha \rangle = \frac{1}{2} \sum_{\beta} \sum_{n \neq 0} & \langle \alpha' | \hat{H}_{-(a'-b+n)} \, | \beta \rangle \langle \beta | \, \hat{H}_{a-b+n} | \alpha \rangle \\ & \times \left(\frac{1}{\varepsilon^{(0)}_{\alpha'} - \varepsilon^{(0)}_{\beta} - n\omega} + \frac{1}{\varepsilon^{(0)}_{\alpha} - \varepsilon^{(0)}_{\beta} - n\omega} \right). \end{aligned} \tag{S34}$$

Pagaliau, trečios eilės išraiška yra

$$\begin{aligned}
\langle\alpha'|\hat{W}_{\mathrm{D}}^{(3)}|\alpha\rangle &= \frac{1}{2}\sum_{\beta,\gamma}\sum_{p\neq 0}\Bigg[\frac{1}{\varepsilon_\beta-\varepsilon_\gamma-p\omega}\\
&\times\Bigg(\frac{\langle\alpha'|\hat{H}_{b-a'}|\beta\rangle\langle\beta|\hat{H}_{c-b-p}|\gamma\rangle\langle\gamma|\hat{H}_{a-c+p}|\alpha\rangle}{\varepsilon_\gamma-\varepsilon_{\alpha'}+p\omega}\\
&\quad+\frac{\langle\alpha'|\hat{H}_{c-a'-p}|\gamma\rangle\langle\gamma|\hat{H}_{b-c+p}|\beta\rangle\langle\beta|\hat{H}_{a-b}|\alpha\rangle}{\varepsilon_\gamma-\varepsilon_\alpha+p\omega}\Bigg)\\
&+\langle\alpha'|\hat{H}_{b-a'-p}|\beta\rangle\langle\beta|\hat{H}_{c-b}|\gamma\rangle\langle\gamma|\hat{H}_{a-c+p}|\alpha\rangle\\
&\times\left(\frac{1}{(\varepsilon_{\alpha'}-\varepsilon_\beta-p\omega)(\varepsilon_{\alpha'}-\varepsilon_\gamma-p\omega)}+\frac{1}{(\varepsilon_\alpha-\varepsilon_\beta-p\omega)(\varepsilon_\alpha-\varepsilon_\gamma-p\omega)}\right)\Bigg]\\
&-\frac{1}{12}\sum_{\beta\gamma}\sum_{p\neq 0}\sum_{q\neq 0,p}\langle\alpha'|\hat{H}_{b-a'-p}|\beta\rangle\langle\beta|\hat{H}_{c-b+p-q}|\gamma\rangle\langle\gamma|\hat{H}_{a-c+q}|\alpha\rangle\\
&\times\Bigg[\frac{3}{\varepsilon_\beta-\varepsilon_\alpha+p\omega}\left(\frac{1}{\varepsilon_\alpha-\varepsilon_\gamma-q\omega}+\frac{1}{\varepsilon_\beta-\varepsilon_\gamma+(p-q)\omega}\right)\\
&\quad+\frac{3}{\varepsilon_{\alpha'}-\varepsilon_\gamma-q\omega}\left(\frac{1}{\varepsilon_\beta-\varepsilon_\gamma+(p-q)\omega}+\frac{1}{\varepsilon_\beta-\varepsilon_{\alpha'}+p\omega}\right)\\
&\quad+\frac{1}{\varepsilon_\beta-\varepsilon_\gamma+(p-q)\omega}\left(\frac{1}{\varepsilon_\beta-\varepsilon_{\alpha'}+p\omega}+\frac{1}{\varepsilon_\alpha-\varepsilon_\gamma-q\omega}\right)\\
&\quad+\frac{2}{(\varepsilon_\alpha-\varepsilon_\gamma-q\omega)(\varepsilon_\beta-\varepsilon_{\alpha'}+p\omega)}\Bigg].
\end{aligned}\tag{S35}$$

Būtina skleidinio (S21) konvergavimo sąlyga yra

$$r\equiv\frac{|\langle\alpha'|\hat{H}_{a-a'-n}|\alpha\rangle|}{|\varepsilon_{\alpha'}^{(0)}-\varepsilon_\alpha^{(0)}-n\omega|}\ll 1,\tag{S36}$$

kuri turi galioti visoms būsenoms $|\alpha\rangle$, $|\alpha'\rangle$ ir visiems sveikiesiems skaičiams n, išskyrus rezonansinius atvejus, pašalintus sumavimuose (S34) ir (S35) lygtyse.

Teorijos tikslumą patikrinsime lygindami kvazienergijų spektrus, gautus diagonalizuojant $\hat{W}_{\mathrm{D}}^{[3]}$, su skaitiškai tiksliais. Skaitiškai tiksliuosius spektrus skaičiavome diagonalizuodami vieno periodo evoliucijos operatorių, gaunamą propaguojant Šriodingerio lygtį [17]. Taip pat lyginsime rezultatus su gautais taikant standartinę trečios eilės išsigimusią perturbacijos teoriją (DPT) [109, 157]. Teoriją taikysime žadinamam Bozė ir Hubardo (BH) modeliui, kurį aprašo hamiltonianas

$$\hat{H}'(t)=-J\sum_{\langle ij\rangle}\hat{a}_i^\dagger\hat{a}_j+\frac{U}{2}\sum_j\hat{n}_j(\hat{n}_j-1)+\sum_j\hat{n}_jx_jF\cos\omega t.\tag{S37}$$

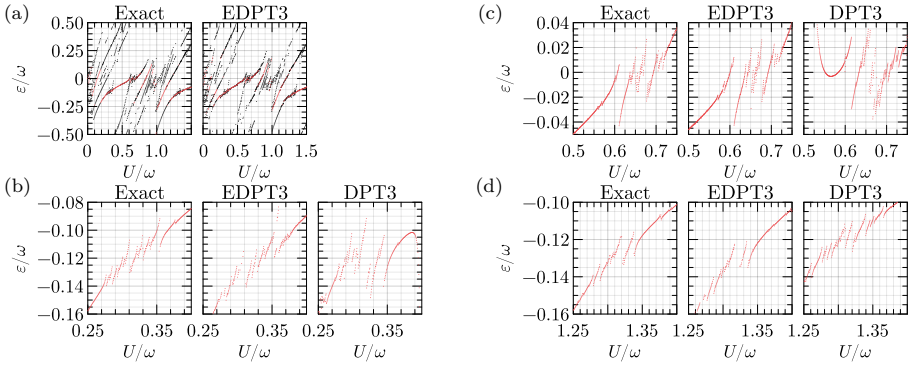

S3 pav.: Aštuonių dalelių BH sistemos DPT ir EDPT tikslumo įvertinimas 2×4 gardelėje, kai $F/\omega = 2$, $\omega/J = 20$. (a) Kvazienergijos spektras kai $U \in [0, 1.5\omega]$. Pateiktos dešimties Flokė modų, turinčių didžiausią sanklotą su MI būsena, kvazienergijos; modos su didžiausia sanklota kvazienergijos paryškintos raudonai. Kiti grafikai rodo žadinamos MI būsenos kvazienergijas (b) $U = \frac{1}{3}\omega$, (c) $U = \frac{2}{3}\omega$ ir (d) $U = \frac{4}{3}\omega$ aplinkoje.

Čia J kontroliuoja artimiausių kaimynų tuneliavimo stiprius, U – bozonų sąveikos energijos stiprį, F – išorinio žadinimo stiprį. Metodų tikslumo analizė atliekama pasirenkant žadinimo stiprį F ir dažnį ω ir skaičiuojant kvazienergijas varijuojant U. Sutelksime dėmesį į „žadinamą Moto izoliatoriaus (MI) būseną“, kuria vadinsime Flokė būseną, turinčią didžiausią sanklotą su MI būsena. Tai yra pagrindinė neperturbuotos sistemos būsena kai $U \gg J$, atitinkanti energiją $E = 0$.

Panagrinėkime metodų tikslumus studijuodami BH sistemą, apibrėžtą 2×4 periodinėje gardelėje su 8 bozonais; tegul $F/\omega = 2$ ir $\omega/J = 20$. Grafikai S3(a) paveiksle parodo kvazienergijas dešimties Flokė modų, turinčių didžiausią sanklotą su MI būsena kai $U \in [0, 1.5\omega]$. Žadinamos MI būsenos kvazienergijos paryškintos raudonai. Kairysis grafikas rodo tikslius rezultatus, o dešinysis – gautus naudojant trečios eilės EDPT. Tuo tarpu DPT metodas gali būti taikomas tik tam tikro rezonanso aplinkoje, ir negali būti naudojamas kvazienergijų skaičiavimui plačiame U intervale. Ryškiausias antikrosingas, matomas ties $U \approx \omega$, atitinka pirmos eilės procesą – dalelės ir skylės sužadinimą MI būsenoje, kai dalelė „peršoka“ iš vieno mazgo į kaimyninį [155]. Kai $U = \omega$, perėjimai tarp visų sistemos lygmenų tampa rezonansiniai, todėl visi diagonalieji $\bar{Q}'$ elementai tam tikrame diagonaliniame bloke turi tą pačią vertę. Atitinkamai, kvazienergijos pakankamai tiksliai aprašomos jau pirmos eilės nariu (S33). Antros ir trečios eilės pataisos prie $\hat{W}_{\mathrm{D}}$ suteikia nedidelį rezultatų patikslinimą ir visumoje lemia puikų sutapimą su tiksliais rezultatais, kaip matyti S3(a) pav. Paminėtina, kad EDPT rezultatai išlieka pakankamai tikslūs ir nutolstant nuo rezonanso.

Toliau išanalizuokime žadinamos MI būsenos kvazienergijas rezonanso $U = \frac{1}{3}\omega$ aplinkoje [žr. S3(b) pav.]. Stebimas antikrosingas yra antros eilės proceso rezultatas, kuomet dvi dalelės iš MI būsenos peršoka į jų bendrojo kaimyno mazgą, tokiu būdu sukuriant trigubai užimtą mazgą ir lemiant būsenos energiją $E = 3U$. Antikrosingo egzistavimą nurodo tiek EDPT, tiek DPT, nors sutapimas su tiksliais rezultatais yra tik kokybinis. Tuo tarpu atvejais $U = \frac{2}{3}\omega$ ir $U = \frac{4}{3}\omega$ EDPT leidžia pasiekti didesnį tikslumą, suteikiant pastebimą tikslumo pagerinimą lyginant su DPT [žr. S3(c) ir (d) pav.].

Išvados

Apibendrinkime rezultatus. Pateikėme standartinės išsigimusios perturbacijos teorijos išplėtimą, kuris pagerina periodiškai žadinamų sistemų kvazienergijų spektrų skaičiavimo tikslumą. Teorijos taikymas žadinamai BH sistemai parodė, kad trečios eilės EDPT duoda rezultatus, kurie kiekybiškai atitinka tikslius rezultatus. Nors tikslų teorijos taikymo kriterijų sunku suformuluoti, paprasta sąlyga (S36) kartu su pateiktais skaičiavimo pavyzdžiais gali būti naudojami tikslumui numatyti. Bendru atveju, teorijos tikslumas bus tuo didesnis, kuo aukštesnis žadinimo dažnis.

Atlikta analizė parodė, kad naudojant DPT gautų kvazienergijų tikslumas yra gerokai mažesnis nei EDPT. Be to, DPT gali būti taikoma tik esant rezonansui, o EDPT išlieka naudinga net jei žadinimas nėra rezonansinis. Tačiau EDPT privalumai atsiranda padidėjusių skaitinių resursų sąskaita, nes gaunamas efektyvinis hamiltonianas yra tokio pat dydžio kaip ir neperturbuotas. Didelėms sistemoms diagonalizavimas tampa pernelyg brangus, todėl gali tekti sumažinti nagrinėjamų būsenų skaičių, pavyzdžiui, neįtraukiant aukštai sužadintų būsenų. Kita galimybė – pritaikyti schemą, kuri yra tarpinė tarp DPT ir EDPT, kad tiksliai būtų įskaitomos tik kai kurios sąveikos tarp būsenų Flokė zonoje, o kitos būtų įskaitomos perturbatyviai. Atitinkamas formalizmas buvo pateiktas šiame darbe.

Optiškai sukurti lokalizuoti sūkuriai kelių komponenčių Bozė ir Einšteino kondensatuose

Šiame skyriuje tirsime kelių komponenčių Bozė ir Einšteino kondensato (BEK) sąveiką su šviesos laukais Λ tipo konfigūracijoje. Naudodami šviesos pluoštus, turinčius orbitinį impulso momentą, teoriškai parodysime, kaip sukurti stabilią sūkurio konfigūraciją tokią, kad besisukančios komponentės atomai būtų apsupti antrosios, besūkurės komponentės atomais. Sūkurį sudarantys atomai gali būti lokalizuoti daug mažesniame erdvės tūryje lyginant su antrosios komponentės atomų užimamu turiu. Taip pat parodysime, kad sūkurio padėtį galima keisti dinamiškai, judinant lazerio pluoštus, jei pluoštus judėjimo greitis išlieka mažesnis už garso greitį. Tai leidžia naudoti lokalizuotą sūkurį antrosios komponentės maišymui, ir nustatyti supertakumo kritinį greitį.

Nagrinėsime trijų lygmenų atominę sistemą Λ tipo atomo ir šviesos sąveikos konfigūracijoje, parodytoje S4 pav. [9, 10, 202, 203, 193–195, 204]. Šviesos pluoštai lemia priklausančius nuo koordinatės būsenų sukabinimus ir yra aprašomi Rabi dažniais

$$\begin{aligned} \Omega_1(\boldsymbol{r}) &= \Omega_0 \left(\frac{\rho}{a}\right)^s \mathrm{e}^{-\rho^2/w_0^2} \mathrm{e}^{\mathrm{i}k_z z + \mathrm{i}s\varphi}, \\ \Omega_2(\boldsymbol{r}) &= \Omega_0 \mathrm{e}^{-\rho^2/w_0^2} \mathrm{e}^{\mathrm{i}k_z z}, \end{aligned} \tag{S38}$$

čia naudojama cilindrinė koordinačių sistema $\boldsymbol{r} = (\rho, \varphi, z)$, w_0 žymi pluošto diametrą, Ω_0 yra Rabi dažnių amplitudė, o k_z – pluoštų banginis skaičius, aprašantis paraksialinį sklidimą palei z ašį [10, 203, 202]. Ilgio dimensijos parametras a kontroliuoja pirmojo pluošto intensyvumo kitimą erdvėje. Pluoštas, charakterizuojamas Ω_1 dažniu, sukabina atomo vidines būsenas $|1\rangle$ bei $|3\rangle$ ir atitinka Lagero ir Gauso modą LG_0^s su topologiniu krūviu $s > 0$ [205, 206, 198, 200, 207–211]. Tuo tarpu būsenos $|2\rangle$ bei $|3\rangle$ yra sukabintos Gauso pluoštu, aprašomu Rabi dažniu Ω_2.

Kondensatą aprašysime Groso ir Pitajevskio lygčių (GPL) sistema [167], užrašyta trijų komponenčių atveju

$$\begin{aligned} \mathrm{i}\hbar\frac{\partial}{\partial t}\Phi_1 &= \left(-\frac{\hbar^2}{2m}\Delta + V + g_{11}|\Phi_1|^2 + g_{12}|\Phi_2|^2\right)\Phi_1 + \hbar\Omega_1^*\Phi_3, \\ \mathrm{i}\hbar\frac{\partial}{\partial t}\Phi_2 &= \left(-\frac{\hbar^2}{2m}\Delta + V + g_{12}|\Phi_1|^2 + g_{22}|\Phi_2|^2\right)\Phi_2 + \hbar\Omega_2^*\Phi_3, \\ \mathrm{i}\hbar\frac{\partial}{\partial t}\Phi_3 &= \left(-\frac{\hbar^2}{2m}\Delta + V - \delta - \mathrm{i}\frac{\Gamma}{2}\right)\Phi_3 + \hbar\Omega_1\Phi_1 + \hbar\Omega_2\Phi_2. \end{aligned} \tag{S39}$$

Čia $V(\boldsymbol{r})$ yra gaudyklės kuriamas potencialas, m – atomo masė, δ – būsenų $|1\rangle$ ir $|3\rangle$ sukabinimo išderinimas (žr. S4 pav.), Γ – būsenos $|3\rangle$ spontaninio

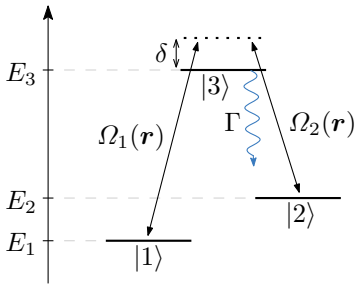

S4 pav.: Λ tipo schema.

spinduliavimo sparta. Atomų sąveikos su trečia komponente Φ_3 nėra įskaitytos laikant, kad šios komponentės užpilda yra nykstamai maža visais laikais. Tai galioja toliau nagrinėjamu atveju, kai atomai adiabatiškai seka tamsinę būseną. Koeficientai g_{ij}, charakterizuojantys atomų sąveiką, yra skaičiuojami iš sklaidos ilgio a_{ij} pagal $g_{ij} = 4\pi\hbar^2 a_{ij}/m$. Daugiakomponentė BEK banginė funkcija yra normuota į pilnąjį dalelių skaičių, $\sum_{i=1}^{3} \int \mathrm{d}^3 r\, |\Phi_i|^2 = N$. Toliau taip pat naudosime parametrus η_i, charakterizuojančius komponenčių santykines užpildas:

$$\eta_i = \frac{1}{N} \int |\Phi_i|^2 \, \mathrm{d}^3 r. \tag{S40}$$

Siekdami gauti lygtį atomams, adiabatiškai sekantiems tamsinę būseną, įvedame šitokias Φ_1 ir Φ_2 funkcijų superpozicijas:

$$\begin{aligned} \Phi_\mathrm{D} &= \frac{1}{\sqrt{1+|\zeta|^2}}(\Phi_1 - \zeta^* \Phi_2), \\ \Phi_\mathrm{B} &= \frac{1}{\sqrt{1+|\zeta|^2}}(\zeta \Phi_1 + \Phi_2), \end{aligned} \tag{S41}$$

čia

$$\zeta(\boldsymbol{r}) = \frac{\Omega_1(\boldsymbol{r})}{\Omega_2(\boldsymbol{r})} = \left(\frac{\rho}{a}\right)^s \mathrm{e}^{\mathrm{i}s\varphi}. \tag{S42}$$

Darydami adiabatinę prielaidą, kad atomų masių centro judėjimas yra daug lėtesnis už perėjimų tarp vidinių būsenų procesą, ir laikydami, kad visos netiesinės sąveikos yra lygios ($g_{11} = g_{12} = g_{22} = g$), gauname GPL tamsinei būsenai [202]

$$\mathrm{i}\hbar \frac{\partial}{\partial t} \Phi_\mathrm{D} = \frac{1}{2m}(-\mathrm{i}\hbar\nabla - \boldsymbol{A})^2 \Phi_\mathrm{D} + (U+V)\Phi_\mathrm{D} + g|\Phi_\mathrm{D}|^2 \Phi_\mathrm{D}. \tag{S43}$$

Kadangi ši lygtis funkcijai Φ_D atsikabino nuo lygties spinduliuojančiai būsenai Φ_3, o pati funkcija Φ_D yra tik funkcijų Φ_1 ir Φ_2 superpozicija, būsena Φ_D yra apsaugota nuo populiacijos mažėjimo spinduliavimo kanalu.

Lygtyje (S43) atsiranda geometriniai kalibraciniai potencialai, kurie pasi-

rinktų pluoštų (S38) atveju įgyja pavidalą

$$\begin{aligned} \boldsymbol{A} &= -\frac{\hbar s}{a}\frac{\left(\frac{\rho}{a}\right)^{2s-1}}{1+\left(\frac{\rho}{a}\right)^{2s}}\boldsymbol{e}_{\varphi}, \\ U &= \frac{1}{m}\left(\frac{\hbar s}{a}\right)^{2}\frac{\left(\frac{\rho}{a}\right)^{2s-2}}{\left[1+\left(\frac{\rho}{a}\right)^{2s}\right]^{2}}, \end{aligned} \tag{S44}$$

čia $\boldsymbol{e}_{\varphi}$ yra vienetinis vektorius azimutine kryptimi.

Dabar panagrinėsime stacionarias kondensato būsenas, kuomet komponenčių banginės funkcijos turi pavidalą $\Phi_i(\boldsymbol{r},t) = \mathrm{e}^{-\mathrm{i}\mu t}\psi_i(\boldsymbol{r}) = \mathrm{e}^{-\mathrm{i}\mu t}f_i(\rho)\mathrm{e}^{\mathrm{i}\ell_i\varphi}$, čia μ – cheminis potencialas. Žemiau bus parodyti rezultatai, gauti sprendžiant pilnąją sistemą (S39) tam, kad būtų įskaityti skirtingi sąveikos stipriai g_{ij}. Skaičiavimai rodo, kad priėmus, jog visos sąveikos yra vienodos, sistemos sprendiniai sutampa su gaunamais sprendžiant tamsinės būsenos lygtį (S43). Tai reiškia, kad adiabatinė prielaida iš tikrųjų galioja nagrinėjamų parametrų verčių atveju.

Analizuosime BEK cilindrinėje radiuso R gaudyklėje ir studijuosime kvazidvimatį kondensatą fiksuoto z plokštumoje. Toliau naudosime bedimensius matavimo vienetus, matuodami ilgį R vienetais ir energiją $E_R = \hbar^2/2mR^2$ vienetais. Atvejis, kai $a = 0.02 \ll R$ ir $s = 1$ pristatytas S5 pav. Kaip matyti S5(a) pav. apatiniame grafike, ρA_{φ} artėja prie $-s$ vertės vos tik nutolus nuo koordinačių pradžios, todėl (S43) lygties pagrindinės būsenos sprendinys turi pavidalą $\Phi_{\mathrm{D}} \sim \mathrm{e}^{\mathrm{i}\ell\varphi}$ su $\ell = -s = -1$. Grįždami prie komponenčių Φ_1 ir Φ_2 gauname, kad antroji būsena yra besūkurė, o pirmoji komponentė yra sūkurinėje būsenoje ir ji yra stipriai lokalizuota arti koordinačių pradžios [žr. S5(b) pav.]. Tiksliau, pirmos komponentės tankis yra sukoncentruotas srityje, kurios plotis yra ξ_2 eilės, čia $\xi_2 = \sqrt{S/g_{22}} = 0.086$ yra antrosios komponentės koherentiškumo ilgis. Sūkurio lokalizacija yra nulemta $\frac{1}{\sqrt{1+|\zeta|^2}}$ nario [žr. (S41) lygtį], kuris faktiškai užgesina sūkurį, kai $\rho \gg a$. Tai taip pat lemia mažą pirmos komponentės populiaciją, kuri siekia $\eta_1 = 0.25\%$. Mažinant parametrą a galima labiau lokalizuoti sūkurį, tačiau tuo pačiu mažėja jį sudarančių atomų skaičius.

Pirmoji sužadinta kondensato būsena, parodyta S5(c) pav., atitinka atvirkštinį atvejį – antroji komponentė yra sūkurinėje būsenoje, o sūkurio centre lokalizuoti pirmosios komponentės atomai. Antroji sužadinta būsena yra parodyta S5(d) pav. Šios dvi būsenos atitinka (S43) lygties $\ell = 0$ ir $\ell = -2$ sprendinius ir yra beveik išsigimusios.

Dabar panaudosime lokalizuotą sūkurį, esantį pirmojoje komponentėje, kaip zondą, leidžiantį nustatyti antrosios komponentės kritinį supertakumo greitį v_{c}. Tokiu atveju sūkurys veikia kaip priemaiša, kuri gali judėti be pasipriešinimo,

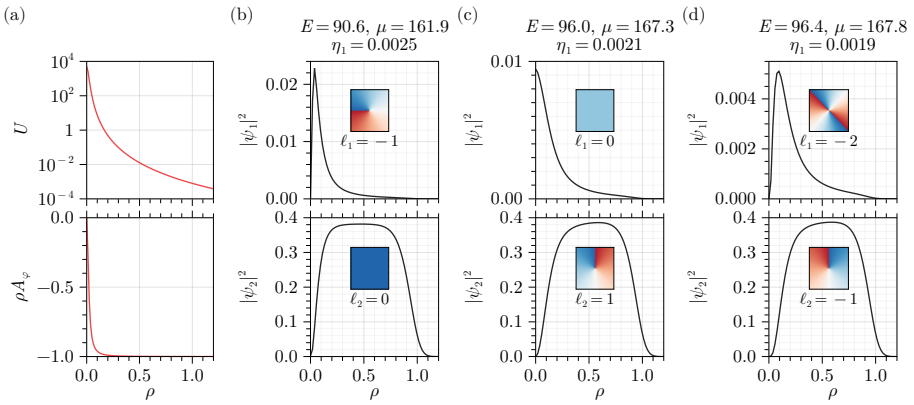

S5 pav.: Potencialai U ir ρA_φ ir (S39) sistemos sprendiniai atveju $s = 1$ ir $a = 0.02$. (a) Potencialai U ir ρA_φ (b), (c) ir (d) rodo, atitinkamai tris žemiausios energijos sistemos (S39) sprendinius; banginės funkcijos sunormuotos pagal $\sum_{i=1}^{3} \int_S |\psi_i|^2 \,\mathrm{d}S = 1$. Trečios komponentės užpilda yra nykstamai maža visais atvejais, todėl ji nėra rodoma. Dėl šios priežasties galima laikyti, kad antrosios komponentės populiacija $\eta_2 = 1 - \eta_1$. Komponenčių topologiniai krūviai ℓ_i yra nurodyti žemiau atitinkamų dvimačių grafikų, rodančių komponenčių fazinius profilius xy plokštumoje. Fazė yra koduojama spalvomis šitaip: tamsiai mėlyna $= -\pi$, balta $= 0$, tamsiai raudona $= \pi$.

jei jos greitis išlieka mažesnis nei v_c. Remiantis Landau kriterijumi, kondensato fononinis sužadinimo spektras nustato kritinį greitį, lygų garso greičiui v_s [168]. Mūsų atveju turime $v_\mathrm{s} = \hbar/(m\xi_2\sqrt{2}) = 400\,\mu\mathrm{m/s}$. Tačiau tiek eksperimentiniai rezultatai [91, 92, 94, 95], tiek teoriniai tyrimai [96–98] nurodo į tai, kad v_c paprastai yra mažesnis, priklausomai nuo tokių faktorių kaip priemaišos dydis [94], priemaišos kuriamo potencialo pobūdis (pritraukiantis ar stumiantis) [96] ir priemaišų trajektorija (linijinė arba apskritiminė) [96, 98]. Norėdami įvertinti v_c mūsų sistemoje, modeliuojame sūkurio judėjimą apskritimine spindulio 0.5 trajektorija, judindami lazerių pluoštus 0.1 s laiko intervale tiesiniu greičiu v. Fiksuojame energiją $E(t)$, tenkančią vienai dalelei, ir aprašome ją tiesine funkcija, kad gautume energijos didėjimo greitį $\kappa = \mathrm{d}E/\mathrm{d}t$. Kadangi pirmosios komponentės populiacija yra daug mažesnė nei antrosios, $E(t)$ faktiškai atspindi atomų energiją antrojoje komponentėje. Rezultatai, gauti lazerių judėjimo greičių v intervale nuo $0.1v_\mathrm{s}$ iki $1.2v_\mathrm{s}$ parodyti S5 pav., kur atskleidžiamas aiškus slenkstinis elgesys – κ sparčiai didėja, kai greitis viršija tam tikrą kritinę vertę. Šią vertę nustatome aprašydami duomenis funkcija

$$\kappa(v) = \kappa_0 + b \max(v^2 - v_\mathrm{c}^2, 0), \tag{S45}$$

čia κ_0, b ir v_c yra laisvieji optimizavimo parametrai. Ši priklausomybė tinka 2D sistemų aprašymui [93] ir yra sėkmingai taikoma eksperimentinių duomenų analizei [94, 97]. Optimizavimo metu buvo gauta vertė $v_\mathrm{c} = 0.8v_\mathrm{s}$; atitinkama

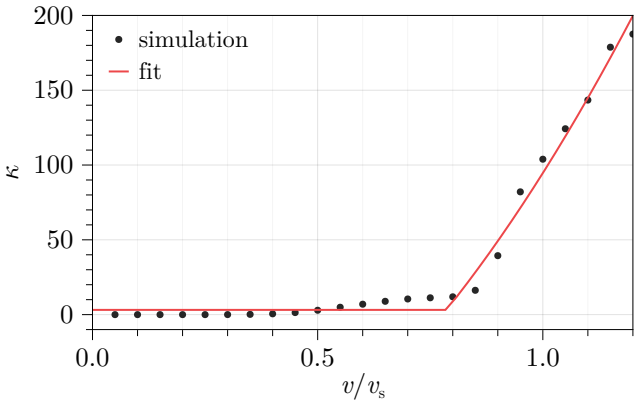

S6 pav.: Kondensato energijos didėjimo greičio priklausomybė nuo pluoštų judėjimo greičio.

kreivė yra parodyta S5 pav. Kaip ir buvo tikėtasi, gautas kritinis greitis yra mažesnis už garso greitį.

Išvados

Reziumuojant, mes ištyrėme dviejų komponenčių BEK sąveiką su šviesos laukais Λ tipo konfigūracijoje ir ištyrėme stacionariąsias tamsines būsenas. Vieno iš dviejų lazerio pluoštų nešamas orbitinis impulso momentas $s\hbar$ per fotoną lemia tai, kad viena arba abi komponentės yra sūkurinėse būsenose, o jų topologiniai krūviai skiriasi s vienetais. Režime $a \ll R$ stacionariųjų būsenų struktūrą lemia vektorinio potencialo narys. Šioje riboje, $\boldsymbol{A}$ artėja prie $-\frac{s}{\rho}\boldsymbol{e}_\varphi$ ir jo indėlis į greičio lauką (taigi ir į kinetinę energiją) gali būti sukompensuotas, jei tamsinė būsena aprašoma bangine funkcija $f(\rho)\mathrm{e}^{-\mathrm{i}s\varphi}$. Mes parodėme, kad žemiausios energijos tamsinė būsena iš tiesų turi tokią formą. Šiuo atveju pirmoji komponentė (sąveikaujanti su LG pluoštu) turi sūkurį, kurio topologinis krūvis yra s, o antroji komponentė yra besūkurė. Sūkurio centras sutampa su pluošto centru, o sūkurio tankio profilis rodo stiprų lokalizacijos laipsnį, kadangi tankis mažėja tolstant nuo sūkurio centro kaip $[1 + (\rho/a)^2]^{-1/2}$. Tokį sūkurį galima judinti aplink gaudyklę judinant lazerio spindulius. Jei judėjimo greitis yra mažesnis nei maždaug pusė garso greičio antrojoje komponentėje, sūkurio forma judėjimo metu išlaiko savo struktūrą, o antrosios komponentės tankis neiškraipomas. Tiksliau sakant, judinant sūkurį greičiu, mažesniu už kritinę vertę, lygia $0.8v_\mathrm{s}$, kondensato energija beveik nedidėja, o tai rodo jo supertakų pobūdį.

Vilnius University Press
Saulėtekio av. 9, III bld., LT-10222 Vilnius
info@leidykla.vu.lt, www.leidykla.vu.lt
www.bookshop.vu.lt, www.journals.vu.lt
Print run: 15

NUO / SINCE 1579

Fragmentas iš Vilniaus universiteto auklėtinio Alberto Diblinskio (1601–1665) vieno geriausių XVII a. astronomijos veikalų *Centuria astronomica* (Vilnius, 1639), kuriame pateikta astronomijos pasiekimų apžvalga, remiantis stebėjimais teleskopu, atliktais kartu su kitu VU mokslininku, matematiku ir astronomu Osvaldu Krygeriu (apie 1598–1655).

VU biblioteka, BAV 47.10.21

Fragment from *Centuria astronomica* (Vilnius, 1639), one of the most well-known works on astronomy from the 17th c., written by Vilnius University graduate Albertas Diblinskis (1601–1665). It presents an overview of achievements in the field of astronomy, based on observations using a telescope together with another VU scientist, mathematician, and astronomer Osvaldas Krygeris (c. 1598–1655).

VU Library, BAV 47.10.21

https://doi.org/10.15388/vu.thesis.860